7-2021

Applications of MASW and MHVSR Techniques for Infrastructure Evaluation with a Focus on the Effects of Different Transformation Techniques and Near-field Effects on Derived Dispersion Data

Salman Rahimi
University of Arkansas, Fayetteville

Citation
Rahimi, S. (2021). Applications of MASW and MHVSR Techniques for Infrastructure Evaluation with a Focus on the Effects of Different Transformation Techniques and Near-field Effects on Derived Dispersion Data. *Graduate Theses and Dissertations* Retrieved from https://scholarworks.uark.edu/etd/4128

Applications of MASW and MHVSR Techniques for Infrastructure Evaluation with a Focus on the Effects of Different Transformation Techniques and Near-field Effects on Derived Dispersion Data

A dissertation submitted in partial fulfillment
of the requirements for the degree of
Doctor of Philosophy in Engineering with a concentration in Civil Engineering

by

Salman Rahimi
Ferdowsi University of Mashhad
Bachelor of Science in Civil Engineering, 2005
University of Tehran
Master of Science in Geotechnical Engineering, 2013

July 2021
University of Arkansas

This dissertation is approved for recommendation to the Graduate Council.

Clinton M. Wood, PhD.
Dissertation Director

Liam Wotherspoon, Ph.D.
Committee Member

Christopher L. Liner, Ph.D.
Committee Member

Sarah V. Hernandez, Ph.D.
Committee Member

Michelle L. Barry, Ph.D.
Committee Member

Abstract

This dissertation is aimed at understanding two aspects of active surface wave methods to improve the accuracy and reliability of this method. These include (1) the performance of four common wavefield transformation methods for the multichannel analysis of surface wave (MASW) data processing and (2) near-field effects. Toward this end, extensive field measurements were conducted considering different factors affecting these two topics. The MASW and microtremor horizontal to vertical spectral ratio (MHVSR) were then employed to examine their efficiency for infrastructure health monitoring.

Regarding the performance of the four common transformation techniques, it was observed that for sites with a very shallow and highly variable bedrock topography with a high-frequency point of curvature (>20 Hz), the Phase Shift (PS) method leads to a very poor-resolution dispersion image compared to other transformation methods. For sites with a velocity reversal, the Slant Stack (τp) method fails to resolve the dispersion image for frequencies associated with layers located below the velocity reversal layer. Overall, the cylindrical frequency domain beamformer (FDBF-cylindrical) method was determined to be the best method under most site conditions. This method allows for a stable, high-resolution dispersion image for different sites and noise conditions over a wide range of frequencies, and it mitigates the near-field effects by modeling a cylindrical wavefield. However, the FDBF-cylindrical was observed to be dominated by higher modes at complex sites. Therefore, the best practice is to use more than one transformation method (FDBF-cylindrical and FK methods) to enhance the data quality.

Regarding the near-field effects for active surface wave methods, it was observed that near-field effects are independent of surface wave type (Rayleigh and Love) and depth to

impedance contrast. For sites with a very shallow impedance contrast, the FDBF-cylindrical transformation technique outperforms others in terms of dispersion resolution by significantly mitigating near-field effects. It is also revealed that source type is an important parameter, influencing the normalized array center distance criteria required to mitigate near-field effects. The best practical criteria for near-field mitigation include a normalized array center distance of 1.0 or greater for low-output impulsive sources such as a sledgehammer and a normalized array center distance of 0.5 for high-output harmonic sources such as a vibroseis. These criteria should not be violated when using a limited number of source offsets (≤2). But, if the multiple source offset approach (≥3 source offsets) is used where some of the source offsets meet the criteria, the near-field criteria can be violated for other source offsets. Additionally, it is recommended to use the multiple source offset approach along with the FDBF-cylindrical for data processing to mitigate near-field effects.

For health monitoring of earthen hydraulic infrastructures, MASW was determined to be effective for detecting weak zones of such structures. In this regard, it is very important to use the reference shear wave velocity profiles to avoid misinterpretation of the results. Additionally, the grid pattern MHVSR method was determined to very effective for landslide evaluations for sites with shallow and complex bedrock topography, where bedrock is a key feature in the slope stability model.

Acknowledgment

I would like to express my sincere gratitude to my advisor, Dr. Clinton M. Wood, for his guidance, inspiration, and continuous support during my doctoral studies. It was my honor to work with him closely, and I genuinely believe that he is a perfect model of a knowledgeable advisor, researcher, and teacher. He supported me in all the way possible, not only as my advisor but also as a friend. I greatly appreciate the time, effort, and funding he provided to make my Ph.D. study as productive as possible.

I would like to thank my committee members, Dr. Christopher L. Liner, Dr. Michelle L. Barry, Dr. Sarah V. Hernandez, and Dr. Liam Wotherspoon, for their valuable comments and suggestions.

I would like to also thank my fellow graduate students at the Geotechnical Earthquake Engineering Laboratory at the University of Arkansas, who helped me along the way.

Also, thank you to several funding agencies for their financial support. This dissertation is based on works supported by the Arkansas Department of Transportation (ARDOT) under Project TRC1803, the U.S. Geological Survey under Grant No. G18AP00078, and U.S. Department of Transportation under Grant Award Number DTRT13-G-UTC50 for the Maritime Transportation Research and Education Center at the University of Arkansas.

Finally and above all, I would like to thank my wonderful wife and son for their love and encouragement during this period. This work would not have been possible without their help and support. I also like to thank my family and family-in-law for their patience and encouragement.

Dedication

This dissertation is dedicated to my wife, Atiyehsadat, my son, Aaron, my parents, sister, brother, and family-in-law. Without their love, support, encouragement, and understanding, I could not have finished this work.

Table of Contents

List of Figures

List of Tables

List of publications

Chapter 3: Rahimi, S., Wood, C. M., Teague, D. P. (2021). Performance of Different Transformation Techniques for MASW Data Processing Considering Various Site Conditions, Near-Field Effects, and Modal Separation. Surveys in Geophysics (under review).

Chapter 4: Rahimi, S., Wood, C. M., Himel, A. K., (2021). Practical Guidelines for Near-field Mitigation on Array-based Active Surface Wave Testing. Geophysical Journal International (under review).

Chapter 5: Rahimi, S., Wood, C. M., Coker, F., Moody, T., Bernhardt-Barry, M., & Kouchaki, B. M. (2018). The combined use of MASW and resistivity surveys for levee assessment: A case study of the Melvin Price Reach of the Wood River Levee. Engineering Geology, 241, 11-24 (published).

Chapter 6: Rahimi, S., Wood, C. M., & Bernhardt-Barry, M. (2021). The MHVSR technique as a rapid, cost-effective, and noninvasive method for landslide investigation: case studies of Sand Gap and Ozark, AR, USA. Landslides, 1-16. (published).

1 CHAPTER 1: INTRODUCTION

1.1 Overview and motivation

Any geotechnical infrastructure failure (e.g. levees, embankment dams) can have severe direct and indirect socio-economic consequences affecting human life. An example of such types of events is the failure of the levees during Hurricane Katrina in New Orleans, in which 85% of Greater New Orleans was flooded, more than 1500 people died, and the total damage cost of this event was approximately $81 billion (Sills *et al.*, 2008). This indicates the urgent need for regular inspection and health monitoring of geotechnical infrastructures to ensure safety during their lifespan and prevent failure of these structures in future events.

The primary step towards health monitoring of geotechnical infrastructures is assessing their current subsurface conditions to detect their potential problematic zone(s), if any exist. Currently, subsurface conditions are commonly assessed using various field measurements, including but not limited to Standard Penetration Test (SPT), Cone Penetration Test (CPT), Pressuremeter Test (PMT), and Flat Dilatometer Test (DMT). These methods provide an acceptable level of accuracy for sites where soil and rock layers are consistent in depth and thickness, but significant errors can occur when conditions are variable across the project area. This is because these methods only provide information regarding subsurface layering and material types at discrete testing locations, and the subsurface conditions are predicted based on engineering judgment between the available discrete testing locations. Additionally, these methods are not ideal for sites that involve rough terrain (e.g. steep slopes) and sites densely covered with trees and bushes (e.g. a proposed highway alignment passing through such areas), as well as for health monitoring of infrastructures such as hydraulic earthen structures (e.g. levees and embankment dams) where invasive field tests are typically discouraged. Therefore, in order to fully assess the subsurface conditions for such project sites, there is a dire need for methods capable of providing an accurate 2D or 3D image of subsurface conditions. In this regard, geophysical methods can be considered a suitable candidate capable of fulfilling all the above-mentioned criteria.

Various geophysical techniques can be employed to monitor and assess the performance of geotechnical infrastructures. Of these techniques, seismic stress wave methods and electrical-based methods are commonly used in the literature for geotechnical applications (Tingey *et al.*, 2007; Naudet *et al.*, 2008; Sjödahl *et al.*, 2010; Panzera *et al.*, 2012; Samyn *et al.*, 2014). Using these methods, a continuous image of subsurface conditions can be acquired in a rapid, cost-effective, and non-invasive manner. Furthermore, these methods can be easily implemented for different site conditions, where conventional field measurements are difficult to make.

Among seismic stress wave methods, MASW is becoming the most popular technique among researchers and practitioners in the geotechnical community. This is due to its non-invasive nature, and more importantly, its accuracy, effectiveness, rapidness, and low cost for near-surface site characterization, which is the target depth for the majority of geotechnical projects. Initially, the MASW method was utilized to retrieve a 1D shear wave velocity profile. However, nowadays, this method has been employed for a variety of geotechnical applications, including but not limited to 1D site characterization (Rix *et al.*, 2002), 2D or 3D subsurface imaging (Ismail *et al.*, 2014; Pilecki *et al.*, 2017; Rahimi *et al.*, 2019a), landslide evaluation (Harba *et al.*, 2019); rock rippability estimation (Rahimi et al. 2021), infrastructure evaluation (Cardarelli *et al.*, 2014), V_{S30} estimation (Comina *et al.*, 2011; Martinez-Pagan *et al.*, 2012; Rahimi *et al.*, 2020c), and soil liquefaction prediction (Mahvelati *et al.*, 2020a; Rahimi *et al.*, 2020a). Despite the increasing popularity of the MASW method for geotechnical applications over the past years, several aspects of this method still require studies to further improve the capabilities of this method.

The two main aspects of the MASW technique that have not received enough attention in the literature are (1) the effects of different transformation techniques that can be used for data processing for the MASW method on the experimental dispersion curve resolution and (2) near-field effects. In the current practice, researchers and users of the MASW method are blindly selecting one of the transformation techniques for data processing due to the lack of information regarding the advantages and limitations of each transformation technique. This sometimes results in significant mispredictions of the shear wave velocity profile retrieved from the MASW method. Another common issue with the current practice for data processing of the MASW method is near-field corruption, which limits its applications in the geotechnical and geophysical communities. In this regard, no suitable criteria are available in the literature that allows mitigating near-field effects for various conditions that might be encountered during field measurements.

Therefore, the main focus of this dissertation is to investigate these topics for the MASW technique and then apply this method for health monitoring of geotechnical infrastructures. In addition to the MASW method, the single station Microtremor Horizontal to Vertical Spectral Ratio (MHVSR) is also utilized to investigate their efficiency for geotechnical infrastructure evaluation. Therefore, two main topics are considered in this dissertation: (1) investigating several aspects of the MASW method to advance our knowledge in this regard and establish the best practice guideline for this method and (2) applying this method along with some other geophysical methods for geotechnical infrastructure evaluations.

1.2 Current issues with the MASW technique

In this dissertation, two important topics that have rarely been investigated in the literature for the MASW technique are studied.

1- *<u>Effects of different transformation techniques on the derived dispersion data (dispersion curve):</u>* Construction of the experimental dispersion curve is one of the most important parts of MASW data processing, which controls the final results. The higher the resolution of the experimental dispersion curve, the higher the accuracy and the reliability of the final inverted shear wave velocity profile. Four different transformation methods are commonly used for developing the experimental dispersion curve. To date, no study has comprehensively investigated the advantages, limitations, and differences of these transformation methods for developing the experimental dispersion curve. It is currently assumed that the four transformation methods result in the same resolution experimental dispersion image. Therefore, the transformation method is selected blindly by users and researchers for MASW data processing without considering the subsurface layering, wavefield, and noise conditions. To fill in the gap in our knowledge in this regard, in this dissertation, the performance of each transformation method is evaluated for developing the experimental dispersion curve for sites with different conditions. Toward this end, more than 500 MASW measurements were collected for sites with different subsurface and wavefield conditions (e.g. sites with a deep bedrock layer, sites with a shallow bedrock layer, sites with a velocity reversal layer, sites with or without considerable environmental noise, and sites with clear near field effects). The sites were carefully selected so that the collected data can be used first for investigating the performance of different transformation techniques for MASW data processing and then for further processing regarding the efficiency of the MASW method for geotechnical infrastructure evaluation. Two sites are considered to examine the capabilities of the MASW method for geotechnical infrastructure evaluation. These include a levee system that has recently experienced significant sand boil issues (Melvin-Price reach of the Wood River Levee), and an active landslide that has recently experienced considerable movements within the slope (Ozark Landslide). Therefore, the MASW data collected for these sites are used to develop the experimental dispersion curve using different transformation methods to identify their resolution differences for various site conditions and then used for further processing for health monitoring of geotechnical infrastructures.

2- *Near-field effect*: Near-field effect is one of the main issues in the MASW method corrupting the low-frequency portion of the experimental dispersion data. The low-frequency dispersion data are of significant importance because they have the information regarding deeper subsurface layers (e.g. stiff soils or bedrock units). The dispersion data corrupted with the near-field effects should not be used for the inversion process to retrieve 1D Vs profiles. However, sometimes it is not easy to detect the data corrupted with near-field effects, and therefore the inclusions of these data in the inversion process lead to mispredictions of the subsurface layers' properties. It is, therefore, critical to be able to mitigate the near-field effects in the MASW technique. Despite the importance of this topic, a limited number of research groups have developed guidelines for near-field mitigations. These guidelines are generally site-specific as they fail to consider different factors influencing near-field effects. Therefore, in this dissertation, near-field effects are investigated considering different site conditions (very shallow and very deep impedance contrasts), surface wave types (Rayleigh and Love), source offsets (i.e. distance between the source location and the first geophone in the array), source type (sledgehammer and vibroseis), and transformation techniques used for data processing. The aim is to establish a reliable, practical guideline for near-field mitigation on array-based active surface wave methods.

1.3 Hypothesis

While the MASW method has been widely used for geotechnical applications in recent years, some aspects of this method are still not fully understood in geotechnical engineering. One aspect of the MASW method that needs further investigation is the differences that may appear in the experimental dispersion curves created using various transformation methods. Since no study has extensively compared the performance of different transformation methods for developing the experimental dispersion curve, it is assumed that their differences are negligible. However, our preliminary work has shown that the resolution of the experimental dispersion data generated using different transformation methods can be different under various subsurface and wavefield conditions. In order to validate this hypothesis, extensive MASW measurements have been conducted at different sites (a levee system, two active landslides, and a proposed highway alignment), and the collected data are used to compare the quality and resolution of the experimental dispersion curves generated using different transformation methods. Sites with different conditions, including sites with a deep bedrock layer, sites with a shallow bedrock layer, sites with a velocity reversal layer, sites with or without considerable environmental noise, and sites with clear near field effects are selected to compare the ability of different transformation methods for developing the experimental dispersion curve.

Another aspect of the MASW method that requires further investigations is the near-field effect. Being able to mitigate such effects is critical as it can enhance the accuracy and reliability of the MASW method. We hypothesize several factors that are generally ignored in the literature, such as subsurface conditions, surface wave types (Rayleigh and Love), source offsets, and source type (sledgehammer and vibroseis), are important for developing accurate, practical guidelines for near-field mitigation. Currently, there is no acceptable practical guideline for near-field mitigation that has been tested for these different conditions. Additionally, the capability of different transformation techniques for near-field mitigation is not fully understood or examined in the previous studies. In order to examine this hypothesis, in this dissertation, the near-field effects are examined considering different conditions with the aim of establishing reliable, practical criteria for mitigating such effects during field measurements.

Therefore, two hypotheses (as mentioned above) are mainly targeted in this dissertation to improve our understanding of several aspects of the MASW technique that needs further investigation. These aspects have been rarely investigated in the literature, even though they are critical for the correct MASW data processing and data interpretation and for improving the reliability of the MASW method. The field data that have been collected to examine these topics are also used for further processing to assess the accuracy and efficiency of the MASW and MHVSR techniques for geotechnical infrastructure evaluation, particularly for sites with complex geology environments. This is important since the current state of practice in geotechnical engineering only provides discrete information regarding subsoil properties, meaning that they are incapable of accurately monitoring geotechnical infrastructure's performance during their life span. Therefore, the geophysical methods may be a suitable alternative to the current state of practice for such purposes. To investigate this hypothesis, two types of geotechnical infrastructures are targeted as below.

1- Melvin-Price levee: a levee system that has experienced considerable piping through the foundation soil, causing numerous sand boils along the landside toe of the levee (Rahimi *et al.*, 2018).
2- Ozark and Sand Gap landslide sites: two active landslides in Arkansas that have experienced considerable slope movements, causing several big cracks within the landslide area.

1.4 Importance of the proposed research for geotechnical and geophysical engineering

The contributions and importance of this dissertation can be divided into three topics: (1) identifying the most suitable transformation technique under different conditions for developing the experimental dispersion curve for active surface wave testing, (2) improving the reliability and accuracy of the MASW method by developing practical guidelines for near-field mitigation, and (3) examining the efficiency of the MASW and MHVSR methods for geotechnical infrastructure evaluation in a rapid, non-invasive, and cost-effective manner. These topics are discussed in more detail below.

Four wavefield transformation techniques are commonly used in MASW data processing for developing the experimental dispersion curve. Researchers and consultants have extensively used these transformation techniques from different institutions and in various software packages. Since no study has compared the performance of these methods under various conditions, it is currently assumed that their differences are negligible. In this dissertation, the performance of the four common transformation methods is compared under various conditions to identify their capabilities for developing experimental dispersion curves. The results of this dissertation benefit researchers and practitioners regarding the advantages and limitations of each transformation method for MASW data processing. This makes a valuable contribution to improving the MASW data processing because it advances our understanding of the most suitable transformation method that should be used for a particular site condition. Additionally, this helps eliminate some potential misinterpretations (e.g. mode misidentification) that often occur in the MASW data processing due to inappropriate transformation technique selection for MASW data processing.

Another contribution of this dissertation to geotechnical and geophysical communities is developing the best practical guidelines to eliminate or reduce near-field effects on array-based active surface wave methods, particularly the MASW method. Advancing our understanding of near-field effects is important for improving the reliability of the active surface wave methods and expanding their applications in geotechnical and geophysical communities. For active surface wave methods, due to high attenuation properties of near-surface layers and limitation in source energy, the common practice is to minimize source offsets (i.e. use shorter source offsets) to acquire a high signal-to-noise ratio. With such array and source offset configurations, the near-field effect is the main issue that leads to a systematic underestimation of the measured phase velocity at low frequencies. This dissertation develops the best practical guidelines for near-field mitigation on active surface wave testing by investigating the influence of all important factors (as mentioned above) on near-field effects. These new guidelines help researchers and practitioners to reduce the near-field effects in their experimental data. Overall, the two topics mentioned above help establish the best practice guideline for the MASW method in the geotechnical and geophysical communities.

The last contribution of this dissertation is regarding the effectiveness of the MASW and MHVSR methods for health monitoring of geotechnical infrastructures by generating a continuous image of the subsurface layering and conditions. Being able to generate a high-resolution and detailed image of subsurface layering is very beneficial for many civil engineering structures. This is particularly important for levees, embankment dams, and landslides since regular inspection of these structures is required to ensure their safety and prevent a potential failure. Therefore, in this dissertation, the MASW and MHVSR methods have been employed for two types of geotechnical infrastructures (i.e. levees and landslides) to determine the capability of these methods for geotechnical infrastructure health monitoring.

1.5 Organization of the dissertation

This dissertation is presented in six chapters. The first two chapters of this dissertation include Introduction (Chapter 1) and Literature review (Chapter 2). The next chapter (Chapter 3) details the accuracy and resolution of the four common transformation techniques for developing the experimental dispersion curve considering different conditions. Chapter 4 discusses the near-field effects observed in the MASW method based on extensive field measurements and provides practical guidelines for near-field mitigation on active array-based surface wave methods. Chapter 5 presents the efficiency of the MASW method for detecting zones of high potential hazard along the Mel-Price reach of the Wood River Levee with regard to the importance of the velocity reversal layer for the MASW data interpretation. The last chapter (Chapter 6) examines the efficacy of the MASW and MHVSR methods for landslide investigations by applying these methods for two active landslides that have recently experienced considerable slope movements.

The results for the last four chapters are provided in the form of journal publications. A journal paper has been submitted to the Surveys in Geophysics Journal based on examining the performance of the four different transformation techniques for developing the experimental dispersion curve entitled “Performance of Different Transformation Techniques for MASW Data Processing Considering Various Site Conditions, Near-Field Effects, and Modal Separation”. The newly developed practical guidelines regarding near-field mitigation on array-based active surface wave methods have been submitted in a journal paper in Geophysical Journal International entitled “Practical Guidelines for Near-field Mitigation on Array-based Active Surface Wave Testing”. The efficacy of the geophysical methods for health monitoring of a levee system (Mel-Price levee) that has experienced considerable sand boils are detailed in a journal paper published in the Engineering Geology Journal entitled “The combined use of MASW and resistivity surveys for levee assessment: A case study of the Melvin Price Reach of the Wood River Levee”. Finally, the advantages of using geophysical methods for landslide investigations are highlighted in a journal paper published in the Landslides Journal entitled “The MHVSR Technique as a Rapid, Cost-Effective, and Non-invasive Method for Landslide Investigation: Case Studies of Sand Gap and Ozark, Arkansas, USA”.

2 CHAPTER 2: LITERATURE REVIEW

2.1 Chapter overview

This chapter provides an overview of the topics related to the seismic wave propagations of body and surface waves. Additionally, backgrounds regarding the MASW and MHVSR methods, as the primary geophysical methods used in this dissertation for geotechnical infrastructure health monitoring, are presented. For the MASW technique, two topics are discussed in detail as the main focuses of this dissertation. These include (1) the four transformation techniques widely used for data processing of the MASW technique and (2) the near-field effects on the array-based active surface wave methods and the current practice for mitigating such effects.

2.2 Seismic waves

Seismic waves that propagate within a medium with a free surface are categorized into two types: body waves and surface waves. Body waves typically dominate the wavefield at distances on the order of one or two wavelengths from the shot location (source offset). However, for distances greater than that, the contribution of the body waves in the wavefield is negligible, and surface waves carry the majority of the energy generated by the source. This is due to the geometric attenuation factors of the body and surface waves.

While for body waves, the geometric attenuation factor is proportional to the inverse of the square of the distance from the source, for surface waves, this factor is proportional to the inverse of the square root of the distance from the source. Therefore, it is typically assumed that at far-field distances, the wavefield is mainly dominated by surface waves (Stokoe *et al.*, 2000).

2.2.1 Body waves

Body waves include the waves that propagate through the interior of the medium and consist of P-waves and S-waves. For P-waves, also called compression waves, the particle motion is parallel to the direction of the wave propagation (see Figure 2.1a). For S-waves, also called shear waves, the particle motion is perpendicular to the direction of the wave propagation (see Figure 2.1b). The S-waves are subdivided into two groups based on the plane of the particle motion, including vertically polarized shear wave (SV) and horizontally polarized shear wave (SH).

Body waves are nondispersive, which means that their velocity of propagation is only a function of the mechanical properties of the medium and its independent of frequency. The P and S-wave velocities of geo-materials in a linear elastic medium are directly linked to the fundamental elastic properties of the geo-materials and can be defined as below (Yoon, 2005; Foti *et al.*, 2014):

$$V_P=\sqrt{\frac{\lambda+2G}{\rho}} \qquad (1)$$

$$V_S=\sqrt{\frac{G}{\rho}} \qquad (2)$$

Where V_P is the P wave velocity, V_S is the S wave velocity, λ is the Lame constant, ρ is the mass density, and G is the shear modulus of materials. It should be mentioned that since the strain level associated with the seismic waves created using non-invasive geophysical methods is typically very small, the linear elastic assumption is always valid for non-invasive geophysical methods.

2.2.2 Surface waves

Seismic surface waves, which include Love and Rayleigh type surface waves, travel near the surface (very shallow depths) and along the free boundary of a medium (i.e. the ground surface). Therefore, surface waves can be easily detected using receivers placed at the free surface. These waves are generated from the interaction of P and S-waves with a free surface.

Rayleigh waves, which are generated from the interaction of the P and SV-waves, involve elliptical motion in the vertical plane (Figure 2.1d). These types of surface waves are commonly used for surface wave testing because they can be easily generated and detected at the ground surface.

On the other hand, Love waves, which are generated from the interaction of the P and SH-waves, produce particle motion perpendicular to the wave travel direction (Figure 2.1c). These types of surface waves mostly develop when a soil layer overlies a half-space with considerably lower seismic wave velocity relative to the half-space layer. Therefore, due to the limited subsurface conditions ideal for the development of the Love waves, they have been rarely used for surface wave testing. However, in recent years, Love waves have been used more frequently for active surface wave testing for geotechnical applications (Mi *et al.*, 2020; Chen *et al.*, no date).

Unlike the body waves in a vertical heterogeneous medium, surface waves are dispersive, meaning that their propagation velocity is a function of frequency. The dispersive nature of the surface waves in vertically heterogeneous media forms the basis of surface wave methods for geotechnical site characterization. Another fundamental property of the surface waves which makes them ideal for geotechnical site characterization is that they are propagating in a two-dimensional (2D) pattern, and so their spatial attenuation is considerably lower than the body waves.

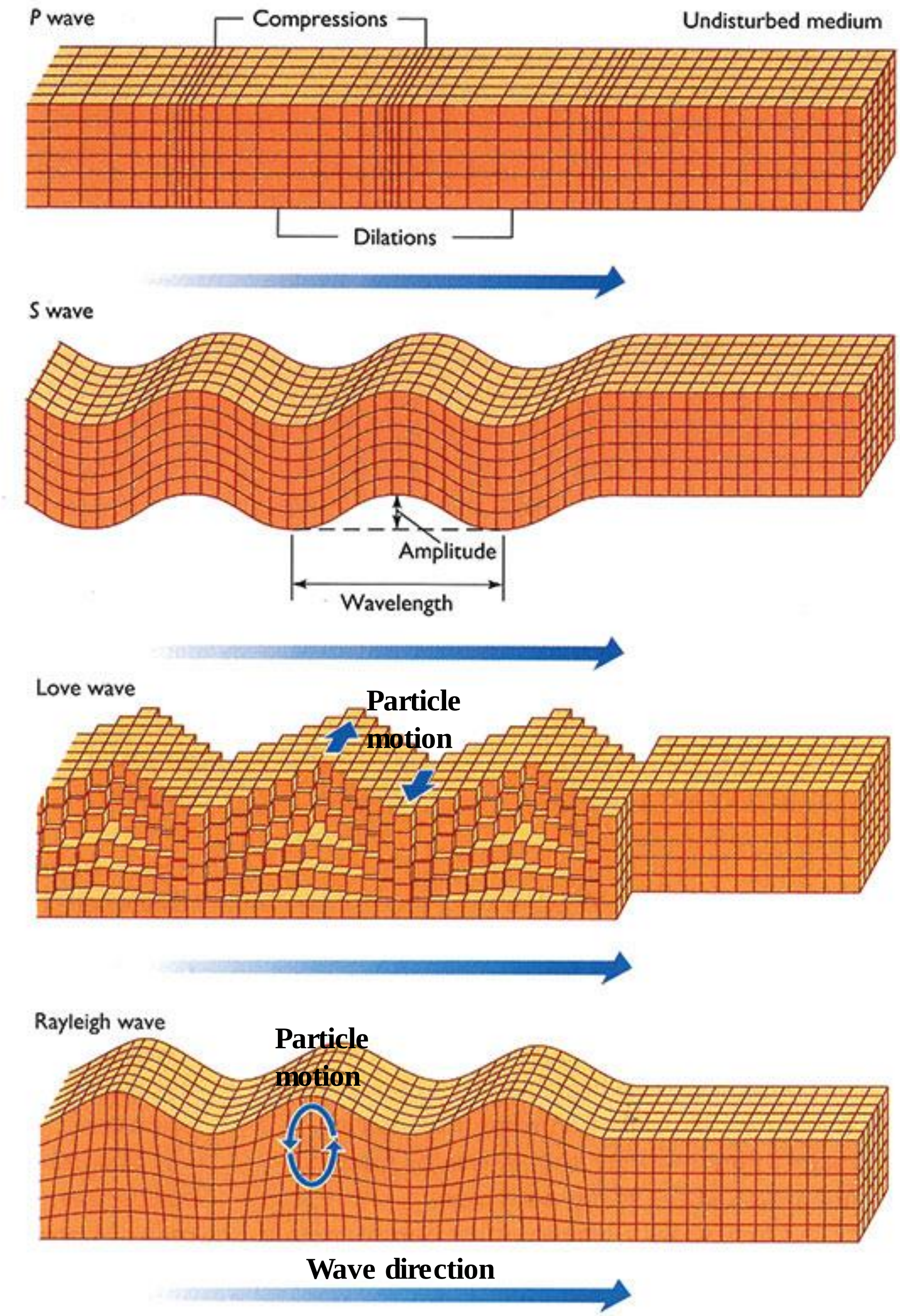

Figure 2.1- Seismic waves. a) P-wave, b) S-wave, c) Love waves, d) Rayleigh waves (modified from www.structuremag.org).

2.2.2.1 Surface wave propagation in a homogeneous half-space condition

Lord Rayleigh (1855) introduced the solution for Rayleigh waves propagating in a homogenous, isotropic, elastic half-space condition. The solution is obtained by imposing the boundary conditions on the equations of motion. Assuming an elastic half-space medium, as shown in Figure 2.2, displacements in X (represented by u) and Z directions (represented by w) can be given in terms of two potential functions (ϕ and ψ):

$$u=\frac{\partial \phi}{\partial X}+\frac{\partial \psi}{\partial Z} \tag{3}$$

$$w=\frac{\partial \phi}{\partial Z}-\frac{\partial \psi}{\partial X} \tag{4}$$

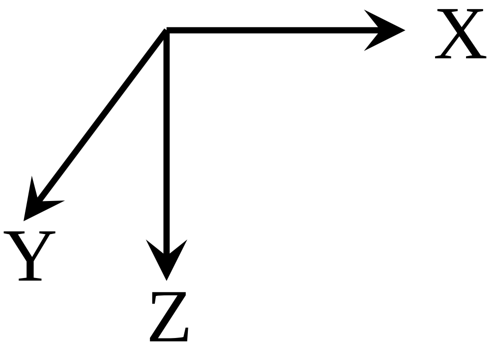

Figure 2.2- Coordinate for an elastic half-space medium

By imposing the boundary conditions and applying the assumptions made for a homogenous, isotropic, elastic half-space medium, the final solution for Rayleigh wave propagation is given by:

$$(2-\frac{V_R^2}{V_S^2})^2-4\times(1-\frac{V_R^2}{V_P^2})^{0.5}\times(1-\frac{V_R^2}{V_S^2})^{0.5}=0 \tag{5}$$

Where V_R is the Rayleigh velocity, Vs is the shear wave velocity, and V_P is the p-wave velocity. Equation (5) is called the Rayleigh waves equation. Based on this equation, for a homogenous, isotropic, elastic half-space medium, the Rayleigh phase velocity (V_R) is only a function of the P-wave (V_P) and S-wave (V_S) velocities. Additionally, from this equation, it is clear that the Rayleigh wave velocity in a homogenous, isotropic, elastic half-space medium is non-dispersive, meaning that its velocity is independent of frequency. Equation (5) can be simplified based on the relationship between V_P, Vs, and Poisson's ratio (ν) as below:

$$V_R = \frac{0.874 + 1.11 \times \nu}{1 + \nu} \times V_S \tag{6}$$

2.2.2.2 Surface wave propagation in a vertically heterogeneous medium

The Rayleigh waves equation in a homogenous, isotropic, elastic half-space medium is generally used to introduce the basic concept of Rayleigh wave propagation. However, the real field conditions are very different than the homogenous, isotropic, elastic half-space medium. Real field conditions generally consist of a stack of homogenous, isotropic, elastic layers, followed by the half-space. Therefore, for the majority of the geotechnical problems, the Rayleigh wave equation for a layered (heterogeneous) medium is used to model the surface wave propagation.

In a vertically heterogeneous (layered) medium, the problem of solving Rayleigh wave propagation becomes more complicated. The elastic properties used for such a medium for each layer include shear wave velocity (Vs), mass density (ρ), Poisson's ratio (ν), and thickness (H), as shown in Figure 2.3.

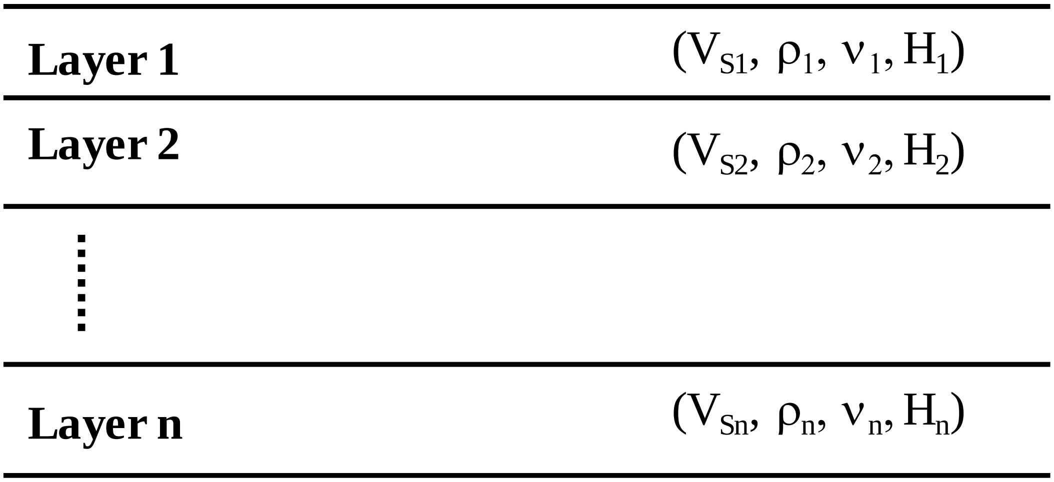

Figure 2.3- An elastic layered (heterogeneous) medium.

In a vertically heterogeneous (layered) medium, Rayleigh propagation is dispersive, meaning that Rayleigh wave velocity is a function of frequency (or wavelength). For such a medium, the boundary conditions of no stress at the surface and zero amplitude at infinite depth are still valid. The final product of Rayleigh wave propagation in a layered medium called the Rayleigh dispersion equation is an implicit relationship between several parameters, including Rayleigh phase velocity, frequency or wavelength, and the properties of elastic layers. This equation is given by (Lai *et al.*, 1998):

$$f(V_R, \upsilon, \rho, H, k, \omega) = 0 \tag{7}$$

Where ω is the wavenumber and k is the circular frequency. Therefore, the main characteristic of surface waves that make them ideal for site characterization is the dispersive nature of these waves in layered media. The penetration depth of the surface wave depends on the wavelength. Long wavelengths (high frequencies) are used to sample deeper subsurface layers, whereas short wavelengths (low frequencies) are used to sample shallow subsurface layers (see Figure 2.4). Therefore, waves with different wavelengths (frequencies) sample different depths of the subsurface layering. Another important characteristic of the surface waves that need to be highlighted is that for a particular wavelength (frequency), multiple solutions (velocities) exist for Rayleigh wave propagations because multiple modes of Rayleigh waves can travel at different phase velocities.

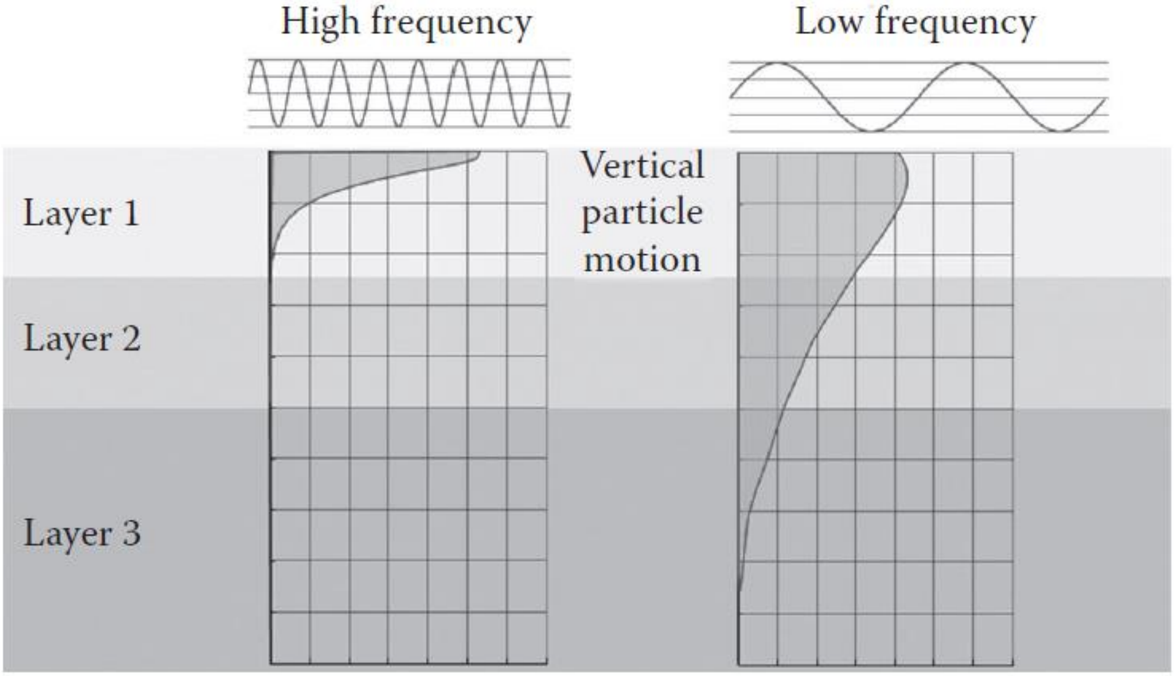

Figure 2.4- Dispersive nature of Rayleigh waves in heterogeneous media (Foti *et al.*, 2014).

2.3 Seismic surface waves methods

While a variety of non-invasive geophysical methods have been introduced for geotechnical infrastructure evaluation (e.g. seismic-based methods, electrical-based methods, gravity methods, magnetic methods, and remote sensing methods), seismic surface wave methods have gained more attention in the last two decades in geotechnical engineering. This is because the seismic surface wave methods can be used for shallow and deep site characterizations, and their results are closely linked to the fundamental properties of geo-materials (compression and shear modulus).

The seismic surface wave methods are mainly divided into two groups:1) active and 2) passive methods. For active surface wave methods, waves are actively created at the desired location and recorded using a linear array of receivers. This type of testing is valuable for near-surface (typically up to 30 m depth) site characterization as they are rich in high-frequencies resulting in good resolution of near-surface material properties. However, no information from the layers located deep below the ground surface can be acquired using active surface wave methods because of the lack of low-frequency components.

On the other hand, passive surface wave methods use ambient vibrations, typically called microtremors, from the environment. Microtremors consist of waves generated from natural sources (e.g. winds acting on trees and ocean waves) and human-related vibrations (e.g. traffic and industry activities). Passive surface wave methods are valuable for deep site characterization as they are rich in low-frequency components (Foti *et al.*, 2014). Therefore, using the combination of active and passive surface wave methods, one can identify both shallow and deep subsurface layers with a reasonable accuracy level.

Several active surface wave methods have been developed and used for geotechnical site characterization during the last two decades. The most commonly used active surface wave method is the MASW using Rayleigh or Love type surface waves (Penumadu *et al.*, 2005; Anbazhagan *et al.*, 2008; Rahimi *et al.*, 2019a). Therefore, the main focus of this dissertation is to improve the data processing and reliability of the MASW method as the most common active surface wave technique that has been used in the geotechnical community.

2.3.1 Active MASW method

The multi-station seismic surface wave methods were first introduced in the 1980s (McMechan *et al.*, 1981; Gabriels *et al.*, 1987), but these methods became popular in many disciplines in the late 1990s and early 2000s with more powerful computers for sophisticated data processing. The multi-station seismic surface wave techniques have several advantages over the traditional two-sensor Spectral Analysis of Surface Waves (SASW) method. Using the multi-station array-based methods, the production rate in the field measurements is remarkably increased, and the data processing and data interpretation become less subjective and more robust (Foti *et al.*, 2014). Additionally, the multi-station seismic surface wave techniques help to mitigate several limitations associated with the traditional two-sensor Spectral Analysis of Surface Waves (SASW) method. This includes poor resolution experimental dispersion image, failure to detect multiple modes of propagation, which could be important for data interpretation, and inability to accurately identify the near-field effects (Zywicki *et al.*, 2005).

The multi-station seismic surface wave techniques came into popular use in geotechnical engineering for near-surface site characterization with the introduction of the MASW method in 1999 by Park et al. (Park *et al.*, 1998). MASW utilizes the dispersive nature of either Rayleigh or Love type surface waves propagating through geomaterials and aims to estimate the variation of shear wave velocity (Vs) with depth. The MASW method is appealing for near-surface site characterization (generally for depths shallower than 30 m) because it is non-destructive, rapid, cost-effective, and it allows for identification and rejection of unwanted data points, including higher modes and near field effects.

The standard procedure for the MASW testing includes three steps as described below: (see Figure 2.5)

1- *Field measurement and data acquisition* **(**Figure 2.5a**):** MASW testing is typically conducted using a linear array of vertical or horizontal geophones (typically 24 or 48 geophones) spaced uniformly (typically 0.5m to 2 m geophone spacing). The spacing between each geophone and the number of geophones are generally determined based on maximum target depth and site conditions. The geophones are typically coupled to the ground surface using spikes. However, for sites where many MASW setups are required, the geophones can be attached via a landstreamer system to increase the testing rate. The landstreamer allows all geophones in the array to be dragged as a single system across the survey line instead of coupling each geophone to the ground via a spike. The disadvantage of the landstreamer system is the reduced experimental data quality (i.e. low-resolution experimental dispersion curve) because the geophones are not coupled as well to the ground surface. A refraction cable is used to connect all geophones to the Geode seismograph. The Geode seismograph is connected to a field laptop to record and view signals during field testing. Waves are actively created using an artificial source such as a sledgehammer or a drop weight. For each MASW setup, waves are generated at different source offsets to identify the potential near-field effects, detect the fundamental mode of surface wave propagation, and estimate the uncertainty associated with the experimental dispersion curve (Cox *et al.*, 2011). Between 3-10 blows are typically generated at each source offset to average together and provide data redundancy.

2- Data processing **(**Figure 2.5b**):** The main part of the MASW data processing is the construction of the experimental dispersion curve (i.e. the variation of phase velocity with frequency). To do so, the raw MASW data, which is in the time-space domain, needs to be transformed into the frequency-wavenumber (f-k), frequency-slowness (f-p), or frequency-velocity (f-v) domain to generate a dispersion image. Four different transformation methods are widely used in the literature to construct the experimental dispersion curve. These methods are discussed in detail in the next section. Dispersion data points generated from each source offset are combined to create the raw experimental dispersion curve, which may include data from the fundamental mode, higher modes, effective mode, and data affected by near field effects. All the points identified as affected by near-field effects or propagating at an effective or higher mode are removed from the raw experimental dispersion curve to isolate the fundamental mode of propagation. Typically, the fundamental mode is considered as the mode of interest for the inversion process (Foti *et al.*, 2014).

3- Inversion (Figure 2.5c)**:** The final experimental dispersion curve obtained from the data processing step is used in an iterative process called inversion to determine the shear wave velocity variation with depth. The inversion process involves an iterative process to find the best shear wave profile, resulting in a theoretical dispersion curve that best fits the experimental one. The assumptions made in the iterative process consist of 1) horizontal soil layering, 2) constant shear wave velocity for each soil layer, and 3) homogenous and isotropic soil layers. The quality of the fit between the experimental and theoretical dispersion curves is evaluated based on both the calculated misfit parameter (collective squared error between the experimental and theoretical dispersion curves) and by visual inspection. The visual inspection is necessary since the misfit parameter is only used to compare the relative quality of the fit between the experimental and theoretical dispersion curves (Rahimi *et al.*, 2018). Like any other inverse problem, one of the main drawbacks of the MASW method is the nonuniqueness of the solution in the inversion process. This means that several shear wave velocity profiles can reasonably fit with the experimental dispersion curve for a given dispersion curve. This limitation can be overcome by adding information from other methods (e.g. boring logs) regarding the subsurface layering of the site to constrain the inversion solution. Additionally, the uncertainty in the inversion process can be mitigated to some extent by joint inversion of the surface wave (e.g. joint inversion of the MASW and the MHVSR results).

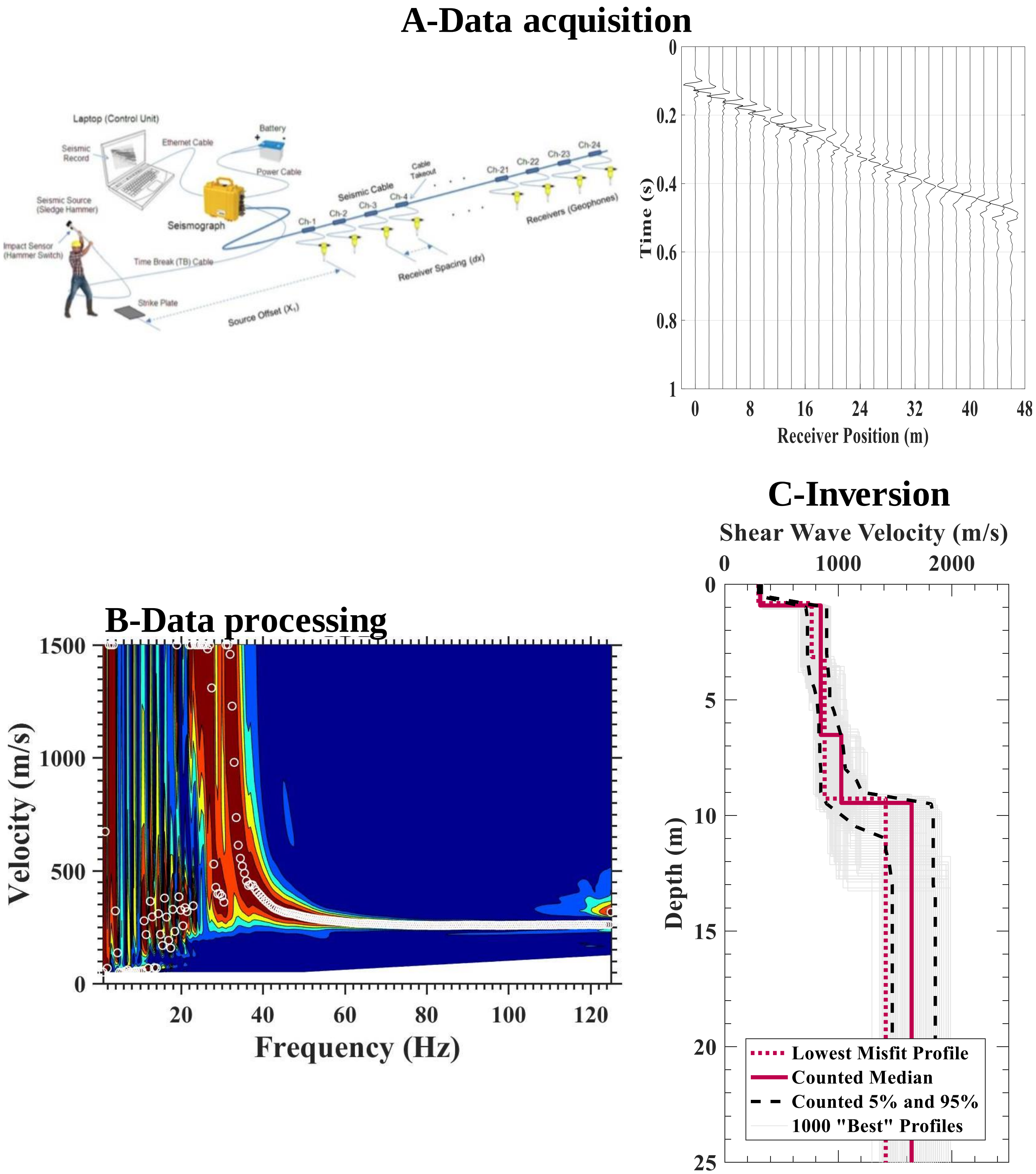

A-Data acquisition

B-Data processing

C-Inversion

Figure 2.5- Standard procedure for MASW testing. a) data acquisition (modified from www.masw.com), b) data processing, c) inversion.

2.3.1.1 Construction of the experimental dispersion curve using transform-based methods

One of the basic tools commonly used in seismic data processing is the wavefield transformation that transforms the wavefield from its original domain into another domain. The wavefield transformation comprises a main portion of the MASW data processing and controls the resolution of the experimental dispersion curve. This is important since the higher the resolution of the experimental dispersion curve, the higher the accuracy of the final MASW results (i.e. inverted shear wave profile). Therefore, for MASW testing, the wavefield transformation is of primary importance since it directly affects the final inverted shear wave profile.

In the transform-based methods used for MASW, the original time-space (t-x) domain data is transformed into the frequency-wavenumber (f-k), frequency-slowness (f-p), or frequency-velocity (f-v) domain to generate a dispersion image that contains information from different modes of propagation. One of the main advantages of transforming the wavefield into the f-k, f-p, or f-v domain is that in the transformed domain, the propagation parameters can be easily identified as spectral maxima (Foti *et al.*, 2014). The other advantage of the transform-based method is that different modes can often be detected and separated in the transformed domain even when the modes are not clearly visible in the time-space domain. The modes typically appear as separate maxima of the power spectrum in the transformed domain. This is particularly important for cases where the accuracy of the inversion analysis can be enhanced by including the higher modes in the inversion process (Beaty *et al.*, 2002; Xia *et al.*, 2003).

Four different transformation methods are commonly used by researchers from different institutions and software packages available for MASW data processing. These methods include the frequency-wavenumber (FK) method (Capon, 1969; Nolet *et al.*, 1976; Gabriels *et al.*, 1987;

Yilmaz, 1987; Foti *et al.*, 2000), Frequency Domain Beamformer (FDBF) method (Zywicki, 1999; Hebeler *et al.*, 2007), phase shift method (Park *et al.*, 1998), and slant stack or frequency-slowness (τ-p) method (McMechan *et al.*, 1981). Depending on the site condition, the resolutions of the four transformation methods could yield differences in the developed experimental dispersion curve. The resolution of the experimental dispersion curve is a critical factor for the MASW technique, particularly for the low-frequency range of the dispersion curve, where the data are typically corrupted by the near field effects or other issues.

Provided in Table 1 is a summary of the transformation methods used by researchers and practitioners from different institutions and in different software packages available for the MASW data processing. According to this table, the FK method is the most common transformation method used for MASW data processing. This is because the FK is the simplest and fastest transformation method for MASW data processing.

The second most common transformation technique is the PS method. This method is widely used in software packages available for MASW data processing. The FDBF transformation technique is the least common method used for MASW data processing. This is because the FDBF transformation technique is more computationally complex as compared to the other transformation techniques. This method is mainly used for research purposes, and it is not common among practitioners. The four transformation methods are explained in detail in the following.

Table 1- Summary of the different transformation methods used by researchers from different institutions and software packages

No	Affiliation	Country	Dispersion processing method	Software
1	Univ. Texas at Austin (Cox et al. 2014)	USA	FDBF, FK, PS, and τp	Matlab
2	Institut des Sciences de la Terra	France	FK	Geopsy
3	Univ. of Iceland (Olafsdottir et al. 2018)	Iceland	PS	MASWaves, Matlab
4	Univ. of Arkansas (Rahimi et al. 2108)	USA	FDBF, FK, PS, and τp	Matlab
5	Zhejiang Univ. (Cheng et al. 2019)	China	FK and τp	
6	Monash Univ. (Volti et al. 2016)	Australia	τp	SeisImager/SW
7	Univ. of Potsdam (Lontsi et al. 2016)	Germany	FK	Geopsy
8	Univ. of Nevada Reno/Optim Inc.	USA	τp	SeisOpt ReMi
9	Western Univ. (Darko et al. 2020)	Canada	FK	Geopsy
10	Politecnico di Torino (Foti et al. 2000)	Italy	FK	Matlab
11	Univ. of Missouri (Rosenblad and Li 2009)	USA	FK	Matlab
12	National Institute of Oceanography and Applied Geophysics	Italy	FK	-
13	Geometrics Inc.	USA	τp	SeisImager/SW
14	Park Seismic LLc.	USA	PS	ParkSEIS
15	Kansas Geological Survey	USA	PS	SurfSeis
16	Geogiga Technology Corp	USA	FK, PS, and τp	Geogiga Surface
17	RadExPro	Russia	FK	RadExPro
18	Eliosoft	Italy	PS	WinMASW
19	GeoVision (Martin et al. 2017)	USA	FK and PS	-

2.3.1.1.1 Slant stack (τ-p) method

The τ-p method, also called slant stack or frequency-slowness method, was first introduced by McMechan and Yedlin in 1981. This method utilizes two linear transformations that allow the decomposition of the shot-gather into its plane-wave linear components. The two linear transformations include a slant stack and a one-dimensional Fourier transform. The original time-space (t-x) domain data is converted into a time intercept-slowness (τ-p) domain using the slant stack transformation. A one-dimensional (1D) Fourier transform is then applied to the τ-p domain data to transform the data into the frequency-slowness (f-p) domain. Therefore, using this method, the original shot-gather, which is in the time-space (t-x) domain, can be transformed into an image of energy density as a function of frequency and slowness (McMechan *et al.*, 1981; Sacchi *et al.*, 1995; Louie, 2001; Foti *et al.*, 2014).

The linear relationship that relates the four variables t, x, τ (time delay at zero offset), and p is defined as:

$$\mathrm{t} = \tau + \mathrm{px} \tag{8}$$

The slant slack transform is expressed as:

$$\mathrm{f}(\tau,\ \mathrm{p}) = \int_{-\infty}^{+\infty} \mathrm{U}(x, t)\mathrm{d}x = \int_{-\infty}^{+\infty} \mathrm{U}(x, \tau + px)\mathrm{d}x \tag{9}$$

This equation can be written in discrete form as follows:

$$\mathrm{f}(\tau,\ \mathrm{p}) = \sum_{j=1}^{m} \mathrm{U}\left(x_j, \tau + px_j\right)\Delta x \tag{10}$$

Shown in Figure 2.6 is an illustration of the linear slant stack transformation. In this linear transformation, for each value of τ, the data in the time-space domain are stacked along a straight line with a slope of p. This means that each straight line in the time-space domain is associated with a constant data pair of (τ-p) in the τ-p domain.

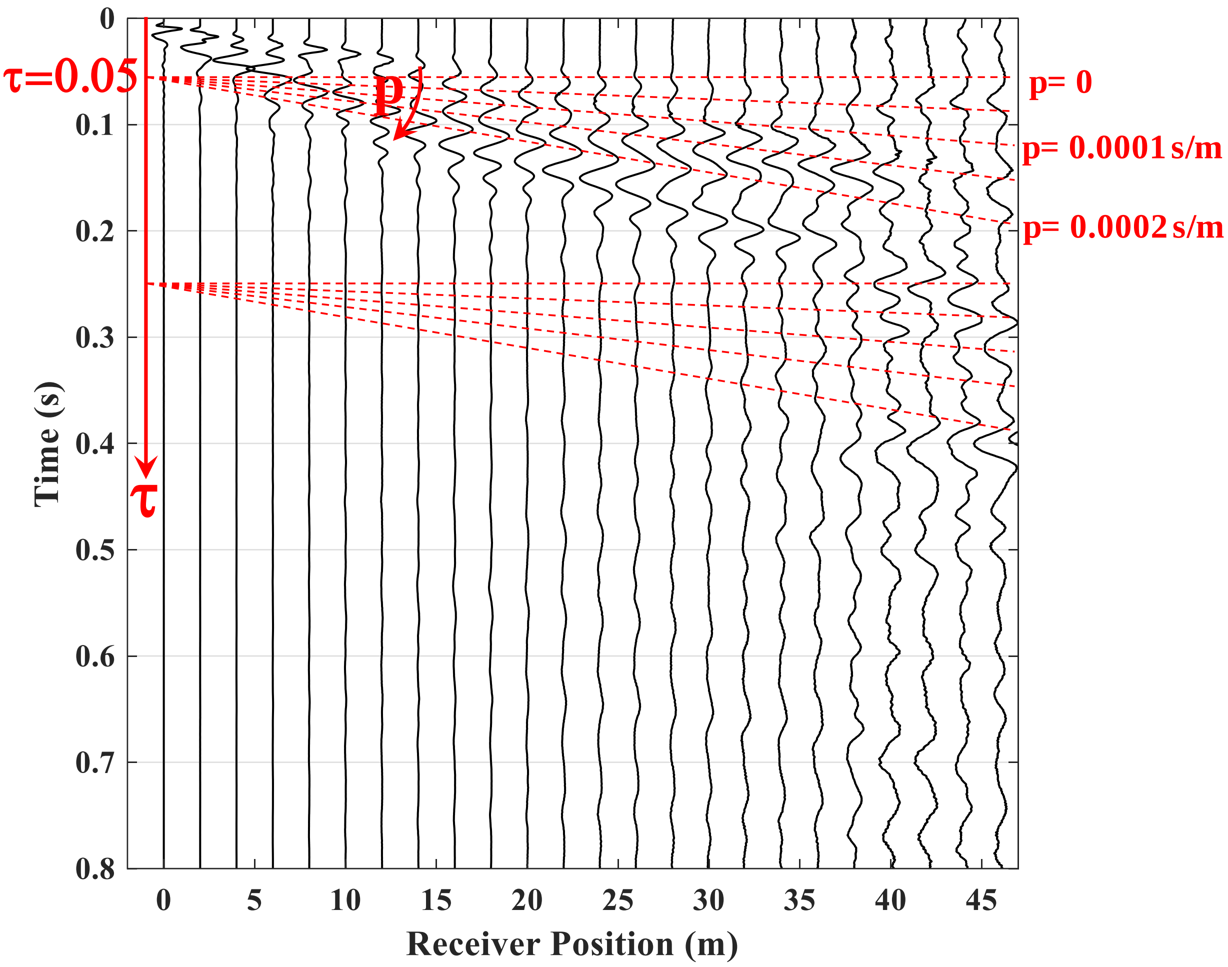

Figure 2.6- An example shot gather data with τ-p transform.

Finally, by applying a one-dimensional Fourier transform over the time intercept variable (τ), the data can be transformed into the frequency-slowness domain (f-p) as below:

$$\mathrm{F}(\mathrm{f},\mathrm{p}) = \int_{-\infty}^{+\infty} \mathrm{f}(\tau,\mathrm{p}) e^{-i2\pi f\tau} \mathrm{d}\tau \tag{11}$$

The frequency-slowness data pair (f-p) associated with the maximum energy is identified at each constant frequency. Then, the phase velocity related to each of the maxima can be easily calculated as below:

$$\mathrm{V_R(f)}=\frac{1}{p} \tag{12}$$

The frequency-phase velocity data pairs associated with the maximum energy are combined to construct the experimental dispersion image, representing the phase velocity variation with frequency.

2.3.1.1.2 Frequency-wavenumber (FK) method

The frequency (f)-wavenumber (k) transformation method was first proposed by Nolet and Panza in 1976 and then used by other researchers for surface waves data processing (Capon, 1969; Nolet *et al.*, 1976; Gabriels *et al.*, 1987; Yilmaz, 1987). In this method, the recorded data, which is in the time-space (t-x) domain, is transformed into the frequency-wavenumber (f-k) domain using a two-dimensional (2D) Fourier transform as below:

$$\mathrm{W}(f,k) = \iint_{-\infty}^{+\infty} \mathrm{U}(x,t)e^{-i(2\pi ft-kx)}dxdt \tag{13}$$

The discrete form of this equation is defined as below:

$$\mathrm{W}(f,k) = \sum_{i=1}^{n}\sum_{j=1}^{m} \mathrm{U}\left(x_j,t_n\right)e^{-i(2\pi ft_l-kx_j)}\,\Delta x\Delta t \tag{14}$$

In the f-k method, the time-space domain data are decomposed into its components at different frequencies and wavenumbers. The raw time-space domain data are transformed into an image of energy density as a function of frequency and wavenumber. Once the data are transformed into the f-k domain, the phase velocity associated with each of the f-k data pairs can be calculated using the equation below:

$$V_R(f)=\frac{f}{k_m(f)} \tag{15}$$

In the transformed domain, the wavenumber and the phase velocity associated with the maximum energy (maximum power) are identified at each frequency. An example of this process is shown in Figure 2.7. Presented in Figure 2.7 a, b, c, and d are examples of normalized power spectral plots versus phase velocity and wavelength at frequencies of 20 and 40 Hz, along with the points associated with the maximum energy at each frequency. Using this information, two experimental dispersion data points can be generated, as shown in Figure 2.7e.

A dispersion curve, representing the variations of phase velocity with frequency, can be created by repeating this process for the range of frequencies of interest. This dispersion curve can then be used for further processing to identify the properties of subsurface layering.

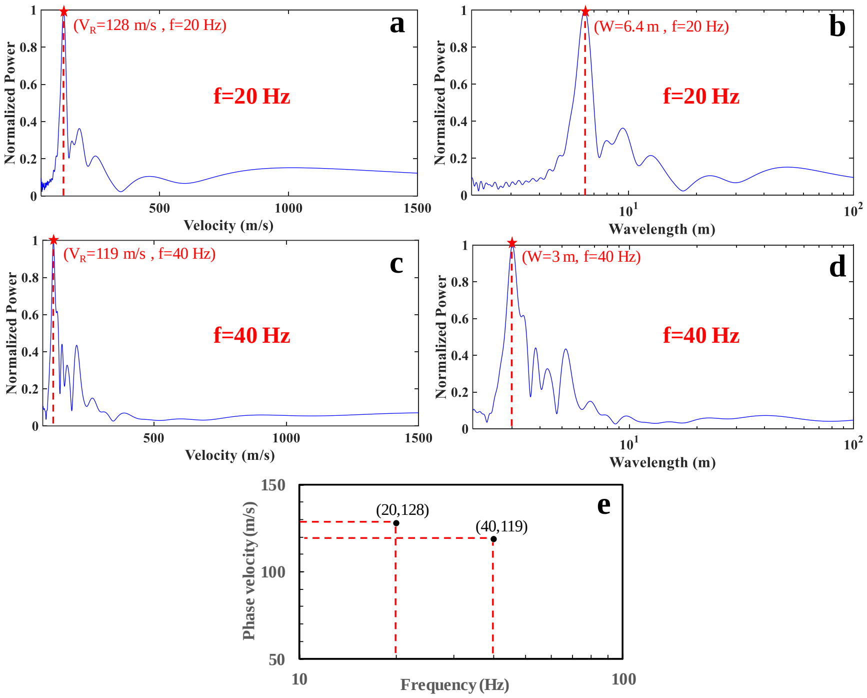

Figure 2.7- Example dispersion data points generated using the FK method. a) velocity versus normalized power at f=20 Hz, b) wavelength versus normalized power at f=20 Hz, c) velocity versus normalized power at f=40 Hz, d) wavelength versus normalized power at f=40 Hz, e) dispersion data points at frequencies of f = 20 and f = 40 Hz.

2.3.1.1.3 Frequency Domain Beam-Former (FDBF) method

Frequency Domain Beam-Former (FDBF) is one of the most commonly used transform-based data processing methods for surface wave testing. This method was first introduced by Lacoss et al. in 1969 and then modified by several other researchers (Zywicki, 1999). The basic concept of this method is very similar to the τ-p transformation method. The term beamformer refers to the ability of an array or signal processing method to focus on a particular direction and the mainlobe of an Array Smoothing Function (ASF), which is called a beam (Johnson *et al.*, 1993).

The FDBF method utilizes a steering vector, which is an exponential phase shift vector, to calculate the power associated with each particular frequency-wavenumber (f-k) data pair. A steering vector is defined as (Zywicki, 1999; Hebeler *et al.*, 2007):

$$\mathrm{e(k)} = [e^{-ik.x_1}, e^{-ik.x_2}, \dots .\, e^{-ik.x_m}]^T \qquad (16)$$

In this equation, e(k) is the phase shift vector, k is the vector wavenumber, x_m denotes the sensor m position in the array, and T denotes the transpose of the vector. For a particular f-k data pair, the power (energy) is calculated by multiplying the spatiospectral correlation matrix (R) by the steering vector and then summing the total power over all the receivers. The steered power spectrum is defined as below:

$$P_{BF}(k,\omega)=e^H W R W^H e \qquad (17)$$

Where H denotes the Hermitian transpose of the vector and W is a diagonal matrix containing the shading weights of each receiver as below:

$$W=\begin{bmatrix} w_1 & \cdots & 0 \\ \vdots & \ddots & \vdots \\ 0 & \cdots & w_m \end{bmatrix} \tag{18}$$

The spatiospectral correlation matrix (R) is also defined as:

$$R(\omega)=\begin{bmatrix} R_{1,1}(\omega) & \cdots & R_{1,m}(\omega) \\ \vdots & \ddots & \vdots \\ R_{m,1}(\omega) & \cdots & R_{m,m}(\omega) \end{bmatrix} \tag{19}$$

where $R_{m,n}$ is the cross power spectrum between receivers *m* and *n*:

$$R_{m,n}(\omega) = S_m(\omega)S_n^H(\omega) \tag{20}$$

Where $S(\omega_0) = [S(x_1, \omega_0)\ \ S(x_2, \omega_0)\ \ \ldots . S(x_m, \omega_0)]^T$ is the temporal Fourier transform of the time history at $\omega = \omega_0$ for each of the receivers, which can be calculated as below:

$$S(\omega_0)=\sum_{t=0}^{n-1} s[t]\times e^{\frac{-i2\pi\omega t}{N}} \tag{21}$$

Where N is the number of time-domain samples. The first version of the FDBF transformation method was proposed, assuming a plane seismic surface wavefield. This assumption is also made in all the other transformation methods (τ-p, FK, and phase shift). However, this is not always a valid assumption for the wavefield as surface waves are typically propagating cylindrically in the near-field zone. This is particularly true for surface waves with a longer wavelength (i.e. low-frequency waves). This near-field effect of modeling a cylindrical wavefield with a plane wavefield is called the model incompatibility effect.

The FDBF transformation method was modified in 2005 to account for the model incompatibility effect (Zywicki *et al.*, 2005). In the updated FDBF method, a new steering vector was defined to account for the cylindrical wavefield:

$$h(k)=[e^{-i\phi(H_0(k.x_1)}, e^{-i\phi(H_0(k.x_2)}, \ldots.\ e^{-i\phi(H_0(k.x_m)}\ ]^T \qquad (22)$$

Where ϕ taking the phase angle of each the arguments in parentheses, and $h(k)$ is the Hankel steering vector. The steered power spectrum for the cylindrical wavefield is expressed as below:

$$P_{CBF}(k,\omega)=h^H WRW^H h \qquad (23)$$

Zywicki et al. (2005) have claimed that the updated version of the FDBF method overcomes the limitations of the plane wavefield assumption by accounting for the cylindrical wavefield in the near-field zones.

The construction of the experimental dispersion image in the FDBF method is similar to that of the FK method. At each constant frequency, maximum(s) in the power spectra plot, which is related to the wavenumbers of dominant modes of Rayleigh waves, is selected for further processing. The corresponding phase velocity is then calculated for each f-k data pair using Equation 10.

The FDBF method can be used for both active and passive surface wave testing. For active surface wave measurements, the FDBF uses a one-dimensional (linear) set of receivers. Therefore, this method is simplified for active surface wave testing because the direction of wave propagation is known, and the location of receivers is a scalar value.

2.3.1.1.4 Phase shift method

The phase shift method for surface wave data processing was proposed by Park et al. (1998). In this method, the time-space (t-x) domain data are first converted into the circular frequency-space (ω-x) domain using a one dimensional Fourier transform as shown below (Park *et al.*, 1998):

$$\mathrm{U}(\omega, \mathrm{x}) = \int_{-\infty}^{+\infty} \mathrm{f}(\mathrm{t}, \mathrm{x}) e^{i\omega t} \mathrm{d}t \tag{24}$$

All parameters in Equation 21 are the same as those defined in the preceding sections. The transformed function is then defined as the multiplication of two separate terms, including phase [$\mathrm{P}(\omega, \mathrm{x})$] and amplitude spectrum [$\mathrm{A}(\omega, \mathrm{x})$]:

$$\mathrm{U}(\omega, \mathrm{x}) = \mathrm{P}(\omega, \mathrm{x})\mathrm{A}(\omega, \mathrm{x}) \tag{25}$$

The amplitude parameter preserves the information about the signal attenuation and geometrical spreading, whereas the phase velocity parameter preserves all the information regarding the dispersion properties. Therefore, $\mathrm{U}(\omega, \mathrm{x})$ function can also be expressed as below:

$$\mathrm{U}(\omega, \mathrm{x}) = e^{-i\emptyset x}\mathrm{A}(\omega, \mathrm{x}) = e^{-i\frac{w}{V_R}x}\mathrm{A}(\omega, \mathrm{x}) \tag{26}$$

The final phase shift equation is obtained by applying an integral transformation to $\mathrm{U}(\omega, \mathrm{x})$ function as below:

$$\mathrm{V}(\omega, \emptyset) = \int_{-\infty}^{+\infty} e^{i\emptyset x} \frac{\mathrm{U}(\omega, \mathrm{x})}{|\mathrm{U}(\omega, \mathrm{x})|} \mathrm{d}x \tag{27}$$

Then, the dispersion image can be constructed by calculating the phase velocity corresponding to the maximum of the $\mathrm{V}(\omega, \emptyset)$ function at each circular frequency:

$$C_R(\omega) = \frac{\omega}{\emptyset} \tag{28}$$

2.3.1.1.5 Comparison of different transformation techniques in previous studies

A limited number of studies have investigated the performance of different transformation techniques for MASW data processing. The primary study in this regard was conducted by Dal Moro et al. (2003). They compared the performance of three transformation techniques (FK, PS, and τp methods) for sites with unconsolidated sediments. They claimed that the PS method provides the highest resolution dispersion curve compared to the FK and τp methods for sites with unconsolidated sediments. Finally, they recommended using the PS method for MASW data processing when the fundamental mode of propagation is desired to be utilized for the inversion process.

In another study by Tran and Hiltunen (2008), the performance of the four transformation methods was compared for developing the experimental dispersion curve. In this study, the MASW testing was performed at a site that consists of a 10 m medium dense, fine, silty sand followed by a hard clay layer. Shown in Figure 2.8 are dispersion curves generated using the four different transformation techniques in Tran and Hiltunen's (2008) study. This study concluded that the results from all the transformation techniques are in good agreement, but the FDBF cylindrical leads to a slightly higher resolution dispersion curve compared to the other transformation techniques.

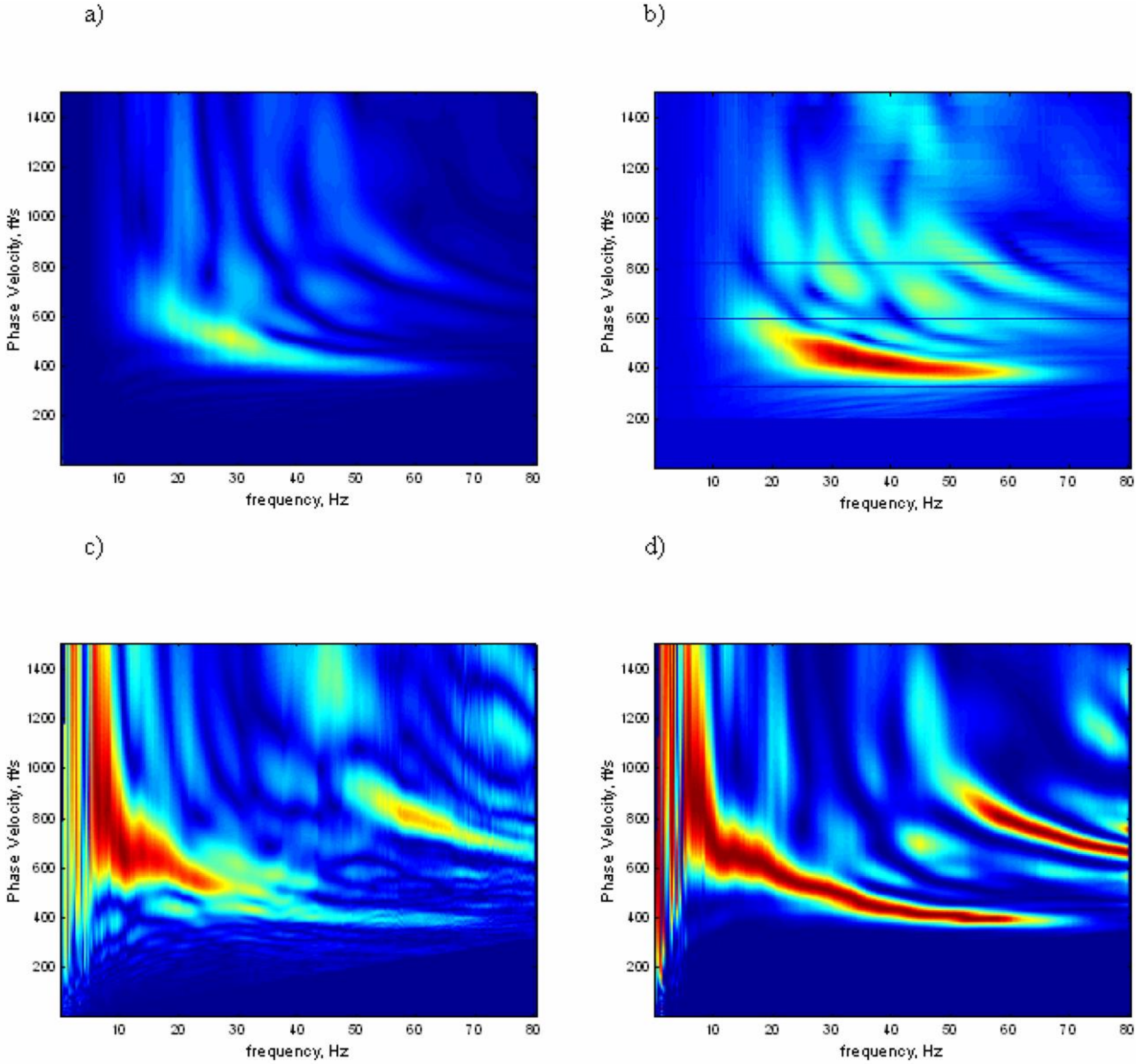

Figure 2.8- Example results from Tran and Hiltunen's (2008) study. a) FK, b) τp, c) PS, and d) FDBF-cylindrical.

Kumar and Naskar (2018) also evaluated the performance of three transformation techniques (FK, PS, and τp methods) for MASW data processing using both synthetic and field data. Shown in Figure 2.9 are dispersion curves generated using three different transformation techniques in Kumar and Naskar's (2018) study. They mentioned that the dispersion curves generated from the three transformation techniques match well (Kumar *et al.*, 2018); however, they recommended the PS method as the best transformation technique for MASW data processing, similar to Dal Moro et al. (2003).

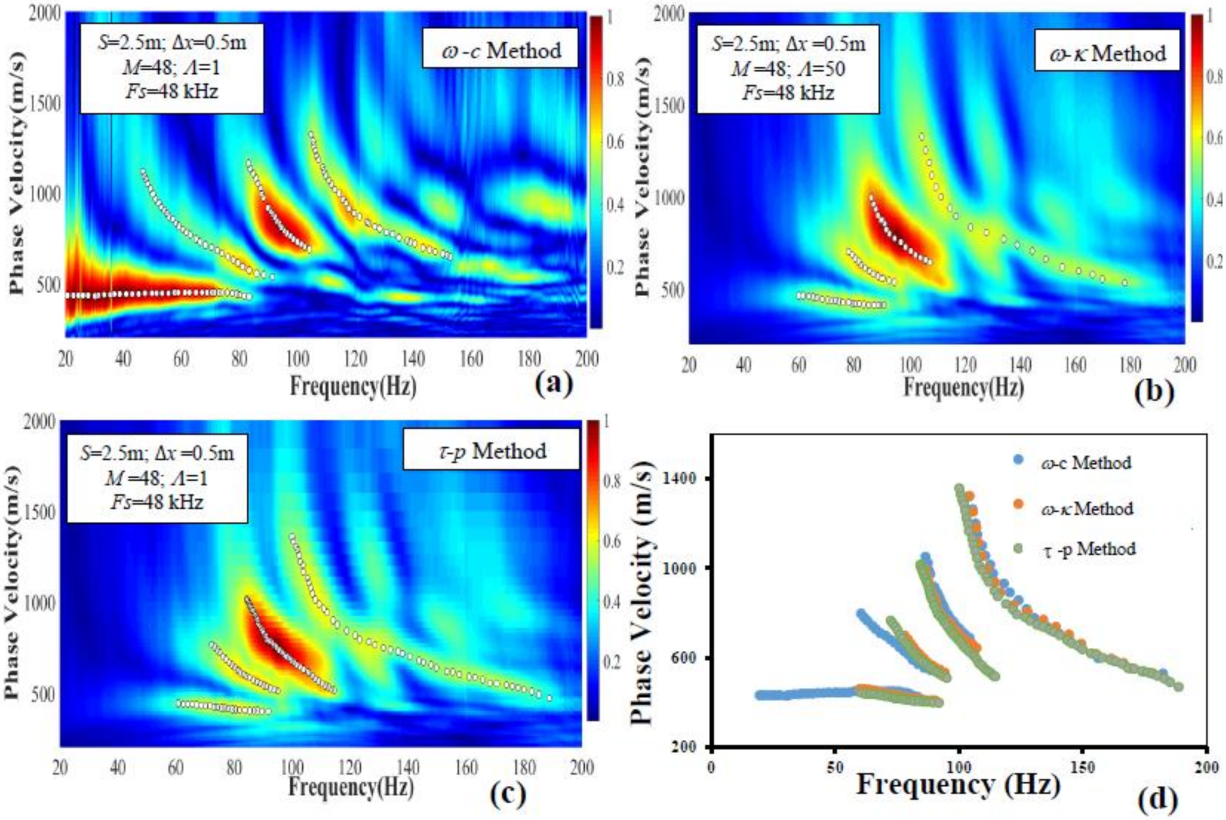

Figure 2.9- Example results from Kumar and Naskar’s (2018) study. a) PS, b)FK, c) τp, and d) combination of all methods.

2.3.1.1.6 Limitation of the previous studies

While the field transformation method is the main part of the MASW data processing controlling the final results, a limited number of studies have investigated the ability and resolution of each of the transformation methods for MASW data processing. The previous studies only compared the performance of different transformation techniques for one particular subsurface and field conditions. This means that their recommendations regarding the performance of different transformation techniques are site-specific and, therefore, cannot be utilized by other researchers. This is the main issue with the previous studies regarding the performance of the four common transformation techniques for MASW data processing.

Another issue with the previous studies is that they failed to provide all critical characteristics of their study areas (e.g. depth to the sharp impedance contrast, wavefield noise conditions). These characteristics are important to truly understand the differences observed in the experimental dispersion curves generated from different transformation techniques. Therefore, in this dissertation, the four transformation methods are used to generate the experimental dispersion curve for different subsurface and wavefield conditions (e.g. sites with a shallow bedrock layer, sites with a deep bedrock layer, sites with a velocity reversal layer, sites without significant environmental noise, sites located in a noisy environment, and sites with clear near field effects) to identify the advantages and limitations of each method.

2.3.1.2 Near-field effects

The near-field effect is the most encountered issue in the MASW method, limiting the application of this method in geotechnical and geophysical communities. The primary assumption made for data processing of surface wave methods is that the wavefield only consists of plane surface waves. In other words, the two main simplifying assumptions for surface waves data processing are (1) plane wavefield with no contributions from cylindrical waves and (2) pure surface waves with no interference from body waves.

Passive surface wave methods generally hold these assumptions reasonable as sources for these methods are located far away from the array of geophones. However, for the active surface wave methods such as the MASW method, source distance from the first receiver (i.e. source offset) is minimized to achieve a high signal-to-noise ratio (Tokimatsu 1995, Zywicki 1999). In addition, long source offsets are not always desirable for active array-based surface wave methods due to the site constraints and lateral variability in the soil profile as array size increases. Therefore, the simplified assumptions made for data processing of active surface wave methods might not be valid for short source offsets (Ryden and Mooney 2009). The regions in the wavefield where these assumptions are invalid are called the near-field. When a source is placed within the near-field, the adverse effects produced on the measured phase velocity due to the contribution of cylindrical spreading waves and interference of body waves are called the near-field effects.

The near-field effects can be categorized into two main categories based on the assumptions made for active surface waves data processing. First, the near-field effect of modeling a cylindrical wavefield with a plane wavefield is called model incompatibility (Zywicki and Rix, 2005). This near-field effect is detected by a clear roll-off in the measured phase velocity at low frequencies. Second, the near-field effects due to body wave interference lead to oscillations in the measured phase velocity at low frequencies.

Provided in Figure 2.12a and b are examples of near-field effects observed in the form of clear roll-off (Figure 2.10a) and oscillation (Figure 2.10b) in the experimental phase velocity at low frequencies. It should be mentioned that for the examples illustrated in Figure 2.10, the near-field effects are very clear in the experimental dispersion data. However, this is not always the case, as sometimes the near-field effects alter the slope of the low-frequency portion of the dispersion curve. This makes the detectability of the near-field effects very difficult.

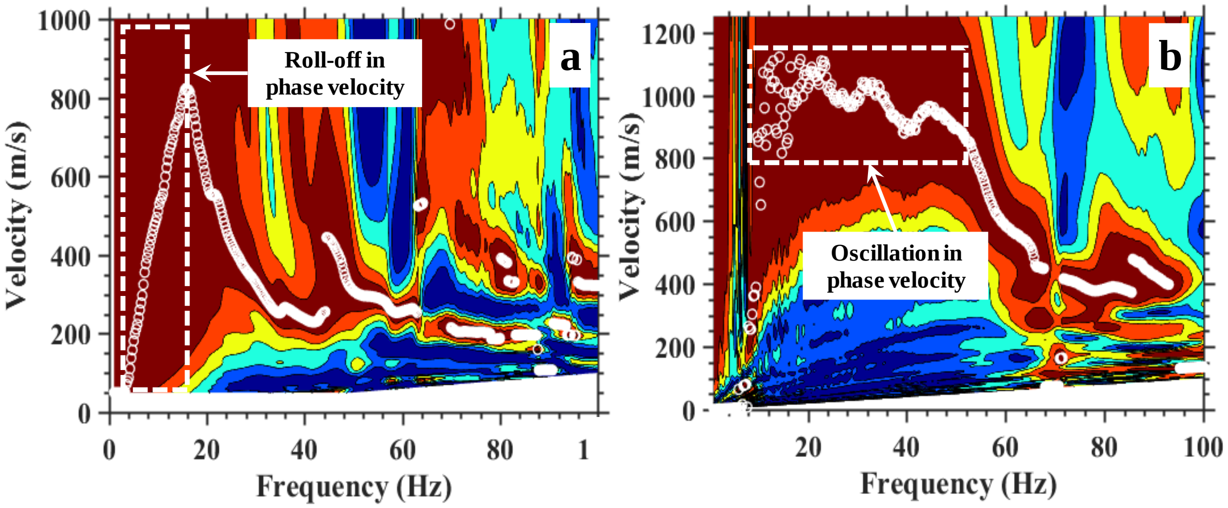

Figure 2.10- Clear examples of near-field effects. a) clear roll-off in the measured phase velocity due to model incompatibility, b) apparent oscillations in the measured phase velocity due to body waves interference.

Overall, the near-field effect is one of the unresolved issues of the MASW method, which corrupts the low-frequency experimental dispersion data so that they cannot be reliably used for the inversion process. Additionally, given that sometimes it is difficult to detect the experimental dispersion data corrupted by near-field effects, these data can be mistakenly used as the true experimental phase velocity. This leads to significant mispredictions (generally underestimation) of the subsurface layers' properties. According to the previous investigation, the measured phase velocity can be underestimated as much as 30% in the low-frequency dispersion data (Yoon *et al.*, 2009). The low-frequency dispersion data, which are sometimes corrupted by near-field effects, are important because they have information regarding deeper subsurface layers (e.g. stiff soil layers or bedrock units). It is, therefore, critical to be able to mitigate near-field effects on active surface wave methods (e.g. MASW).

2.3.1.2.1 Previous studies on near-field effects

In the last decade, many research groups have investigated the near-field effects on the traditional two-sensor SASW method. However, a limited number of studies examined the near-field effects on array-based active surface wave methods such as the MASW method. These limited studies aimed to develop ways to eliminate or reduce the near-field effects on array-based active surface wave methods. The proposed methods for near-field mitigation in the previous studies include (1) modifying wavefield transformation technique to account for cylindrical waves (Zywicki *et al.*, 2005), (2) increasing distance between the source and first or middle receiver (Xu *et al.*, 2006; Bodet *et al.*, 2009; Yoon *et al.*, 2009), (3) employing multiple source offsets (Wood *et al.*, 2012), (4) utilizing a greater number of receivers (Yoon *et al.,* 2009), and (5) using both phase and group velocity estimates (Tremblay *et al.*, 2019).

One of the primary studies regarding near-field effects on array-based active surface wave testing was conducted by Zywicki and Rix (2005). In this study, a cylindrical FDBF transformation technique was introduced to overcome the simplifying assumption of pure plane wave propagation within the wavefield. This method was extensively discussed in Section 2.3.1.1.3. Shown in Figure 2.11 is the percent difference between the plane and cylindrical models in Zywicki and Rix's (2005) study. From this figure, it is clear that the percent difference between the plane and cylindrical models significantly increases as frequency decreases. This indicates that the near-field effects of model incompatibility are mainly significant at the low-frequency portion of the dispersion curve. They claimed that the proposed cylindrical transformation technique eliminates the near-field effects of model incompatibility by utilizing a cylindrical wavefield model for phase velocity estimation.

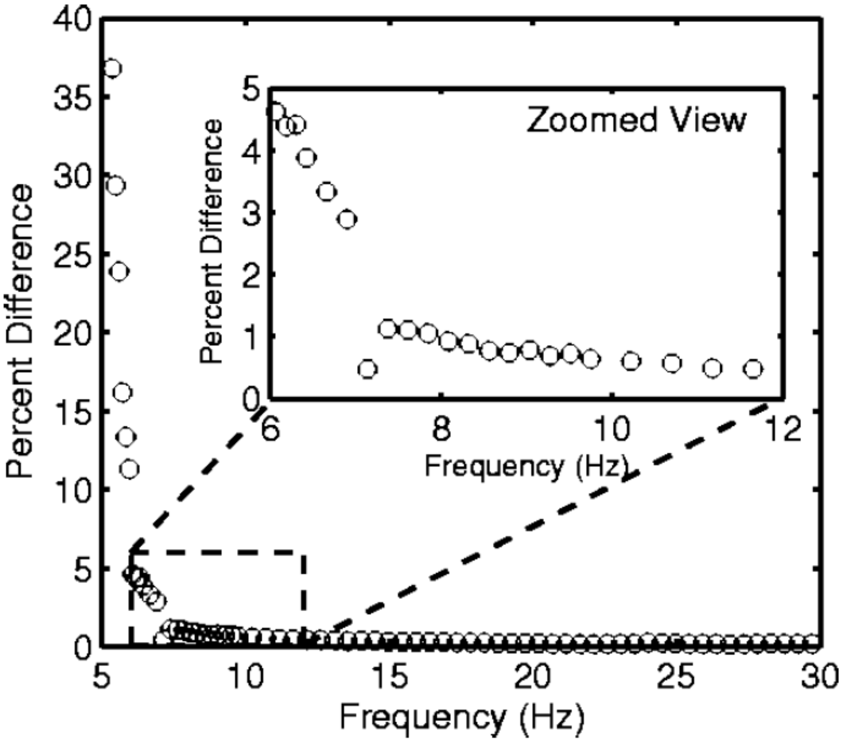

Figure 2.11- Percent difference between the plane and cylindrical models (Zywicki *et al.*, 2005).

Bodet et al. (2009) evaluated the near-field effects on array-based active surface wave methods using both numerical modeling and field measurements. Based on the results of the numerical modeling and field measurements, they observed that the measured phase velocity was underestimated by up to 5% of the real phase velocity for wavelengths of approximately half of the array size and up to 10% of the real phase velocity for wavelengths approximately equal to array size. Accordingly, they concluded that the underestimations in the measured phase velocity due to the near-field effects become significant (> 5%) when the measured wavelength exceeds half of the array size.

Yoon and Rix (2009) performed a thorough study on the near-field effects of array-based surface wave methods. In this study, two normalized parameters were introduced to investigate near-field effects. These parameters include a normalized phase velocity parameter defined as the ratio of the measured phase velocity (with near-field corruptions) to the true phase velocity (without near-field corruptions) and a normalized array center distance (hereafter normalized ACD) given by:

$$\frac{\bar{x}}{\lambda} = \frac{\left({}^{1}\!/_{M}\right)\sum_{m=1}^{M} x_m}{\lambda} \tag{29}$$

Where $\bar{x}$ is the mean distance of all receivers relative to the source offset, λ is the wavelength, and M is the number of receivers.

Yoon and Rix (2009) performed numerical modeling, laboratory testing, and several field measurements to investigate near-field effects. Presented in Figure 2.12 are the results of numerical modeling, laboratory testing, and field measurements from Yoon and Rix's (2009) study in a plot of normalized Rayleigh phase velocity versus normalized ACD.

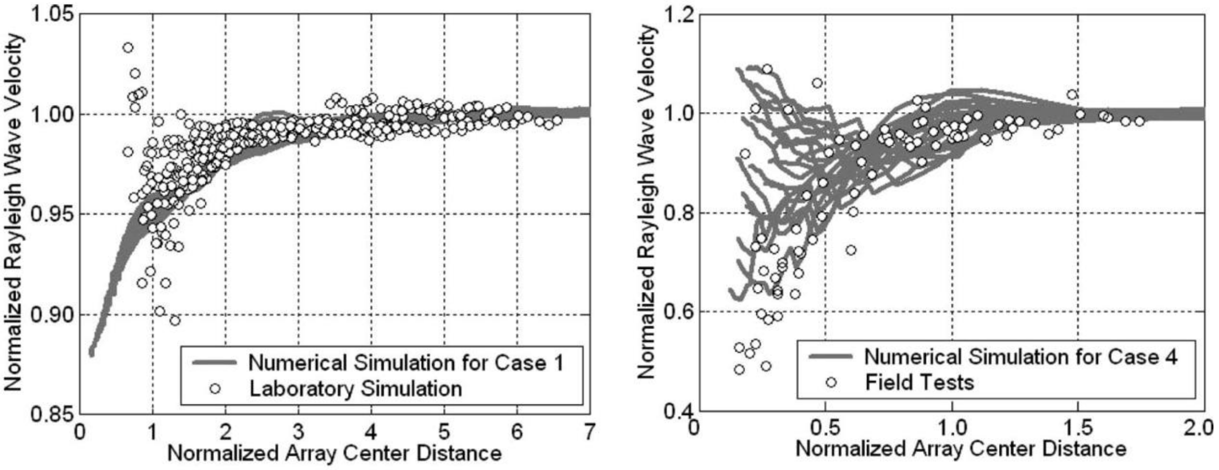

Figure 2.12- Numerical, laboratory, and field results of the Yoon and Rix study (modified from Yoon and Rix, 2009).

Based on the results of the numerical modeling, laboratory testing, and field measurements, Yoon and Rix (2009) have proposed two practical guidelines for near-field mitigation of array-based active surface wave methods. These include using a normalized ACD greater than 1 to limit errors in the measured phase velocity due to the near-field effects to less than 10-15% and a normalized ACD greater than 2 to limit errors in the measured phase velocity due to the near-field effects to less than 5%.

Li and Rosenblad (2011) performed field measurements at eleven sites with very deep impedance contrast (i.e. bedrock) in the upper Mississippi embayment in the Central U.S. They used various source offsets (ranging between 3-200 m) and geophone spacings (ranging between 1-25 m) for the active surface wave testing. Using the field measurement results, they followed the procedure defined by Yoon and Rix (2009) to generate the normalized ACD plots and define the near-field mitigation criteria. Presented in Figure 2.13 is an example normalized ACD plot from Li and Rosenblad's (2011) study.

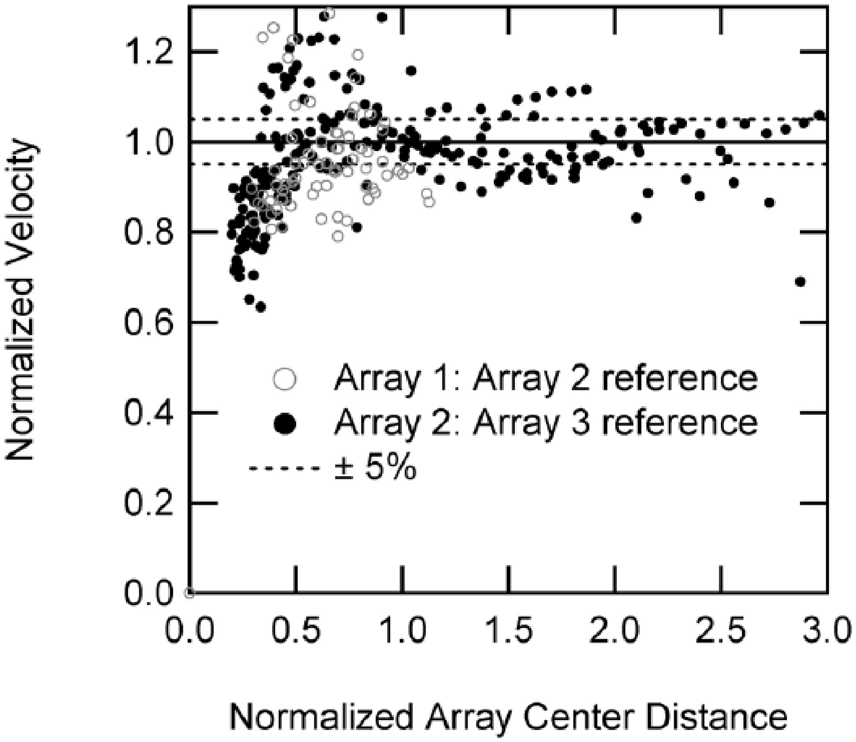

Figure 2.13- Example normalized ACD plot from Li and Rosenblad's (2011) study.

From Figure 2.13, it is clear that the normalized ACD criterion for near-field mitigation defined by Li and Rosenbald (2011) is approximately 0.5. This finding is very different than the normalized ACD criteria defined by Yoon and Rix (2009). Li and Rosenbald (2011) have claimed that the inconsistency in the normalized ACD criteria defined in their study with the findings of Yoon and Rix (2009) is due to different values of Poisson's ratio in the two studies. They mentioned that the criteria defined by Yoon and Rix (2009) are based on a constant Poisson’s ratio of 0.3, which is related to unsaturated soil conditions. However, all of the sites tested in their study had a very high Poisson’s ratio (0.4-0.49) due to the shallow water table location (ranging between 3-5 m). Therefore, they concluded that Poisson’s ratio is an important factor influencing near-field effects on array-based active surface wave testing. According to their obtained results, a less restrictive normalized ACD should be used for sites with a high Poisson’s ratio. For sites with a very high Poisson’s ratio, they recommended a normalized ACD of 0.5 to limit the measured phase velocity errors due to the near-field effect to 5% or less.

Roy and Jakka (2017) performed a numerical study using Finite Element modeling in Plaxis along with the field measurement only for one site to examine the influence of impedance contrast on near-field effects for the array-based active surface wave testing. In this study, different subsurface layering with varying impedance contrasts was modeled using Plaxis software. Presented in Figure 2.14 are example experimental observations from this study, which include the dispersion data for active and passive measurements along with the normalized array center plot. They claimed that the impedance contrast has a significant impact on near-field effects. According to this investigation, the underestimation in the measured phase velocity due to the near-field effects increases at lower normalized ACD as impedance contrast increases.

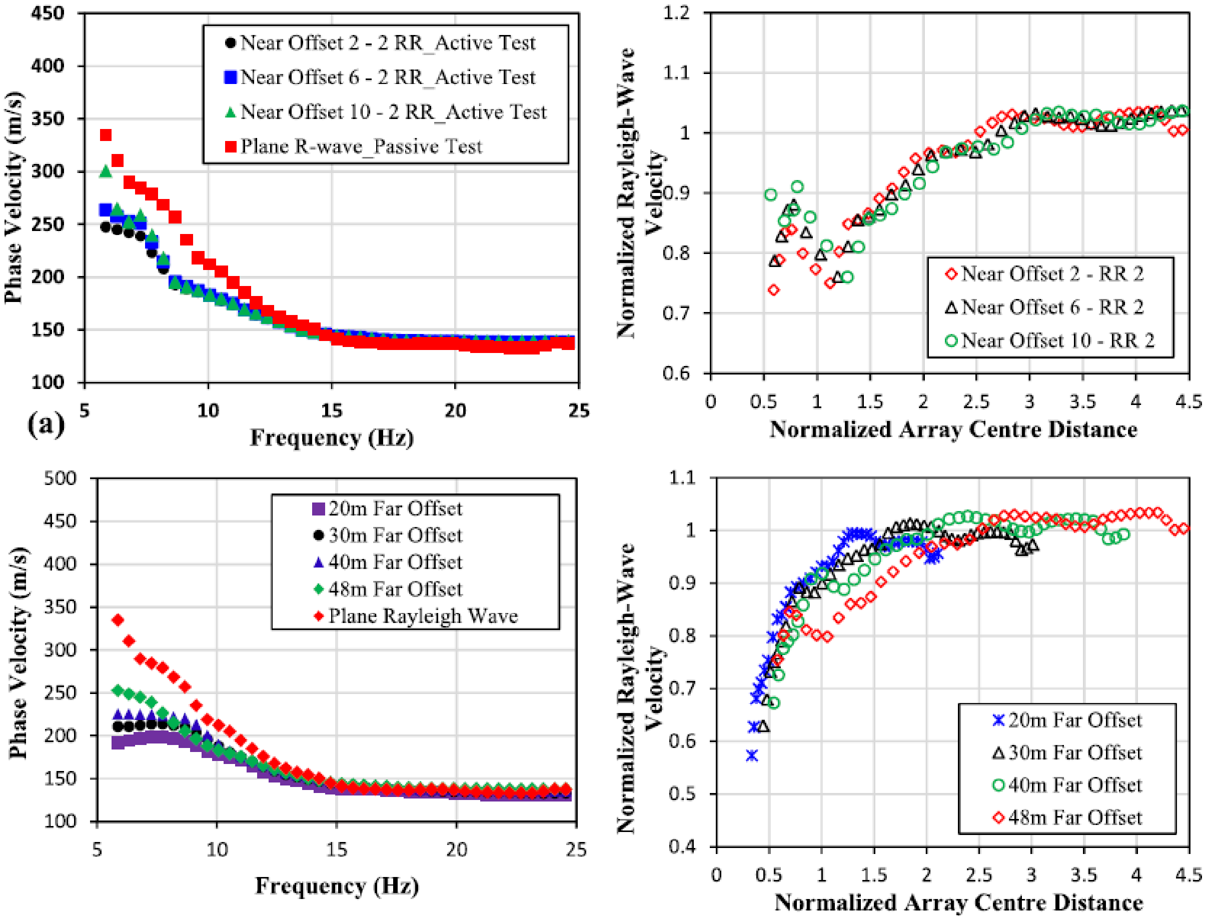

Figure 2.14- Near-field effects observed in Roy and Jakka's (2017) study. Results from field tests for different near offset distance: (a) comparison of active and passive test dispersion curves, and (b) Near-field effects in terms of normalized parameters; For different far offset distances: (c) comparison of active and passive test dispersion curves, and (d) Near-field effects in terms of normalized parameters.

In another study by Tremblay and Karry (2019), some practical considerations for near-field mitigation on array-based active surface wave testing were presented. Using numerical modeling and experimental measurements, they showed that using a longer array length or larger number of receivers does not always guarantee the mitigation of near-field effects. They suggested using both phase velocities and group velocities for experimental phase velocity estimates to mitigate near-field effects on active array-based surface wave testing.

2.3.1.2.2 Limitations of the previous studies

While near-field effects are adversely impacting the reliability of the results obtained from the active array-based surface wave methods and constraining the application of these methods in engineering practice, a limited number of studies have attempted to examine the near-field effects. These studies have investigated some of the factors influencing near-field effects, but there is still a dire need to perform more research in this regard to fully capture the parameters influencing near-field effects. Additionally, the apparent inconsistency between the findings of the previous studies regarding the most suitable normalized ACD criteria for near-field mitigation is another indicator of the need for more comprehensive investigations to improve our understanding of near-field effects. Practical guidelines provided in the previous studies are generally site-specific as they fail to consider different factors influencing near-field effects. Currently, there are no generally accepted practical criteria for near-field mitigation on array-based active surface wave testing.

Therefore, in this dissertation, in order to develop the best practical guideline for near-field mitigation, extensive field measurements were performed considering different factors influencing near-field effects. These factors include depth to sharp impedance contrast (i.e. bedrock unit), source offset, source type (sledgehammer and vibroseis), surface wave type (Rayleigh and Love), and the transformation technique used for data processing (FDBF, FK, PS, and τp). Therefore, one of the motivations of this dissertation is to fill this knowledge gap in this topic and develop the best practical guidelines for near-field mitigation during field measurements.

2.4 MHVSR method

2.4.1 Introduction

The MHVSR technique, which was first introduced by Nogoshi and Igarashi in 1971 and then popularized by Nakamura in 1989, is a passive geophysical method that has been widely utilized for seismic microzonation and estimation of the fundamental frequency of a site (Eker *et al.*, 2015; Wood *et al.*, 2019b). According to Nakamura's studies (Nakamura, 1989, 2000, 2019), the peak frequency from the MHVSR is approximately equal to the fundamental frequency of a site. Nakamura also suggested that the amplitude of the MHVSR at the peak frequency can be used as the seismic site amplification factor. However, other studies (Haghshenas *et al.*, 2008; Rong *et al.*, 2017) suggested that the amplitude of the MHVSR has a weak correlation with the true seismic site amplification factor of the site, and hence it should not be directly used as the seismic site amplification factor.

Another application of the MHVSR method is for the construction of the experimental dispersion curve at low (0.2-7 Hz) to intermediate (7-30 Hz) frequency ranges (Vantassel *et al.*, 2018; Wood *et al.*, 2019a), where the dispersion data from the active surface wave methods are generally corrupted with near-field effects and low signal to noise ratio.

The MHVSR technique is based on the analysis of the ratio between the amplitude of horizontal and vertical components (H/V) of microtremors or environmental noise. This ratio is calculated to identify the peak H/V linked to a fundamental property of a site. The microtremor wavefield can involve different sources, including human activities (e.g. construction and traffic) or natural phenomena (e.g. wind and ocean waves). In most cases, the microtremor wavefield is dominated by the surface waves; however, the effects of body waves cannot be neglected in some conditions (Irikura, 1999; Foti *et al.*, 2014). Assuming that surface waves dominate the microtremor wavefield, the vertical component of the microtremors is only affected by Rayleigh waves, whereas the horizontal components of the microtremors are affected by both Rayleigh and Love type surface waves. This is because Rayleigh waves create particle motions in both vertical and horizontal directions, whereas Love waves only created particle motions in a horizontal direction.

The amplitude of the surface waves and the H/V peak(s) is a function of the source properties and subsurface velocity structure, but for a given source, the H/V peak is mainly controlled by the subsurface velocity structure of the site. Studies have proven that peak(s) of MHVSR typically occur at or close to the fundamental frequency (f_r) of the site, which indicates the presence of a sharp Vs impedance contrast (ratio) in the subsurface (Fäh *et al.*, 2001; Malischewsky *et al.*, 2004; Yilar *et al.*, 2017). The Vs Impedance Ratio (IR) is defined as the ratio of the product of mass density (ρ) and shear wave velocity (Vs) of two layers.

$$\mathrm{IR}= \frac{\rho_2 \times V_{s2}}{\rho_1 \times V_{s1}} \tag{30}$$

If a peak satisfies the requirements of a reliable peak, as proposed in the SESAME (2004) guidelines, it can then be used to estimate depth to the sharp impedance contrast (i.e. depth to bedrock) of the site (Acerra *et al.*, 2004).

The raw MHVSR data is typically processed in general accordance with the SESAME (2004) guideline. The raw microtremor data is divided into several non-overlapping time windows to allow for uncertainty in the MHVSR results to be estimated. The Fourier Amplitude Spectra (FAS) of each component (Vertical, North, and East) is estimated for each of the time windows and then smoothed using a Konno and Ohmachi smoothing filter (Konno *et al.*, 1998). This smoothing function is recommended for the MHVSR data processing because it ensures a constant number of points for both low and high frequencies. Additionally, the amplitude of the H/V peak determined from this smoothing function is sometimes linked to the site amplification factor, particularly for sites where the contribution of the Rayleigh type surface waves in microtremors are approximately 0.4 (Konno *et al.*, 1998). The Konno and Ohmachi function is a logarithmic smoothing filter, which is defined as below:

$$\mathrm{W(f, fc)}= \left[(\sin (\log_{10}(\frac{\mathrm{f}}{\mathrm{fc}})^{\mathrm{b}}))\Big/(\log_{10}\left(\frac{\mathrm{f}}{\mathrm{fc}}\right)^{\mathrm{b}})\right]^{4} \tag{31}$$

Where f and fc are frequency and center frequency, respectively, and b is the smoothing bandwidth. The smoothing bandwidth is the main factor controlling the smoothing function. A smoothing bandwidth of 40 is typically used for MHVSR data processing.

The geometric mean of the two horizontal components ($H_{E\text{-}W}$ and $H_{N\text{-}S}$) FAS is divided by the vertical FAS to calculate the amplitude of the MHVSR ratio as below:

$$\mathrm{Amp(MHVSR)}=\frac{\sqrt{[\mathrm{FAS}(\mathrm{H}_{\mathrm{E\text{-}W}})]\times[\mathrm{FAS}(\mathrm{H}_{\mathrm{N\text{-}S}})]}}{\mathrm{FAS(V)}} \tag{32}$$

The mean MHVSR is computed from different time windows and used to determine the frequency(s) associated with the peak MHVSR. The final output of the MHVSR measurements is a plot of H/V amplitude versus frequency, as shown in Figure 2.15. Anomalous time windows (see Figure 2.15a) are removed from the data, and the rest of the time windows are used to calculate the mean MHVSR spectra ratio with associated standard deviation (Figure 2.15b).

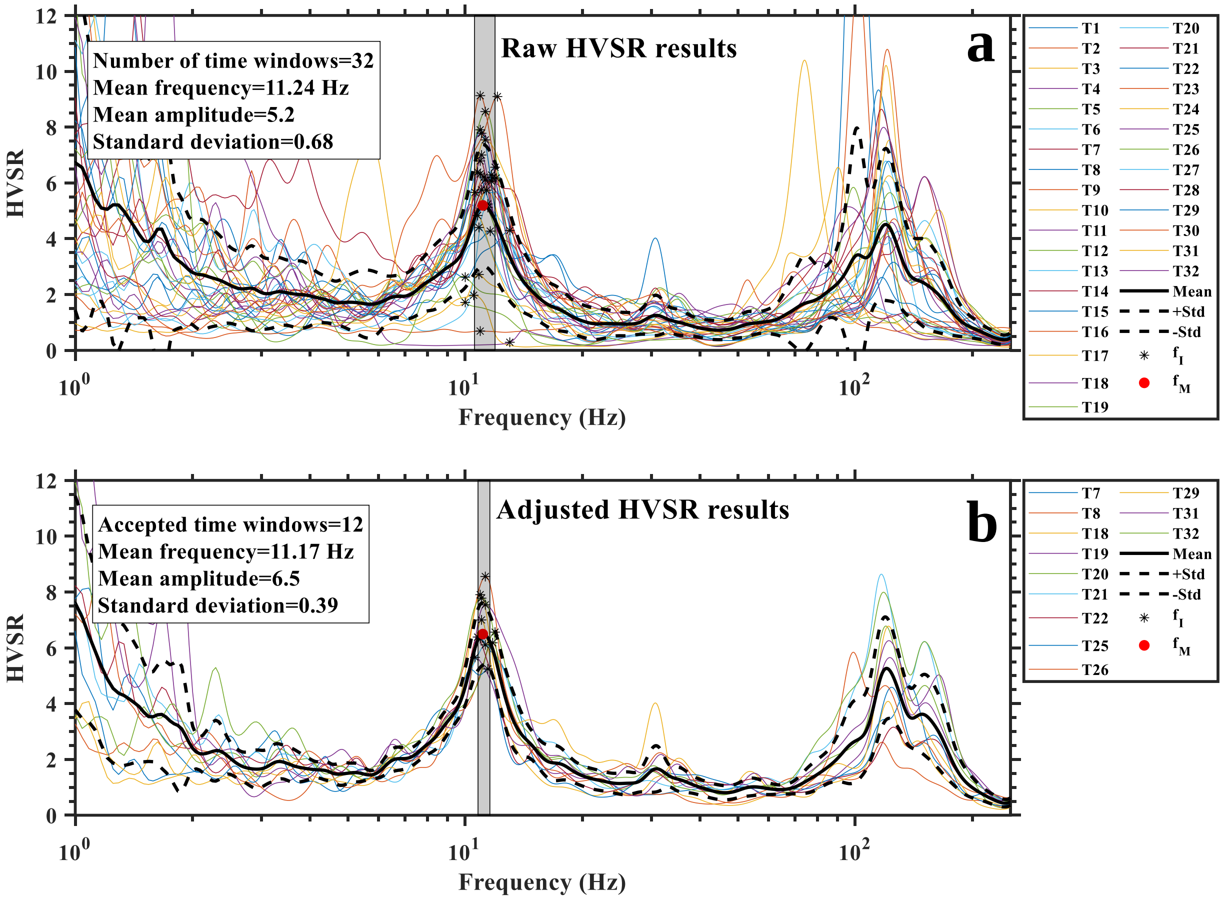

Figure 2.15- An example of HVSR data processing. a) HVSR curve before excluding the anomalous time windows, and b) final HVSR results after excluding the anomalous time windows.

Suppose peak(s) of the MHVSR measurement meets the requirements of a true and reliable peak (SESAME 2004). In that case, it can be used for further processing to estimate depth to the sharp impedance contrast (i.e. depth to bedrock) of the site using the quarter-wavelength equation as below.

$$H= (V_{s,avg}/4f_r) \tag{33}$$

Where H is the thickness of sediments above the impedance contrast, $V_{s,avg}$ is the average shear wave velocity of the materials above the sharp impedance contrast, and f_r is the frequency associated with the peak MHVSR (fundamental frequency). According to the quarter-wavelength equation, the average shear wave velocity of the sediments located above the sharp impedance contrast is needed to calculate the H value. In this regard, several methods can be used, as explained below.

2.4.2 Estimating the average shear wave velocity of top sediments

Different methods can be used to estimate the $V_{s,avg}$ value, including direct field measurements and empirical correlations between Vs and other geotechnical properties of soil. While direct field measurement is preferred over indirect correlations, this is not always economically feasible. Additionally, for sites with rough terrains such as steep slopes, it is difficult to perform field measurements to estimate the $V_{s,avg}$. Therefore, three methods are suggested in this study for $V_{s,avg}$ estimation as below.

2.4.2.1 Direct field measurements

Several field measurements can be used to measure the $V_{s,avg}$ of a site, including seismic cone penetration testing, seismic refraction, down-hole and cross-hole, and surface wave methods (MASW or Microtremor Array Measurements, MAM). All these techniques have been widely used and verified by other researchers for soil $V_{s,avg}$ estimation, and site characterization (Cox *et al.*, 2014; Wotherspoon *et al.*, 2015; Garofalo *et al.*, 2016).

2.4.2.2 SPT-Vs correlation method

The average Vs of top sediments can be back-calculated from the blow count (N) of the Standard Penetration Test (SPT) using some empirical SPT-Vs correlations. The relationship between the SPT N value and shear wave velocity of soils has been extensively investigated and debated in the literature (Dikmen, 2009; Akin *et al.*, 2011; Fabbrocino *et al.*, 2015; Rahimi *et al.*, 2018, 2020c). A power-type function with two constants of A and B are typically used for SPT-Vs correlation as below:

$$Vs= A\times(N_{SPT})^{B} \quad (34)$$

Given that the SPT-Vs correlations that have been developed in the previous studies vary significantly, even for a given soil type (Rahimi *et al.*, 2020c), it is quite challenging to find the empirical correlation that best fits the study area. Although this method allows for simple, rapid, and cost-effective $V_{s,avg}$ estimation, it may lead to incorrect $V_{s,avg}$ estimation (underestimation or overestimation) due to the great uncertainty associated with the previous correlations.

2.4.2.3 Reference Vs method

While the SPT-Vs correlation method is more popular for indirect estimation of soil Vs, the reference Vs method can provide a more accurate estimation of soil Vs typically for sites with young Holocene age soils. This is because the reference Vs method accounts for several important factors influencing the Vs of soils, including soil stiffness, soil type, and confining stress level.

For sites where information regarding soil type and soil stiffness are available from the boring logs, the reference Vs profiles (available for various soil types) can be generated to estimate the $V_{s,avg}$ value. It has been shown that the Vs of soils can be calculated as a function of the confining stress as follows (Menq, 2003; Lin *et al.*, 2014; Rahimi *et al.*, 2019b):

$$V_{sz}= V_{s0}+(V_{s(@z=zcr)} -V_{s0}) \times (z/z_{cr}) \qquad \text{for } z<z_{cr} \quad (35)$$

$$V_{sz}= V_{s,ref} \times(\sigma_v'/Pa)^\wedge n_s \qquad \text{for } z> z_{cr} \quad (36)$$

Where V_{sz} is the shear wave velocity at depth z, σ_v' is the mean effective stress, V_{s0} is the initial shear wave velocity at the ground surface, $V_{s,ref}$ is the shear wave velocity at 1 atm mean effective stress, $V_{s(@z=zcr}$ is the shear wave velocity at z_{cr}, Pa is the atmospheric pressure, and n_s is the exponent of the normalized effective mean stress. The z_{cr} is defined as the ratio of the atmospheric pressure to the total moist unit weight of the soil (Rahimi *et al.*, 2019b).

Given that these parameters (n_s, $V_{s,ref}$, and V_{s0}) are available for various soil types, the reference Vs profile can be generated for a soil profile, and then the $V_{s,avg}$ can be calculated from the generated Vs profile. As an example, this method is shown in Figure 2.16 for a site that consists of a 10 m soft clay layer, a loose sand layer from 10-20 m, underlain by the bedrock. The average Vs of the top sediments is determined from the combined Vs profile, as shown in Step 3 of Figure 2.16.

Overall, while this method has been rarely used in the literature for $V_{s,avg}$ estimation, it can predict the $V_{s,avg}$ more accurately than the SPT-Vs correlation method.

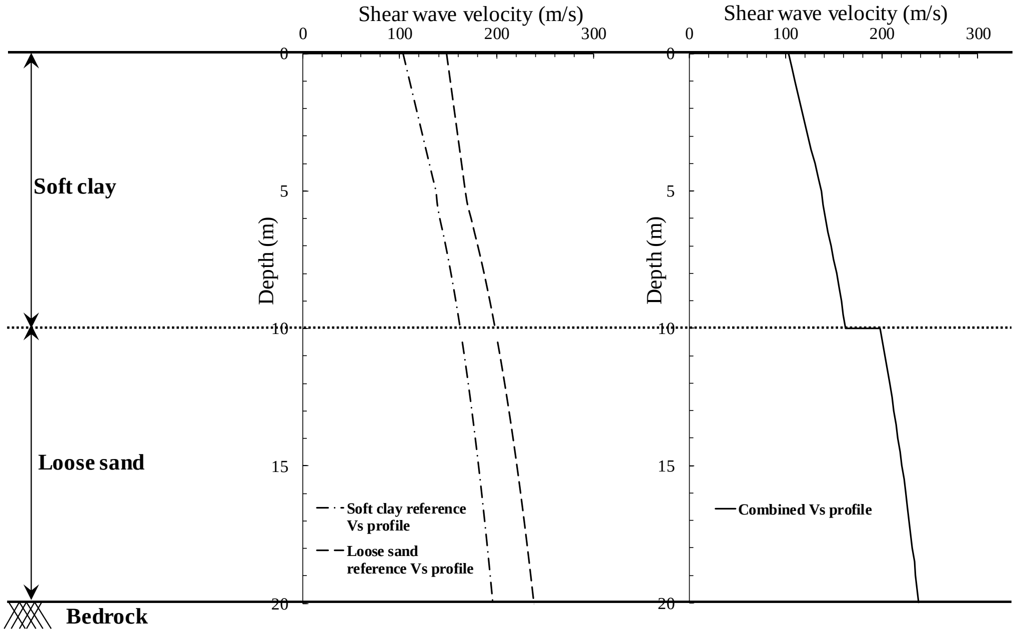

Step1: Defining subsurface layers

Step2: Developing Vs profile for each layer

Step3: Generating combined Vs profile

Figure 2.16- Generating Vs profile for a site using the reference Vs curves.

2.4.3 Joint inversion of MASW and MHVSR

For sites where the co-located MHVSR and MASW data are available, the experimental dispersion curve from the MASW method can be jointly inverted with the peak frequency from the MHVSR method to increase the reliability of the inversion process. The joint inversion of the MASW and MHVSR can significantly improve the accuracy of the final inverted shear wave profile by constraining depth to the sharp impedance contrast in the inversion process. To do so, weighting factors need to be assigned to the dispersion curve from the MASW method and peak frequency from the MHVSR. Teague et al. (2018) have proposed weighing factors of 0.8 and 0.2 experimental dispersion curve from the MASW and the peak frequency from the MHVSR, respectively. The combined misfit (m_c) parameter is calculated based on the misfit value related to the dispersion data (m_{disp}) and the misfit value related to the ellipticity peak ($m_{H/V}$) as below:

$$m_c=m_{disp}\times w_{disp}+m_{H/V}\times w_{H/V}=\sqrt{\sum_{i=1}^{n}\frac{(V_{di}-V_{ti})^2}{n_f\times\sigma_i^2}}\times w_{disp}+\sqrt{\frac{(f_{ellp,e}-f_{ellp,t})^2}{\sigma_{f_{ellp}}^2}}\times w_{H/V} \qquad (37)$$

Where V_{di} and V_{ti} are, respectively, the experimental and inverted theoretical Rayleigh phase velocities at frequency f_i, σ_i is the standard deviation related to the experimental dispersion data at frequency f_i, n_f is the number of frequency samples used for misfit calculation, $f_{ellp,e}$ and $f_{ellp,t}$ are the experimental (HVSR) and theoretical ellipticity peaks, and σ_{ellp} is the standard deviation associated with the experimental HVSR peak.

An example of the MASW and MHVSR joint inversion results is provided in Figure 2.17. Presented in Figure 2.17 a, b, and c are the inverted V_s profile, the sigma $\ln(V_s)$, and the experimental MHVSR measurements along with the theoretical ellipticity curve, respectively.

The low-frequency peak (f_1=6.9 Hz) from the MHVSR measurement, as shown in this figure, helps constrain depth to the sharp impedance contrast in the shear wave velocity profile.

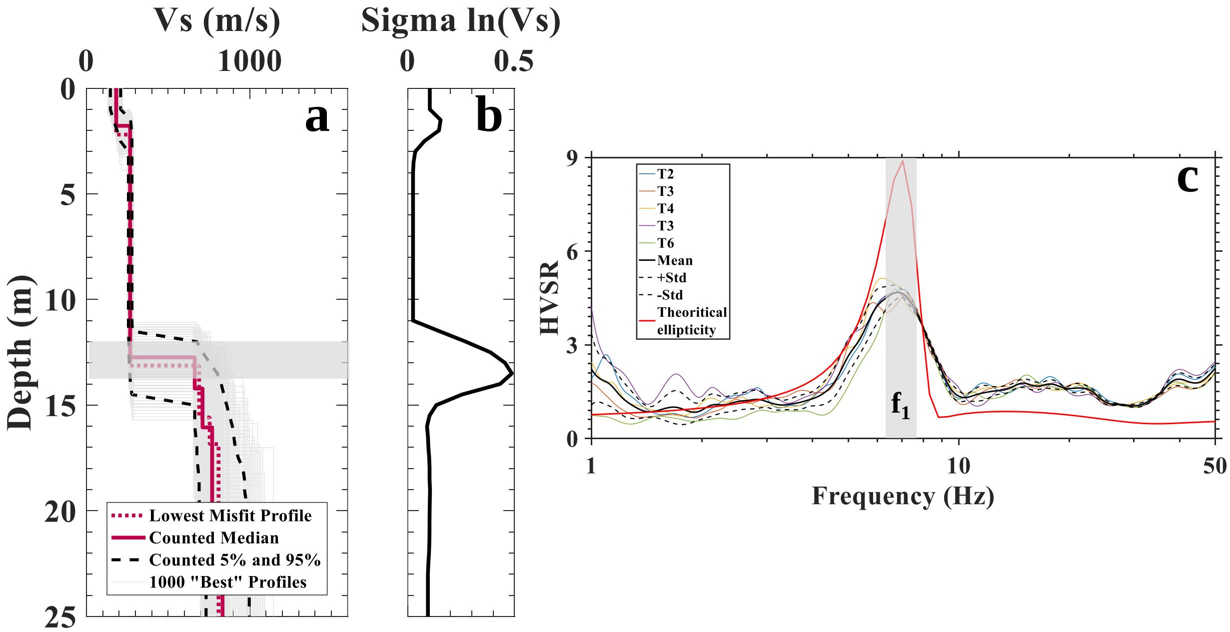

Figure 2.17- An example joint inversion results from the MASW and MHVSR measurements with one impedance contrast at subsurface. a) V_s profile, b) sigma ln (V_s), c) experimental MHVSR along with the theoretical ellipticity curve.

2.4.4 Summary

The MHVSR method has been widely used for applications such as seismic microzonation, estimation of the fundamental frequency, construction of the experimental dispersion curve at low to intermediate frequency ranges. However, this method has been rarely used for geotechnical infrastructure evaluation (e.g. landslide characterization). For example, for landslides with a very shallow and highly variable bedrock layer with complex bedrock topography where a full understanding of the bedrock layer is required to conduct a precise slope stability analysis, the MHVSR method can be considered as a suitable technique for bedrock mapping. Therefore, in this dissertation, the reliability and efficiency of the MHVSR method as a potential candidate to complement the conventional in-situ methods or array-based geophysical methods by providing information across a larger spatial extent for landslide investigations is investigated. Additionally, a new frequency-domain window rejection tool was developed in this study for MHVSR data processing to reduce the uncertainty in the MHVSR peak frequency estimates. This tool provides several useful features for MHVSR data processing, allowing automatic time window rejection for time windows that fail to satisfy the required criteria.

3 CHAPTER 3: PERFORMANCE OF DIFFERENT TRANSFORMATION TECHNIQUES FOR MASW DATA PROCESSING FOR DEVELOPING EXPERIMENTAL DISPERSION CURVES

3.1 Chapter overview

This chapter examines the performance of different transformation techniques that are widely used for MASW data processing considering various site conditions, near-field effects, and modal separation. In this regard, the performance of each transformation technique is assessed, and then the advantages and limitations of each transformation technique are discussed. Finally, some guidelines are provided regarding the most suitable transformation technique that should be used for different conditions for MASW data processing. The results are provided in the form of a journal paper that has been submitted in Surveys in Geophysics Journal.

3.2 Performance of Different Transformation Techniques for MASW Data Processing Considering Various Site Conditions, Near-Field Effects, and Modal Separation

Reference

Rahimi, S., Wood, C. M., Teague, D. P. (2021). Performance of Different Transformation Techniques for MASW Data Processing Considering Various Site Conditions, Near-Field Effects, and Modal Separation. Surveys in Geophysics.

3.3 Abstract

Multichannel Analysis of Surface Waves (MASW) has received increasing attention in many disciplines in recent years. However, there are still issues with this method, which require further investigation. The most common issues include a potentially poor-resolution experimental dispersion image, near-field effects, and modal misidentification. Therefore, this paper examines the performance of four common wavefield transformation methods for MASW data processing. MASW measurements were performed using Rayleigh and Love waves at sites with different stratigraphy and wavefield conditions. For each site, dispersion curves were generated using the four transformation methods. For sites with a very shallow and highly variable bedrock topography with a high-frequency point of curvature (>20 Hz), the Phase Shift (PS) method leads to a very poor-resolution dispersion image compared to other transformation methods. For sites with a velocity reversal, the Slant Stack (τp) method fails to resolve the dispersion image for frequencies associated with layers located below the velocity reversal layer. Overall, the cylindrical frequency domain beamformer (FDBF-cylindrical) method was determined to be the best method under most site conditions. This method allows for a stable, high-resolution dispersion image for different sites and noise conditions over a wide range of frequencies, and it mitigates the near-field effects by modeling a cylindrical wavefield. However, the FDBF-cylindrical was observed to be dominated by higher modes at complex sites (i.e. sites where multiple modes are present). Therefore, the best practice is to use more than one transformation method (FDBF-cylindrical and FK methods) to enhance the data quality, particularly for complex stratigraphy environments.

Keywords: MASW, Dispersion curve, Transformation techniques, Near-field effects, Multi-mode detection, Velocity reversal.

3.4 Introduction

After the 1980s, surface wave techniques became popular in many disciplines, such as seismology, geophysics, material science, and engineering. The application of these methods in geotechnical engineering was initiated by the introduction of the Spectral Analysis of Surface Waves (SASW) method in 1994 (Stokoe *et al.*, 1994), but its widespread use began after the development of array-based methods such as the Multi-channel Analysis of Surface Waves

(MASW) in 1998 (Park *et al.*, 1998). MASW utilizes the dispersive nature of Rayleigh or Love type surface waves propagating through geomaterials to estimate the variation of shear wave velocity (V_s) with depth. MASW has several advantages over the traditional two-sensor SASW. For MASW, data processing and data interpretation become faster, less subjective, and require less operator knowledge (Foti *et al.*, 2014). Additionally, MASW helps to mitigate several limitations associated with the SASW. These include the inability to separate multiple modes of propagation and accurately identify near-field effects (Zywicki *et al.*, 2005).

Currently, MASW is widely used in geotechnical engineering for various applications, including but not limited to near-surface site characterization (Lai *et al.*, 2002; Rix *et al.*, 2002; Socco *et al.*, 2004; Hebeler *et al.*, 2007, 2007; Wood *et al.*, 2017a), liquefaction assessment (Wood *et al.*, 2017b; Rahimi *et al.*, 2020a), infrastructure evaluation (Cardarelli *et al.*, 2014; Rahimi *et al.*, 2019a), and V_{S30} estimation (Comina *et al.*, 2011; Martinez-Pagan *et al.*, 2012; Rahimi *et al.*, 2020c). The standard procedure for MASW involves three steps: field measurements, data processing, and inversion. A key part of MASW data processing that controls the final results is developing the experimental dispersion curve (i.e. phase velocity versus frequency plot). This is a critical step in the MASW method because the higher the resolution of the experimental dispersion curve, the higher the reliability of the inverted V_s profile. Therefore, the resolution of the experimental dispersion image is of primary importance in the MASW method.

To develop the experimental dispersion curve, wavefield transformation techniques are commonly used to transfer the original time-space (t-x) domain data into another domain, such as the frequency-wavenumber (f-k), the frequency-slowness (f-p), or the frequency-velocity (f-v) domains. The advantages of transforming the data into another domain are that in the transformed domain, the propagation properties of surface waves can be easily identified as spectral maxima, and different modes of propagation can often be detected and separated even when they are not clearly visible in the original time-space domain (Foti *et al.*, 2014). Resolving different modes of propagation is important because the inversion analysis's accuracy can be enhanced by including multiple modes in the inversion process (Xia *et al.*, 2003).

Four transformation techniques are commonly used in the MASW method for developing the experimental dispersion curve. These include slant stack or frequency-slowness (τp) (McMechan *et al.*, 1981), frequency-wavenumber (FK) (Nolet *et al.*, 1976; Yilmaz, 1987; Foti *et al.*, 2000), Frequency Domain Beamformer (FDBF) (Zywicki, 1999; Hebeler *et al.*, 2007), and phase shift (PS) (Park *et al.*, 1998). Additionally, varying approaches within the FDBF method can model a planar or cylindrical wavefield (Zywicki *et al.*, 2005). These methods are explained in detail in the next section.

While differences may appear in the experimental dispersion curves developed using each transformation technique, to date, no study has exclusively compared the limitations and advantages of each transformation technique considering different subsurface layering and wavefield conditions. In this regard, the limited previous studies (Dal Moro *et al.*, 2003; Tran *et al.*, 2008) only compared the performance of transformation techniques for a specific subsurface layering, meaning that their results are site-specific and cannot be applied to other site conditions. For instance, Dal Moro et al. (2003) mentioned that the PS method provides the highest resolution dispersion curve compared to the FK and τp methods for sites with unconsolidated sediments. Tran and Hiltunen (2008) compared the four transformation techniques for a particular site. They claimed that the results from all the transformation techniques are in good agreement, but the FDBF cylindrical leads to a slightly higher resolution dispersion curve.

Another issue with the previous studies is that they failed to provide all critical characteristics of their study area (e.g. sharp impedance contrast depth, wavefield noise conditions). These characteristics are important to truly understand the differences observed in the experimental dispersion curves from different transformation techniques. Despite the lack of investigation in this regard, it is important to understand each transformation technique's limitations and advantages. This is particularly important for identifying multiple modes of propagation and the low-frequency portion of the dispersion curve, where near-field effects or low signal-to-noise ratios typically corrupt the experimental data.

This study evaluates the performance of four common wavefield transformation techniques for developing the experimental dispersion curve for MASW using both Rayleigh and Love type surface waves. Toward this end, more than 500 MASW tests were conducted at sites with different subsurface layering, wavefield, and noise conditions to understand potential differences between the transformation techniques.

The paper begins by reviewing the four common transformation methods and the issues most often encountered in the MASW technique. Information regarding the field measurements, subsurface layering, and wavefield conditions of each study site are then provided. Finally, the resolution of the Rayleigh and Love experimental dispersion curves generated using the four transformation methods are compared for sites with deep and shallow sharp impedance contrast (i.e. bedrock), sites with a velocity reversal layer, sites with noisy and quiet environments, sites with apparent near-field effects, and sites with clear higher modes. The conditions where each transformation technique performs well and poorly are highlighted and discussed with conclusions on the most appropriate method based on the available data.

3.5 Common transformation techniques used for MASW data processing

Four wavefield transformation techniques are commonly used in MASW data processing for developing the experimental dispersion curve. Researchers and consultants have extensively used these transformation techniques from different institutions and in various software packages, as summarized in Table 2. Due to the lack of investigations regarding the advantages and limitations of each transformation technique, users generally ignore potential differences and assume similar performance from these four transformation techniques.

All transformation methods used in MASW are aimed at converting the raw time-space domain data into another domain where the propagation properties of the surface waves (i.e. frequency, wavenumber, and phase velocity) can be identified as a spectral peak (maximum energy). Once the data is converted into such a domain, the experimental dispersion curve is generated by identifying the wavenumber and the phase velocity associated with the maximum energy at each frequency. The procedure used by each method to transform the data is discussed below.

Table 2- Summary of different transformation methods used by researchers and consultants from different institutions and software packages.

No	Affiliation	Country	Dispersion processing method	Software
1	Univ. Texas at Austin (Cox et al. 2014)	USA	FDBF, FK, PS, and τp	Matlab
2	Institut des Sciences de la Terra	France	FK	Geopsy
3	Univ. of Iceland (Olafsdottir et al. 2018)	Iceland	PS	MASWaves, Matlab
4	Univ. of Arkansas (Rahimi et al. 2108)	USA	FDBF, FK, PS, and τp	Matlab
5	Zhejiang Univ. (Cheng et al. 2019)	China	FK and τp	
6	Monash Univ. (Volti et al. 2016)	Australia	τp	SeisImager/SW
7	Univ. of Potsdam (Lontsi et al. 2016)	Germany	FK	Geopsy
8	Univ. of Nevada Reno/Optim Inc.	USA	τp	SeisOpt ReMi
9	Western Univ. (Darko et al. 2020)	Canada	FK	Geopsy
10	Politecnico di Torino (Foti et al. 2000)	Italy	FK	Matlab
11	Univ. of Missouri (Rosenblad and Li 2009)	USA	FK	Matlab
12	National Institute of Oceanography and Applied Geophysics	Italy	FK	-
13	Geometrics Inc.	USA	τp	SeisImager/SW
14	Park Seismic LLc.	USA	PS	ParkSEIS
15	Kansas Geological Survey	USA	PS	SurfSeis
16	Geogiga Technology Corp	USA	FK, PS, and τp	Geogiga Surface
17	RadExPro	Russia	FK	RadExPro
18	Eliosoft	Italy	PS	WinMASW
19	GeoVision (Martin et al. 2017)	USA	FK and PS	-

3.5.1 Slant Stack (τp)

The τp method also called the slant stack or frequency-slowness, was first introduced by McMechan and Yedlin (1981). This method utilizes two linear transformations that allow the decomposition of the shot-gather into its plane-wave linear components. The two linear transformations include a slant stack and a one-dimensional Fourier transform. Using the slant stack transformation, the original time (t)-space (x) domain data is converted into the time intercept (τ)-slowness (p) domain. A one-dimensional (1D) Fourier transform is then applied to the τp domain data to transform the data into the frequency (f)-slowness (p) domain (McMechan *et al.*, 1981; Foti *et al.*, 2014). The linear relationship that relates the four variables t, x, τ, and p is given by:

$$t = \tau + px \tag{38}$$

The slant slack transform is expressed as follows:

$$\mathrm{f}(\tau, \mathrm{p}) = \int_{-\infty}^{+\infty} \mathrm{U}(x, t)\mathrm{d}x = \int_{-\infty}^{+\infty} \mathrm{U}(x, \tau + px)\mathrm{d}x \tag{39}$$

Where $\mathrm{U}(x, t)$ is the signal recorded at distance x from the source. For each value of τ in the slant stack transformation, the data in the time-space domain are stacked along a straight line with a slope of p. Therefore, each straight line in the time-space domain is associated with a constant data pair of τ-p in the τp domain. Finally, by applying a one-dimensional Fourier transform over the time intercept variable, the data is transformed into the frequency-slowness domain:

$$\mathrm{F}(\mathrm{f}, \mathrm{p}) = \int_{-\infty}^{+\infty} \mathrm{f}(\tau, \mathrm{p}) e^{-i2\pi f\tau}\mathrm{d}\tau \tag{40}$$

3.5.2 Frequency-Wavenumber (FK)

The frequency-wavenumber transformation method was first proposed by Nolet and Panza (1976) and then used by other researchers for surface wave data processing (Gabriels *et al.*, 1987; Yilmaz, 1987; Foti *et al.*, 2000). FK is the simplest and fastest method for MASW data processing. In the FK method, the time-space domain data are decomposed into its components at different frequencies and wavenumbers. In this regard, the data in the time-space domain is transformed into the frequency-wavenumber domain using a two-dimensional (2D) Fourier transform:

$$\mathrm{F}(f,k) = \iint_{-\infty}^{+\infty} \mathrm{U}(x,t)e^{-2\pi i(ft+kx)}dxdt \tag{41}$$

3.5.3 Frequency Domain Beamformer (FDBF)

Frequency Domain Beamformer (FDBF) was first introduced by Gabriels et al. (1987) and then modified and popularized by Zywicki (1999) for surface wave data processing. The basic concept of this method is very similar to τp. The term beamformer refers to the ability of an array or signal processing method to focus on a particular direction and the mainlobe of an Array Smoothing Function (ASF), which is called a beam (Gabriels *et al.*, 1987). The FDBF method utilizes a steering vector, which is an exponential phase shift vector, to calculate the power associated with each particular frequency-wavenumber data pair (Zywicki, 1999; Hebeler *et al.*, 2007) :

$$\mathrm{e(k)} = [e^{-ik.x_1}, e^{-ik.x_2}, \ldots . e^{-ik.x_m}]^T \tag{42}$$

Where e(k) is the phase shift vector, k is the vector wavenumber, x_m denotes the sensor m position in the array, T denotes the transpose of the vector, and i is the imaginary number. For a particular f-k data pair, the power is calculated by multiplying the spatiospectral correlation matrix (R) by the steering vector and then summing the total power over all receivers. The steered power spectrum is given by:

$$P_{BF}(k,\omega)=e^H\mathbf{WRW}^He \tag{43}$$

Where H denotes the Hermitian transpose of the vector and **W** is a diagonal matrix, containing the shading weights of each receiver:

$$\mathbf{W}=\begin{bmatrix} w_1 & \cdots & 0 \\ \vdots & \ddots & \vdots \\ 0 & \cdots & w_m \end{bmatrix} \tag{44}$$

The spatiospectral correlation matrix (**R**) is expressed by:

$$\mathbf{R}\ (\omega)=\begin{bmatrix} R_{1,1}(\omega) & \cdots & R_{1,m}(\omega) \\ \vdots & \ddots & \vdots \\ R_{m,1}(\omega) & \cdots & R_{m,m}(\omega) \end{bmatrix} \tag{45}$$

Where $R_{m,n}$ is the cross power spectrum between receivers *m* and *n*:

$$R_{\mathbf{m,n}}(\boldsymbol{\omega}) = S_m(\omega)S_n^H(\omega) \tag{46}$$

Where S_m and S_n are the Fourier spectra of the m^{th} and n^{th} receivers, respectively. The first version of the FDBF transformation method was proposed assuming a plane wavefield. This assumption is also made in all other transformation methods (τp, FK, and PS). This assumption is reasonable for passive surface wave methods, as ambient vibrations are typically generated by sources located at far distances. However, for active surface wave methods (e.g. MASW), it is not always valid to assume a pure plane wavefield because active surface waves are generated at relatively close source offsets. This means that the active waves can propagate cylindrically in the near-field zone. The near-field effect of modeling a cylindrical wavefield with a plane wavefield is called the model incompatibility effect.

The FDBF transformation was modified in 2005 to account for the model incompatibility effect (Zywicki *et al.*, 2005). In the updated version of the FDBF, a new steering vector was defined to account for the cylindrical wavefield:

$$h(k)=[e^{-i\phi(H_0(k.x_1))}, e^{-i\phi(H_0(k.x_2))}, \ldots.\ e^{-i\phi(H_0(k.x_m))}\ ]^T \tag{47}$$

Where ϕ is the phase angle of each argument in parentheses, h(k) is the Hankel steering vector, and Hankel function H_0 is given by:

$$H_0(k\ .\ x)=J_0(k\ .\ x) + iY_0(k\ .\ x) \tag{48}$$

Where J_0 is Bessel function of the first kind of order zero, and Y_0 is Bessel function of the second kind of order zero. Then, the steered power spectrum for the cylindrical wavefield is given by:

$$P_{CBF}(k,\omega)=h^{H}\mathbf{W}\mathbf{R}\mathbf{W}^{H}h \tag{49}$$

Zywicki and Rix (2005) claimed that the updated version of the FDBF overcomes the limitations of the plane wavefield assumption by accounting for the cylindrical wavefield in the near-field zone.

3.5.4 Phase Shift (PS)

The phase-shift method for surface wave data processing was proposed by Park et al. (1998). In this method, the time-space domain data are first converted into the circular frequency (ω)-space (x) domain using a one dimensional Fourier transform:

$$\mathrm{U}(\omega, \mathrm{x}) = \int_{-\infty}^{+\infty} \mathrm{f}(\mathrm{t}, \mathrm{x}) e^{i\omega t} \mathrm{d}t \tag{50}$$

The transformed function is then defined as the multiplication of two separate terms, the phase [$\mathrm{P}(\omega, \mathrm{x})$] and amplitude spectrum [$\mathrm{A}(\omega, \mathrm{x})$]:

$$\mathrm{U}(\omega, \mathrm{x}) = \mathrm{P}(\omega, \mathrm{x})\mathrm{A}(\omega, \mathrm{x}) \tag{51}$$

The amplitude parameter preserves the information about the signal attenuation and geometrical spreading, whereas the phase velocity parameter preserves all the information regarding the dispersion properties. Therefore, $\mathrm{U}(\omega, \mathrm{x})$ function can also be given by:

$$\mathrm{U}(\omega, \mathrm{x}) = e^{-i\emptyset x}\mathrm{A}(\omega, \mathrm{x}) = e^{-i\frac{w}{V_R}x}\mathrm{A}(\omega, \mathrm{x}) \tag{52}$$

The final equation is obtained by applying an integral transformation to $\mathrm{U}(\omega, \mathrm{x})$ function:

$$\mathrm{V}(\omega, \emptyset) = \int_{-\infty}^{+\infty} e^{i\emptyset x} \frac{\mathrm{U}(\omega, \mathrm{x})}{|\mathrm{U}(\omega, \mathrm{x})|} \mathrm{d}x \tag{53}$$

3.6 Common issues in active surface wave methods

3.6.1 Near-field effects

Near-field effects are the most commonly encountered issue in MASW data processing, significantly reducing the maximum resolvable depth, resolution, and reliability of the derived dispersion data. Near-field effects are mainly caused due to two assumptions: (1) plane wavefield surface waves and (2) pure surface waves in the wavefield with no interference from body waves. The region where these assumptions is invalid are called the near-field. The near-field effect of modeling a cylindrical wavefield with a plane wavefield is called the model incompatibility effect. The model incompatibility effect can lead to a clear roll-off (Figure 3.1a) in the phase velocity at low frequencies, whereas the interference of the body waves can generate some oscillations in the phase velocity at low frequencies (Figure 3.1b). These near-field effects are corrupting the low-frequency portion of the dispersion data so that they cannot be reliably used for the inversion process.

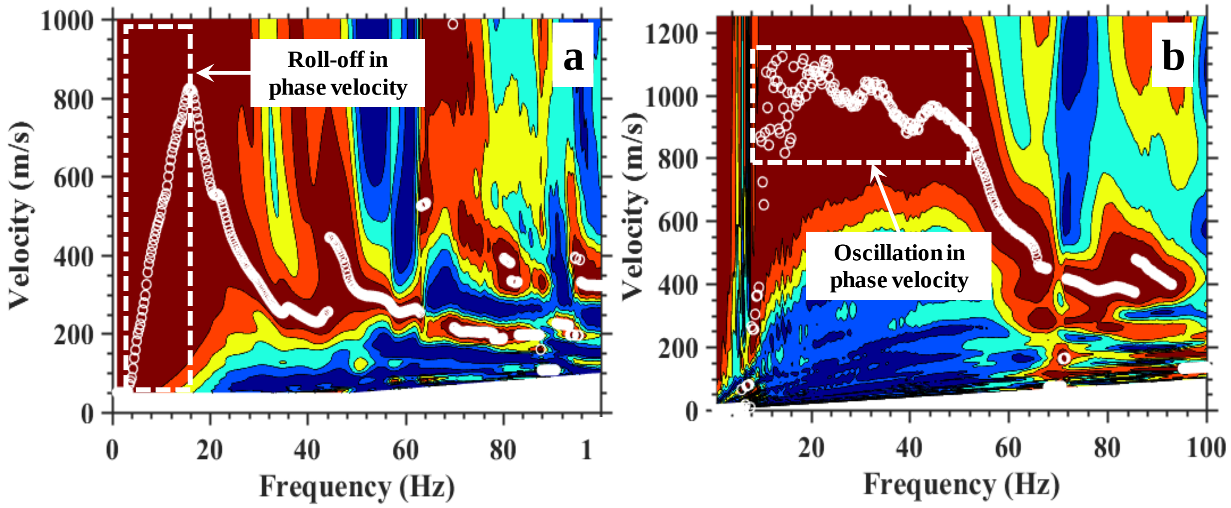

Figure 3.1- Example of near-field effects. a) clear roll-off in phase velocity in the low-frequencies portion of the dispersion curve due to model incompatibility, b) apparent oscillations in phase velocity in the low-frequencies portion of the dispersion curve due to body waves interference.

A limited number of studies have investigated near-field effects and suggested some methods to mitigate such effects. These methods include modifying the transformation technique to account for the cylindrical wavefield (Zywicki *et al.*, 2005), increasing the distance between the source and receivers (Xu *et al.*, 2006; Yoon *et al.*, 2009; Tremblay *et al.*, 2019), using multiple source-offsets (Wood *et al.*, 2012), and increasing the number of receivers (Yoon *et al.*, 2009). One of the primary investigations regarding near-field effects was conducted by Yoon and Rix (2009), in which they defined two normalized parameters, including a normalized phase velocity defined as the ratio of the experimental phase velocity to the true phase velocity and a normalized array center distance given by:

$$\frac{\bar{x}}{\lambda}=\frac{\left({}^{1}\!/_{M}\right)\sum_{m=1}^{M} x_m}{\lambda} \tag{54}$$

Where $\bar{x}$ is the mean distance of all receivers relative to the source, λ is the wavelength, and M is the number of receivers. To date, the majority of the previous investigations have focused on the geometry of the MASW test to investigate the near-field effects, and no attempt has been made to assess the influence of different transformation methods on near-field effects. Therefore, this topic is investigated in this study by comparing the performance of different transformation techniques for sites with apparent near-field effects.

3.6.2 Mode misidentification or mode-kissing

In the MASW method, it is possible to observe multiple modes of propagation at a single temporal frequency for sites with a heterogeneous soil profile. Identifying different modes of propagation is important in the MASW method because it can prevent mode misidentification, and it can enhance the accuracy of the inversion results by including multiple modes in the inversion process. However, the presence of different modes of propagation in the experimental dispersion data makes the mode identification complex, and sometimes it can lead to mode misidentification (Zhang *et al.*, 2003; Foti *et al.*, 2014; Gao *et al.*, 2014, 2016). This means that the dispersion data points related to the effective or higher modes may be mistaken as the fundamental mode for sites with a poor-resolution dispersion image. Therefore, for sites where different modes of propagation are expected, the experimental dispersion curve's resolution is critical to avoid mode misidentification. One of the parameters that may affect the resolution of the experimental dispersion curve is the transformation method used for data processing. This topic has not received adequate attention in the literature. Therefore, one of the present study goals is to examine the capability of different transformation methods for multi-mode detection.

3.7 Field measurements and study areas

To investigate the performance of the four transformation methods for developing the experimental dispersion curve, more than 500 MASW tests were collected at eight different sites located in the USA. The sites were carefully selected in such a way to cover a wide range of subsurface layering, wavefield, and noise conditions.

Summarized in Table 3 are the key characteristics of each site, including the site location, sharp impedance contrast or bedrock depth (shallow or deep), whether or not a velocity reversal is present, noise conditions (ranked high to low), geophone coupling (spike or landstreamer), surface wave type (Raleigh or Love), number of geophones, geophone spacing, and number of setups. It should be mentioned that for all sites in the present study, the sharpest impedance contrast in the subsurface, which significantly alters the shape of the experimental dispersion curve if it’s within the resolvable depth of the MASW measurements, is located at the soil/bedrock interface. Therefore, depth to the sharpest impedance contrast is called hereafter bedrock depth. The bedrock layer located within the top 15 m is classified as very shallow, bedrock depth ranging between 15-35 m is classified as shallow, and the bedrock layer located at depths greater than 100 m is classified as deep.

For each site, both Rayleigh and Love type surface waves were first used for several array setups to determine the wave type that resulted in a higher resolution experimental dispersion curve. Therefore, the results presented in this study include both Rayleigh and Love type surface waves. Testing was performed using 24 vertical or horizontal geophones, spaced 1 or 2 meters apart. For sites where a significant number of MASW tests were performed, a landstreamer system was used to increase the rate of field measurements. However, spikes generally result in better coupling to the ground surface.

Based on a review of the geology at each site and the shape of the experimental dispersion curves, the majority of the sites in this study are normally dispersive, meaning that V_s increases with depth. However, irregular dispersion curves were observed at some locations along the Melvin-Price site, indicating the presence of a velocity reversal layer (i.e., a low-velocity layer underneath a stiffer layer) in the near-surface. More information regarding the site locations, subsurface layering, and field measurements of each site are provided in Rahimi et al. (2018), Wood and Himel (2019), and Rahimi et al. (2020).

Sites with high noise levels were located near busy highways or in highly urbanized environments, sites with medium noise levels were located near roads with medium traffic volume, and sites with low noise levels were located far away from highways and urbanized areas. In this regard, representative signal-to-noise ratio (SNR) curves in decibels (dB) for sites with high (Ozark), medium (Melvin-Price), and low noise (Hardy) levels are shown in Figure 3.2. From this figure, the SNRs are considerably different for all ranges of frequencies (1-100 Hz). However, this becomes more important for the low-frequency range, where the SNR is typically low and can corrupt the experimental dispersion data points. For this study, a value of 10 dB (Wood *et al.*, 2012) is considered as the threshold SNR, below which the experimental dispersion data points become unreliable due to the substantial contribution of the background noise. Accordingly, the frequency associated with the threshold SNR is considered as the threshold frequency. As observed in Figure 3.2, while the threshold frequency is very low (approximately 1 Hz) for sites with a low noise level, this value abruptly increases for sites with a high noise level (~ 16 Hz). It should be noted that this threshold does not necessarily mean reliable data will be retrieved to those frequencies, just that the SNR is high at those frequencies.

Table 3- Key characteristics of the study areas and field measurements.

Project name	**Location**	**Bedrock depth**	**Velocity reversal**	**Noise level**	**Coupling method**	**Type of surface waves**	**Geophone number**	**Geophone spacing (m)**	**Number of setups**
Ozark	Arkansas	Very shallow to shallow (5-17 m)	No	High	Spike	Rayleigh	24	1 and 2	76
Hot Springs	Arkansas	Very shallow (1-7 m)	No	Low	Landstreamer	Love	24	1	140
Sand Gap	Arkansas	Very shallow (4-10 m)	No	Medium	Spike	Rayleigh and Love	24	1 and 2	22
Hardy	Arkansas	Very shallow (2-15 m)	No	Low	Landstreamer	Rayleigh and Love	24	1	58
Melvin-Price	Illinois	Shallow (25-35 m)	Yes	Medium	Landstreamer	Rayleigh	24	2	202
PVMO	Missouri	Deep (~591 m)	No	Low	Spike	Rayleigh and Love	24	2	2
CUSSO	Kentucky	Deep (~585 m)	No	Low	Spike	Rayleigh and Love	24	2	2
PEBM	Missouri	Deep (~764 m)	No	Low	Spike	Rayleigh and Love	24	2	2

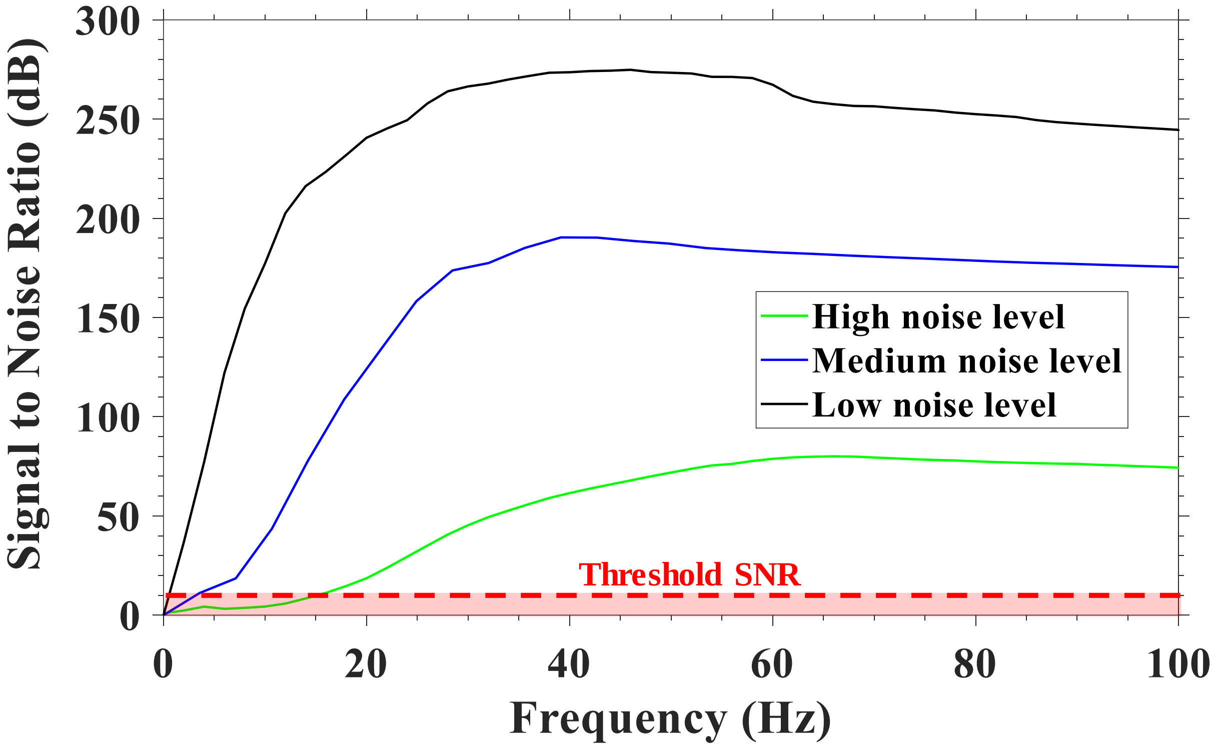

Figure 3.2- Representative signal to noise ratio (SNR) for sites with low, medium, and high noise levels.

3.8 Results and discussions

All MASW data collected from different sites were used to develop the experimental dispersion curves using the four transformation methods. Due to the large number of the experimental dispersion curves processed for this study, only a few examples of each type of behavior are presented here to highlight the influence of the transformation method on the derived dispersion data. Furthermore, for each of the topics discussed in detail in this section, an additional experimental result is provided in the supplementary materials to support the discussions. Moreover, for each topic, an example experimental dispersion result from Rayleigh- and Love-type waves (either in the paper or electronic supplement) is provided to investigate whether the same performance is observed for each transformation method for both Rayleigh and Love surface waves. However, for some sites (e.g. Melvin-Price), only Rayleigh- or Love-type surface waves were used. Therefore, only one type of surface wave is included in the discussions for these sites (see Table 3).

For the FDBF transformation, the experimental dispersion curve can be developed assuming either a plane or cylindrical wavefield (see Section 3.5.3). In this study, only the cylindrical FDBF (FDBF-cylindrical) is used for the comparisons since the experimental dispersion curve generated using the FDBF-plane was found to be nearly identical to the FK for the sites considered in this study.

To better illustrate this point, example experimental dispersion curves generated using the FDBF-cylindrical and FDBF-plane, and FK methods are provided in Figure 3.3 for an MASW setup at the Hardy site. In Figure 3.3a, while the dispersion curves of the FDBF-plane and FK methods are nearly identical (see Figure 3.3a), differences are observed in the dispersion curves generated using the FDBF-cylindrical and FDBF-plane (see Figure 3.3b). As shown in Figure 3.3b, the phase velocity estimated using the FDBF-cylindrical is slightly higher (<8 %) than the FDBF-plane at high frequencies, as shown in the zoomed-in view. However, the differences between the two methods are significant at low frequencies (<20 Hz), where near-field effects are noticeable. More discussions in this regard are provided later in the paper. Therefore, given these differences, the FDBF-cylindrical is utilized to compare the performance of the four transformation methods for developing the experimental dispersion curve.

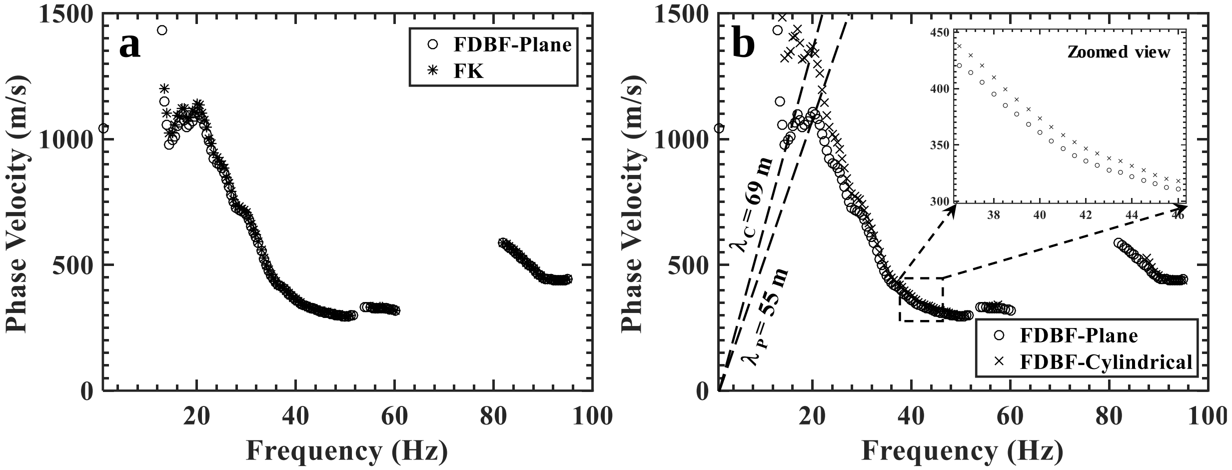

Figure 3.3- Comparison between the cylindrical and plane FDBF and FK methods.

3.8.1 Sites with different subsurface conditions

This section compares the four transformation methods for varying site conditions, including 1) sites with deep bedrock, uniform soil, and low noise conditions, 2) sites with very shallow and highly variable bedrock, and high and low noise levels (using traditional spikes and a landstreamer), and 3) sites with a velocity reversal layer.

3.8.1.1 Sites with a deep bedrock, uniform soil conditions, and low noise levels

Provided in Figure 3.4 are the experimental Rayleigh wave dispersion curves generated using the four transformation methods for the PVMO site, which has a deep bedrock depth (~591 m) and low noise levels. The same input parameters (e.g. frequency interval) were used to generate each transformation method's dispersion image. Additionally, to avoid spatial aliasing, the data related to wavelengths less than the minimum resolvable wavelength are removed from the dispersion images. In Figure 3.4, the dispersion curve can be divided into two main portions, a flat portion for frequencies ranging between 50-9 Hz, and a curved portion with a nearly continuous increase in phase velocity for frequencies lower than 9 Hz. The frequency at the start of the curved portion, which separates these two portions (9 Hz for this example), is termed the point of curvature herein and is important for assessing the performance of the transformations.

As shown in Figure 3.4, the four transformation methods have produced almost identical dispersion curves for the frequency range of interest (5-50 Hz). This is clearer in Figure 3.5, where the spectral peak dispersion curves from the four transformation methods are plotted in one figure using different markers.

In Figure 3.5, it is apparent that the results from the four dispersion curves are identical for the wavelengths ranging between 4-75 m. Similar behavior was observed in terms of the dispersion curve resolution for the other MASW tests at this site and the other sites with low noise levels and, more importantly, with a similarly deep bedrock layer and a low-frequency point of curvature (<10 Hz) (CUSSO and PEBM sites in Table 3). In this regard, another example dispersion image from the PEBM site is provided in Supplement A. To investigate this topic for both Rayleigh and Love waves, the example provided in Supplement A is for Love waves, whereas the one in the paper is for Rayleigh waves. These indicate that for sites with a deep bedrock layer with a low-frequency point of curvature, relatively uniform soil conditions, and low noise levels, the performance of the four transformation methods is almost identical for both Rayleigh and Love waves.

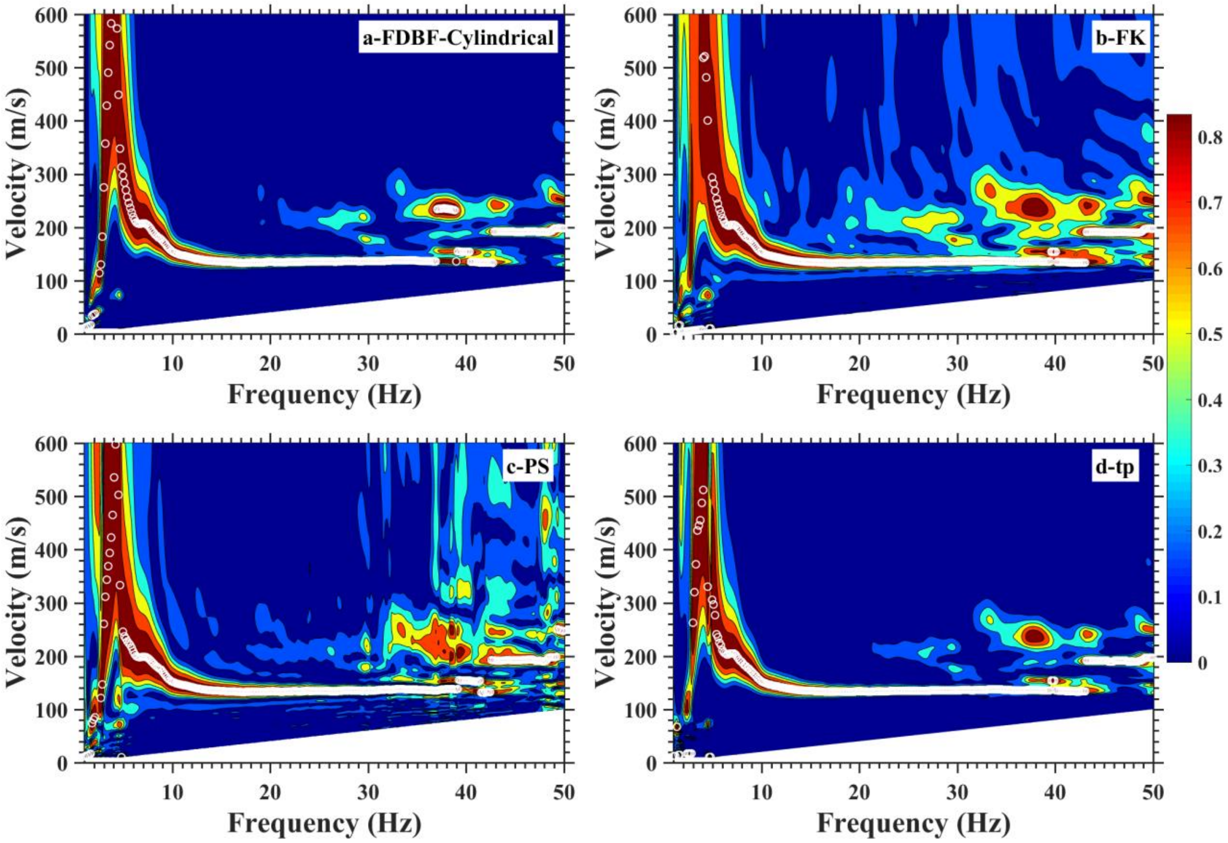

Figure 3.4- Rayleigh wave dispersion curves generated using the four transformation methods for the PVMO site with a deep bedrock layer, a low-frequency point of curvature, and low noise levels. a) FDBF-cylindrical, b) FK, c) PS, and d) τp.

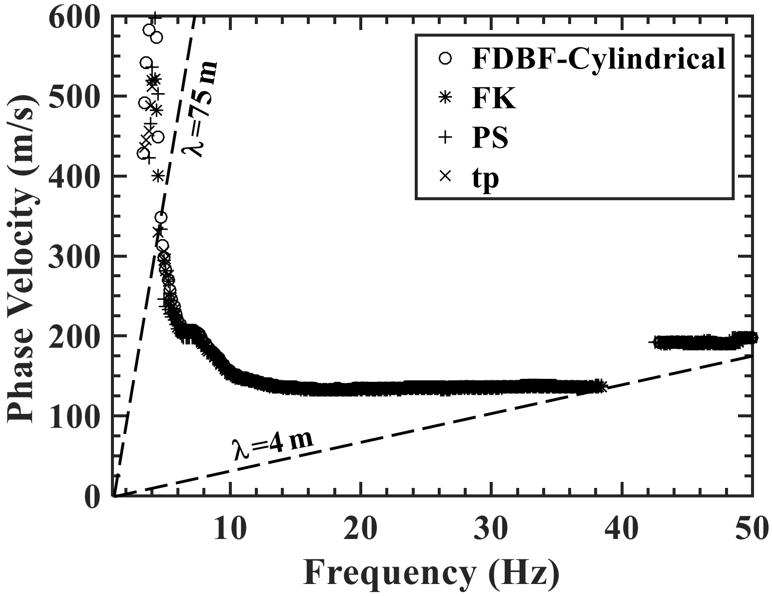

Figure 3.5- Comparison of the four transformation methods for Rayleigh waves for the PVMO site.

3.8.1.2 Sites with a very shallow and highly variable bedrock

To evaluate the performance of each transformation method for sites with a very shallow and highly variable bedrock layer for both Rayleigh and Love waves, examples from both Rayleigh (Ozark site) and Love (Hot Springs site) waves are provided in this section.

3.8.1.2.1 Site with high noise levels using spikes

Presented in Figure 3.6 are the experimental Rayleigh wave dispersion curves generated using the four transformation methods for the Ozark site with a very shallow and complex (highly variable) bedrock topography and high noise levels. For this site, geophones were coupled to the ground via spikes. From this figure, a high-frequency point of curvature (~ 40 Hz) is observed for this site. As shown in Figure 3.6, the FDBF-cylindrical, FK, and τp methods generated a high resolution and almost identical dispersion image (Figure 3.6a, b, and d). However, the PS method generated a very poor-resolution dispersion image (see Figure 3.6c) with no clear trend for the fundamental mode of propagation.

A better illustration of the PS resolution issue is provided in Figure 3.7, in which the spectral peak dispersion data points from the FDBF-cylindrical, FK, and τp methods are shown in Figure 3.7a, and the spectral peak dispersion data points of the PS method are shown in Figure 3.7b. As observed in Figure 3.7a, the dispersion data points of the FDBF-cylindrical, FK, and τp methods are clear and relatively consistent for wavelengths ranging between 2.1-29.7 m. However, the PS method results in very poor resolution dispersion data (see Figure 3.7b) in such a way that only a small portion of the dispersion curve (wavelengths ranging between 8.9-16.7 m) is clear. This type of behavior is observed for most of the dispersion curves generated using the PS method for sites with very shallow and highly variable bedrock layers (e.g. Ozark, Hot Springs, and Hardy) and a high-frequency point of curvature (> 20 Hz). To provide further evidence in this regard, another example of MASW results from the Ozark site with the same issue for the PS method is provided in Supplement B. The example in Supplement B is from a different MASW setup and location at the Ozark site. It should be noted that the poor performance of the PS method was verified by processing the same MASW setups with PS issues using the MASWaves software package (Olafsdottir *et al.*, 2018).

To better understand the poor performance of the PS method, the normalized spectrum for frequencies of 46 and 47 Hz are shown in Figure 3.8 for each transformation method. As observed in Figure 3.8a, b, and d, the normalized spectrum plots of the FDBF-cylindrical, FK, and τp methods have a clear and dominant peak, indicating most of the energy concentrates at this peak. However, the normalized spectrum plot for the PS method (see Figure 3.8c) has several ripples, causing a significant difference in the phase velocities associated with the peak frequencies (i.e. 723 m/s at the frequency of 46 Hz and 342 m/s at the frequency of 47 Hz) due to the spread between the various ripples.

Another important point regarding the differences between various transformation methods is that the phase velocity estimated using the FDBF-cylindrical is slightly higher than the other methods for all ranges of frequencies, as shown in the zoomed view dispersion curve in Figure 3.7a (also see Figure 3.4b). This behavior is observed in all the dispersion images of the current study. These differences are caused due to the model incompatibility effects in the FK, PS, and τp methods, in which the cylindrical spreading wavefield is modeled using a plane wavefield. This results in biased phase velocity estimates for the surface waves using these three transformation methods. The higher phase velocity estimates in the FDBF-cylindrical is also confirmed by Zywicki and Rix (2005). This indicates that the FDBF-cylindrical may provide more correct estimates of the phase velocity of surface waves compared to the other transformation methods by using a cylindrical model.

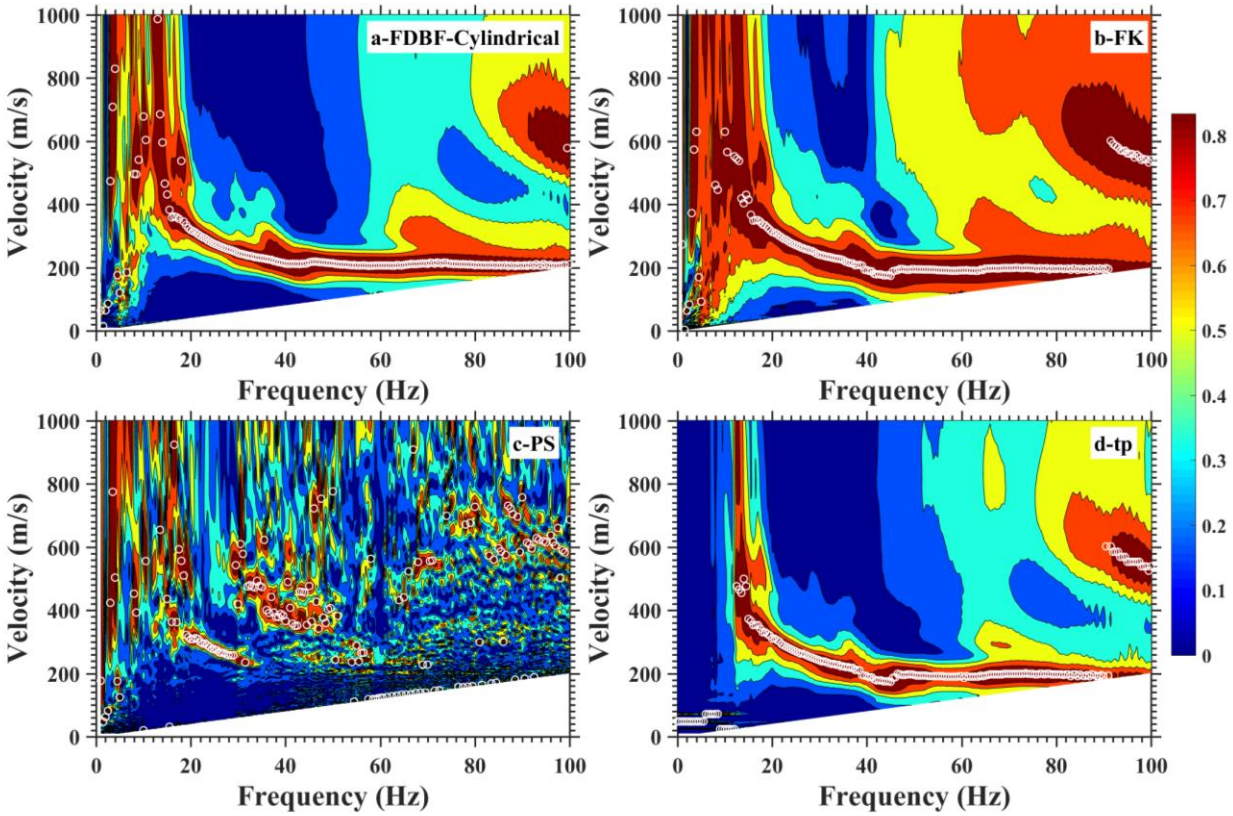

Figure 3.6- Rayleigh wave dispersion curves generated using the four transformation methods for the Ozark site with a very shallow and complex bedrock topography, a high-frequency point of curvature, and high noise levels. a) FDBF-cylindrical, b) FK, c) PS, and d) τp.

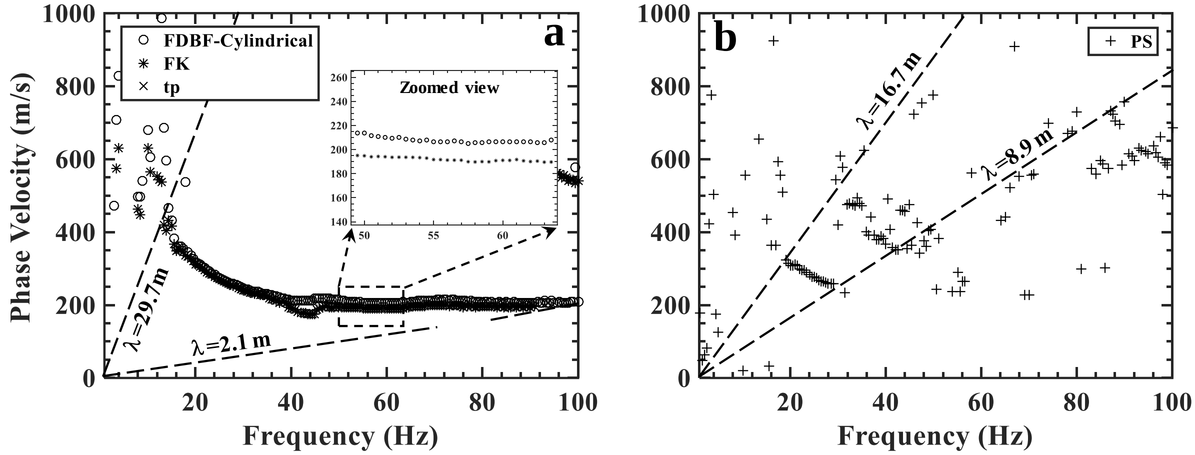

Figure 3.7- Comparison of the four transformation methods for Rayleigh wave for the Ozark site, a) FDBF-cylindrical, FK, and τp, b) PS.

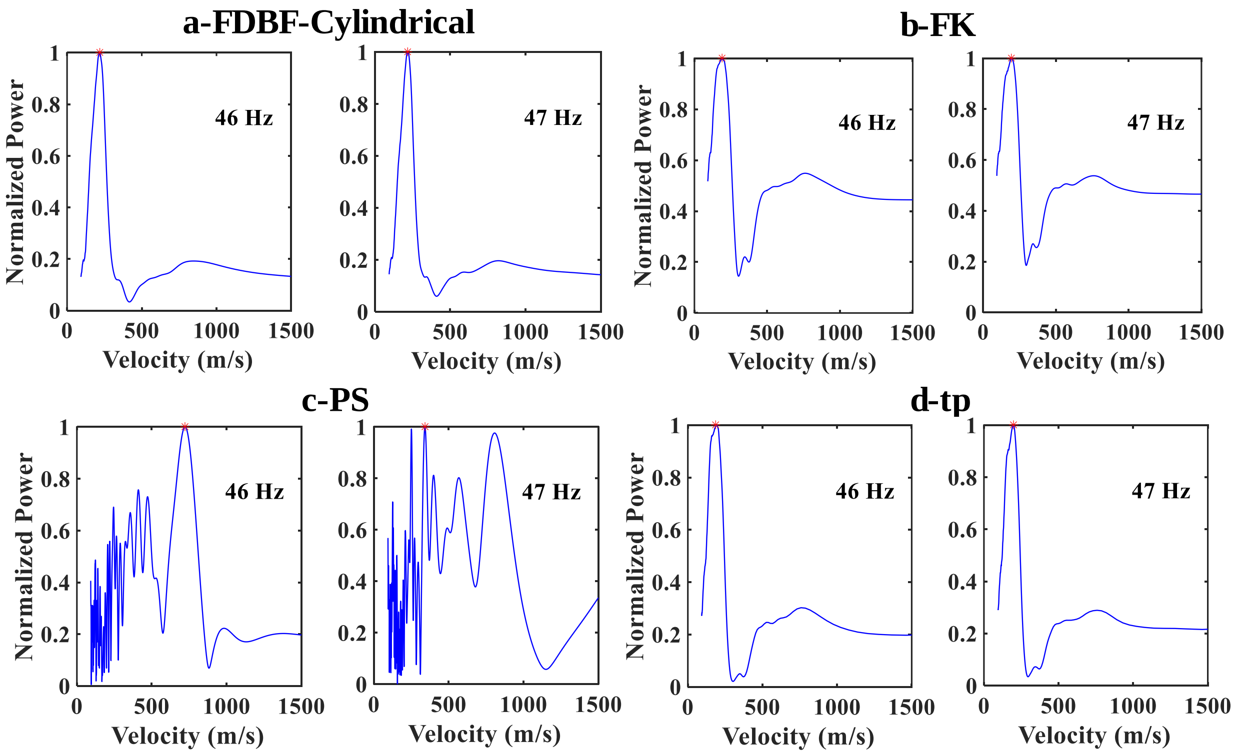

Figure 3.8- Comparison of the normalized spectrum plots for the four transformation methods at 46 and 47 Hz frequencies for the Ozark site. a) FDBF-cylindrical, b) FK, c) τp, and d) PS.

3.8.1.2.2 Site with low noise levels using a landstreamer

Shown in Figure 3.9 are Love wave dispersion curves generated using the four transformation methods for the Hot Springs site with very shallow and complex bedrock topography and low noise levels. To increase the rate of field measurements for this site, MASW testing was conducted using a landstreamer system, which typically reduces the dispersion data quality because of poorer geophone coupling to the ground surface compared to traditional spikes. Like the Ozark site, a high-frequency point of curvature (~ 45 Hz) is observed for this site, as shown in Figure 3.9. Additionally, in Figure 3.9, it is clear that the FDBF-cylindrical, FK, and τp methods yield an identical dispersion image dominated by the fundamental mode of propagation. However, the PS method leads to a poor-resolution dispersion image dominated by higher modes, as observed in Figure 3.9c. The resolution issue with the PS method is more apparent in Figure 3.10, which represents the dispersion data points measured at three different source offsets of 5, 10, and 15 m. For the FDBF-cylindrical, FK, and τp methods in Figure 3.10, the dispersion data points from source offsets at 5 and 10 m are dominated by the fundamental mode of propagation, and only the data points from the 15-m source offset is dominated by higher modes at frequencies greater than 50 Hz. Additionally, these methods result in a similar dispersion curve for wavelengths ranging between 2-24.6 m with some variations at the low-frequency portion of the dispersion curve due to near-field effects.

On the other hand, for the PS method in Figure 3.10c, the dispersion data points from all three source offsets are dominated by higher modes for a wide range of frequencies (from 41 to 95 Hz), and the fundamental mode dominates only a small portion of the dispersion curve. This leads to a very low-resolution experimental dispersion curve from the PS method. While only two example experimental dispersion images are provided here (see Figure 3.6 and Figure 3.9), the resolution issue of the PS method is also observed for most of the sites with a very shallow and highly variable bedrock layer and a high-frequency point of curvature (>20 Hz). Another example experimental dispersion curve showing the PS issue is provided in Supplement C. The example in Supplement C is from a different MASW setup and location at the Hot Springs site.

Overall, the PS method is one of the most popular transformation methods for MASW data processing and is the method initially used for MASW data processing. However, in this study, it has been shown that the PS method has some severe resolution issues for both Rayleigh (Figure 3.6 and Supplement B) and Love (Figure 3.9 and Supplement C) surface waves for sites with very shallow and highly variable bedrock and a high-frequency point of curvature (>20 Hz), regardless of the geophone coupling conditions (good coupling using spikes or poor coupling using landstreamer) and site noise levels. This contrasts with previous studies that have claimed that the PS method provides the best resolution experimental dispersion curve (Dal Moro *et al.*, 2003) compared to the FK and τp methods. It is worth mentioning that the primary difference between this study and previous studies (Dal Moro *et al.*, 2003; Tran *et al.*, 2008) is that the previous studies did not include various subsurface layering, wavefield, and noise conditions. Therefore, their results are site-specific and cannot be applied by other researchers for sites with different conditions.

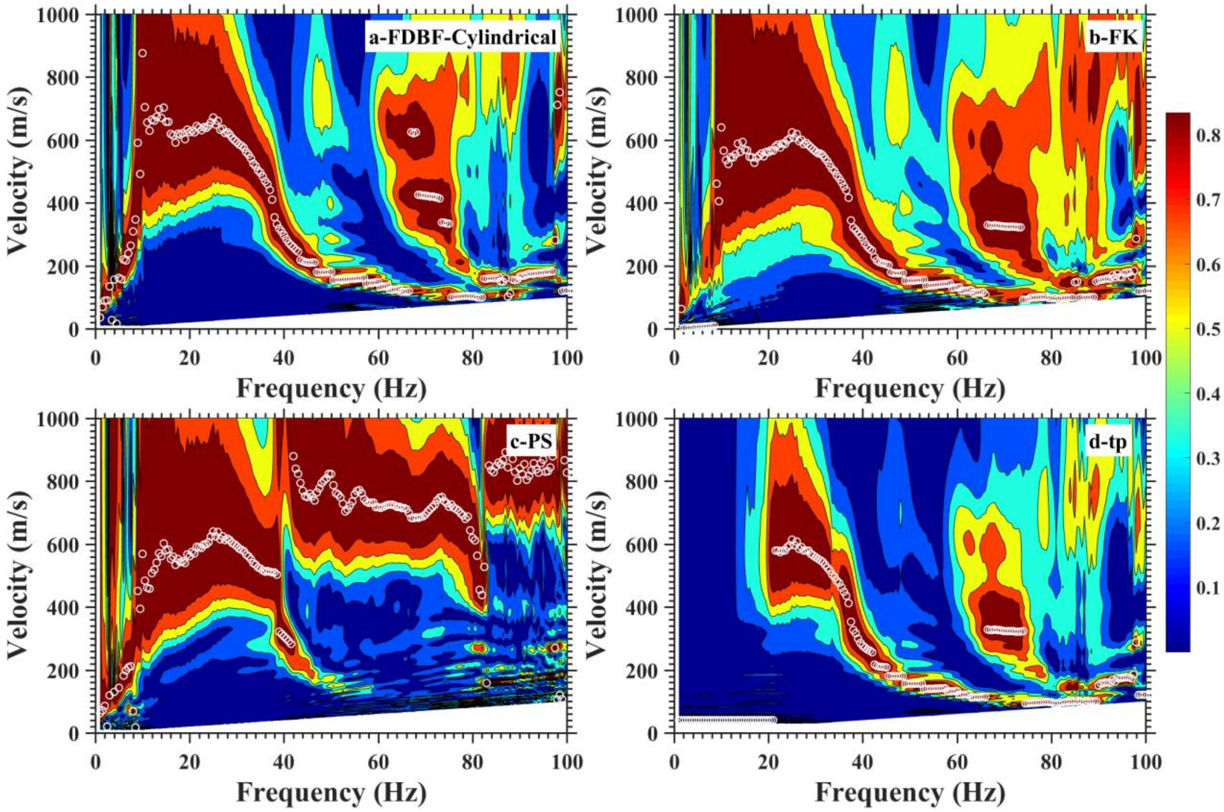

Figure 3.9- Love wave dispersion curves generated using the four transformation methods for the Hot Springs site with a very shallow and complex bedrock topography, high-frequency point of curvature, and low noise levels. a) FDBF-cylindrical, b) FK, c) PS, and d) τp.

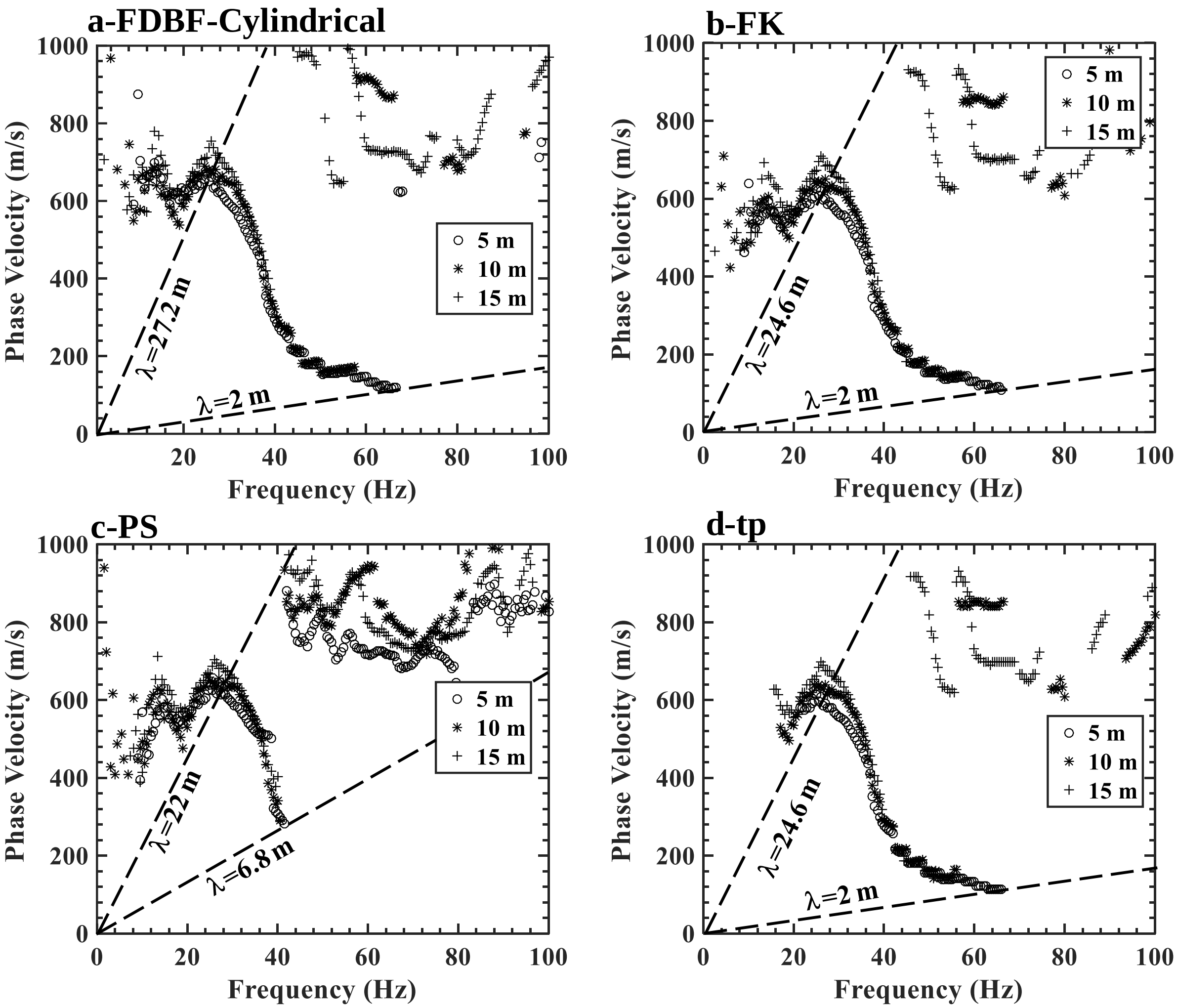

Figure 3.10- Love wave dispersion data points generated from different source offsets using the four transformation methods for the Hot Springs site. a) FDBF-cylindrical, b) FK, c) PS, and d) τp.

3.8.1.3 Site with velocity reversal

Presented in Figure 3.11 are the Rayleigh wave dispersion curves generated using the four transformation methods for one of the MASW setups at the Melvin-Price site that includes a velocity reversal layer (i.e. reversal in velocity at depth or irregularly dispersive dispersion curve) and medium noise levels. The velocity reversal presence is evident from the dispersion images (e.g. Figure 3.11a) since the phase velocity decreases with frequency at frequencies ranging between 7-30 Hz. Additionally, the existence of the velocity reversal is also confirmed by geologic information available for the site (Rahimi *et al.*, 2018).

In Figure 3.11, the dispersion data associated with the fundamental mode of propagation is clear for the FDBF-cylindrical, FK, and to some extent, for the PS methods over a broad range of frequencies (3-90 Hz). However, the τp method (see Figure 3.11d) fails to provide any clear dispersion data at frequencies less than 17 Hz, which is related to the layers below the velocity reversal. This portion of the dispersion curve is important since it has information regarding the deeper layers, including the inverse layer, stiff soils, and bedrock layers. This issue is further highlighted in Figure 3.12, in which the dispersion curves are presented on a semi-log scale.

In Figure 3.12a, it is apparent that similar dispersion curves are generated using the FDBF-cylindrical, FK, and PS methods for wavelengths ranging between 2-72 m. However, for the τp method in Figure 3.12b, the low-frequency portion of the dispersion image is missing, and so the maximum resolvable wavelength is approximately 14 m, which is significantly lower than the other transformation methods (72 m). This issue with the τp method is observed for all the MASW setups that include a velocity reversal. In this regard, another example of this issue with the τp method is provided in Supplement D from a different MASW setup and location at the Melvin-Price site. It is also worth mentioning that the resolution of the PS method is lower than the FDBF-cylindrical and FK methods.

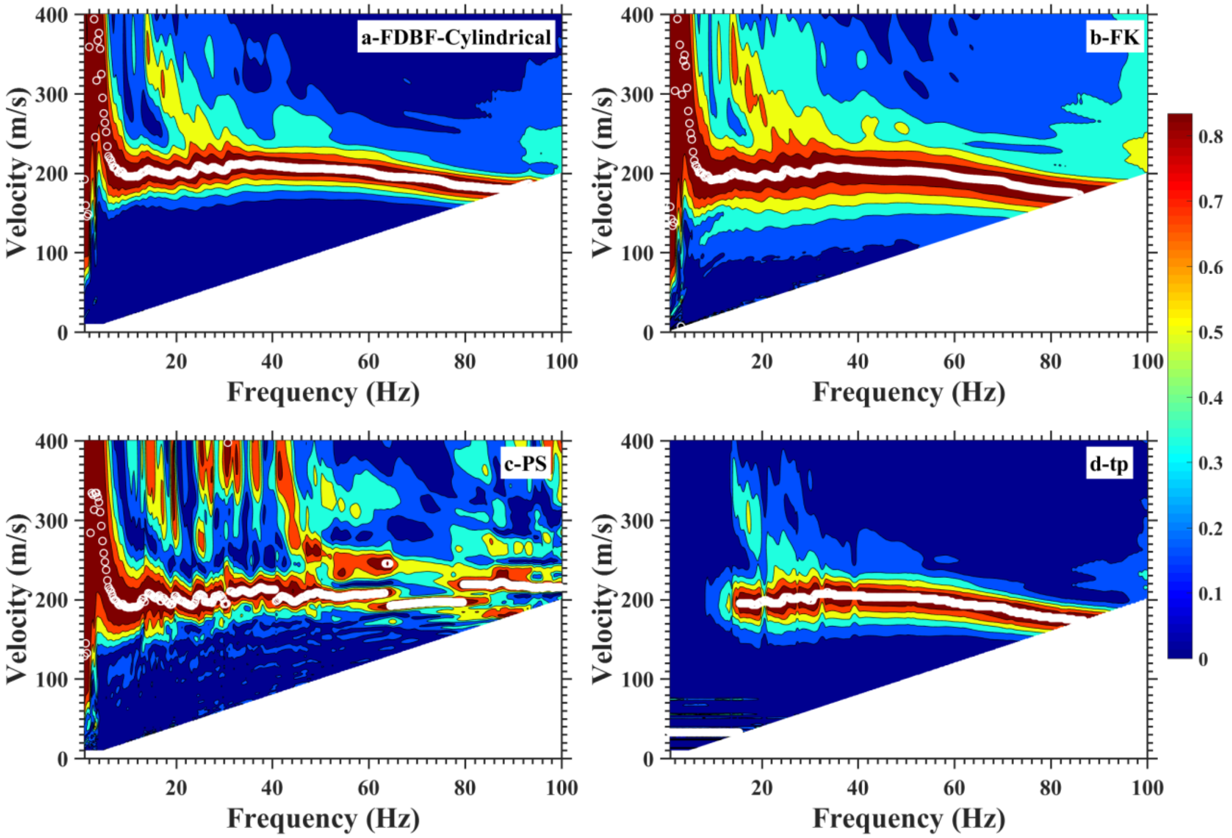

Figure 3.11- Rayleigh wave dispersion curves generated using the four transformation methods for the Melvin-Price site with a velocity reversal layer and moderate noise levels. a) FDBF-cylindrical, b) FK, c) PS, and d) τp.

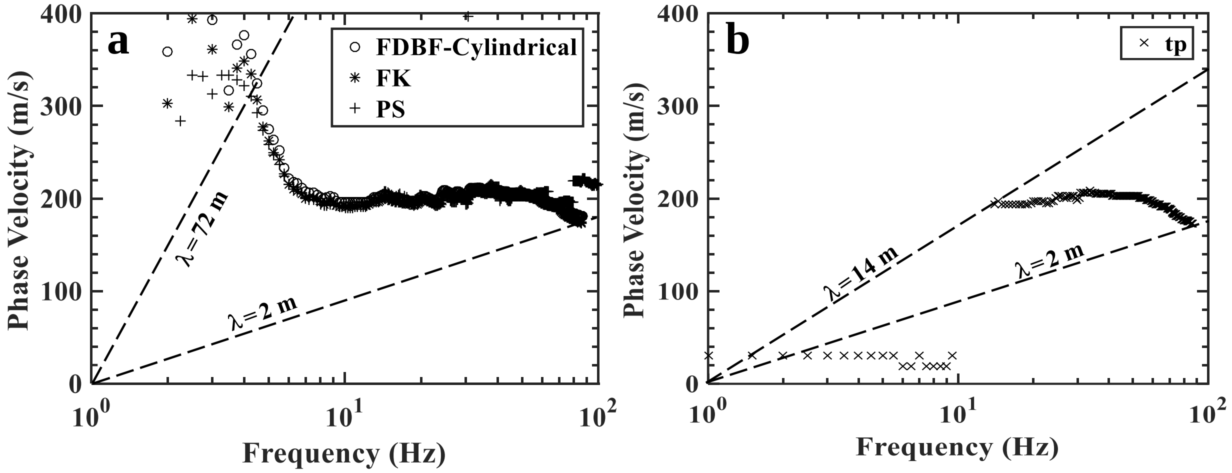

Figure 3.12- Comparison of the four transformation methods for Rayleigh wave for the Melvin-Price site for a location with a velocity reversal layer (irregular dispersive dispersion curve). a) FDBF-cylindrical, FK, and PS, b) τp.

To ensure this is not a common issue for all dispersion curves when using the τp method at the Melvin-Price site, dispersion curves are generated using the four transformation method for another location at the Melvin-Price site where no velocity reversal layer is present, but similar subsurface layering exists otherwise. These results are shown in Figure 3.13. As observed in the figure, the dispersion curve from the τp method (Figure 3.13b) is similar to those of the FDBF-cylindrical, FK, and PS methods (Figure 3.13a) in terms of the shape and the minimum (2 m) and maximum (24 m) resolvable wavelengths for a normally dispersive subsurface layering. This confirms that the issue with the τp method in Figure 3.11 and Figure 3.12 is related to the presence of a velocity reversal in the near-surface, and it is not related to the other factors such as wavefield and noise conditions.

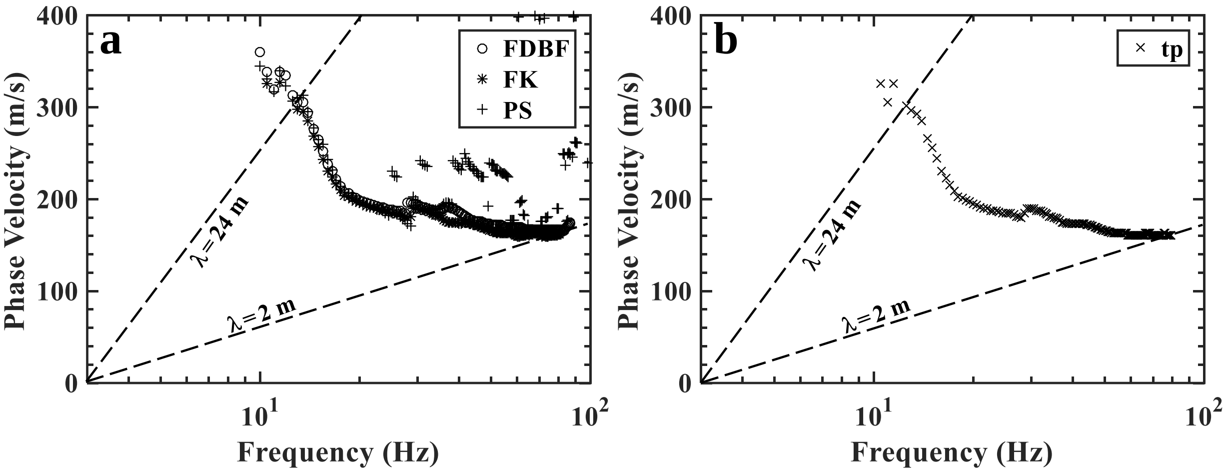

Figure 3.13- Comparison of the four transformation methods for Rayleigh wave for the Melvin-Price site at a location without a velocity reversal layer (normally dispersive dispersion curve). a) FDBF-cylindrical, FK, and PS, b) τp.

3.8.2 Near-field effects

Shown in Figure 3.14 are Love wave dispersion curves generated using the four transformation methods for the Hot Springs site with clear near-field effects. As shown in this figure, the near-field effects are caused by model incompatibility because of the clear roll-off in the phase velocity without any oscillations in the low-frequency portion of the dispersion curve. For the FK and τp methods in Figure 3.14b and 14d, respectively, it is apparent that the near-field effect corrupts a large portion of the low frequency (< 23 Hz) dispersion data. However, for the FDBF-cylindrical and PS methods in Figure 3.14a and 14c, respectively, a smaller portion of the dispersion curve is corrupted by the near-field effect. The FDBF-cylindrical provided the highest resolution (i.e. longest resolvable wavelength) experimental dispersion curve.

To better compare the performance of the four transformation methods in the presence of clear near-field effects, the experimental dispersion data points of the four transformation methods are plotted together in Figure 3.15. As shown in this figure, the majority of the dispersion data points are related to the fundamental mode of propagation except for frequencies ranging between 47-67 Hz, which are dominated by a higher mode. The capability of each transformation method to mitigate the near-field effect is visible in this figure. The differences between the four methods regarding the near-field effect are highlighted in the zoomed view in Figure 3.15. From this figure, the maximum resolved wavelength using the FK and τp methods is 19 m, whereas this value is 37 m for the PS method and 51 m for the FDBF-cylindrical method, illustrating significant differences between the transformation methods. This indicates that in the presence of model incompatibility effects, the performance of the FDBF-cylindrical is considerably better than the other transformation techniques because it mitigates the near-field effect by using a cylindrical wavefield model. Similar behavior is observed for all the MASW dispersion data with clear near-field effects.

To provide more evidence in this regard, another example of an experimental Rayleigh wave dispersion image with clear near-field effects is provided in Supplement E. It should be noted that the example in Supplement E is for Rayleigh waves, whereas the example in the paper in Figure 3.14 is for Love waves. While Rayleigh and Love waves are very different in terms of wave characteristics, wave propagation, and near-field effects, both examples illustrate the superior performance of the FDBF-cylindrical over the other methods when considering near-field effects.

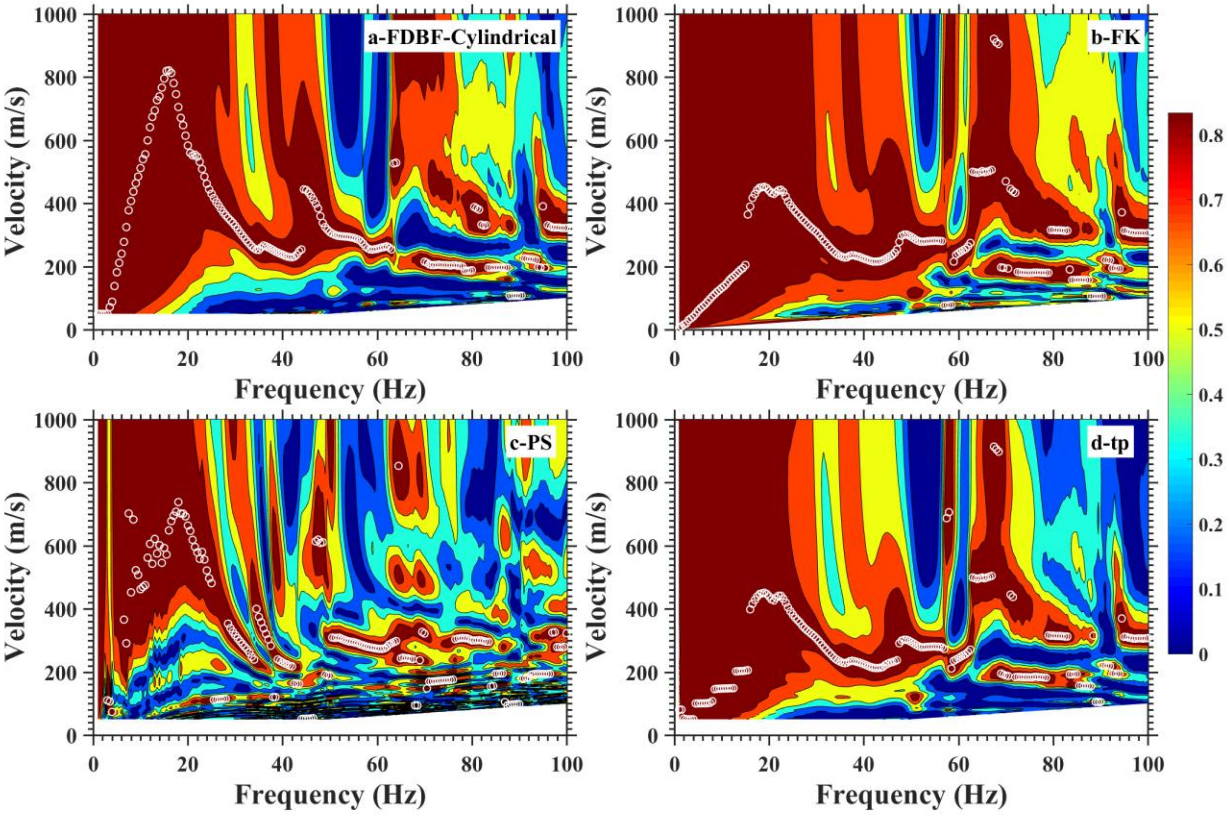

Figure 3.14- Love wave dispersion curves generated using the four transformation methods for the Hot Springs site with clear near-field effects and low noise levels. a) FDBF-cylindrical, b) FK, c) PS, and d) τp.

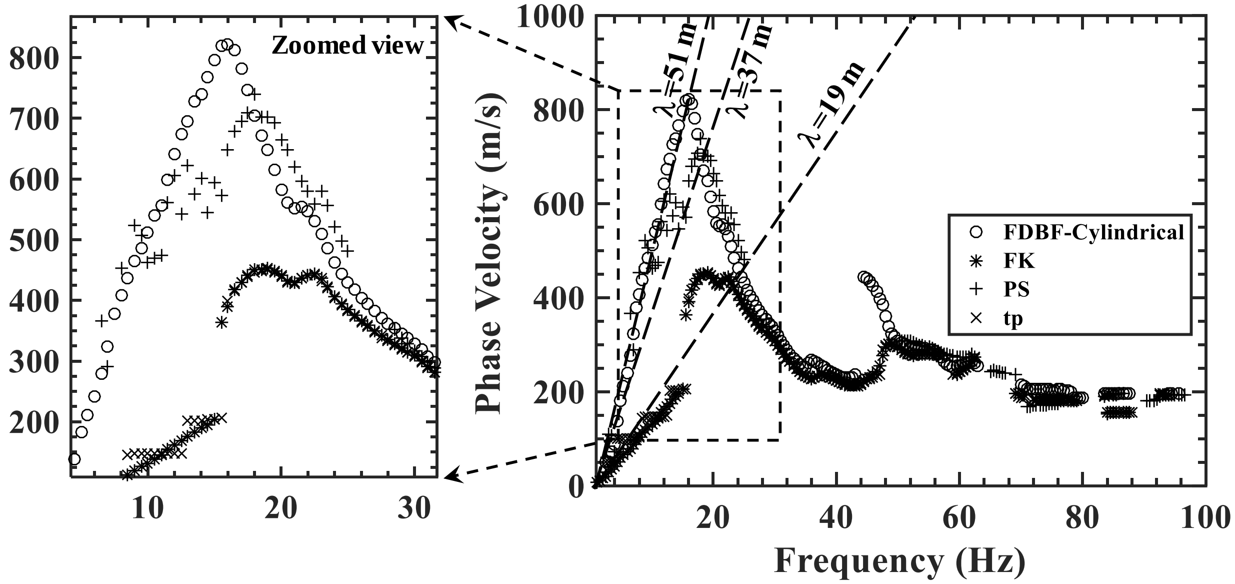

Figure 3.15- Comparison of the four transformation methods for Love wave for the Hot Springs site with clear near-field effects using Love type surface waves.

3.8.3 Multiple mode resolution

Shown in Figure 3.16 are the Rayleigh dispersion curves generated using the four transformation methods for the Ozark site. From this figure, it is apparent that the four transformation methods have different sensitivities to higher modes. While most of the dispersion data points from the FDBF-cylindrical are related to a higher mode (see Figure 3.16a), the other transformation methods are dominated by the fundamental mode.

The differences between the FDBF-cylindrical and the other transformation methods are clearer in Figure 3.17, in which the dispersion data points of the FDBF-cylindrical and the other methods (FK, PS, and τp) are shown in Figure 3.17a and 17b, respectively. As observed in Figure 3.17a, for the FDBF-cylindrical, all the dispersion data points with a frequency greater than 35 Hz are related to the first higher mode. However, for the FK, PS, and τp, only the dispersion data points for frequencies ranging between 40-66 Hz and 90-100 Hz are associated with the first higher mode. This behavior is observed for several other dispersion images with apparent higher modes. Another example in this regard from a different MASW setup and location at the Ozark site is provided in Supplement F. Therefore, for complex sites where higher modes are present, caution should be exercised when solely relying on the FDBF-cylindrical for developing the dispersion curve. It should be mentioned that the resolution of the τp method is not as high as the other methods, as shown in Figure 3.16, due to a shallow and highly variable bedrock layer and a high-frequency point of curvature for this site.

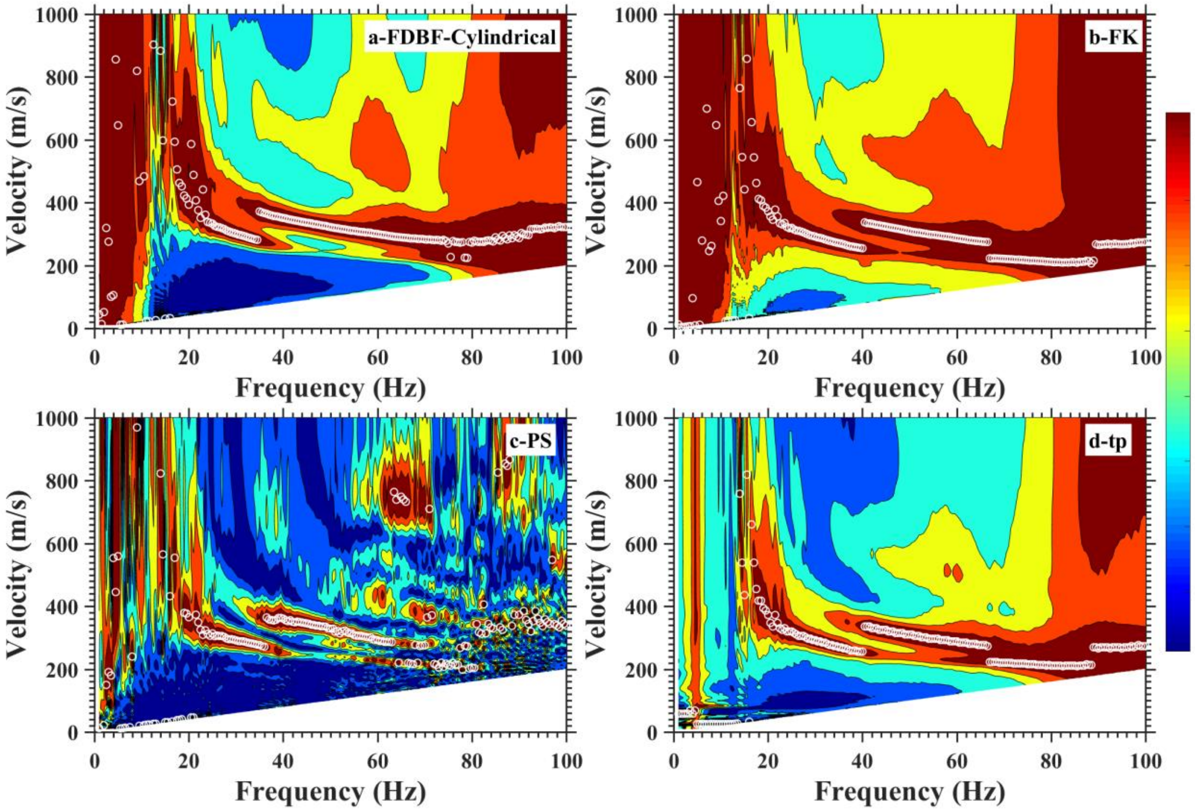

Figure 3.16- Rayleigh wave dispersion curves generated using the four transformation methods for the Ozark site with the FDBF-cylindrical method dominated with a higher mode. a) FDBF-cylindrical, b) FK, c) PS, and d) τp.

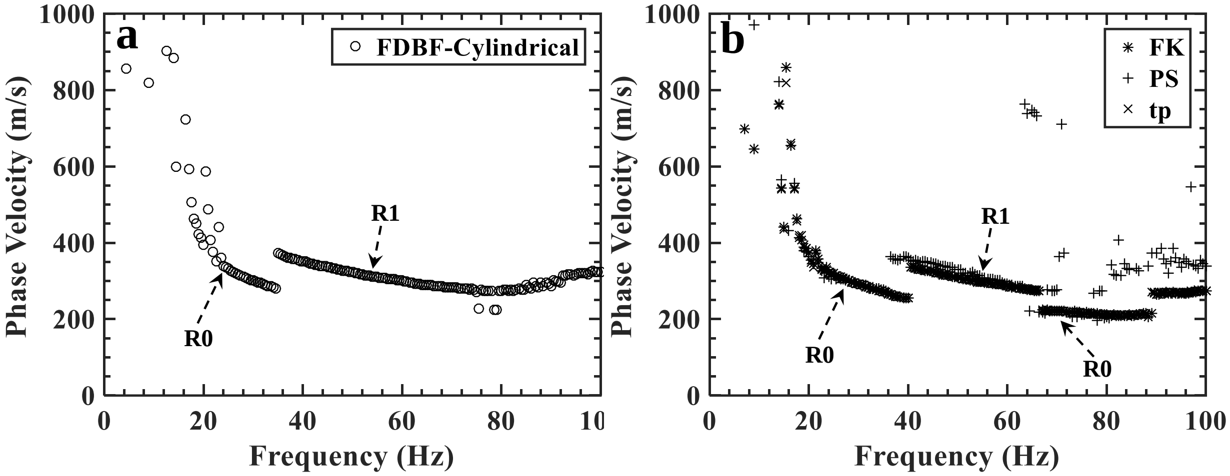

Figure 3.17- Rayleigh wave dispersion curves for the Ozark site. a) FDBF-cylindrical with clear first higher mode (R1) domination, b) FK, PS, and τp methods dominated with the fundamental mode (R0).

Overall, the FDBF-cylindrical has been more sensitive to higher modes than the other transformation methods. At first glance, this might seem like a drawback for the FDBF-cylindrical because it can sometimes lead to mode misidentification if this method is solely used for developing the dispersion curve. However, if the dispersion curves from different transformation techniques are used (see Figure 3.18), the FDBF-cylindrical would provide additional higher mode data, which can be used in the inversion process. This would increase the reliability of the inverted shear wave profile by including the higher modes in the inversion process. Therefore, for complex sites where higher modes are present, combining the dispersion results from different transformation methods is recommended. For instance, shown in Figure 3.18 is the combined dispersion curve of the four transformation methods for the MASW setup presented in Figure 3.17. The combined dispersion curve can be used as a means to (1) effectively define different modes of propagation, (2) allow the uncertainty to be estimated in the experimental dispersion curves developed using different transformation methods, (3) determine the potential near-field effects, if any are present, and (4) improve the reliability of the inversion results by performing a multi-modal inversion.

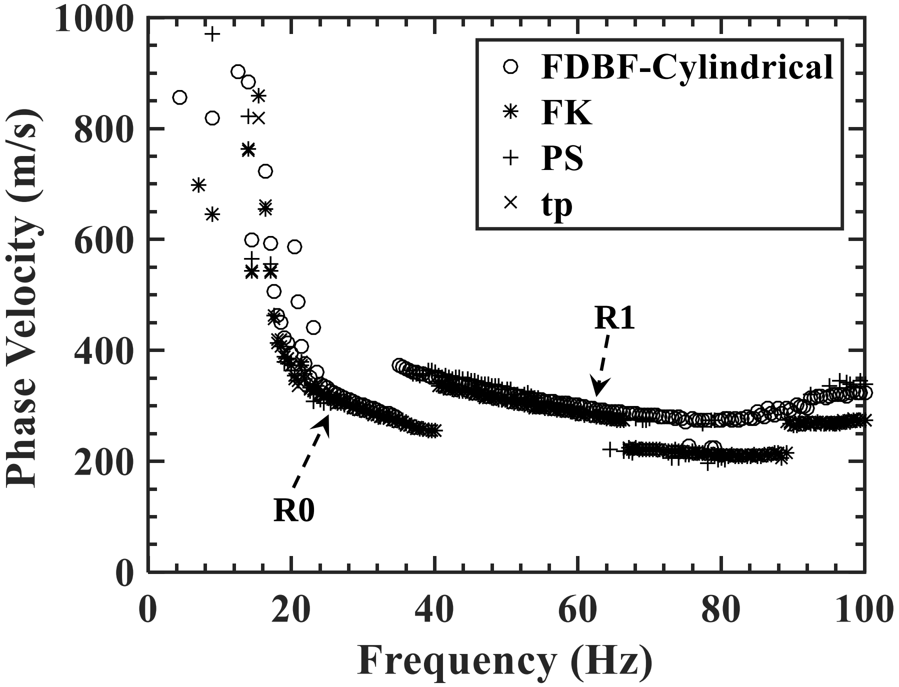

Figure 3.18- Combination of all transformation methods with clear fundamental and first higher Rayleigh mode dispersion curves.

3.9 Conclusion

This study examines the performance of the four transformation methods (FDBF-cylindrical, FK, PS, and τp), which are commonly used for MASW data processing to develop the experimental dispersion curve. In this regard, extensive MASW measurements were conducted at sites with different subsurface layering and noise conditions, including sites with deep and shallow bedrock, sites with a velocity reversal, sites in a noisy and quiet environment, sites with apparent near-field effects, and sites with clear higher modes. Based on the comparison of the performance of the four transformation methods for developing the experimental dispersion curves, the following conclusions are derived:

1- The performance of the four transformation methods is judged to be identical for both Rayleigh and Love waves for sites with a deep bedrock layer, a low-frequency point of curvature (<10 Hz), relatively uniform soil conditions, and low noise level (see Figure 3.4). Therefore, any of the four transformation methods can be used for these sites.

2- It is observed that for sites with a very shallow and complex (highly variable) bedrock topography and a high-frequency point of curvature (>20 Hz), regardless of the site noise level and geophone coupling conditions, the PS method resulted in a very poor-resolution dispersion image for both Rayleigh and Love waves in such a way that no clear dispersion curve could be extracted from the experimental results (see Figure 3.6, Figure 3.9, Supplement B, and Supplement C). However, the other transformation methods (FDBF-cylindrical, FK, and τp) generated a clear, high-resolution dispersion image for both Rayleigh and Love waves for the same sites. Therefore, it is recommended not to use the PS method for sites with very shallow and complex bedrock topography with a high-frequency point of curvature (>20 Hz). If the PS method is used for such a site, the experimental dispersion curve from the PS method should be compared to one of the other transformation methods to ensure the accuracy of the derived dispersion data.

3- For sites with a velocity reversal (i.e. stiff over soft soil layer), it is determined that the τp method fails to generate Rayleigh dispersion data points for the layers located below the velocity reversal layer. However, the other transformation methods developed an experimental Rayleigh dispersion curve that contains information from the velocity reversal layer and the layers below it (see Figure 3.11 and Supplement D). Therefore, it is suggested not to use the τp method for sites with a velocity reversal layer located within the MASW target depth.

4- For sites with clear near-field effects, the FDBF-cylindrical method provided a significantly higher resolution dispersion image than the other transformation methods (FK, PS, and τp), which were corrupted by the near-field effects at low frequencies (see Figure 3.15 and Supplement E). It is observed that the FDBF-cylindrical considerably mitigates the near-field effects for both Rayleigh and Love waves, particularly the effects of model incompatibility by using a cylindrical wavefield model rather than a plane wavefield model.

5- The FDBF-cylindrical was more sensitive to effective and higher modes than the other transformation methods (see Figure 3.16 and Supplement F). This means that more dispersion data points from effective and higher modes can be generated using the FDBF-cylindrical. However, caution should be taken to use the FDBF-cylindrical for sites with effective and higher modes, as sometimes it can lead to mode misidentification (see Figure 3.16). Therefore, a combined dispersion image using different transformation methods is suggested to avoid potential mode misidentification and to be able to identify different modes of propagation.

6- Overall, by comparing the performance of the four common transformation methods for both Rayleigh and Love waves for sites with different subsurface layering, wavefield, and noise conditions, it was observed that the FDBF-cylindrical generally outperforms the others (FK, PS, and τp) transformation methods. The FDBF-cylindrical provides a stable, high-resolution dispersion image for various subsurface layering and noise conditions, mitigates the near-field effects by modeling a cylindrical wavefield, and provides a high-resolution dispersion image over a broad range of frequencies, including the low frequencies portion of the dispersion curve. The FDBF-cylindrical is, therefore, recommended to be used as the primary method if users are willing to only use one transformation technique for MASW data processing.

7- The best practice is to combine all the transformation methods or at least use two different transformation methods (FDBF-cylindrical and FK) for MASW data processing, particularly for complex stratigraphy environments (e.g. sites where higher modes are present). The combined method can be used as a means to enhance the quality and reliability of the experimental dispersion curve, reduce the uncertainty regarding the experimental dispersion curves and the final inverted V_s profile, accurately determine different modes of propagation, and define and remove data corrupted by near-field effects if any are present.

Supplement A: Site with a deep bedrock, uniform soil conditions, and low noise levels

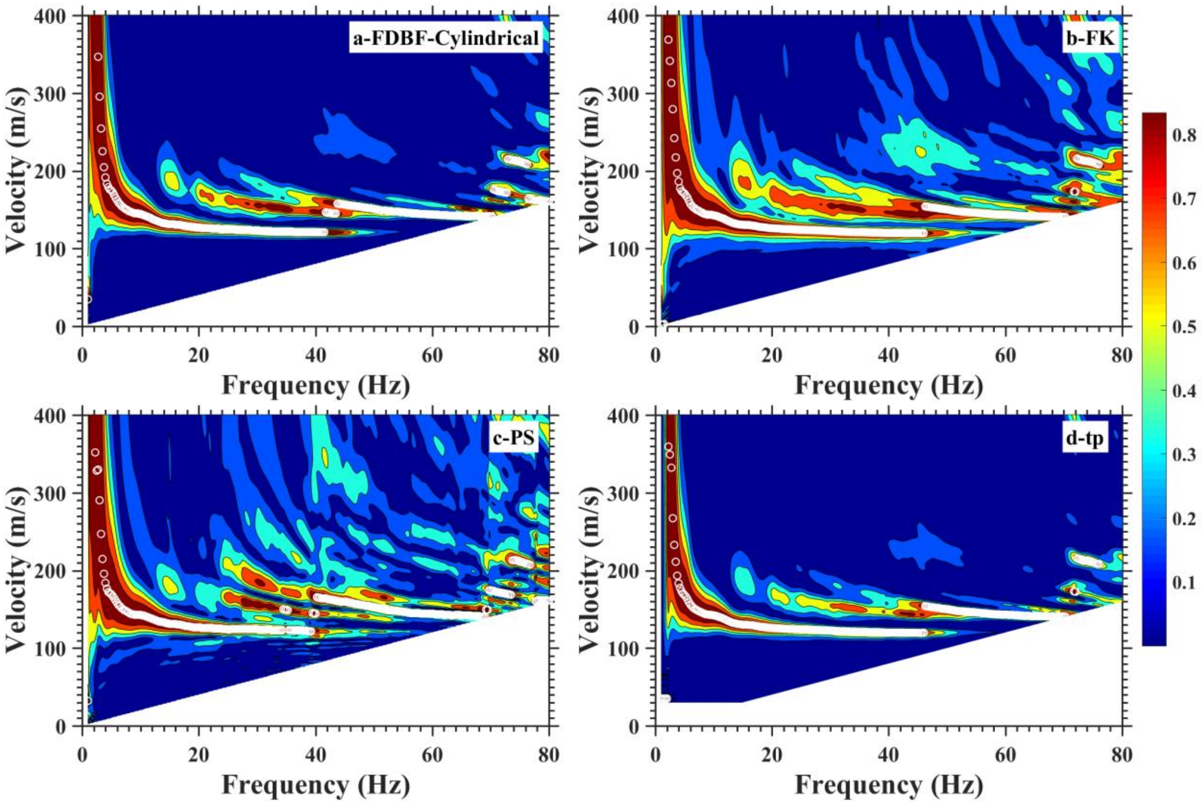

Figure 3.19- Love wave dispersion curves generated using the four transformation methods for the PEBM site with a deep bedrock layer, a low-frequency point of curvature, and low noise levels. a) FDBF-cylindrical, b) FK, c) PS, and d) τp.

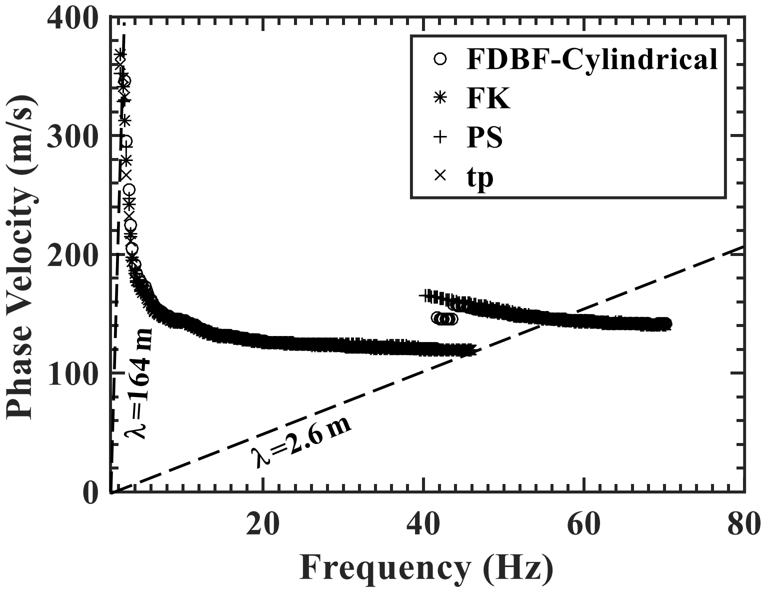

Figure 3.20- Comparison of the four transformation methods for Love waves for the PEBM site, a) FDBF-cylindrical, FK, and τp, b) PS.

<u>Supplement B</u>: Site with a very shallow and highly variable bedrock layer using spikes.

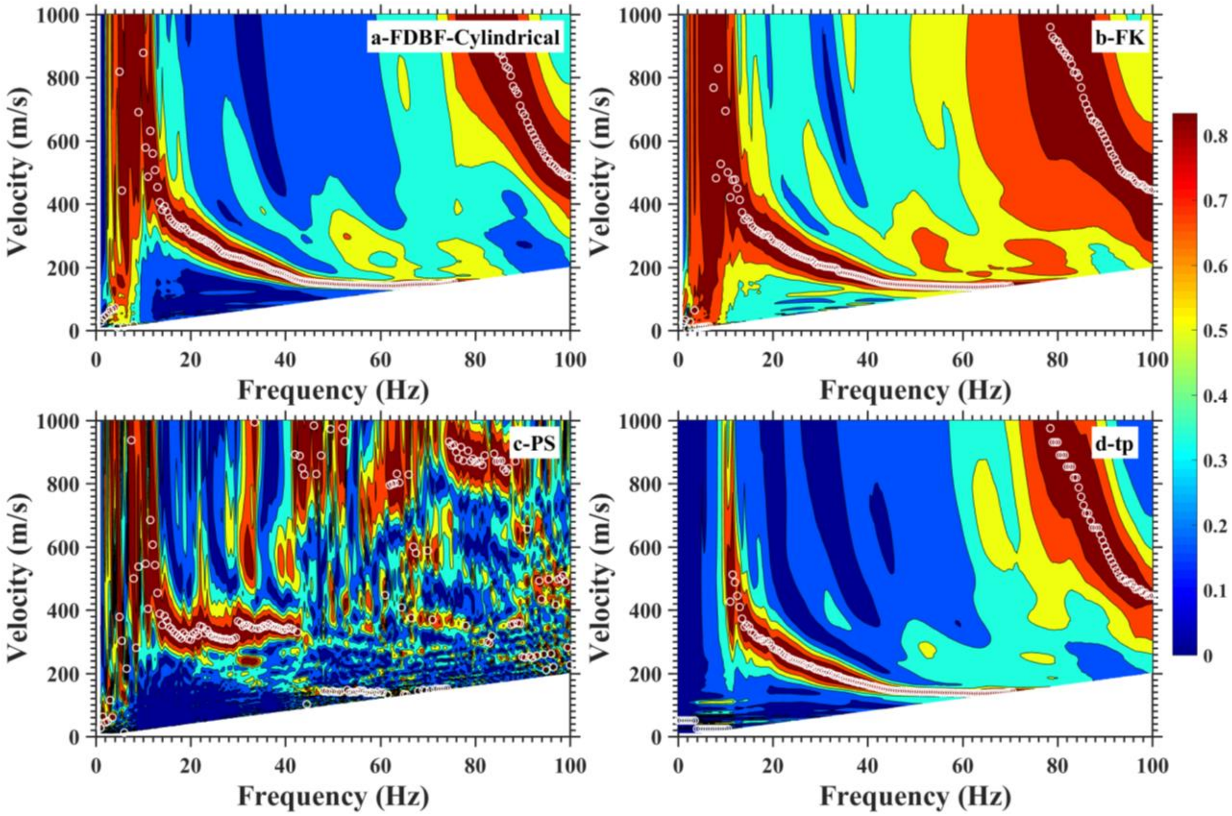

Figure 3.21- Rayleigh wave dispersion curves generated using the four transformation methods for the Ozark site with a very shallow and complex bedrock topography, a high-frequency point of curvature, and high noise levels. a) FDBF-cylindrical, b) FK, c) PS, and d) τp.

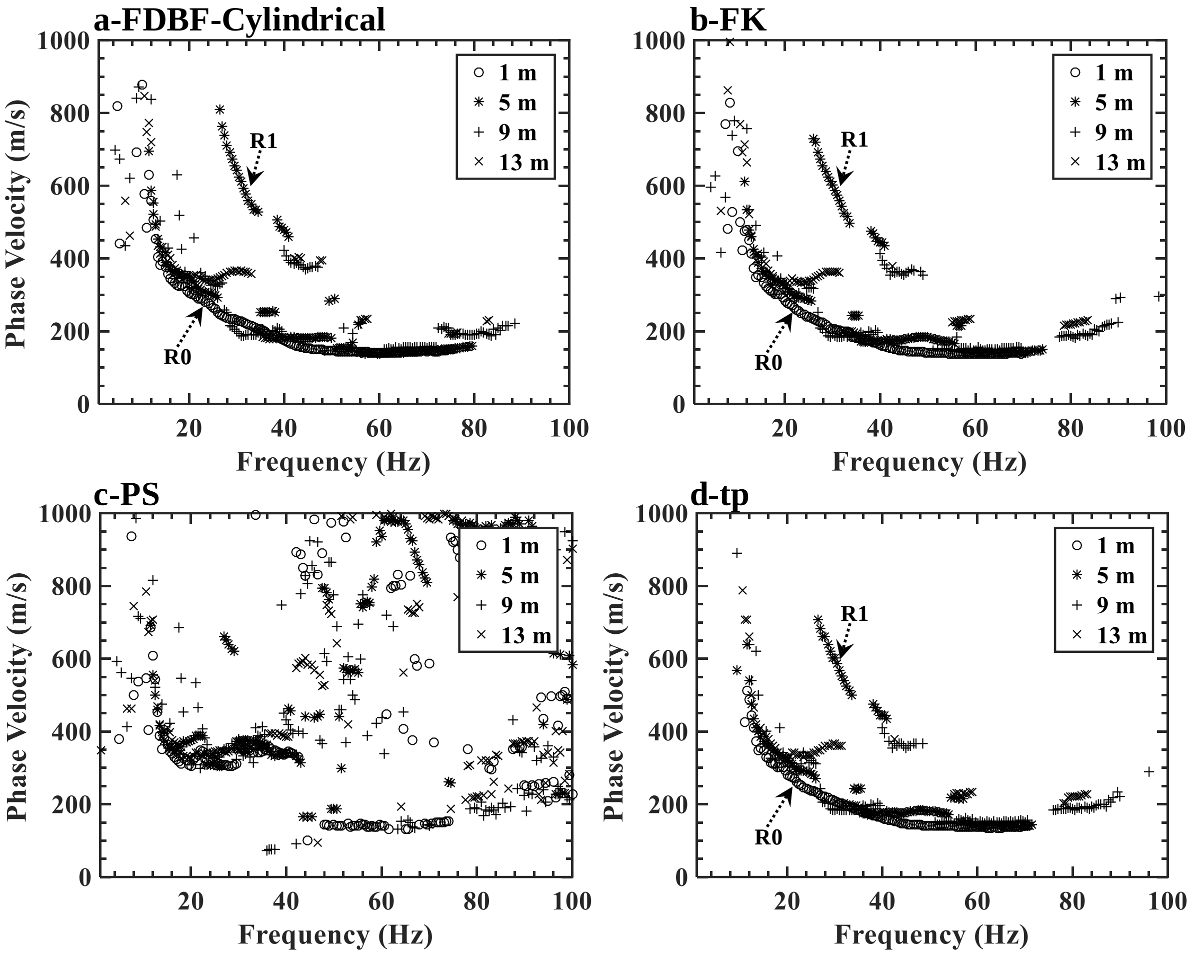

Figure 3.22- Comparison of the four transformation methods for Rayleigh wave for the Ozark site, a) FDBF-cylindrical, FK, and τp, b) PS.

Supplement C: Site with a very shallow and highly variable bedrock layer using a landstreamer.

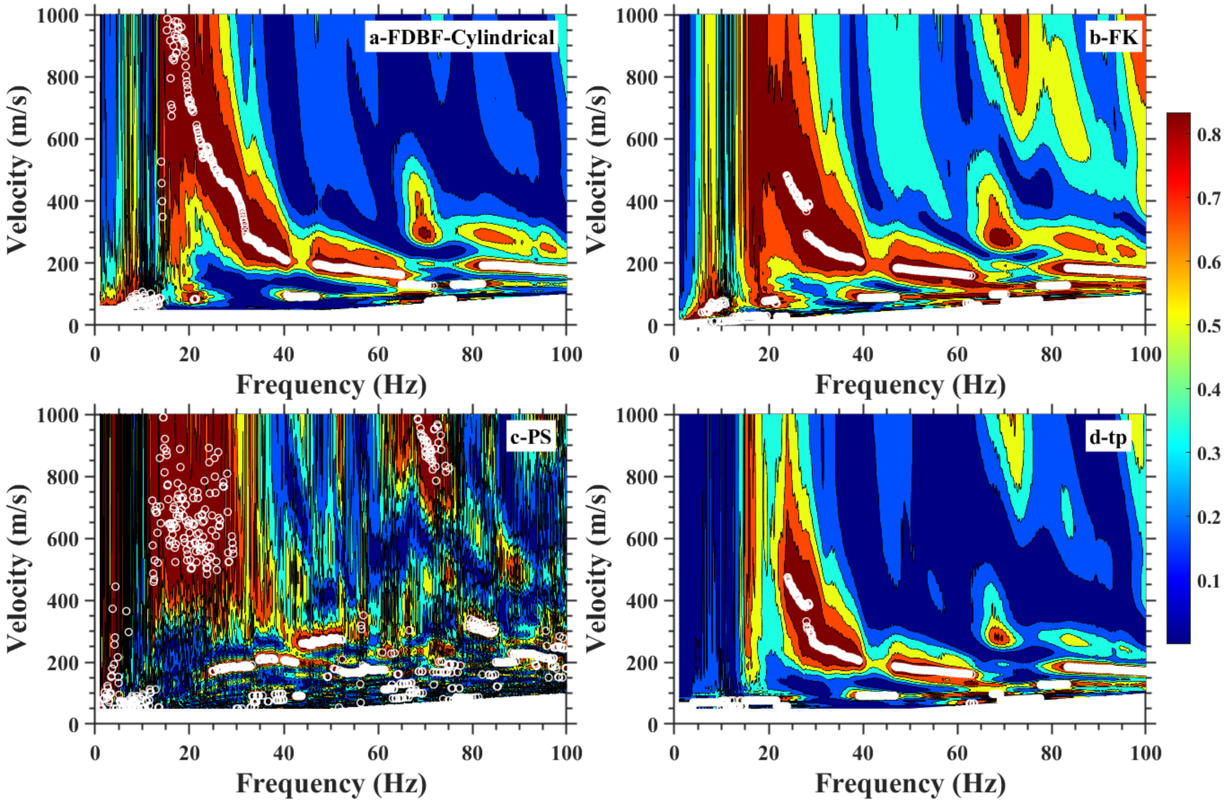

Figure 3.23- Love wave dispersion curves generated using the four transformation methods for the Hot Springs site with a very shallow and complex bedrock topography, a high-frequency point of curvature, and low noise levels. a) FDBF-cylindrical, b) FK, c) PS, and d) τp.

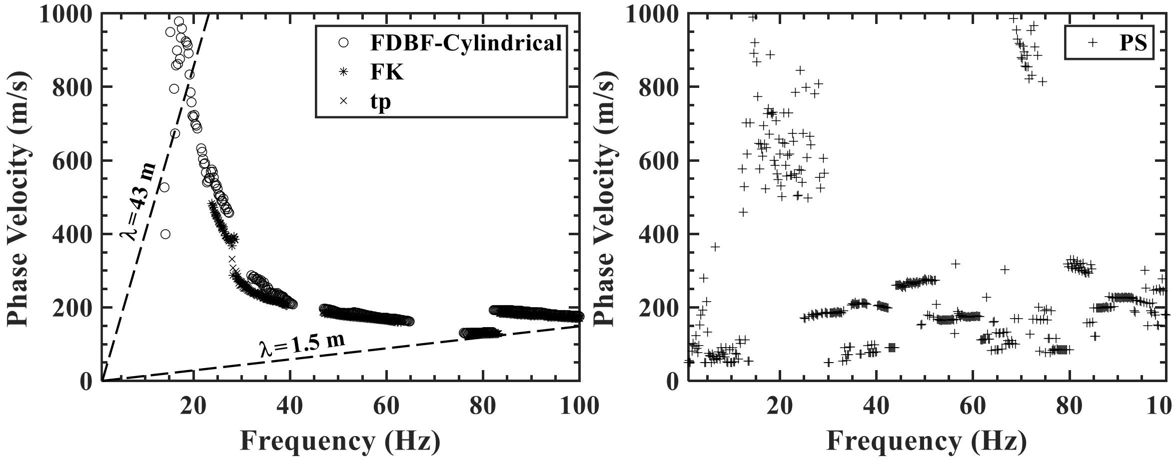

Figure 3.24- Comparison of the four transformation methods for Love wave for the Hot Springs site, a) FDBF-cylindrical, FK, and τp, b) PS.

Supplement D: Site with a velocity reversal layer.

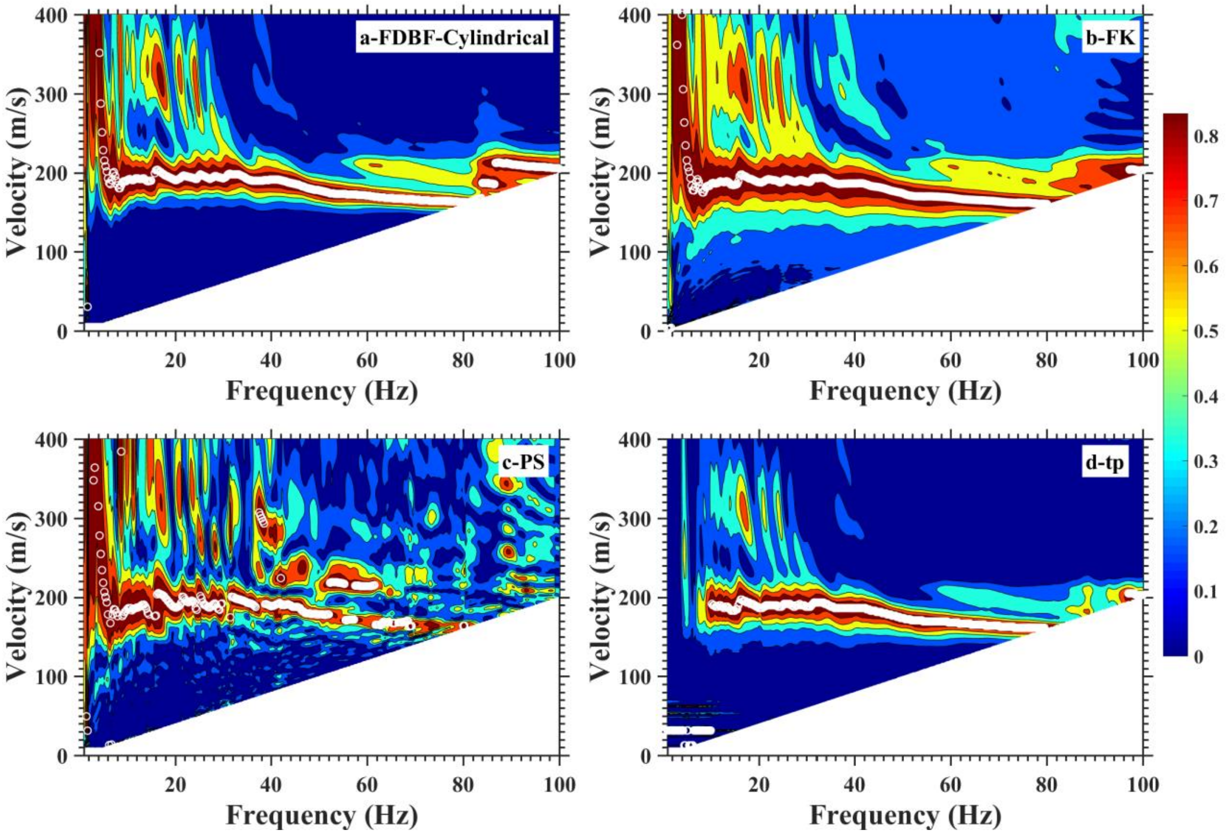

Figure 3.25- Rayleigh wave dispersion curves generated using the four transformation methods for the Melvin-Price site with a velocity reversal layer and moderate noise levels. a) FDBF-cylindrical, b) FK, c) PS, and d) τp.

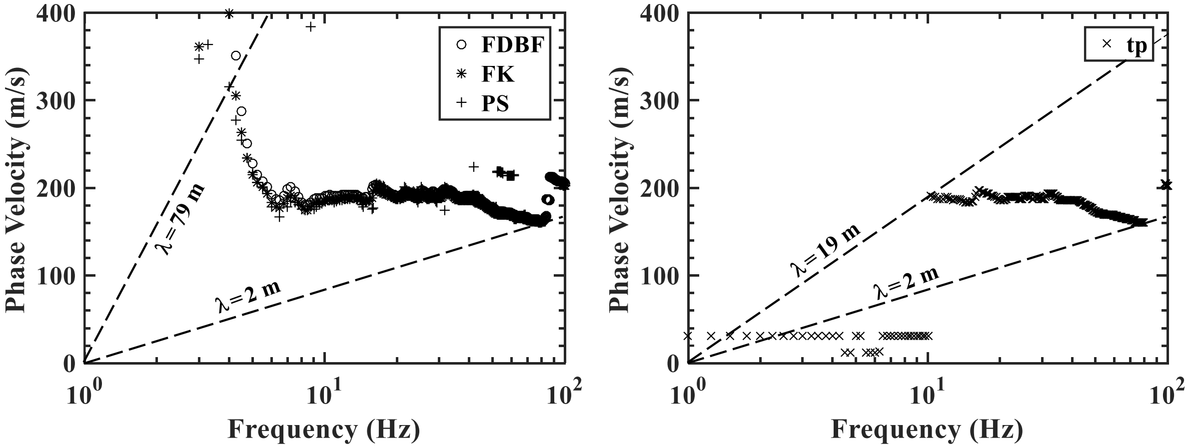

Figure 3.26- Comparison of the four transformation methods for Rayleigh wave for the Melvin-Price site for a location with a velocity reversal layer (irregular dispersive dispersion curve). a) FDBF-cylindrical, FK, and PS, b) τp.

Supplement E: Site with clear near-field effects.

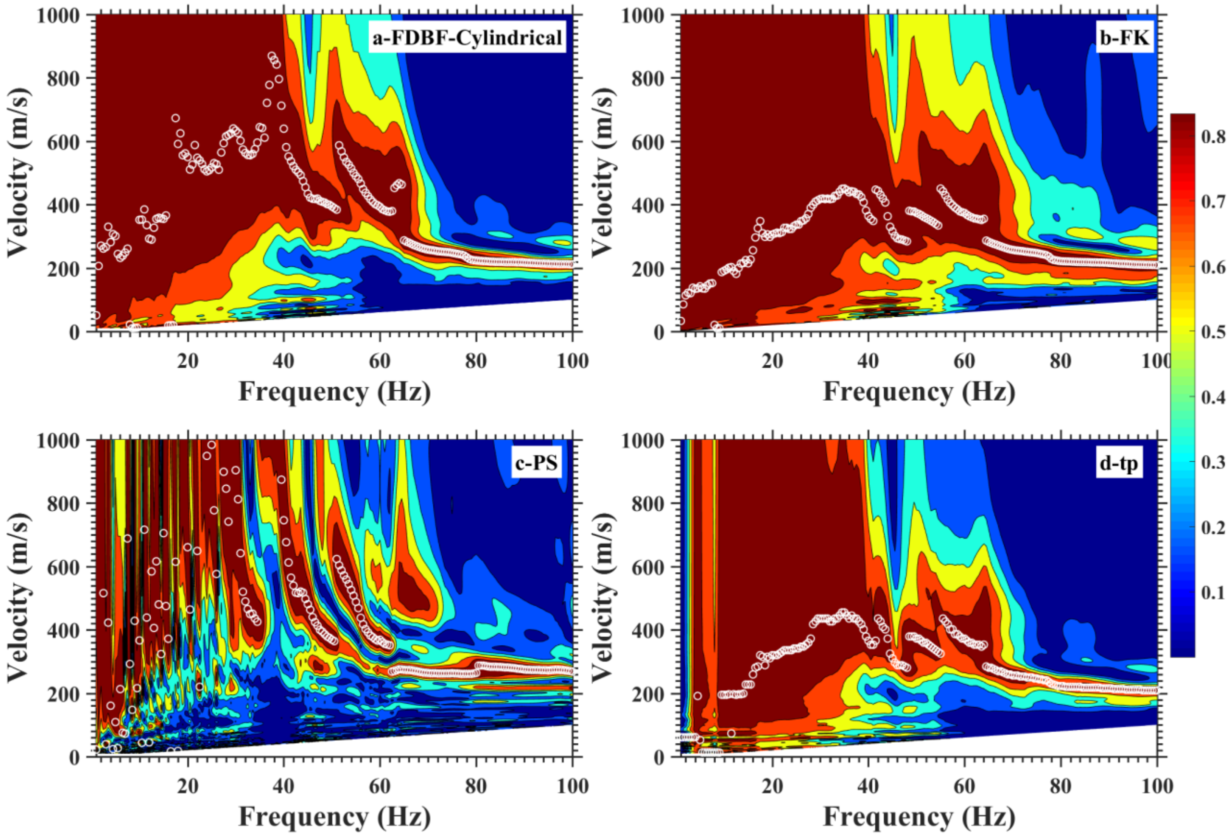

Figure 3.27- Rayleigh wave dispersion curves generated using the four transformation methods for the Hardy site with clear near-field effects and moderate noise levels. a) FDBF-cylindrical, b) FK, c) PS, and d) τp.

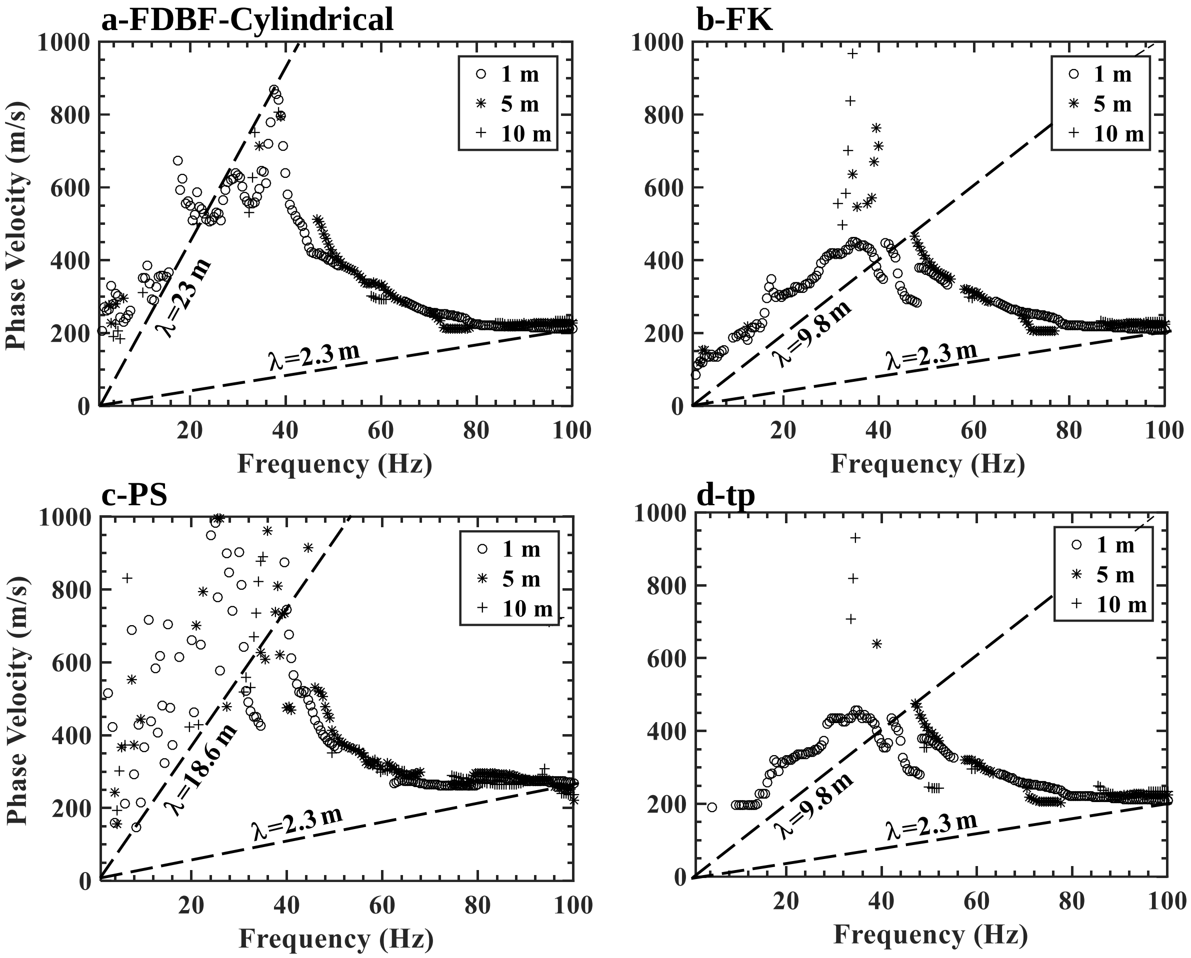

Figure 3.28- Rayleigh wave dispersion data points generated from different source offsets using the four transformation methods for the Hardy site with clear near-field effects and moderate noise levels. a) FDBF-cylindrical, b) FK, c) PS, and d) τp.

Supplement F: Site with clear higher modes.

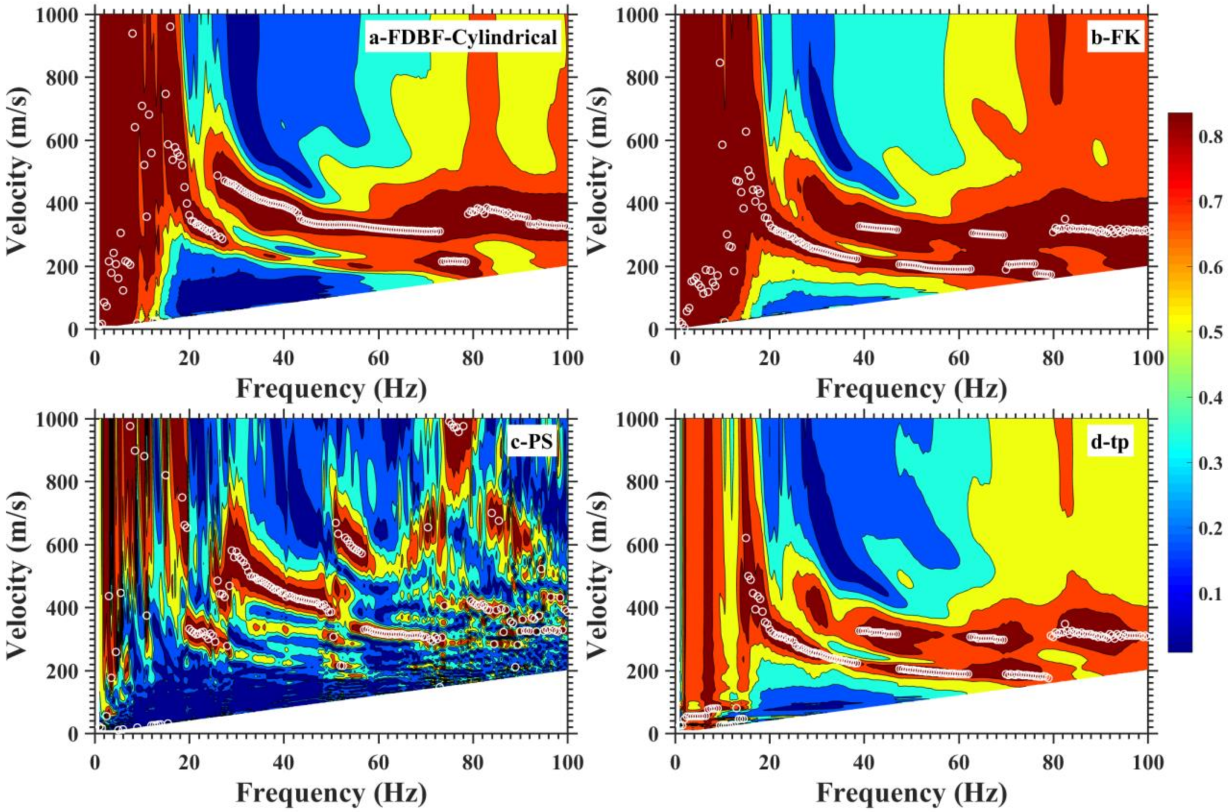

Figure 3.29- Rayleigh wave dispersion curves generated using the four transformation methods for the Ozark site with the FDBF-cylindrical method dominated with a higher mode. a) FDBF-cylindrical, b) FK, c) PS, and d) τp.

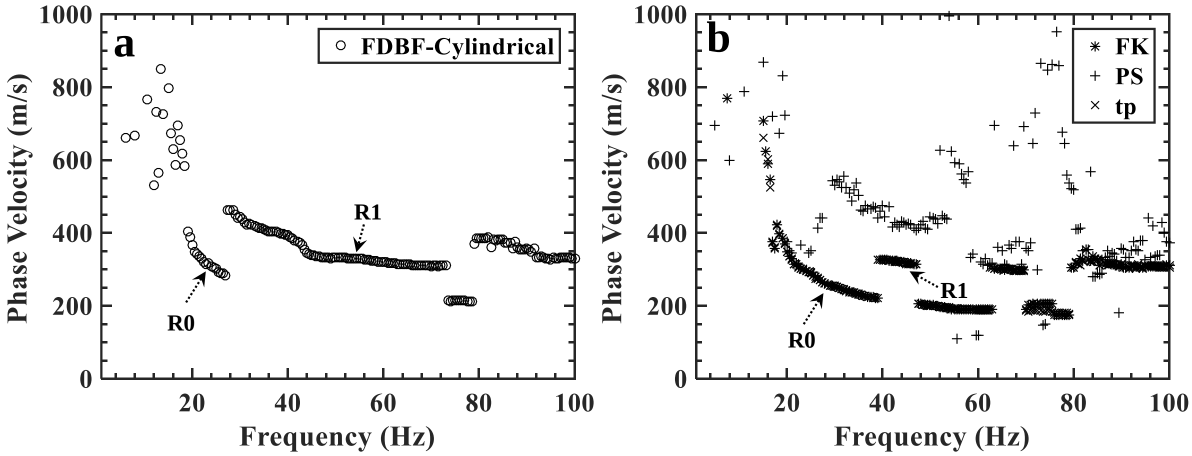

Figure 3.30- Rayleigh wave dispersion curves for the Ozark site. a) FDBF-cylindrical with clear first higher mode (R1) domination, b) FK, PS, and τp methods with dominated with the fundamental mode (R0).

4 CHAPTER 4: DEVELOPING UPDATED GUIDELINES FOR NEAR-FILED MITIGATION FOR ARRAY-BASED ACTIVE SURFACE WAVE TESTING

4.1 Chapter overview

This chapter examines the influence of near-field effects on active array-based surface wave testing considering different conditions, including depth to impedance contrast (very shallow and very deep impedance contrasts), source offset, source type (sledgehammer and vibroseis sources), surface wave type (Rayleigh or Love), and transformation technique (FDBF, FK, PS, and τp techniques) used for data processing. The results of the extensive field measurements are first compared with the previous guidelines and then used to develop comprehensive near-field criteria considering all the parameters mentioned above. The results are provided in the form of a journal paper that has been submitted to Geophysical Journal International.

4.2 Practical Guidelines for Near-field Mitigation on Array-based Active Surface Wave Testing

Reference

Rahimi, S., Wood, C. M., Himel, A. K., (2021). Practical Guidelines for Near-field Mitigation on Array-based Active Surface Wave Testing. Geophysical Journal International.

4.3 Abstract

This paper aims to develop practical guidelines for near-field mitigation for active source surface wave testing. To this end, extensive field measurements were performed considering different factors, including depth to impedance contrast, source offset, source type, surface wave type (Rayleigh or Love), and transformation technique used for data processing. According to the results, near-field effects are independent of surface wave type and depth to impedance contrast. For sites with a very shallow impedance contrast, the FDBF-cylindrical transformation technique outperforms others in terms of dispersion resolution by significantly mitigating near-field effects. On the other hand, for sites with a very deep impedance contrast, the four transformation techniques provide the same dispersion resolution when only considering near-field effects. It is also revealed that the normalized array center distance criteria required to mitigate near-field effects is a function of source type. Using 10-15 % as the accepted error boundary, a normalized array center distance of 1.0 or greater is recommended for low-output impulsive sources such as a sledgehammer source, whereas, for high-output harmonic sources such as a vibroseis, a normalized array center distance of 0.5 is recommended. These criteria should not be violated when using a limited number of source offsets (1 or 2). But, if the multiple source offset approach (≥3 source offsets) is used where some of the source offsets meet the criteria, the near-field criteria can be violated for other source offsets, given that the near-field effects can be mitigated using the composite dispersion data generated from different source offsets if those offsets produce acceptable dispersion data.

Keywords: Near-field effects, Source offset, Source type, Rayleigh and Love, transformation techniques, impedance contrast.

4.4 Introduction

Over the past decade, surface wave methods have received increasing attention among researchers and practitioners in the geotechnical community. Among surface wave methods, active source surface wave testing using Multi-channel Analysis of Surface Waves (MASW) is becoming one of the most popular methods in the geotechnical community. This is due to its noninvasive nature, and more importantly, its effectiveness, rapidness, and low cost for near-surface site characterization, which is the target depth for the majority of geotechnical projects.

MASW is an array-based active source geophysical method that employs the dispersive nature of Rayleigh or Love type surface waves to characterize the subsurface (Park *et al.*, 1998). Initially, the MASW method was utilized to retrieve 1D shear wave velocity profiles. However, nowadays, this method has been employed for a variety of geotechnical applications, including 1D site characterization (Michel *et al.*, 2014), 2D or 3D subsurface imaging (Ismail *et al.*, 2014; Pilecki *et al.*, 2017; Rahimi *et al.*, 2019a), landslide evaluation (Harba *et al.*, 2019; Hussain *et al.*, 2020); rock rippability estimation (Choudhury et al., 2009; Rahimi et al. 2021), infrastructure evaluation (Cardarelli *et al.*, 2014), V_{S30} estimation (Martinez-Pagan *et al.*, 2012; Rahimi *et al.*, 2020d), and soil liquefaction prediction (Mahvelati *et al.*, 2020b; Rahimi *et al.*, 2020a). Despite the increasing popularity of MASW for geotechnical applications over the past years, there still remain issues with this method.

The near-field effect is one of the most commonly encountered issues for the MASW method, leading to the underestimation of shear wave velocities. For most surface wave methods, it is assumed that the wavefield is only composed of planar surface waves. In other words, the two main simplifying assumptions for surface waves data processing are (1) a plane wavefield with no contributions from cylindrical waves and (2) pure surface waves in the wavefield with no interference from body waves. Passive surface wave methods are likely to hold these assumptions reasonable as surface wave sources are presumed far from the receivers. However, for the active MASW method, source distance from the first receiver (i.e. source offset) is minimized to achieve a high signal-to-noise ratio (Tokimatsu, 1997; Zywicki, 1999). Therefore, the surface wave data processing assumptions might not be valid for these closely placed source offsets (Ryden *et al.*, 2009). The region where these assumptions are invalid is called the near-field.

When a source is placed within the near-field, the effects observed on the measured dispersion data are called near-field effects. The near-field effects can be divided into two main categories based on the assumptions made for surface waves data processing. First, the near-field effect of modeling a cylindrical wavefield as a plane wavefield is the model incompatibility effect (Zywicki *et al.*, 2005). This near-field effect is identified by a clear roll-off in the measured phase velocity at low frequencies (long wavelengths). Second, the near-field effect due to body wave interference leads to oscillations in the measured phase velocity at low frequencies (Rahimi et al. 2021). The near-field effect is a primary issue for the MASW method because it corrupts the low-frequency experimental dispersion data so that a reliable inversion result cannot be obtained, leading to mispredictions of the subsurface properties. The low-frequency dispersion data are important because it contains information regarding deeper subsurface layers which are often desired to estimate bedrock depth or Vs30. It is, therefore, critical to mitigating near-field effects when conducting MASW testing.

Despite the importance of near-field effects, a limited number of research groups have attempted to develop methods to mitigate such effects. These methods include modifying wavefield transformation techniques to account for cylindrical waves (Zywicki *et al.*, 2005), increasing distance between the source and first or middle receiver (Xu *et al.*, 2006; Bodet *et al.*, 2009), employing multiple source offsets (Wood *et al.*, 2012), utilizing a greater number of receivers (Yoon *et al.*, 2009), and using both phase and group velocity estimates (Tremblay *et al.*, 2019). The most robust near-field effects criteria were developed by Yoon and Rix (2009), in which two normalized parameters were introduced. These parameters include a normalized phase velocity parameter defined as the ratio of the measured phase velocity (with near-field corruption) to the true phase velocity (without near-field corruption) and a normalized array center distance (hereafter normalized ACD) given by:

$$\frac{\bar{x}}{\lambda} = \frac{(1/M)\sum_{m=1}^{M} x_m}{\lambda} \tag{55}$$

Where $\bar{x}$ is the mean distance of all receivers relative to the source offset, λ is the wavelength, and M is the number of receivers. Yoon and Rix (2009) have proposed two practical guidelines for near-field mitigation, including using a normalized ACD greater than one to limit near field errors to less than 10-15% and a normalized ACD greater than two to limit errors to less than 5%.

In a recent study by Li and Rosenblad (2011), a less restrictive normalized ACD of 0.5 is proposed to limit errors to less than 5%. Li and Rosenblad (2011) suggested that the inconsistency in their proposed normalized ACD guideline with those recommended by Yoon and Rix (2009) is due to the high Poisson's ratio values for their study areas, a condition that was not investigated by Yoon and Rix (2009). In addition to Poisson's ratio, it has been shown that the impedance contrast observed in the subsurface is another important factor influencing the near-field effects (Roy *et al.*, 2017). Roy and Jakka (2017) have shown that as the impedance ratio increases, the phase velocity underestimation due to near-field effects increases at lower normalized ACD.

Overall, practical guidelines provided in previous studies are generally site-specific as they fail to consider different factors influencing near-field effects. These include subsurface and wavefield conditions, source offset, source type (sledgehammer and vibroseis), surface wave type (Rayleigh and Love), and the transformation technique used for data processing. There is, therefore, a need for a comprehensive investigation to develop practical guidelines for near-field mitigation considering the factors mentioned above. Therefore, this study aims to fill this knowledge gap in these topics and develop the best practical guidelines for near-field mitigation during field measurements. Toward this end, extensive field measurements were performed at sites with different subsurface conditions using both Rayleigh and Love type surface waves and sledgehammer and vibroseis sources. The data are then analyzed using four common wavefield transformation techniques. The paper begins with the site locations targeted in this study. Information regarding field measurements and data processing are then provided. The near-field effects observed for different site conditions (very shallow and very deep impedance contrasts), surface wave types (Rayleigh and Love), source offsets, source type (sledgehammer and vibroseis), and transformation techniques are then discussed. Finally, new practical criteria for near-field mitigation are proposed.

4.5 Site description and field measurements

To explore the near-field effects for different subsurface conditions, approximately 400 MASW array setups were performed at 19 sites within the USA, as tabulated in Table 4. The sites were selected in such a way that they cover a variety of subsurface conditions. Several of the sites are comprised of a very shallow impedance contrast (i.e. bedrock layer) ranging from 1-17 meters, whereas the rest of the sites are comprised of a very deep impedance contrast ranging from 252-1110 m (see Table 4). For all these sites, the impedance contrast is located at the soil/bedrock interface.

The general geology for sites with a very shallow impedance contrast includes very thin soil layers followed by a highly variable and complex bedrock layer which results in a heterogeneous soil profile within the target depth of active surface wave testing. The general geology of the sites with a very deep impedance contrast consists of thick, unconsolidated sediments followed by a very deep bedrock layer. This indicates that for these sites, the soil profile is almost homogenous within the target depth of active surface wave testing. For sites with a very deep impedance contrast, depth to the highly saturated soil layer, which is shown to be an important factor affecting near-field effects (Li, 2011; Li *et al.*, 2011), is also presented in Table 4. These depths were determined based on P-wave refraction measurements. According to the P-wave refraction results, the highly saturated soil layer is located near the surface (~3-14.3 m) within the target depth of the MASW.

Table 4- Key characteristics of the study areas and field measurements.

Site name	Impedance contrast depth (m)	Saturation depth (m)	Source type	Coupling method	Surface wave type	Geophone spacing (m)	Number of setups
North Little Rock	Very shallow (1-4)	-	SH[1]	S[2]	R[3]	2	35
Hot Springs	Very shallow (1-7)	-	SH	L	L[4]	1	140
Little Rock	Very shallow (1-8)	-	SH	S	R and L	1 and 2	35
Sand Gap	Very shallow (4-10)	-	SH	S	L	1 and 2	22
Hardy	Very shallow (2-15)	-	SH	L	R	1	58
Ozark	Very shallow (5-17)	-	SH	S	R	1 and 2	76
McDougal	Very deep (252)	3.7	SH	S	R and L	2	2
Fontaine	Very deep (291)	11.4	SH	S	R and L	2	2
Monette	Very deep (680)	5.4	SH	S	R and L	2	2
Manila	Very deep (810)	3.9	SH	S	R and L	2	2
Marmaduke	Very deep (492)	3	SH	S	R and L	2	2
Wynne	Very deep (850)	15.7	SH & V[5]	S	R and L	2 and 4	2
Athelstan	Very deep (860)	4.3	SH	S	R and L	2	2
Palestine	Very deep (960)	14.3	SH	S	R and L	2	2
Earle	Very deep (1020)	9.5	SH & V	S	R and L	2 and 4	2
Greasy Corner	Very deep (1070)	9.2	SH	S	R and L	2	2
Aubrey	Very deep (1110)	9.7	SH	S	R and L	2	2
Bay	Very deep (518)	6.7	SH & V	S	R and L	2	2
Amagon	Very deep (349)	7.2	SH & V	S	R and L	2 and 4	2

[1] Sledgehammer

[2] Spike

[3] Rayleigh type surface wave

[4] Love type surface waves

[5] Vibroseis

MASW testing was conducted using 24, 4.5 Hz vertical or horizontal geophones spaced 1, 2, or 4 meters apart. Both Rayleigh and Love type surface waves were performed for most of the sites listed in Table 4. For sites where a significant number of MASW setups were collected (Hot Springs and Hardy), a landstreamer system was used to increase the rate of field measurements. However, for most sites, spikes, which generally result in better coupling to the ground surface, were used. Rayleigh and Love type surface waves were mostly generated using a 4.5 kg sledgehammer source. However, for four of the sites with a very deep impedance contrast (Wynne, Earle, Bay, and Amagon), a vibroseis source was used in addition to the sledgehammer to examine the influence of source type on near-field effects. For the vibroseis source, testing was performed using a stepped-sine approach for frequencies ranging from 2-50 Hz (Wood et al., 2012). For each MASW array setup, waves were generated for at least three source offsets. Several sledgehammer blows were stacked at each source offset to improve the reliability of the collected data and signal-to-noise ratio. For sites with a very shallow impedance contrast, source offsets of 1, 2, 5, 10, 13, or 25 m were used. But for sites with a very deep impedance contrast, longer source offsets of 2, 5, 10, 20, 30, and 40 m were utilized. More information about site descriptions, stratigraphy, and field measurements are provided in Wood et al. (2019) and Rahimi et al. (2021).

4.6 Data processing

MASW data was processed to develop the experimental dispersion curve, representing the variation of Rayleigh or Love wave phase velocity versus frequency. For each MASW array setup, the experimental dispersion curve was generated using four transformation techniques. These techniques consist of slant stack or frequency-slowness (τp) (McMechan *et al.*, 1981), frequency-wavenumber (FK) (Nolet *et al.*, 1976; Yilmaz, 1987; Foti *et al.*, 2000), frequency domain beamformer (FDBF) (Zywicki, 1999; Hebeler *et al.*, 2007), and phase shift (PS) (Park *et al.*, 1998). These are the four primary transformation techniques that have been extensively used by researchers, practitioners, and software packages for MASW data processing (Rosenblad *et al.*, 2009; Cox *et al.*, 2014; Lontsi *et al.*, 2016; Olafsdottir *et al.*, 2018; Cheng *et al.*, 2019).

For the FDBF technique, two different approaches are proposed, one for planar and one for cylindrical wavefield. In this study, only the cylindrical version of the FDBF method is considered because the experimental dispersion curve generated using the FDBF-plane was observed to be nearly identical to the FK. Details regarding each transformation technique are provided in Rahimi et al. (2021). Generally, dispersion data collected at different source offsets are compared and combined to eliminate the data corrupted by near-field effects. However, in this study, each source offset was processed individually to be able to investigate the near-field effect. The final dispersion curve was developed for each transformation technique by automatically picking the maximum spectral peak in the frequency-wavenumber domain. The dispersion data related to an effective or higher mode were eliminated, but data corrupted by near-field effects were kept in the final dispersion data to identify near-field effects.

4.7 Results and discussions

The results of this study are presented in two main sections: near-field effects for sites with a very shallow and highly variable impedance contrast and near-field effects for sites with a very deep impedance contrast. Near-field effects are examined considering different conditions, including Rayleigh and Love type surface waves, various transformation techniques, different source offsets, and different source types (sledgehammer or vibroseis). For the results section presented below, the sledgehammer was used for the active surface wave testing unless it is stated otherwise. Due to the extensive number of MASW setups, only a few examples are provided in each section. However, the behavior observed in these examples was observed in the other numerous dataset investigated for this study.

4.7.1 Near-field effects for sites with a very shallow and highly variable impedance contrast

4.7.1.1 Rayleigh type surface waves

4.7.1.1.1 Different transformation techniques

Presented in Figure 4.1 is an example of raw Rayleigh wave dispersion curves generated using the four transformation techniques for the Sand Gap site with a very shallow and highly variable impedance contrast. All the transformation methods should estimate the phase velocity with less than a 10% error in the absence of near-field effects. From this figure, apparent near-field effects are observed in the form of roll-off in the measured Rayleigh wave phase velocity in the experimental dispersion curves developed using the four transformation techniques. The clear roll-off in the measured phase velocity is observed to occur at a different frequency and phase velocity data pair for each transformation technique. In other words, different maximum wavelengths (i.e. depths) are measured using the four transformation techniques. This indicates that the ability to mitigate near-field effects is different for each transformation technique.

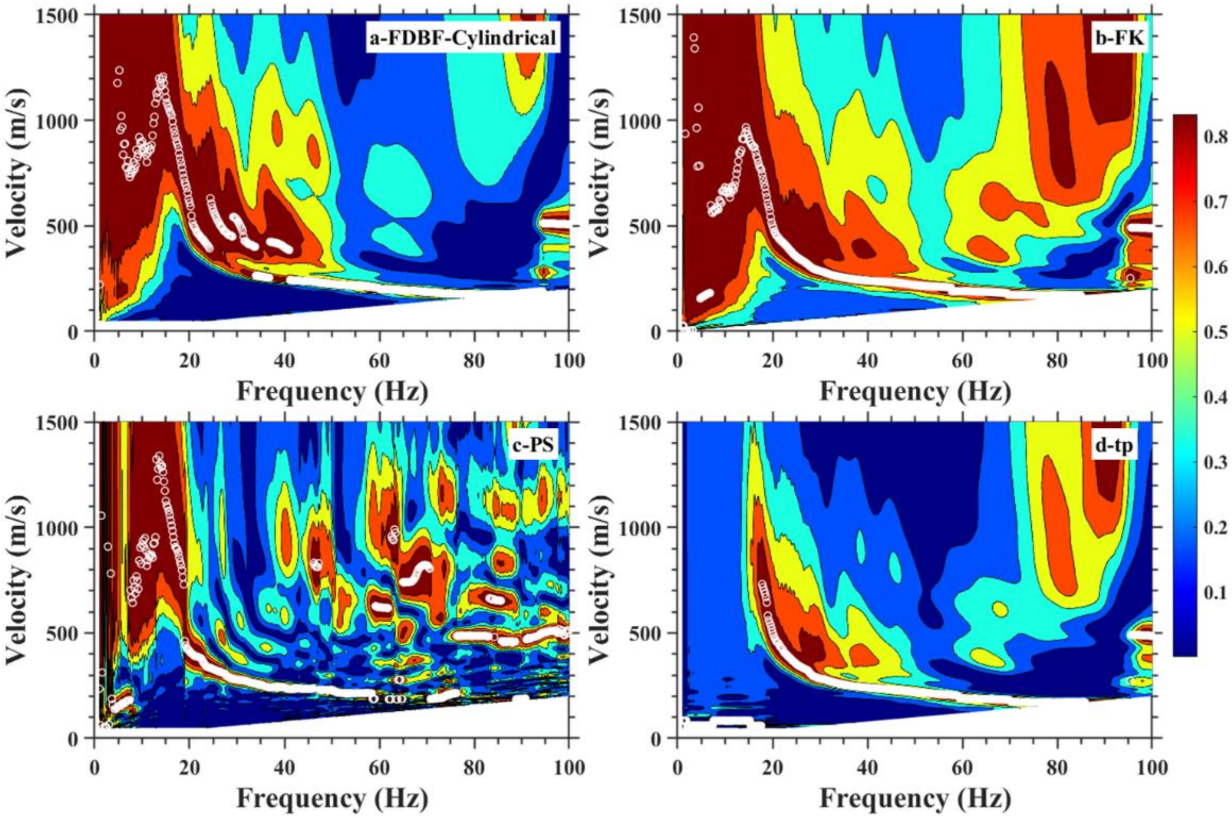

Figure 4.1- Rayleigh wave dispersion curves generated using the four transformation methods for the Sand Gap site with a very shallow and highly variable impedance contrast. a) FDBF-cylindrical, b) FK, c) PS, and d) τp.

The differences between the four transformation techniques are more apparent in Figure 4.2, where the experimental dispersion curves developed using the four transformation techniques are combined. Additionally, the true fundamental (R0, solid curve), first higher (R1, dashed curve), and second higher (R2, dotted curve) dispersion curves are shown to ensure the dispersion data generated using each transformation technique is related to the true fundamental mode. These modes are generated by forward modeling of the P-wave velocity profile estimated from the P-wave refraction measurements and boring log information. Based on the zoomed-in view of this figure, the maximum resolved wavelength (prior to roll-off) for FDBF-cylindrical and PS methods is 80 m, whereas this value is 50 m and 40 m for the FK and τp methods, respectively. This indicates that the experimental dispersion curves developed using the τp and FK methods are more corrupted by near-field effects than the FDBF-cylindrical and PS methods.

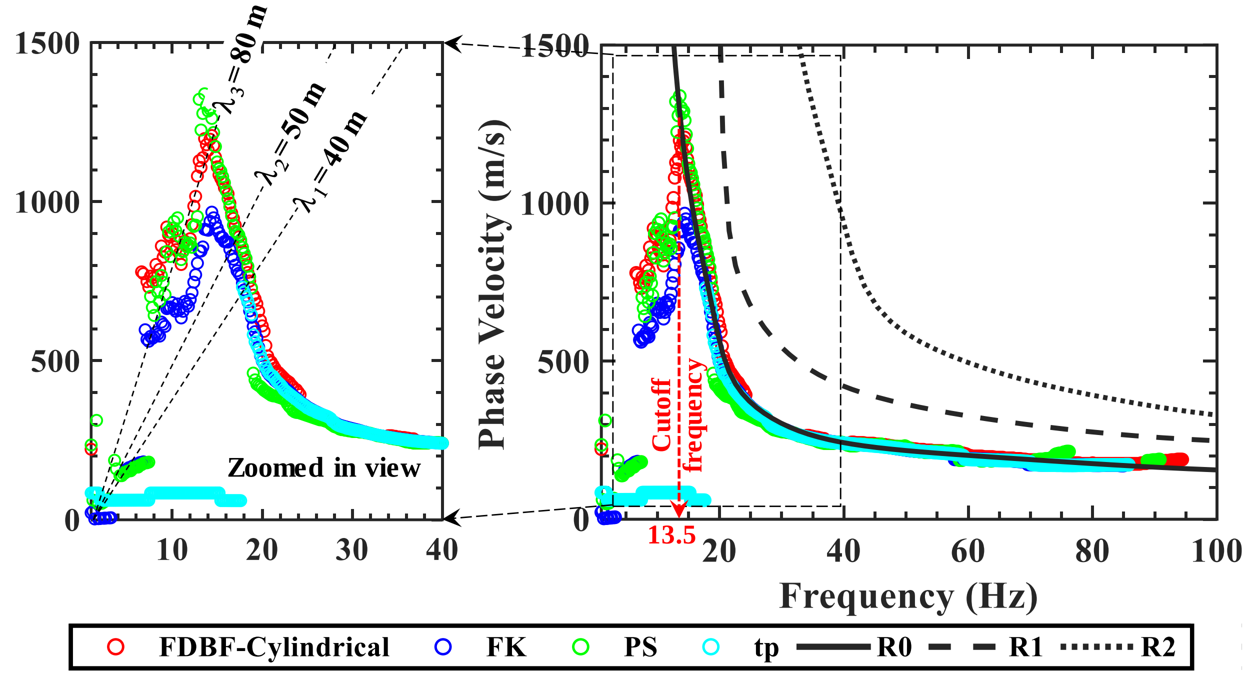

Figure 4.2- Comparison of the near-field effects observed for different transformation techniques for the Sand Gap site. The true fundamental (R0), first higher (R1), and second higher (R2) modes are shown with solid, dashed, and dotted curves, respectively.

4.7.1.1.2 Different source offsets

Data from different source offsets for the same MASW setup presented in Figure 1 are used to investigate the impacts of the multiple source offset approach on near-field mitigation. Shown in Figure 4.3 is the Rayleigh wave dispersion data generated at different source offsets of 1, 13, and 25 m using the four transformation techniques along with the true fundamental (R0), first higher (R1), and second higher (R2) modes. In this figure, it is apparent that similar dispersion resolution is obtained in terms of near-field effects from the four transformation techniques when using the multiple source offset approach. In other words, the near-field effects observed for the FK and τp methods in Figure 4.2 are mitigated by using data from longer source offsets at lower frequencies. For example, for the FK method in Figure 4.3, it is evident that the low-frequency dispersion data generated using the 13 m (blue) and 25 (green) m source offsets correspond well with the true fundamental mode (no near-field effects), while the dispersion data from the 1 m source offset (red) are corrupted by the near-field effects at the same frequencies.

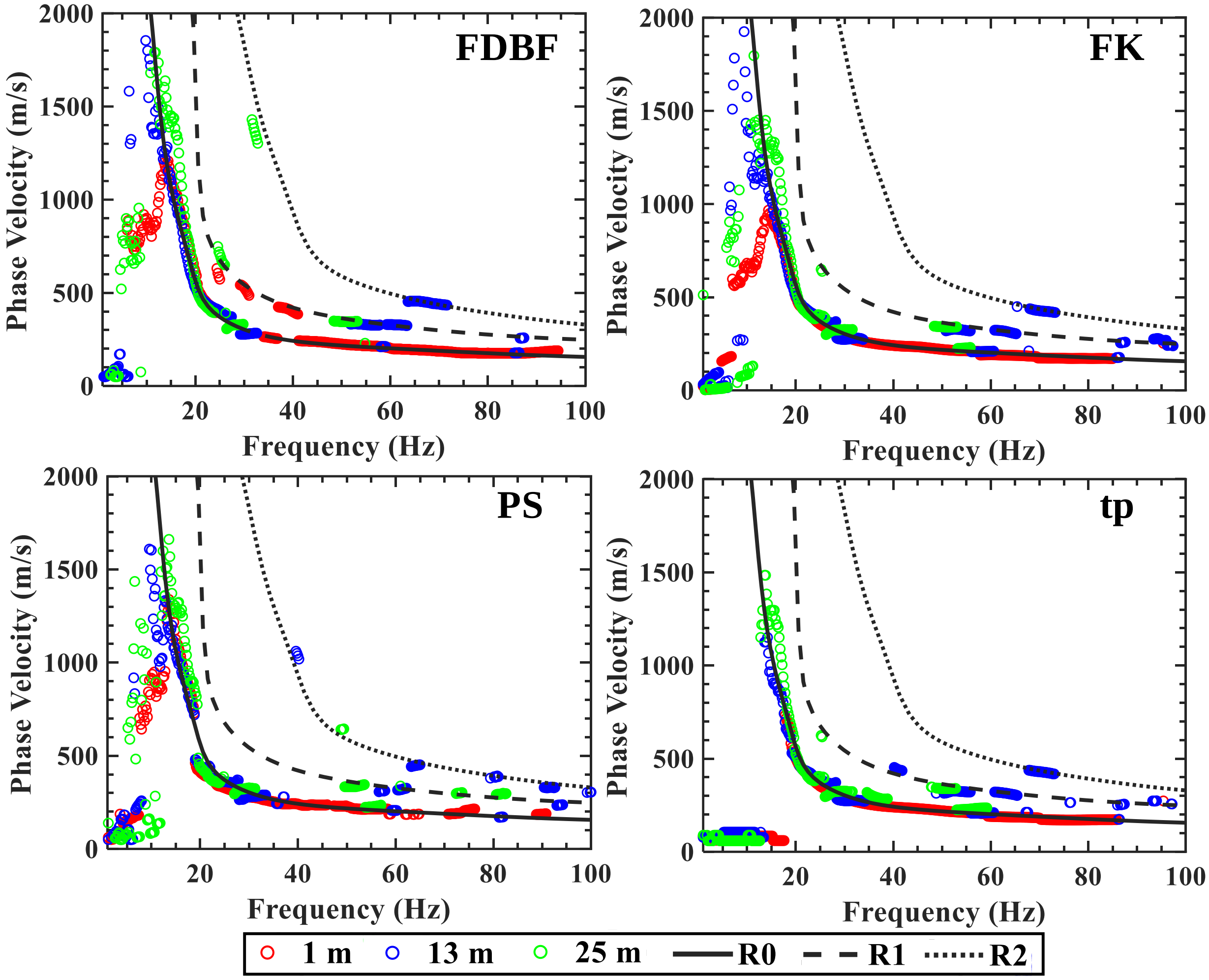

Figure 4.3- Rayleigh wave dispersion data points generated using the four transformation methods at different source offsets for the same MASW setup shown in Figure 1. The true fundamental (R0), first higher (R1), and second higher (R2) modes are shown with solid, dashed, and dotted curves, respectively.

Shown in Figure 4.4 is another example of Rayleigh wave dispersion data generated at different source offsets using the four transformation techniques for the Ozark site with a very shallow and highly variable impedance contrast. Additionally, the true fundamental (R0), first higher (R1), and second higher (R2) modes are shown with solid, dashed, and dotted curves, respectively. A similar procedure used for the MASW setup in Figure 4.3 was followed to produce the dispersion curves from different modes of propagation.

Unlike the previous example in Figure 4.3, where the multiple source offset approach allowed the mitigation of near-field effects, for the MASW setup for the Ozark site in Figure 4.4, no improvements in the dispersion resolution are obtained in terms of near-field effects when using the multiple source offset approach. For this MASW setup in Figure 4.4, it is apparent that the dispersion data from long source offsets (13 and 25 m) are mainly dominated by the R1 mode (particularly data from the 13 m source offset). Most of the data related to the fundamental mode (R0), which is the primary mode of interest in surface wave testing, are generated through the 1 m source offset. This is reasonable given the very shallow impedance contrast for this site, which leads to higher mode domination for source offsets located far from the array.

From the dispersion data generated using the Fk and τp methods for the 1 m source offset (red circle) in Figure 4.4, apparent roll-off is observed in the measured phase velocity due to the near-field effect at a frequency of 19.5 Hz (wavelength of 18 m). However, the roll-off in the FDBF-cylindrical method occurs at a frequency of 12 Hz (wavelength of 51 m), meaning that a significantly longer wavelength experimental dispersion curve is generated using the FDBF-cylindrical method. Another point that should be highlighted is that the dispersion data from the PS method are scattered over different modes, which leads to a poor resolution experimental dispersion curve compared to the other methods. The PS resolution issue for sites with a very shallow and highly variable impedance contrast and the reason behind such observations are discussed in detail in Rahimi et al. (2021).

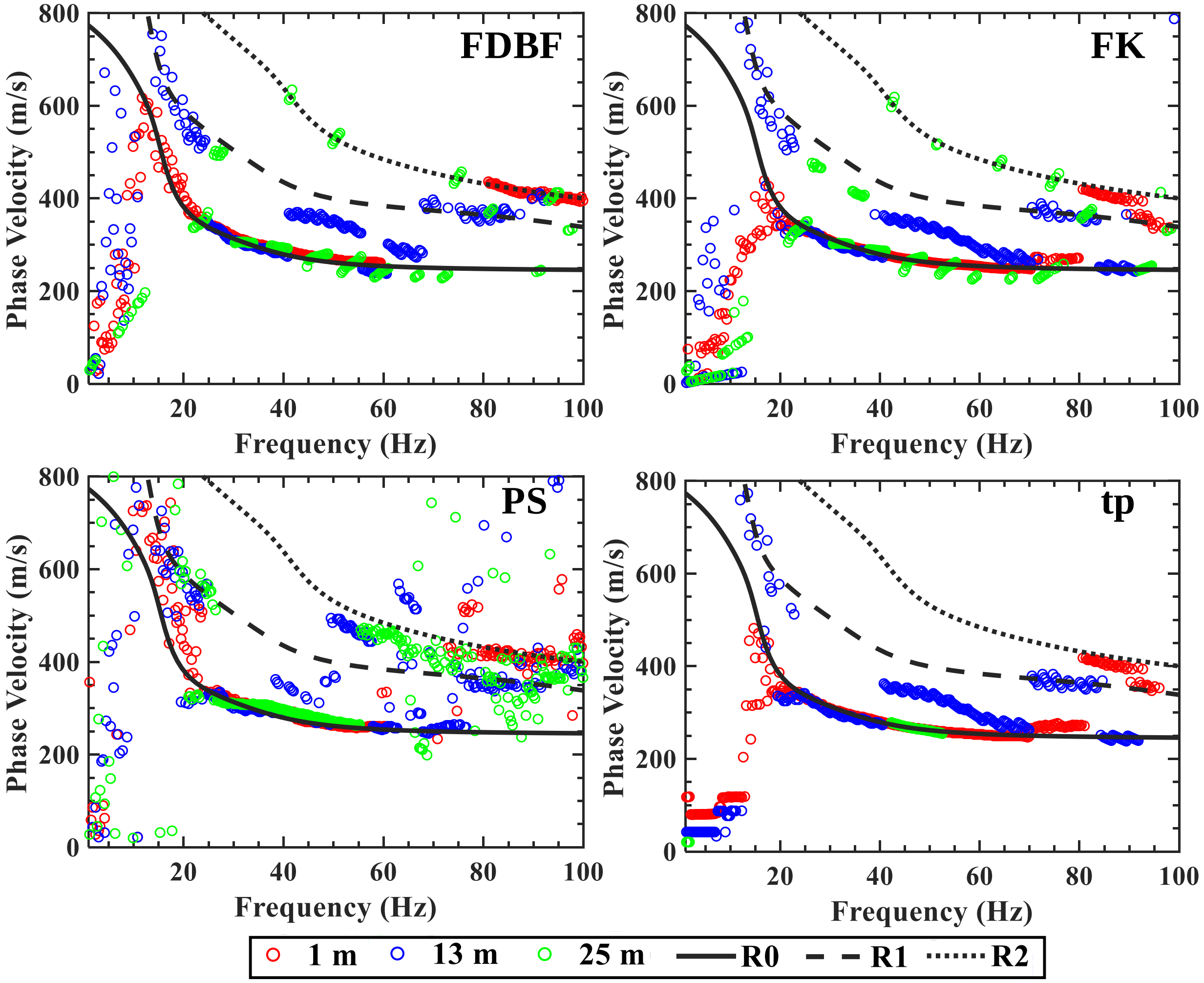

Figure 4.4- Rayleigh wave dispersion data points generated using the four transformation methods at different source offsets for the Ozark site with a very shallow and highly variable impedance contrast. The true fundamental (R0), first higher (R1), and second higher (R2) modes are shown with solid, dashed, and dotted curves, respectively.

4.7.1.1.3 Threshold normalized ACD

Data from all the Rayleigh wave MASW setups are combined to generate the normalized ACD plot to identify the most suitable ACD criteria regarding near-field mitigation. Toward this end, the dispersion data related to an effective or a higher mode were first eliminated to develop the final experimental dispersion data. Each data pair of phase velocity versus wavelength in the final dispersion plot was then moved to the normalized ACD versus normalized phase velocity

(VR) domain. The normalized ACD parameter was calculated based on the wavelength and array geometry using Equation 1. To calculate the normalized VR parameter, a true (reference) phase velocity is required. The true phase velocity is typically determined using passive surface wave methods because dispersion data from such methods are often free of near-field effects. However, considering the number of MASW setups collected at sites with a very shallow impedance contrast (see Table 4), passive surface wave measurements were not an ideal option due to their long recording time. Therefore, in this study, the true phase velocity was determined using the measured phase velocity from the FDBF-cylindrical method since the FDBF-cylindrical reduces/eliminates the near-field effects of model incompatibility (Yoon *et al.*, 2009). It should be highlighted that the dispersion data from the FDBF-cylindrical was used as the true phase velocity only up to a cutoff frequency where the data was free of near-field effects, given that the cylindrical wavefield model does not eliminate all the near-field effects. For example, the cutoff frequency for the MASW setup in Figure 4.2 was 13.5 Hz (wavelength of 80 m), as illustrated in this figure.

Shown in Figure 4.5 is the normalized ACD plot for Rayleigh waves using all the data from sites with a very shallow and highly variable impedance contrast. Data included in this figure are related to either the 1 m or 5 m source offset. Only dispersion data from the FK and τp are included in this plot due to the PS resolution issues for sites with a very shallow and highly variable impedance contrast (see Rahimi et al. 2021). Additionally, two boundaries of 5% and 10% phase velocity errors (Yoon *et al.*, 2009) and their associated zonations are provided with blue and red colors, respectively. The 5% and 10-15% error boundaries are used to define the normalized ACD criteria for near-field mitigation.

From Figure 4.5, it is observed that due to the uncertainty in the experimental data, a range of normalized ACD is associated with the 5% and 10-15% error boundaries. Such behavior is also observed in the previous studies (Yoon *et al.*, 2009; Li *et al.*, 2011) and indicates the site dependence and variability in the near field effect. In this study, the onset of the considerable reduction (underestimation) in the measured phase velocity is used to determine the criteria for near-field effects mitigation. This provides the most conservative normalized ACD criteria for near-field mitigation based on the experimental data. According to the 5% and 10-15% error boundaries, the wavefield can be divided into two zones: Zone I, with almost no near-field effects in the measured phase velocity, and Zone II, where the measured phase velocities are underestimated due to the near-field corruptions. A normalized ACD approximately greater than 1.5 is sufficient to limit errors in the measured phase velocity due to the near-field effect to 5% or less. Additionally, a normalized ACD approximately greater than 1.0 is required to limit the errors in the measured phase velocity due to the near-field effect to 10-15% or less.

By comparing the 1 m and 5 m source offset results in the figure, there is some bias observed between the two source offsets with the 5 m source offset generally having shorter NACD without near-field effects compared to the 1 m source offset. However, similar shorter NACD are observed for some of the 1 m source offset data indicating normal data variability may be causing the observed differences. It is worth mentioning that the errors in the measured phase velocity are not caused by lateral variability in the subsurface layering because, in such a case, values would have been scattered both above and below the expected normalized VR value of 1.0. However, as shown in Figure 4.5, a consistent trend of decrease in normalized phase velocities is observed at low normalized ACDs, indicating clear near-field effects.

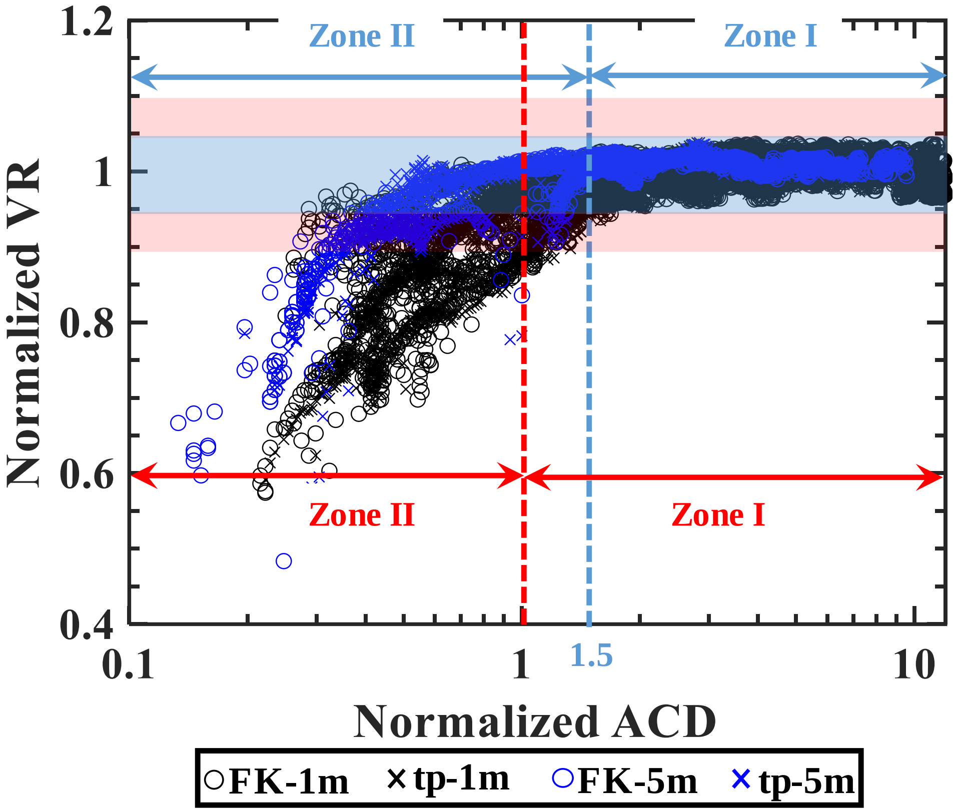

Figure 4.5- Normalized ACD for Rayleigh waves for sites with a very shallow and highly variable impedance contrast.

4.7.1.2 Love type surface waves

4.7.1.2.1 Different transformation techniques

Presented in Figure 4.6 is an example of raw Love wave dispersion curves generated using the four transformation techniques for the Hot Springs site with a very shallow and highly variable impedance contrast. In this figure, it is clear that the four transformation techniques provide different resolutions for the experimental dispersion curve. Similar to Rayleigh waves, the FDBF-cylindrical delivers a considerably longer wavelength dispersion curve than the other transformation methods. Moreover, the PS has a severe resolution issue so that no coherent fundamental mode trend can be determined based on the experimental dispersion data. For more information in this regard, see Rahimi et al. (2021).

To better illustrate the differences between the four transformation techniques, the Love wave dispersion data from the four transformation techniques are combined, and the results are presented in Figure 4.7 along with the theoretical fundamental (L0), first higher (L1), and second higher (L2) modes. The theoretical results were based on forward modeling of downhole measurements and dispersion data measured near the surface wave array. From the zoomed-in view of this figure, the maximum resolved wavelength for the FK and τp methods is 20 m. However, the FDBF-cylindrical provides high-quality dispersion data over the entire range of frequencies with a maximum resolved wavelength of 50 m. Therefore, for Love waves, similar to Rayleigh waves, the FDBF-cylindrical outperforms other transformation methods in terms of near-field effects and dispersion resolution.

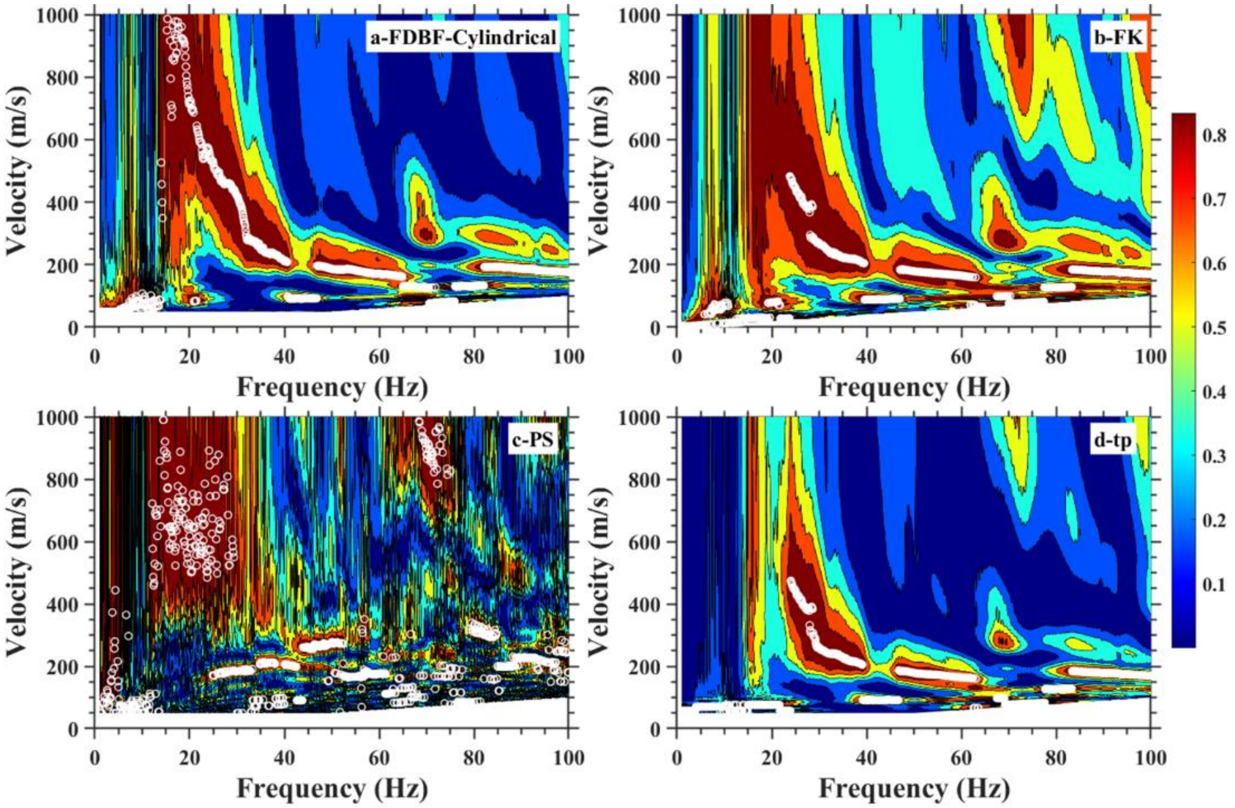

Figure 4.6- Love wave dispersion curves generated using the four transformation methods for the Hot Springs site with a very shallow and highly variable impedance contrast. a) FDBF-cylindrical, b) FK, c) PS, and d) τp.

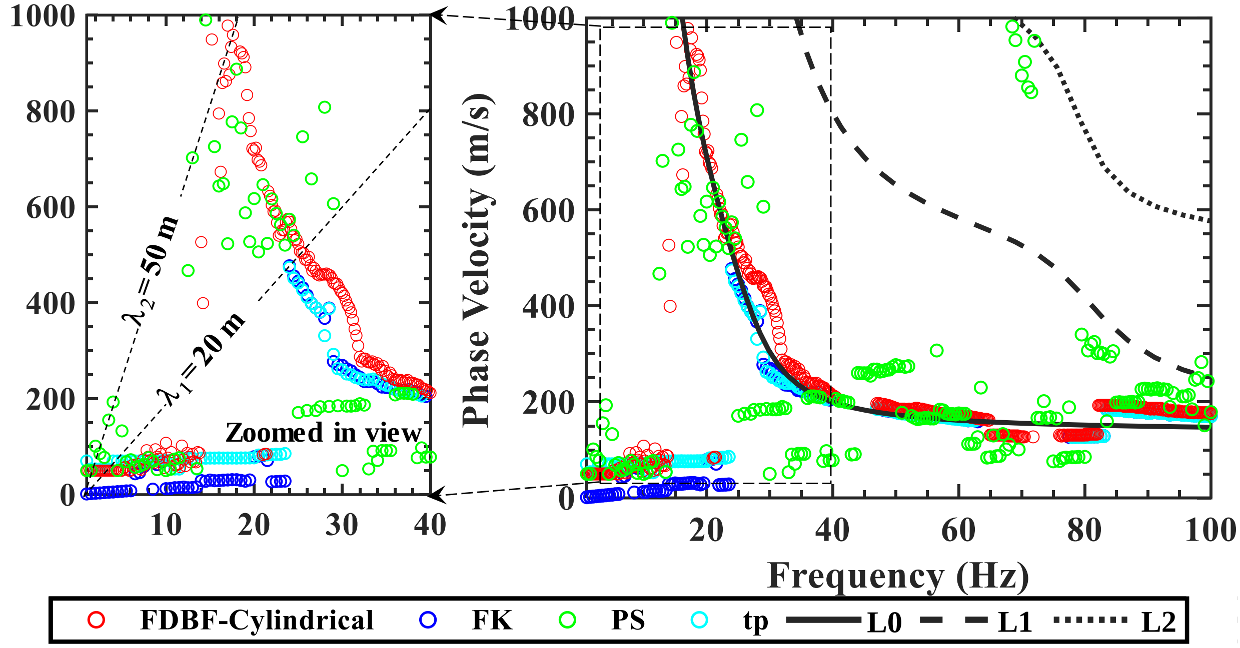

Figure 4.7- Comparison of the near-field effects observed for different transformation techniques. The true fundamental (R0), first higher (R1), and second higher (R2) modes are shown with solid, dashed, and dotted curves, respectively.

4.7.1.2.2 Different source offsets

Data from different source offsets for the same MASW setup presented in Figure 4.6 are processed to examine the impacts of the multiple source offset approach on near-field mitigation. Shown in Figure 4.8 is the Love wave dispersion data generated at different source offsets of 1, 2, and 5 m using the four transformation techniques along with the true fundamental (L0), first higher (L1), and second higher (L2) modes. As observed in this figure, the multiple source offset approach mitigates near-field effects to some extent for the FK and τp methods. For these methods, the dispersion data from the 2 m (blue) and 5 m (green) source offsets extend to lower frequencies than the 1 m source offset. However, even the combined dispersion curves for the FK and τp methods using the multiple source offset approach are not as clear as the FDBF-cylindrical using a single source offset of 1 m. For the PS method, similar to the 1 m source offset, the other source offsets provide very poor quality experimental dispersion data with no clear trend for the fundamental mode. These findings for Love waves correspond well with those for Rayleigh waves in the previous section, highlighting the better performance of the FDBF-cylindrical compared to the other transformation methods considering near-field effects.

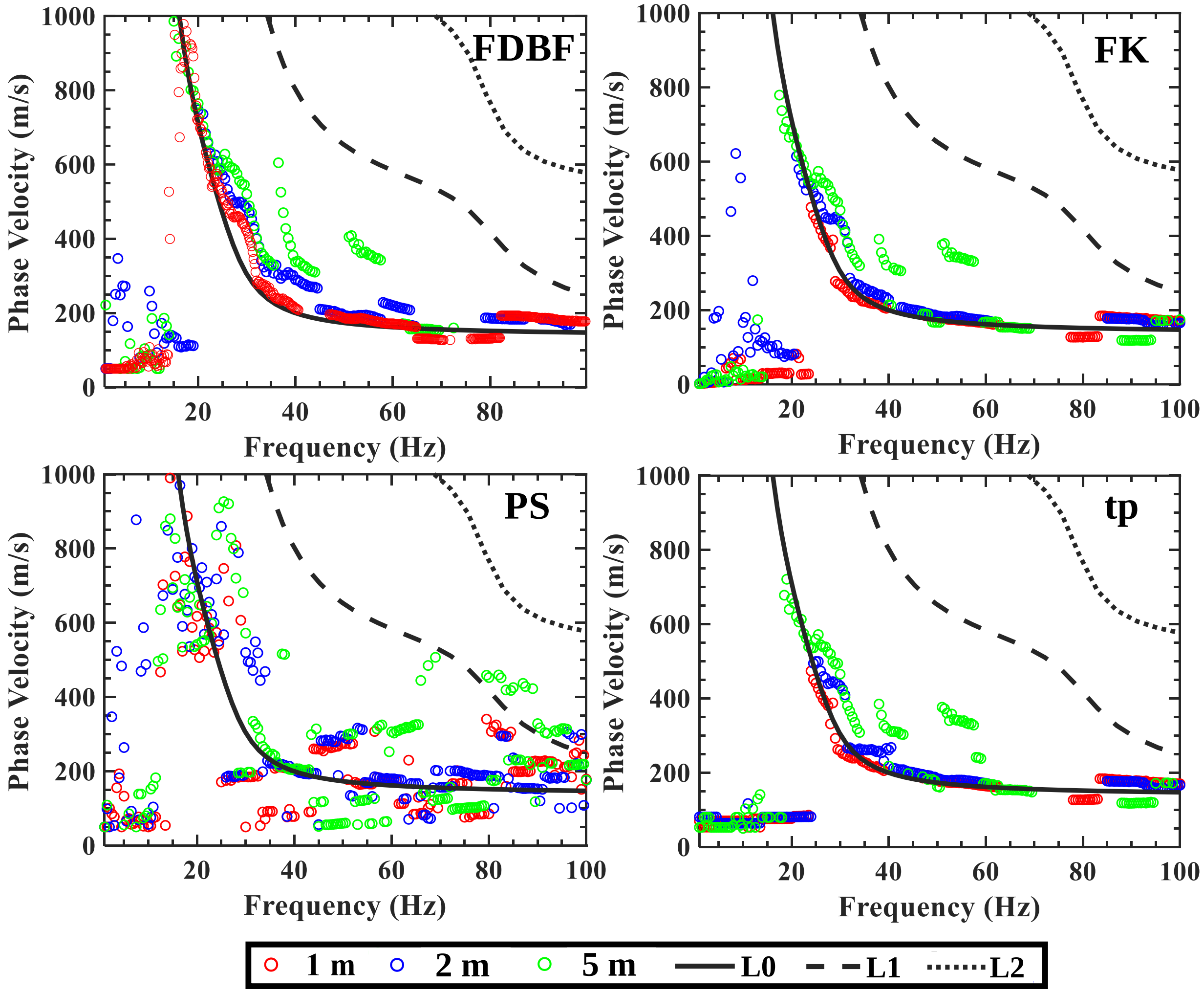

Figure 4.8- Love wave dispersion data points generated using the four transformation methods at different source offsets for the same MASW setup shown in Figure 6. The true fundamental (R0), first higher (R1), and second higher (R2) modes are shown with solid, dashed, and dotted curves, respectively.

Presented in Figure 4.9 is another example of Love dispersion data generated at different source offsets of 1, 2, and 10 m using the four transformation techniques along with the true fundamental (L0), first higher (L1), and second higher (L2) modes. Unlike the previous example in Figure 4.8, where the multiple source offset approach mitigated the near-field effect to some extent for the FK and τp methods, for the MASW setup in Figure 4.9, the dispersion data from 2 m and 10 m source offsets are dominated by effective or higher modes (L1 and L2). Therefore, no data from the fundamental mode (L0) is obtained for the low-frequency portion of the dispersion curve, where near-field corruptions occur, using 2 m and 10 m source offsets. This is consistent with the results from Rayleigh waves in Figure 4.4, indicating that for sites with a very shallow and highly variable impedance contrast, the multiple source offsets approach is not always beneficial for near-field mitigation.

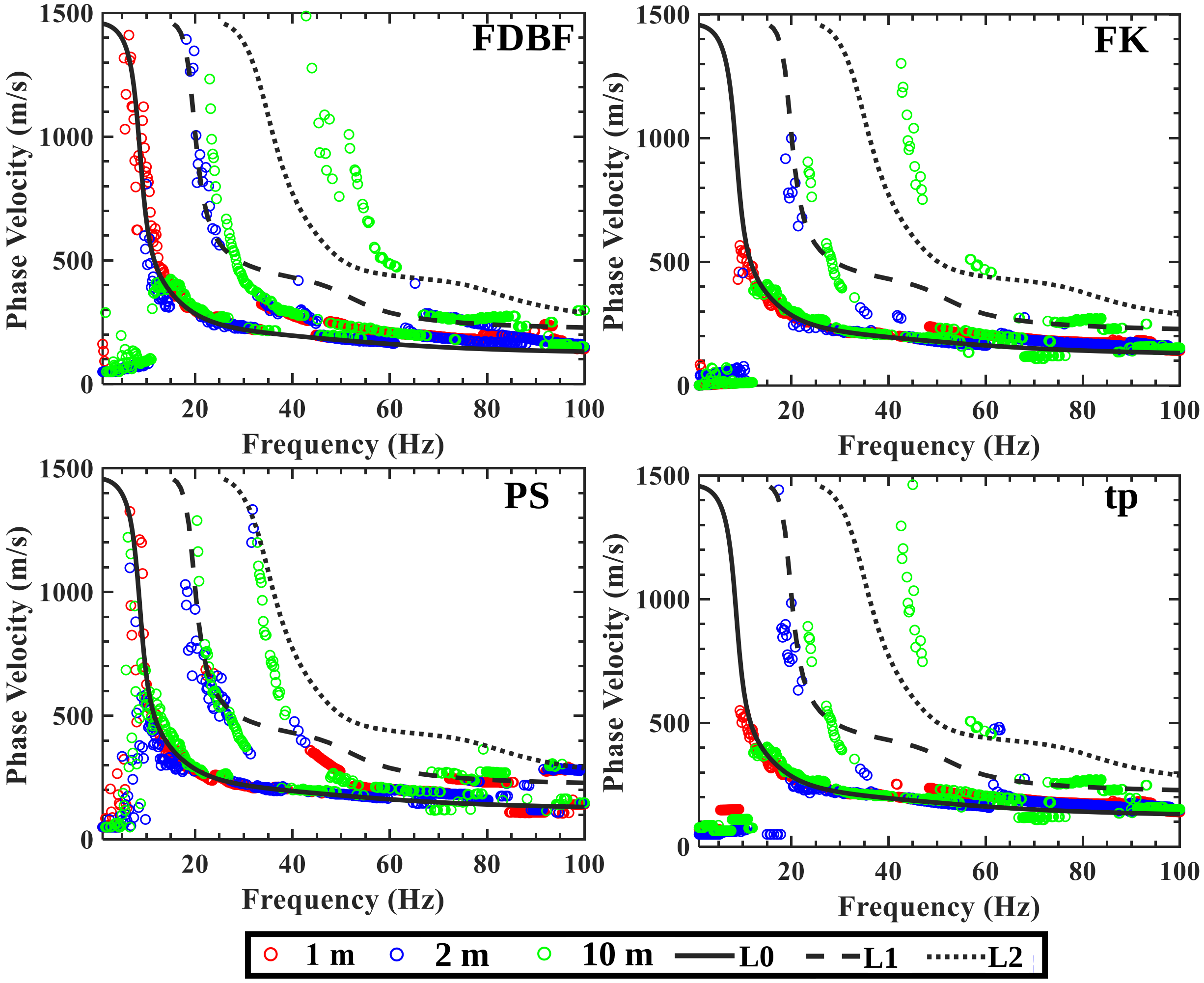

Figure 4.9- Love wave dispersion data points generated using the four transformation methods at different source offsets for the Hot Springs site with a very shallow and highly variable impedance contrast. The true fundamental (R0), first higher (R1), and second higher (R2) modes are shown with solid, dashed, and dotted curves, respectively.

4.7.1.2.3 Threshold normalized ACD

Shown in Figure 4.10 is the normalized ACD plot for Love waves using all the dispersion data for sites with a very shallow and highly variable impedance contrast along with the boundaries and zonations for the 5% (blue) and 10% (red) errors. Data related to different source offsets (1, 5, and 10 m) are marked with different colors in this figure. This plot was generated similar to the procedure explained for Rayleigh waves in the previous section. Similar to Rayleigh waves, the onset of the 5% or 10-15% errors in the measured phase velocity is used to determine the near-field criteria. According to the 5% and 10-15% error boundaries, the wavefield can be divided into two zones: Zone I, with almost no near-field contamination, and Zone II, where the measured phase velocities are significantly underestimated due to near-field effects. According to the field measurement results, a normalized ACD of approximately greater than 1.5 is required to limit errors to 5% or less, and a normalized ACD of approximately greater than 1 is needed to limit errors to 10-15% or less. These zonations are the same as those determined for Rayleigh waves in the previous section. It is also observed that the source offset does not play a significant role in the NACD criteria when the data is normalized by the ACD.

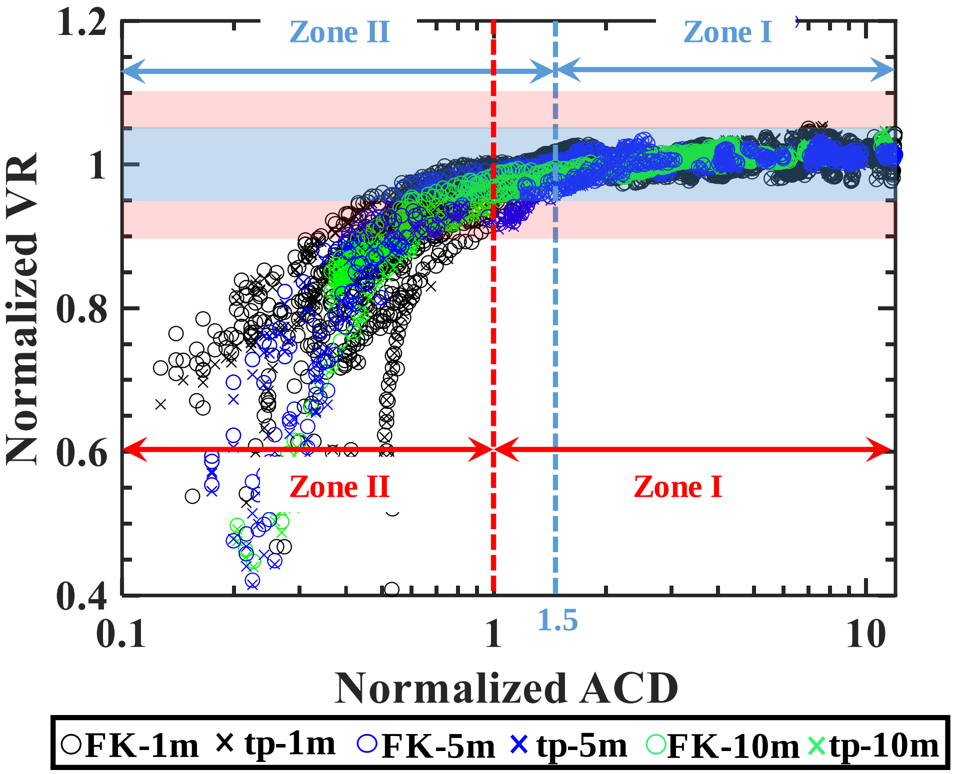

Figure 4.10- Normalized ACD for Love waves for sites with a very shallow and highly variable impedance contrast.

4.7.2 Near-field effects for sites with a very deep impedance contrast

This section details the near-field effects for sites with a very deep impedance contrast, as listed in Table 4. For these sites, similar performance is observed for the four transformation techniques (for both Rayleigh and Love waves) in terms of near-field effects and dispersion resolution. As an example, the Rayleigh wave dispersion data generated using the four transformation techniques for the Aubery site with a very deep impedance contrast (1110 m) is presented in Figure 4.11. According to this figure, the same dispersion data are obtained for the entire range of frequencies using the four transformation methods. This behavior at sites with a very deep impedance contrast is also observed and confirmed in previous studies (J. Li & Rosenblad, 2011; Rahimi et al. 2021). More information in this regard is provided in Rahimi et al. (2021). Therefore, in this section, the performance of the four transformation techniques regarding near-field mitigation is not discussed, given that each provides nearly identical experimental dispersion data when only considering near-field effects.

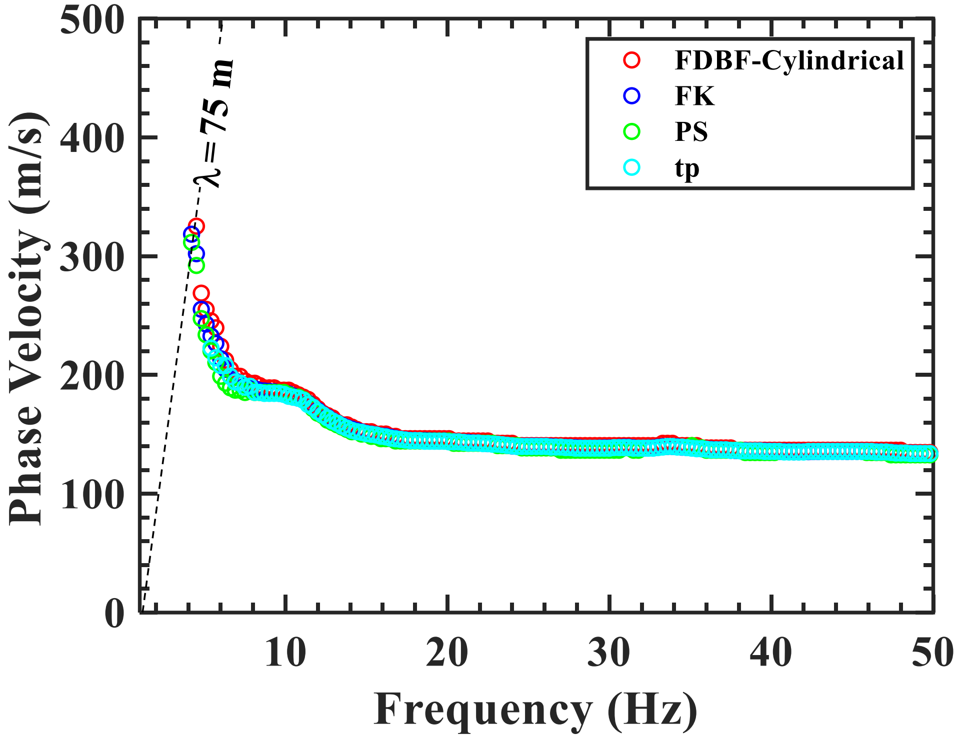

Figure 4.11- Rayleigh wave dispersion data from the four transformation methods for the Aubrey site with a very deep impedance contrast.

4.7.2.1 Rayleigh type surface waves

4.7.2.1.1 Different source offsets

The Rayleigh wave dispersion data generated at different source offsets of 2, 5, 10, 20, and 40 m, along with passive dispersion data (i.e. true phase velocity) for four sites with a very deep impedance contrast (Aubery, Marmaduke, Palestine, and Monette) are provided in Figure 4.12. Additionally, the maximum resolved wavelength for each source offset is also provided in this figure. Passive surface wave testing was performed for these sites using large diameter (50-500 m) circular arrays and processed using the HRFK and MSPAC methods to estimate the true phase velocity and identify active data contaminated with near-field effects. The passive dispersion data are presumed free from near-field effects as their sources are located far away from the receiver array, ensuring pure planar surface waves within the wavefield. Information regarding the data processing of the passive surface wave testing for these sites is provided in Himel and Wood (2021) and Wood et al. (2019). It should be mentioned that all the active dispersion data in Figure 4.12, which were generated using a sledgehammer source, are associated with a signal to noise ratio greater than the recommended cutoff value of 10 decibels (dB) (Wood *et al.*, 2012) even at very low frequencies (i.e. 3-5 Hz).

As shown in Figure 4.12, the dispersion data from the 2 m source offset demonstrates clear near-field effects at very short wavelengths, varying between 14-21 m. Clear near-field effects are also observed for the 5 m source offsets at wavelengths ranging between 32-55 m. The 10 and 20 m source offsets resulted in the longest wavelengths ranging between 44-71 and 44-140 m, respectively. For the 40 m source offset, while it is expected to obtain the longest wavelength compared to the other (shorter) source offsets, phase velocities are overestimated at short wavelengths for the Marmaduke, Palestine, and Monette sites indicating the likely influence from far-field effects due to attenuation of wave energy. Overall, the multiple source offset approach is observed to mitigate near-field effects up to a certain distance from the first geophone. The 20 m source offset is observed to be the most effective as it emulates the passive data quite well and provides the highest resolved wavelength.

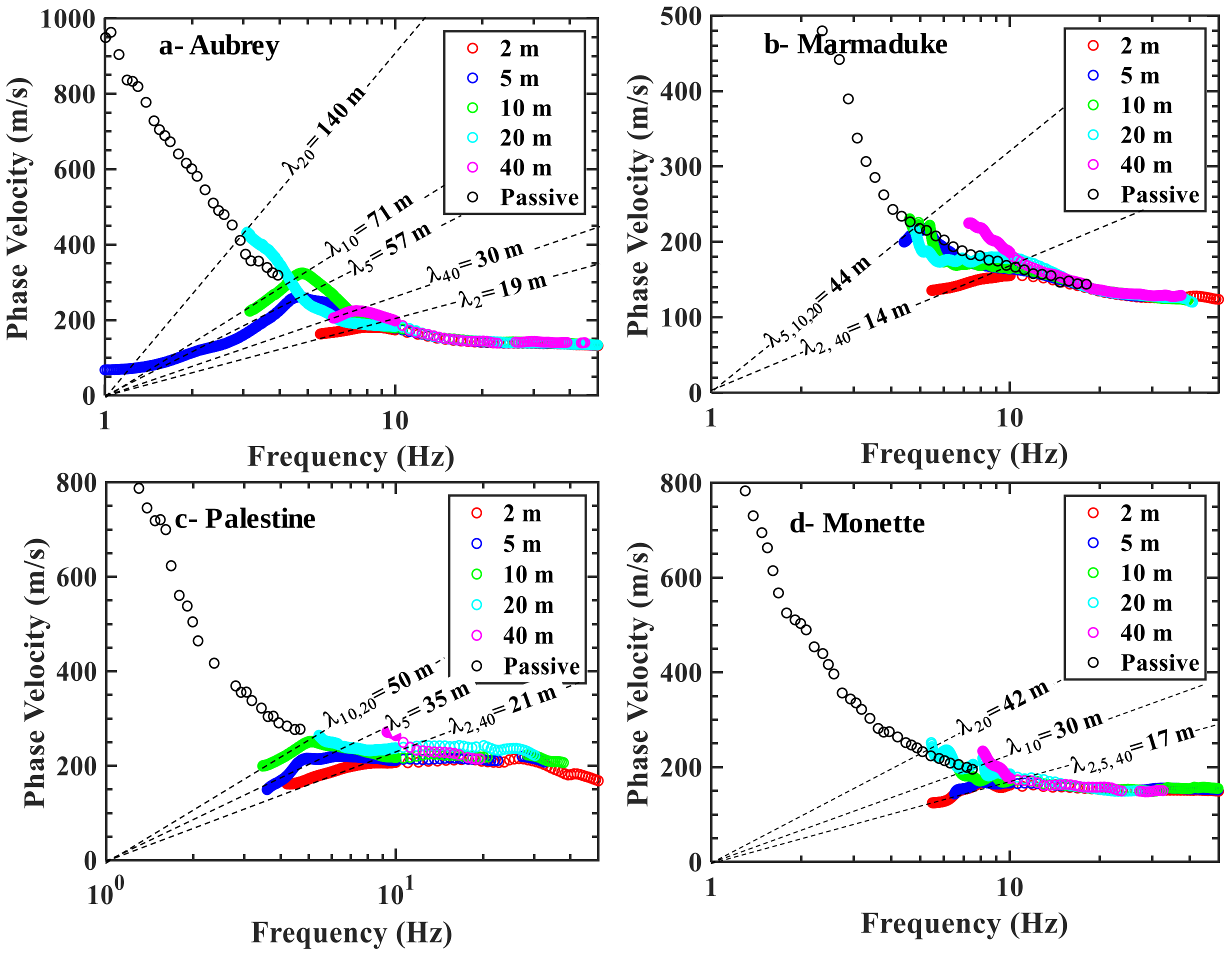

Figure 4.12- Active Rayleigh wave dispersion data generated at different source offsets along with the passive data for sites with a very deep impedance contrast. a) Aubrey, b) Marmaduke, c) Palestine, d) Monette.

4.7.2.1.2 Threshold normalized ACD

The Rayleigh dispersion data generated at different source offsets from all the sites with a very deep impedance contrast are combined, and the results are shown in Figure 4.13a to define some practical guidelines regarding near-field mitigations. Additionally, for each source offset except for 40 m, the power regression curve fitted through the experimental data is presented in Figure 4.13b. The 40 m source offset is not included in Figure 4.13b because the errors in the dispersion data of this source offset are related to effects other than near-field. The normalized phase velocity was computed as the ratio of the measured active phase velocity (i.e. MASW) to the passive (true) phase velocity (i.e. HRFK or SPAC) at frequencies where the active and passive data overlap.

In Figure 4.13a, different markers and colors are used for data generated at different source offsets to be able to differentiate between them. In addition, the 5% and 10% error boundaries and zonations are shown with blue and red colors, respectively. From Figure 4.13a and b, the majority of the data with significant near-field contamination are associated with the 2 and 5 m source offsets, while longer offsets tend to be associated with shorter normalized ACD when exceeding the 5% and 10-15% boundaries. This indicates that the ACD normalization corrects for much of the differences in array geometry but does not account for all the differences when considering different source offsets. The shorter 2 m source offset results in poorer near-field performance than observed with the other longer source offsets.

Overall, based on the 5% and 10-15% error boundaries and the results obtained from the field measurements, the wavefield can be divided into two main zones regarding near-field effects: Zone I with negligible near-field effects and zones II with considerable underestimation in the measured phase velocity due to the near-field contaminations. Based on the field measurement results, a normalized ACD of approximately greater than 1.5 is sufficient to limit errors to 5% or less, and a normalized ACD of approximately greater than 1 is sufficient to limit errors to 10-15% or less.

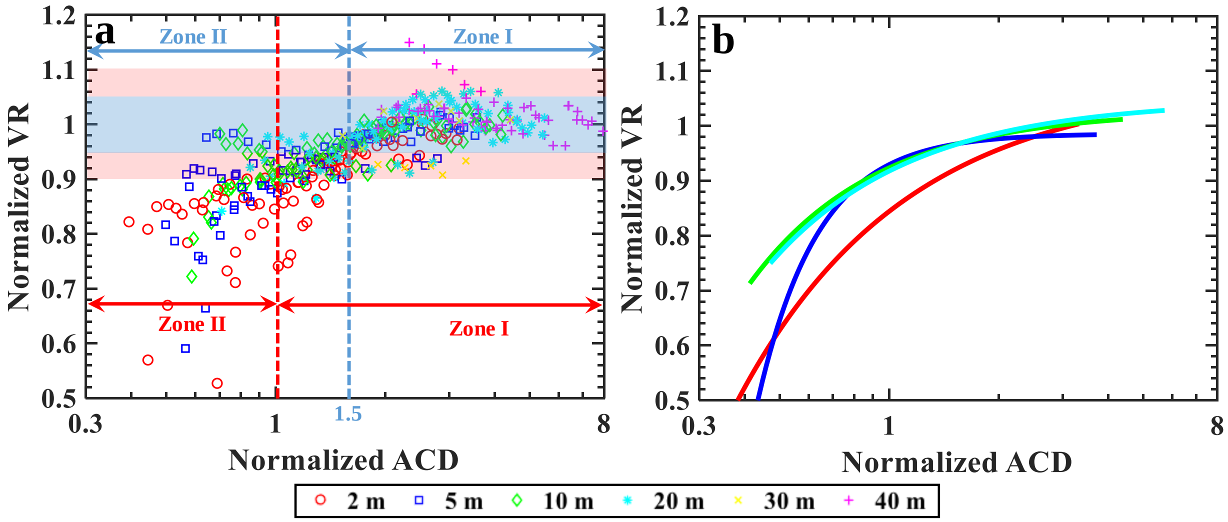

Figure 4.13-Normalized ACD for Rayleigh waves for sites with a very deep impedance contrast. a) experimental dispersion data, b) power regression curve for each source offset.

4.7.2.1.3 Influence of source type (sledgehammer versus vibroseis) on near-field effects

To investigate the influence of source type on near-field effects, Rayleigh dispersion data were generated using the co-located sledgehammer and vibroseis source for several of the sites with clear near-field effects (see Table 4). Here only the Wynne site results are presented as an example to investigate the effects of source type. For the Wynne site, the only difference between the sledgehammer and vibroseis measurements was array length (46 m for a sledgehammer and 92 m for vibroseis), meaning that the two arrays sample different regions of the ground. This difference is not expected to alter the experimental dispersion data, given that the Wynne site consists of a thick and homogenous soil profile (i.e. a very deep impedance contrast) with no lateral variability. However, to verify this claim, the vibroseis data were processed using two different suites of geophones: vibroseis1 using geophones 1-24 (96 m array length) and vibroseis2 using geophones 1-12 (46 m array length). Therefore, the regions of the ground sampled by the vibroseis2 array are identical to the sledgehammer.

Shown in Figure 4.14 are the Rayleigh dispersion data generated using the sledgehammer, vibroseis1, and vibroseis2, along with the passive data for the Wynne site with a very deep impedance contrast (850 m). In this figure, it is clear that the dispersion data from the vibroseis1 and vibroseis 2 are almost identical (with slight differences in the measured phase velocities), verifying that array length does not influence the dispersion data of this site. The phase velocity differences observed between vibroseis1 and vibroseis 2 are negligible as these differences are within the generally accepted standard deviation (10%).

From Figure 4.14, apparent near-field effects are observed for the 2 m and 5 m sledgehammer source offsets in the form of roll-off in the measured phase velocity. Comparing the sledgehammer versus vibroseis dispersion data, it is clear that the near-field effects are reduced using a vibroseis source. For instance, for the 5 m source offset, the sledgehammer data are corrupted by near-field effects for wavelengths greater than 21 m, but the vibroseis provides dispersion data up to 120 m wavelengths with only a slightly lower velocity than observed in the passive dispersion data. Therefore, near-field effects can be mitigated to some extent using a high-energy harmonic source (i.e. vibroseis). This is because, for such sources, waves are generated harmonically with each frequency tested individually (stepped-sine), meaning that a single dominant waveform that propagates in-line with the array is produced in each step.

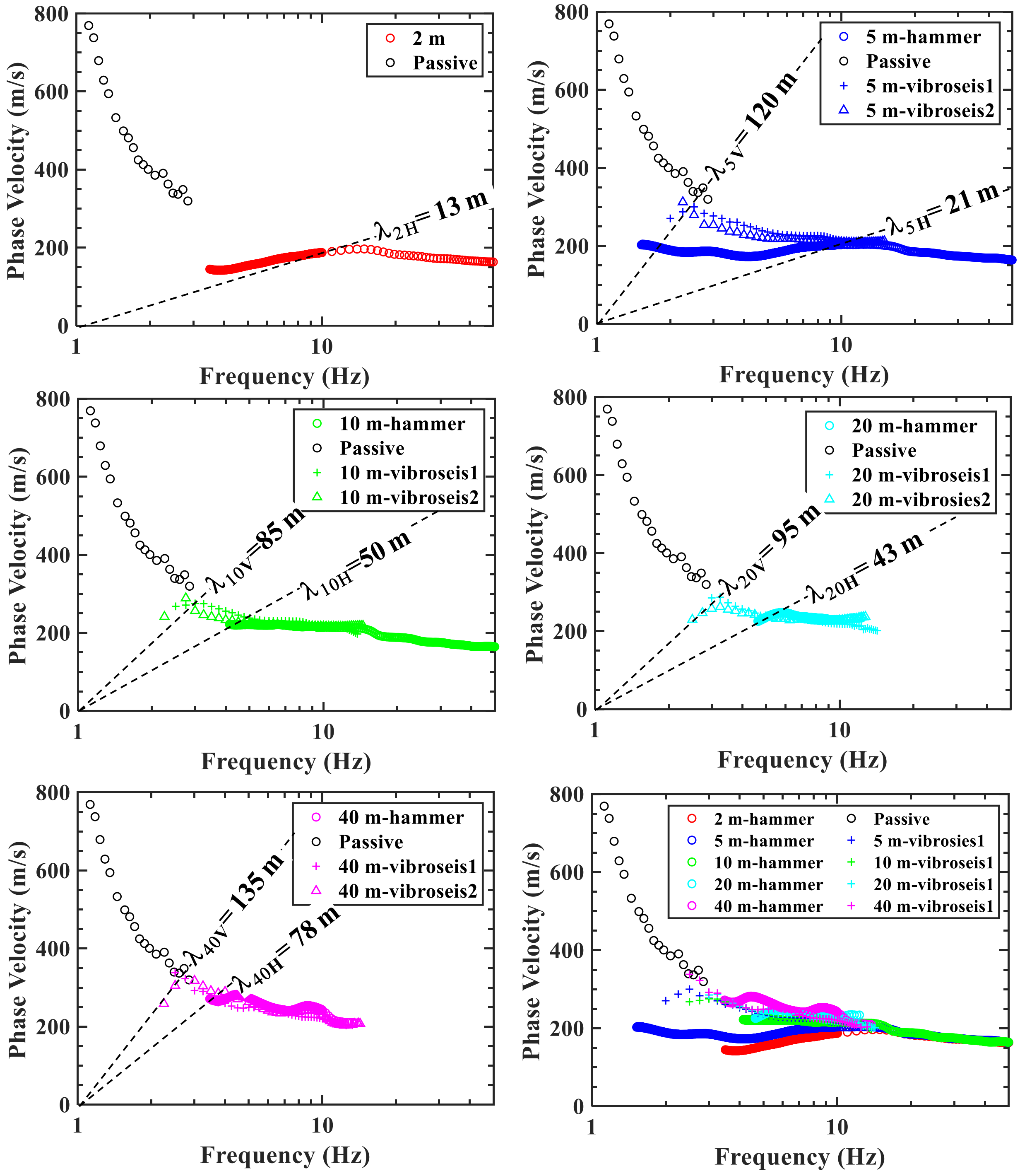

Figure 4.14- Active Rayleigh dispersion data generated using a sledgehammer and vibroseis source for the Wynne site with a very deep (850 m) impedance contrast (hammer: 24 geophones with 2 m spacing, vibroseis1: 24 geophones with 4 m spacing, vibroseis2: 12 geophones with 4 m spacing).

Data from several sites with a vibroseis source, as listed in Table 4, were used to define the normalized ACD criterion for near-field mitigation when using a vibroseis source, and the results are provided in Figure 4.15. Additionally, the 5% and 10% error boundaries and zonations are shown with blue and red colors, respectively. The normalized phase velocity was calculated as the ratio of the active phase velocity (with near-field effects) measured using the vibroseis source to the passive (true) phase velocity (i.e. HRFK or SPAC) at frequencies where the active and passive data overlap. Based on Figure 4.15, for active surface wave testing using a vibroseis source, a normalized ACD of approximately greater than 0.6 is recommended to limit the errors due to the near-field to 5% or less, and a normalized ACD of approximately greater than 0.5 is required to limit errors to 10-15 %. These criteria are less restrictive than those defined for Rayleigh waves using a sledgehammer source.

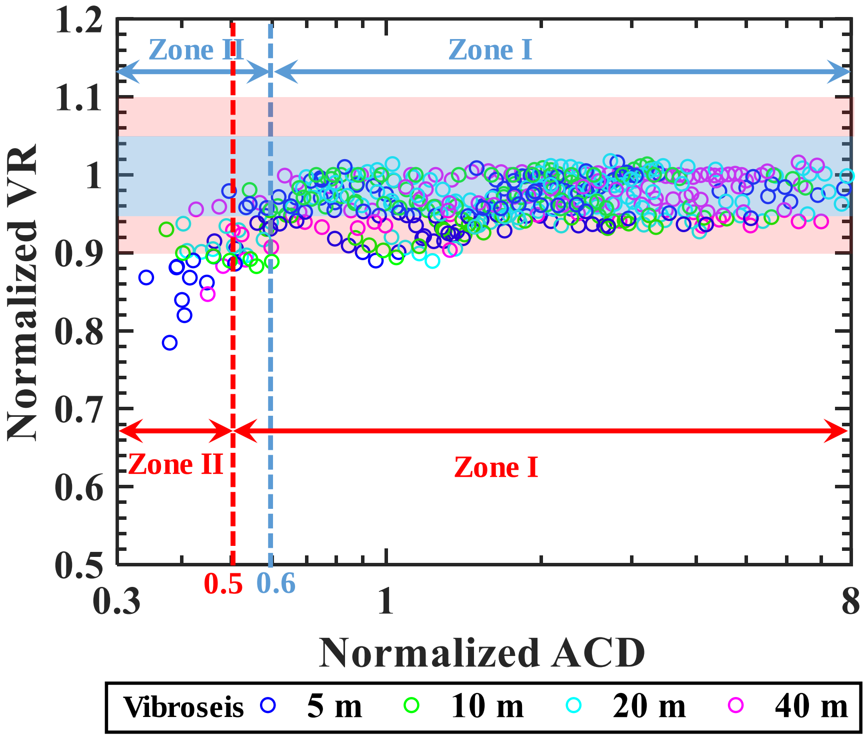

Figure 4.15- Normalized ACD for Rayleigh waves for sites with a very deep impedance contrast using vibroseis source.

4.7.2.2 Love type surface waves

4.7.2.2.1 Different source offsets

For Love type surface wave testing for sites with a very deep impedance contrast, surface wave testing was performed at four different source offsets of 5, 10, 20, and 40 m. Shown in Figure 4.16 are the active Love wave dispersion data (i.e. MASW) generated at different source offsets along with the passive dispersion data for four sites with a very deep impedance contrast. These sites include Fontaine, MacDougal, Aubrey, and Earle, as shown in Figure 4.16a, 15b, 15c, and 15d, respectively. All the active dispersion data shown in Figure 4.16 are associated with a signal-to-noise ratio higher than the cutoff value of 10 dB (Wood *et al.*, 2012). The passive dispersion data represents the true phase velocity at low frequencies. For the 5 m and 10 m source offsets in this figure, clear near-field effects are observed at short wavelengths, ranging between 30-42 m. The near-field effects appear in the shape of roll-off in the measured phase velocity. The 20 m source offset provides the highest resolution experimental dispersion data with maximum resolved wavelengths ranging between 55-82 m. For the 40 m source offset, high-resolution dispersion data are obtained only for the Fontaine site. However, for the rest of the sites, the phase velocities are underestimated or overestimated using the 40 m source offset at very short wavelengths (19-46 m). Overall, the observations of this section for Love waves are in good agreement with those observed in the previous section for Rayleigh waves..

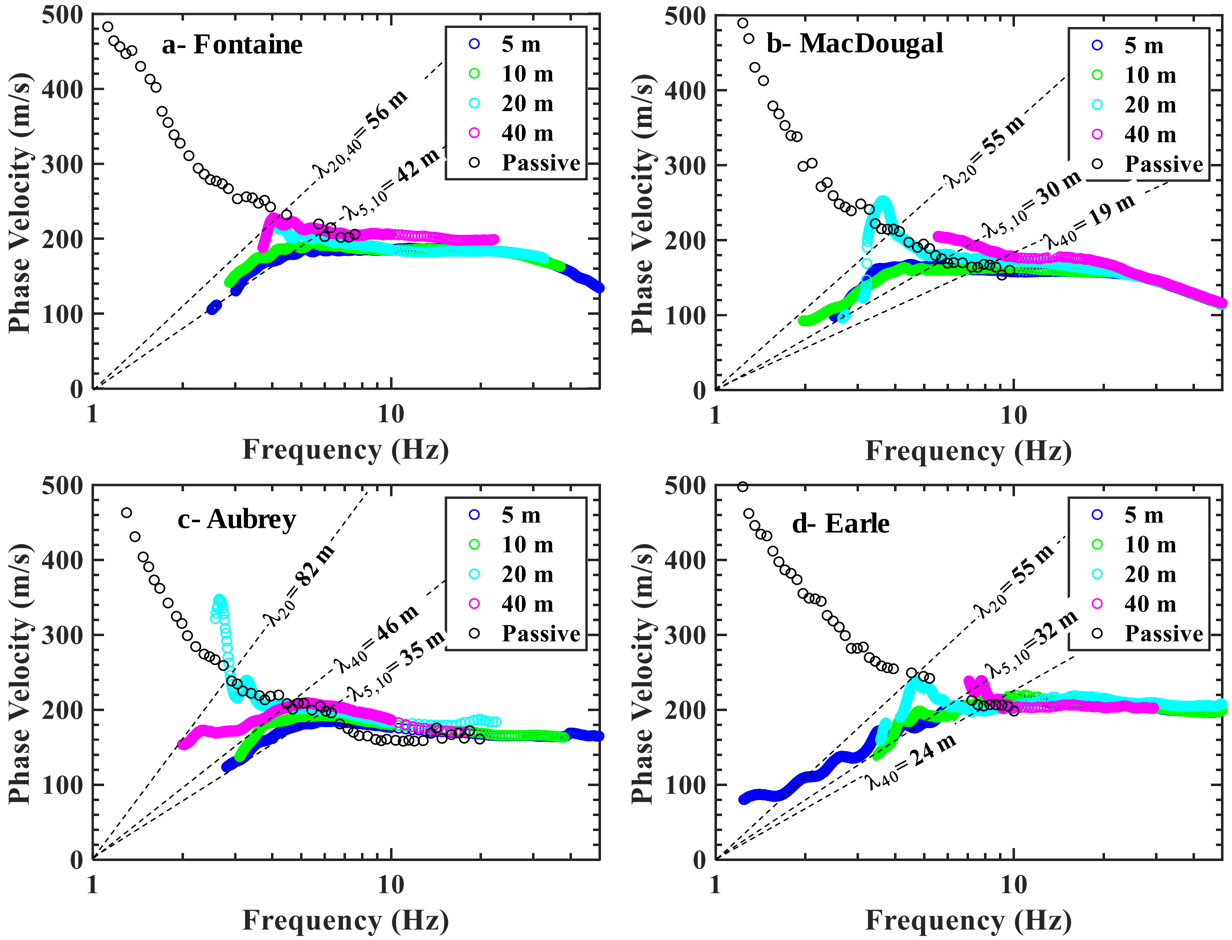

Figure 4.16- Active Love dispersion data generated at different source offsets along with the passive data for sites with a very deep impedance contrast. a) Fontaine, b) MacDougal, c) Aubrey, d) Earle.

4.7.2.2.2 Threshold normalized ACD

Presented in Figure 4.17a is the normalized ACD plot for Love waves using data from all sites with a very deep impedance contrast at frequencies where active and passive dispersion data overlap. Moreover, the zonations and boundaries related to 5% and 10% errors are shown with blue and red colors, respectively. Using the experimental data from Figure 4.17a, the power regression curve for each source offset (except for 40 m) was generated, and the results are presented in Figure 4.17b. In Figure 4.17a, data related to different source offsets are shown using different markers and colors. Using the 5% and 10-15% error boundaries, the wavefield can be divided into two zones with respect to near-field effects: Zone I with no considerable near-field effects, and Zone II with clear near-field effects that lead to underestimating the measured phase velocity.

From Figure 4.17a, errors due to the near-field effects can be limited to 5% or less using a normalized ACD greater than 1.5, and errors can be limited to less than 10-15% using a normalized ACD greater than 1.0. These normalized ACD criteria are consistent with those determined for Rayleigh waves for sites with a very deep impedance contrast when using a sledgehammer source. For Figure 17b, similar NACD results are observed for each source offset with the 20 m source offset, resulting in slightly better performance at short NACD than the 5 m and 10 m source offsets.

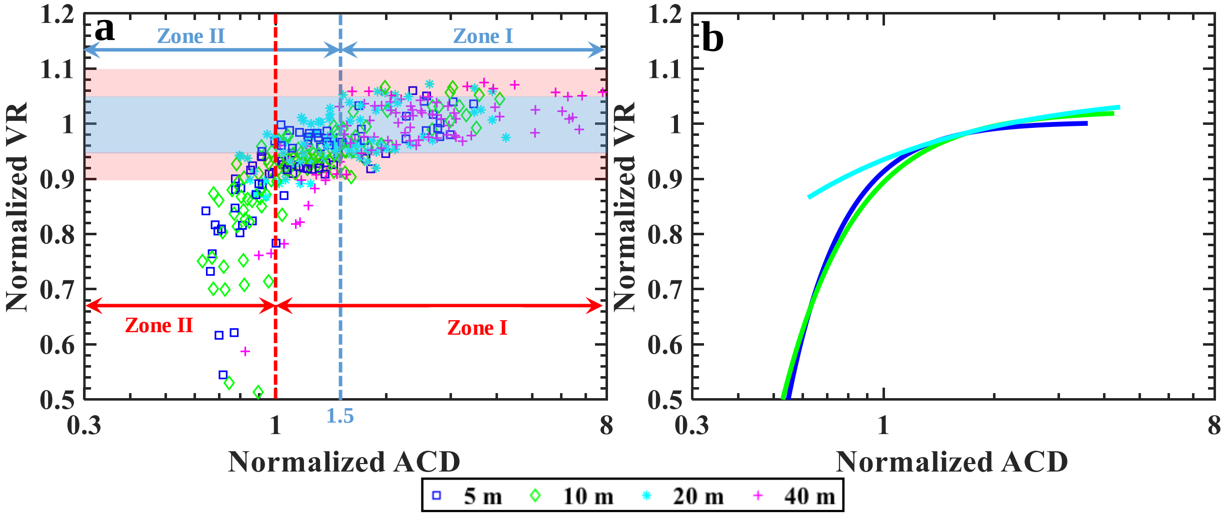

Figure 4.17- Normalized ACD for Love waves for sites with a very deep impedance contrast. a) experimental dispersion data, b) power regression curve for each source offset.

4.8 Discussions

Presented in Table 5 is a summary result of the normalized ACD criteria for near-field mitigation of Rayleigh and Love type surface waves for sites with a very shallow and highly variable (< 30 m) impedance contrast and sites with a very deep (> 250 m) impedance contrast using sledgehammer and vibroseis sources. The 5% and 10-15% error boundaries were used to define the suitable normalized ACD criteria for near-field mitigation. These error boundaries are similar to those used in the previous studies (Yoon *et al.*, 2009; Li *et al.*, 2011), allowing to compare the findings of this study with the previous investigations.

According to the obtained results, the normalized ACD criteria for near-field mitigation of Rayleigh and Love type surface waves and for sites with very shallow and very deep impedance contrasts are identical. This indicates that the normalized ACD criteria for near-field mitigation are independent of surface wave type and depth to the impedance contrast. However, the source type is determined to be an important factor influencing the normalized ACD criteria for near-field mitigation.

For a sledgehammer source, the normalized ACD criteria for near-field mitigation include (1) a normalized ACD greater than 1.5 to limit errors in the measured phase velocity due to the near-field contaminations to 5% or less and (2) a normalized ACD greater than 1.0 to limit errors to 10-15% or less. On the other hand, for a vibroseis source, the normalized ACD criteria for near-field mitigation include (1) a normalized ACD greater than 0.6 to limit errors to 5% or less and (2) a normalized ACD greater than 0.5 to limit errors to 10-15% or less. It should be highlighted that the active surface wave testing using a vibroseis source was only conducted for

Rayleigh waves for several sites with very deep impedance contrast (see Table 4). However, a similar normalized ACD criterion is expected for other conditions (i.e. for Love waves or for sites with a very shallow impedance contrast) since the normalized ACD criteria are determined to be independent of surface wave type and depth to the impedance contrast. Therefore, the normalized ACD criteria determined for Rayleigh waves for sites with a very deep impedance contrast using a vibroseis source are valid for the other conditions

Table 5- Practical criteria for near-field mitigation during field measurements.

Impedance contrast	**Source type**	**Surface wave type**	**Less than 10-15% error due to near-field effects**	**Less than 5% due to the near-field effects**
Very shallow and highly variable	Hammer	Rayleigh	NACD[1] > 1.0	NACD > 1.5
Very shallow and highly variable	Hammer	Love	NACD >1.0	NACD >1.5
Very deep	Hammer	Rayleigh	NACD > 1.0	NACD > 1.5
Very deep	Hammer	Love	NACD > 1.0	NACD > 1.5
Very deep	Vibroseis	Rayleigh	NACD > 0.5	NACD > 0.6

[1] Normalized ACD

In order to compare the criteria of the current study with the previous investigations, the 5% error is considered because Li and Rosenblad (2011) only used the 5% error boundary to define the near-field mitigation criteria. For a sledgehammer source, the normalized ACD criterion defined in this study based on the 5% error (a normalized ACD of 1.5) is slightly less restrictive than the recommended value by Yoon and Rix (2009) (a normalized ACD of 2). However, these two criteria are significantly different from Li and Rosenblad's (2011) findings, which suggest a normalized ACD of 0.5. Li and Rosenblad (2011) have claimed that the discrepancy in their normalized ACD criterion is likely due to the high Poisson’s ratio of their study areas compared to the Yoon and Rix (2009) investigation. However, according to the results of this study, the high Poisson’s ratio is not the primary reason for the discrepancy. This is because the normalized ACD criterion defined in this study for sites with a very deep impedance contrast and sledgehammer source (NACD of 1.5) also consist of sediments with high Poisson’s ratios (i.e. shallow water table, see Table 4), but this criterion is significantly different from Li and Rosenblad (2011) normalized ACD criterion (NACD of 0.5). Therefore, other reasons are behind this discrepancy in the normalized ACD criteria. Comparing all the key characteristics of Li and Rosenblad's (2011) study and this investigation reveals that the two main differences include (1) array length and (2) source type.

The first main difference between the two studies is the array length. Li and Rosenbald (2011) used different array lengths, most of which are longer arrays compared to this study. However, this should not be a primary reason behind the discrepancy in the normalized ACD for two reasons. First, the array length is important for heterogeneous sites with an irregular soil profile where subsurface layers are highly variable within short distances. However, the sites tested in Li and Rosenblad (2011) and the current study consist of an almost homogenous soil profile and a very deep impedance contrast within the tested arrays. The fact that array length does not alter the dispersion data significantly for these sites is also confirmed by the experimental data in Section 4.7.2.1.3, where the experimental dispersion data generated using vibroseis1 with a 46 m array length and vibroseis2 with a 96 m array length were observed to be nearly identical for the Wynne site. Second, in both studies, the normalized ACD parameter is used instead of array length to investigate near-field effects. In other words, the array length is normalized by the measured wavelength to remove the effects of array length on the near field effect. Therefore, the difference in array length is not the primary reason for the discrepancy in the normalized ACD criteria observed in this study and Li and Rosenbald's (2011) study.

The second main difference between the two studies is the source type. In Li and Rosenbald's (2011) study, surface waves were generated using a high-output vibroseis source. However, in this study, a low-output sledgehammer source was primarily used for surface wave testing, with a vibroseis source used at some sites. It should be mentioned that Yoon and Rix (2009) also used a small electromagnetic shaker as the source for their field measurements, but their source was a low-output source compared to the vibroseis used in Li and Rosenblad (2011) and this study. The source type is an important factor influencing the surface wave results because, for a high-output vibroseis source, waves are generated harmonically with each frequency tested individually (stepped-sine), meaning that it produces a single dominant wave (with a particular frequency) at each step. However, the low-output sledgehammer source is impulsive and generates waves with different frequencies all at once. Therefore, contributions of body waves, off-line noise, and/or higher modes for the high-output vibroseis and low-output sledgehammer sources may be significantly different.

The source type is believed to be the primary reason behind the differences observed in the normalized ACD criteria. To verify this claim, surface waves were generated using sledgehammer and vibroseis source types for several of the sites tested in this study (see Table 4). Two different normalized ACD criteria are developed from these measurements, one for a sledgehammer and one for a vibroseis source, and the summary results are presented in Table 5. According to this table, the normalized ACD criterion developed in this study using a vibroseis source (a normalized ACD of 0.5) is identical to the criterion proposed by Li and Rosenblad (2011). However, the normalized ACD criterion developed in this study using a sledgehammer source (a normalized ACD of 1.5) is significantly different than the criterion proposed by Li and Rosenblad (2011). This indicates the influence of source type on the normalized ACD criteria required for near-field mitigation.

To clearly illustrate this point, the normalized ACD plots generated using the co-located sledgehammer and vibroseis source for the Wynne site are presented in Figure 4.18. In this figure, it is observed that while the normalized ACD criterion defined using the sledgehammer data is approximately 1.5, for the vibroseis data, the normalized ACD criterion is approximately 0.5 (similar to the normalized ACD of Li and Rosenblad, 2011). This indicates that the discrepancy in the normalized ACD criterion determined by Li and Rosenblad (2011) versus the current study is mainly caused by the source type used for surface wave generation, not the Poisson’s ratio value. When a low-output source such as a sledgehammer is used, the near field occurs at a greater normalized ACD (shorter wavelengths) than a high-output source because, in such a condition, the contributions of the body waves, off-line noise, and different modes that propagate within the array increase.

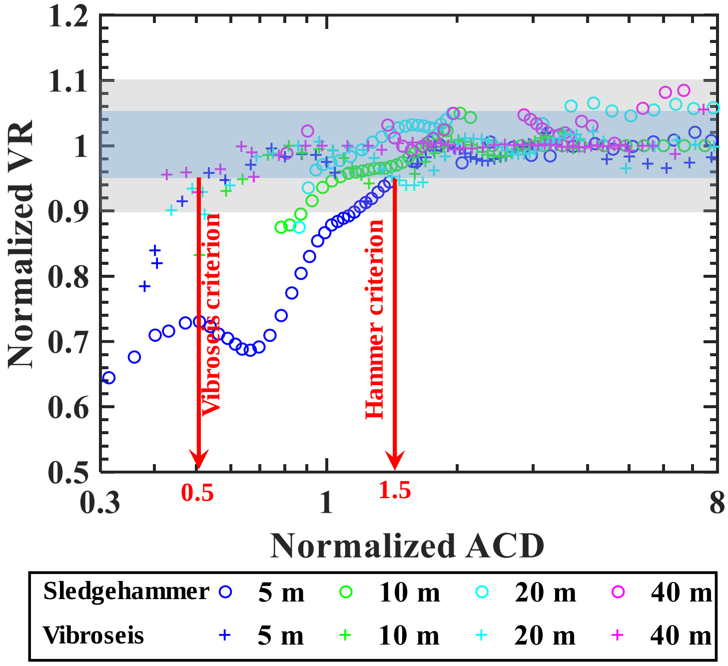

Figure 4.18- Comparing normalized ACD for the sledgehammer and vibroseis source for the Wynne site.

Another point that needs to be highlighted is the capability of different source offsets for near-field mitigation. While some researchers and practitioners commonly use short source offsets (i.e. 2 and 5 m), these source offsets are often contaminated with near-field effects, leading to an underestimated shear wave velocity. Therefore, relying only on such short source offsets could lead to a significant underestimation of subsurface layer properties.

The most suitable source offset for near-field mitigation is a complex function of normalized ACD criteria, subsurface conditions, source type, and array length. Based on the results of this study, shorter source offsets are generally desirable for sites with a very shallow impedance contrast compared to sites with a very deep impedance contrast. This is because, for sites with a very shallow impedance contrast, effective and higher modes dominate dispersion data of long source offsets (e.g. Figure 4.9). Given that identifying the most suitable source offset is a complex function of several parameters mentioned above, the multiple source offset approach is recommended to use. The multiple source offset approach is very beneficial for active surface wave testing because when using this method: (1) the near-field effects can often be mitigated using the composite dispersion data, (2) the normalized ACD criteria can be violated for some of the source offsets as long as others meet the criteria, (3) the true fundamental mode trend can be identified by eliminating data related to near-field effects along with effective and higher modes, (4) higher modes can be identified if needed for multimodal inversion, (5) and the reliability of the experimental data can be improved through the composite dispersion curve. When using the multiple source offset approach, at least three different source offsets located 2-20 m away from the array are recommended. Practitioners can use this method as an effective, rapid, low-cost, and straightforward technique to minimize the near-field effects on active surface wave testing.

Overall, considering the 10-15% error boundary, a normalized ACD of 1.0 should be used as the practical criterion for near-field mitigation of active surface wave testing when using a sledgehammer source. For active surface wave testing using a vibroseis source, a less restrictive normalized ACD of 0.5 should be used as the practical criterion for near-field mitigation. These criteria should not be violated when a limited number of source offsets (1 or 2) are used for active surface wave testing. However, when the multiple source offset approach is employed (> 3 different source offsets), these criteria can be violated to some extent given that a range of normalized ACD is observed to be associated with the 10-15% error boundary (e.g. see Figure 4.5 and Figure 4.10). It should be highlighted that in this study, the 10-15% error boundary is used to define the final practical criteria for near-field mitigation. This is because the 5% error in the measured phase velocity is typically within the normal dispersion data uncertainty from surface wave methods. Therefore, the 10-15% error boundary should be used as the most suitable error boundary for defining the practical criteria for near-field mitigation.

4.9 Conclusions

This study examines the near-field effects for array-based active surface wave methods considering different subsurface conditions, source offsets, surface wave types (Rayleigh or Love), and various transformation techniques that are used for data processing. According to the results of the extensive field measurements, the following practical guidelines are recommended to mitigate near-field effects on array-based active surface wave methods.

1- Near-field effects are observed to be independent of surface wave type (i.e. Rayleigh or Love type surface waves). Accordingly, the normalized array center distance criteria for near-field mitigation of Rayleigh and Love waves were observed to be the same. Therefore, all the recommendations provided below apply to both Rayleigh and Love type surface waves.

2- Near-field effects are observed to be independent of depth to the impedance contrast [i.e. very shallow (~< 30 m) versus very deep sharp (~> 100 m) impedance contrasts]. In this regard, the normalized array center distance criteria for near-field mitigation of sites with very shallow and very deep sharp impedance contrasts were observed to be similar. Therefore, all the recommendations provided below apply to both sites with very shallow and very deep impedance contrasts.

3- For sites with a very shallow impedance contrast within the target depth of surface wave testing (~< 30 m), the FDBF-cylindrical transformation technique provides a significantly longer wavelength dispersion image than the other transformation methods (FK, PS, and τp) with less ill-effects from near-field effects. The FDBF-cylindrical reduces the near-field effect, particularly near-field effects due to mode incompatibility, by using a cylindrical wavefield model rather than a plane wavefield model. Based on all the dispersion data from sites with a very shallow impedance contrast, approximately 30% longer wavelengths can be achieved using the FDBF-cylindrical compared to the other transformation techniques. Therefore, for sites with a very shallow impedance contrast, the FDBF-cylindrical is recommended for data processing to minimize near-field effects and achieve longer wavelengths (i.e. depth of investigation). When FDBF-cylindrical is used for data processing of sites with a very shallow impedance contrast, the typical normalized array center distance criteria for near-field mitigation can be violated. Overall, the best practice for near-field mitigation of sites with a very shallow impedance contrast is to use the multiple source offset approach along with the FDBF-cylindrical transformation technique for data processing.

4- For sites with a very deep impedance contrast, generally, the four different transformation techniques provide the same resolution dispersion image in terms of near-field effects. Therefore, any of the four transformation methods can be used for data processing of these sites.

5- The source type is determined to be an important factor influencing near-field effects. When a more controllable source type such as a vibroseis source is used for active surface wave testing, less restrictive near-field criteria can be used. Accordingly, using a 10-15% error boundary to define the near-field criteria, a normalized array center distance of 0.5 should be used as the practical criterion when using a vibroseis source. However, for a low-output sledgehammer source, a normalized array center distance of 1.0 should be used as the practical criterion for near-field effects mitigation.

6- The criteria defined for near-field mitigation should not be violated when a limited number of source offsets (1 or 2) are used. But, if the multiple source offset approach (≥3 different source offsets) is used for active surface wave testing, the near-field criteria can be violated for some of the source offsets.

7- The multiple source offset approach is an effective method for near-field mitigation, particularly for sites with a very deep impedance contrast. At least three different source offsets located 2-20 m away from the array (given a typically ~25-100 m array length) should be used when using the multiple source offsets approach. The most suitable source offset location is a complex function of normalized ACD criteria, subsurface conditions, source type, and array length. Generally, for sites with a very shallow impedance contrast using a sledgehammer source, shorter source offsets are recommended compared to sites with a very deep impedance contrast. This is because, for these sites, the dispersion data from longer source offsets are sometimes dominated by effective or higher modes due to the very shallow impedance contrast, making data interpretation more complicated.

8- Researchers and practitioners are widely using short source offsets such as 2 and 5 m for active surface wave testing without considering subsurface conditions and confirming the reliability of such short source offsets. These short source offsets are generally effective for generating high frequencies dispersion data (characterizing very near-surface layers). But for low frequencies dispersion data (i.e. long wavelengths), these source offsets were often observed to be contaminated with severe near-field effects. Therefore, relying solely on short source offsets could lead to a significant underestimation of the measured phase velocity and the subsurface layers' properties. Therefore, it is recommended to at least include one longer source offset (e.g. a source offset ranging between 10-20 m) along with the short source offsets to prevent underestimation of the measured phase velocity and verify the reliability of the short source offsets at longer wavelengths.

9- Overall, based on a 10-15% error boundary, a normalized array center distance criterion of 1.0 is suitable for near-field mitigation on active surface wave testing when using a sledgehammer source, and a normalized array center distance criterion of 0.5 is suitable when using a vibroseis source. These values correspond well with the findings of the previous studies (Li and Rosenblad, 2011; Yoon and Rix, 2009). However, previous studies have ignored the effect of source type on normalized array center distance criteria. The source type was determined to be a key factor influencing the normalized array center criteria required for near-field mitigation.

5 CHAPTER 5: APPLICATION OF GEOPHYSICAL METHODS FOR HEALTH MONITORING OF LEVEES

5.1 Chapter overview

This chapter details the application of the MASW method for the health monitoring of a levee system that has recently experienced considerable sand boils. Extensive geophysical measurements were conducted to generate a continuous image of subsurface conditions along the levee. The goal of this study is to determine the most critical zones of the levee for future rehabilitation efforts. The results are provided in the form of a journal paper published in the Engineering Geology Journal.

5.2 The Combined Use of MASW and Resistivity Surveys for Levee Assessment: A Case Study of the Melvin Price Reach of the Wood River Levee

Reference

Rahimi, S., Wood, C. M., Coker, F., Moody, T., Bernhardt-Barry, M., & Kouchaki, B. M. (2018). The combined use of MASW and resistivity surveys for levee assessment: A case study of the Melvin Price Reach of the Wood River Levee. Engineering Geology, 241, 11-24.

5.3 Abstract

Capacitively-Coupled Resistivity (CCR) and Multichannel Analysis of Surface Waves (MASW) were performed on the Melvin Price reach of the Wood River Levee that has experienced considerable piping through the foundation soil, causing numerous sand boils along the landside toe of the levee. Tests were performed along the centerline crest, the landside toe, and the riverside berm of the levee. This study combined the strengths of MASW and CCR testing to resolve the distribution and stiffness of cohesive and non-cohesive materials in the body and foundation of the levee, where invasive testing was not ideal. MASW and CCR were shown to complement each other in the evaluation. CCR successfully classified the near-surface clay and sand deposits along the levee and was particularly effective for soil deposits with a high degree of saturation. MASW revealed that a deeper clay layer appears to be discontinuous at locations where old river bars cross under the levee. These bars may have eroded portions of the deeper clay layer, locally enhancing seepage rates through the foundation materials and influencing the formation of sand boils during large flood events. The use of MASW and CCR also successfully detected the locations of the major utilities crossing the levee. While CCR was the most effective method for detecting conductive utilities, MASW was more effective at detecting utilities which increased the overall stiffness of the subsurface either due to the utility itself or the backfill material around the utility. A site-specific SPT-Vs correlation was developed from the co-located boreholes and shear wave velocity profiles. Comparison of the correlation with previous studies indicates that soil stiffness and geologic age are important factors affecting SPT-Vs correlations. For levee soil deposits, which are typically young, a lower bound SPT-Vs correlation developed using similar soil deposits to the study area should be considered.

Keywords: Levees, Surface wave methods, Electrical resistivity, Problematic zones, SPT-Vs correlation, aging effects.

5.4 Introduction

Levees are typically earthen embankments that have been constructed to serve as flood control systems during large rain events or protect from wave action during coastal storm events. The United States has an estimated 30,000 documented miles of levees that protect millions of people, properties, and agricultural lands (ASCE, 2017). Nearly 70% of levees failed during record flooding of the Midwest in 1993(Tobin, 1995), and a risk assessment study by the U.S. Army Corps of Engineers' indicated that twenty percent of US levees are considered to have a very high to moderate risk of failure, with an estimated cost of $80 billion needed for the repairs over the next 10 years (ASCE, 2017).

The first step in the repair of a levee is the assessment of its current condition, which includes evaluations of the levee body and foundation material to identify zones of the high potential hazard. Because invasive field tests are typically discouraged for evaluation of hydraulic structures such as levees, noninvasive, rapid, and cost-effective methods of levee assessment are desirable to identify these high potential hazard zones for future targeted rehabilitation efforts.

The mechanisms that cause failures in levees are divided into two main categories: structural failure, including damage to the embankment from physical disturbance (Bayoumi *et al.*, 2011), and failure due to hydraulic forces such as underseepage, overtopping or wave erosion, piping, and liquefaction(Foster et al., 2011) (Ellis et al., 2008 and Vrjiling 2003). Overtopping and piping failures combined resulted in 82% of earth dam failures prior to 1986 (Foster *et al.*, 2011) and continue to be the main reasons for levee failure (Harder *et al.*, 2016). While the probability of an overtopping failure depends on the characteristics of the flood events relative to the design height of the levee, the probability of a piping failure is mainly controlled by geotechnical properties of the levee's internal body and foundation, particularly soil erodibility. Briaud (2008) characterized soils into six groups from very high erodibility to nonerodable and found that erodibility is negatively correlated with plasticity and positively correlated with particle size (Briaud, 2008). This is consistent with observations from the Hurricane Katrina New Orleans levee failures, which were primarily levees with relatively non-cohesive sand and silt cores (Sills *et al.*, 2008). Levee evaluations, therefore, need to reliably map the appropriate material properties of the levee core and foundation, particularly soil type and soil stiffness.

Soil type (i.e. cohesive or non-cohesive) and soil stiffness can be geophysically investigated. Previous studies have shown that contrasts in soil type and degree of saturation are detectable using resistivity (Hayashi *et al.*, 2014; Wood *et al.*, 2017a; Kouchaki *et al.*, 2018). Useful attempts have been made to correlate soil resistivity with geotechnical properties such as particle diameter, fines content, and permeability (Inazaki and Hayashi. 2011); however, changes in the degree of saturation of soil deposits affect the measured resistivity values, making it difficult to differentiate between different soil types due to the wide range of water contents at which a soil can exist in the field. Differentiation is optimal when soils are below the water table, but levee cores are usually above the water table (Sjödahl *et al.*, 2010).

Other single techniques such as GPR may be useful to reveal voids and displacements in damaged levees (Nobes *et al.*, 2015), but single-technique evaluations are not usually appropriate (Busato *et al.*, 2016). Equally, multi-technique studies that focus on electrical methods only (Perri *et al.*, 2014) also have limited utility because they do not interrogate the bulk mechanical characteristics of the levees. Surface wave methods, on the other hand, can provide information regarding soil stiffness and soil type above the water table because shear wave velocity (Vs) is mainly controlled by the soil skeleton (Foti *et al.*, 2014). Moreover, since the degree of saturation only causes a slight difference in the inversion process needed for the determination of the Vs profile from the raw surface wave data, surface wave methods can be used for accurate classification of soil deposits with a variety of saturation levels using the reference shear wave velocity profiles and SPT-Vs correlations that are available for many soil types (Foti *et al.*, 2014; Lin *et al.*, 2014). Like an over-focus on electrical methods, however, studies that use seismic methods only (Cardarelli *et al.*, 2014) limit their capacity to reveal compositional information. It is, therefore, reasonable to expect a significant advantage from studies that utilize co-located electrical (particularly variants of resistivity surveys) and seismic techniques (Hayashi *et al.*, 2014; Samyn *et al.*, 2014; Busato *et al.*, 2016).

In this study, two non-invasive geophysics methods, MASW and CCR, were utilized for the evaluation of the Melvin Price reach of the Wood River Levee System. A levee system that has previously been identified as vulnerable due to the detection of sand boils on the landward side of the levee (Geotz, 2016). The goal of this study is to identify whether such methods are capable of resolving the internal body and foundation of the levee and detecting potential problematic zones, which contributed to the formation of sand boils. The site background, geology, and history of the problems of the levee are first presented. This is followed by an explanation of the geophysical methods used in this investigation and a discussion of data processing. The results of geophysical surveys are presented for the centerline, landside toe, and riverside berm of the levee. Comparisons are drawn between the geophysical results and geotechnical in-situ tests taken along the levee. Specific examples of soil classification using Vs and resistivity are provided, along with examples of old river bars and utilities being resolved by the geophysical methods. Finally, using the SPT borehole data and co-located Vs profiles along the landside toe of the levee, a site-specific SPT-Vs correlation is developed for the study area, and the results are compared with previous studies.

5.5 Site Background

The Melvin Price reach of the Wood River Levee System is an approximately 4 km long and 10-meter-tall earthen levee located along the Illinois side of the Mississippi River outside the town of Alton, IL and St. Louis, MO (Figure 5.1). The local geology consists of the Mississippian St. Louis formation limestone bedrock at a depth of approximately 30 meters, overlain with gravelly sand and topped with silty clay. Exploration in the area has found these layer thicknesses to be highly variable both along the length of the levee and perpendicular to it.

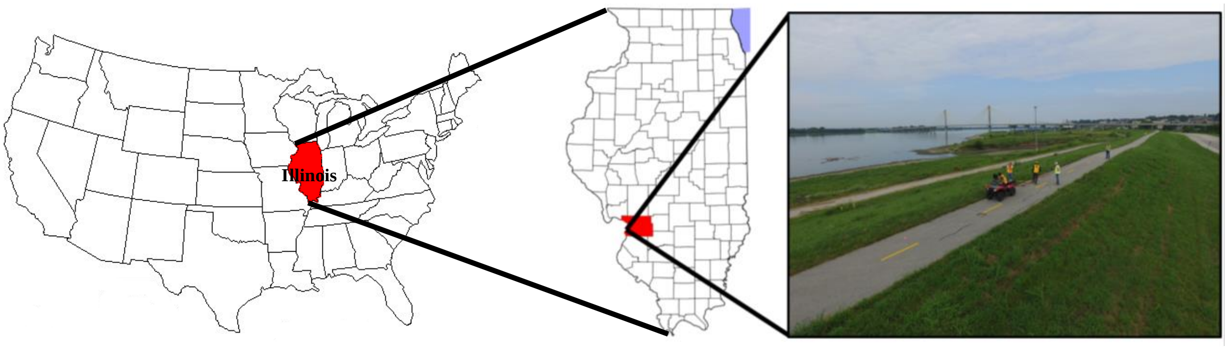

Figure 5.1. Location of the surveyed section of the Wood River Levee System in Madison County, Illinois with geographic coordinates of 38.876768, -90.158164.

Construction of the Melvin-Price lock and dam began in 1979, and the lock and dam opened in 1994, replacing an older dam located two miles upriver. The typical section of the levee consists of a clay cap that covers the top and the riverside berm of the levee from the surface to a depth of approximately 2 m, followed by a sand core layer from 3-10 m, as shown in Figure 5.2 (Geotz, 2016). This is common where clay material is scarce, requiring a major portion of the levee to be built of other materials such as sand. Because the soil gradation difference between the clay cap and the sand core is large, an intervening filter layer prevents the migration of the fine material into the sand core.

Shown in Figure 5.3 is an aerial photo taken in 1941, prior to the construction of the levee. This figure illustrates the complex nature of this portion of the levee, showing three river bars crossing the current location of the levee. The old river bars and previous erosion are considered to contribute to the problems observed along the levee. After construction of the lock and dam, a permanent pool of water began to form from Stations 0+00 to 115+24, effectively moving the river bank further inland. In 2009, clear flowing seepage was observed along the dry-side of the levee, indicating significant amounts of under seepage below the levee. LIDAR and visual inspections identified numerous sand boils (the result of under seepage) between Stations 60+00 and 110+00 (Figure 5.3; Geotz, 2016). To remedy the under seepage and prevent possible erosion, the head differential between the river and the dry-side of the levee was reduced by establishing a permanent pond on the dry-side of the levee. While this ponding will reduce the rate of seepage, it removes the ability to visually monitor problem areas/boils. In addition to the permanent pond, cutoff relief wells were installed along the dry-side of the levee to also reduce the possibility of internal erosion of the levee foundation.

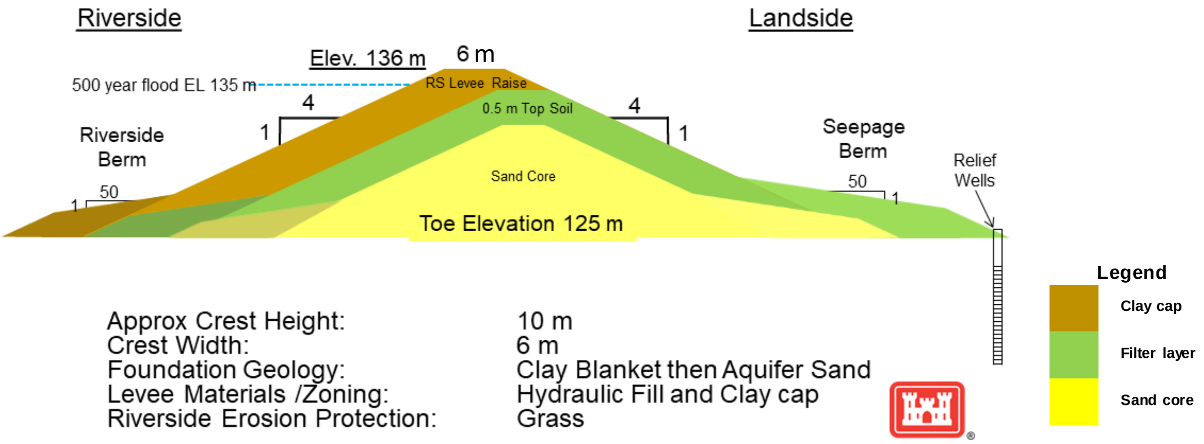

Figure 5.2- Typical levee section for the Melvin-Price reach of the Wood River Levee System (Modified from Goetz, 2016)

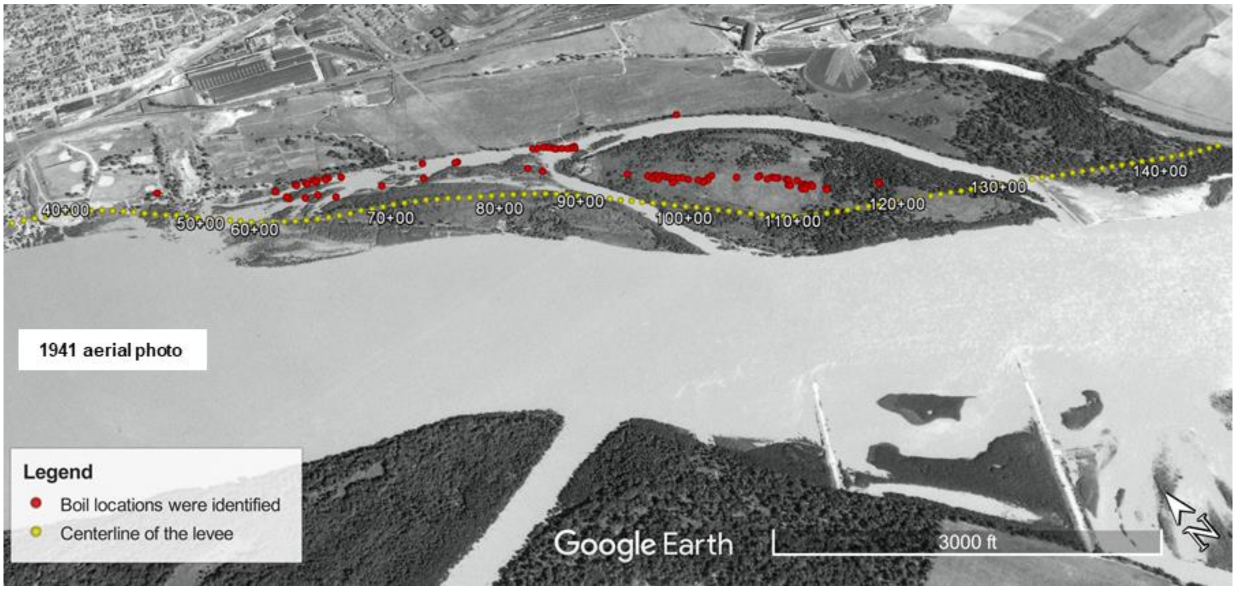

Figure 5.3- Aerial photo taken in 1941 of the future location of the Melvin-Price reach of the Wood River Levee with the levee stations and sand boils overlaid (Modified from Goetz, 2016)

5.6 Geophysical Investigation

The geophysical investigation of the Melvin-Price Reach of the Wood River Levee system (referred to as the levee hereafter) was conducted using a combination of geophysical methods including CCR and MASW from August 8-11, 2016. Data was collected along the centerline crest of the levee (top of levee hereafter), along the dry side of the levee (hereafter landside toe) where seepage and flooding had been observed, and along portions of the bank of the river (hereafter riverside berm). The testing locations, along with testing parameters and data processing parameters, are detailed for each method below.

5.6.1 Capacitively Coupled Resistivity (CCR)

CCR surveys were acquired along the top, landside toe, and riverside berm of the levee using a Geometrics OhmMapper TR5 system. The OhmMapper works by utilizing five receivers to detect current injected into the ground via a transmitter at varying rope lengths. To provide comprehensive measurements of the entire levee, dipole lengths of 5 and 10 meters in combination with rope lengths of 2.5, 5, 20, 30, and 40 meters were utilized during testing. Varying the dipole and rope lengths allows the survey to assess materials at varying depths, i.e. short dipole lengths in combination with short rope lengths measure very near-surface materials while longer dipole lengths and longer ropes lengths measure deeper materials. In Figure 5.4, the CCR survey paths are shown for the top, riverside berm, and landside toe of the levee, along with the locations of utilities crossing the levee.

To develop the resistivity results, the raw OhmMapper data was first processed in Geometrics OhmImager to correct any metadata errors and to combine resistivity data for common locations before being exported to MagMap. MagMap was used to convert GPS data to UTM, remove dropouts and spikes from the apparent resistivity data, and export profile data for use in Res2dinv. Res2dinv uses a smoothness-constrained least-squares method incorporating damping factors to obtain an inversion solution. Res2dinv's large dataset optimization options were utilized during the inversion. Profiles were generated using triangulation with linear interpolation.

For general interpretation of soil classification from the resistivity data, the water table location was estimated based on P-wave refraction surveys and the free water surface elevation across the site, which was very near the surface of the landside toe, but beyond the depth of investigation for the top of levee and riverside berm.

Figure 5.4. Survey paths for MASW and CCR at Melvin Price Reach of the Wood River Levee (Both MASW and CCR were performed along the same paths)

5.6.2 Multichannel Analysis of Surface Waves (MASW)

MASW using Rayleigh type surface waves (V_R) were collected along each of the CCR traverses (top, landside toe, and riverside berm) of the levee (Figure 5.4) using a linear array of 24, 4.5 Hz vertical geophones with a uniform spacing between geophones of two meters, yielding a total array length of 46 meters. The geophones were attached via a Geostuff landstreamer system to increase the rate of testing. Testing was conducted on both grassy areas and thin asphalt sidewalks. A sledgehammer was used to generate Rayleigh waves with source positions of 5, 10, and 20 meters from the first geophone at each array location. At each source position, three sledgehammer blows were stacked to improve the signal-to-noise ratio of the data. After each setup, the array of receivers was pulled forward to the next testing location. Testing locations were spaced at 30 meters for the top, 50 meters for the riverside berm, and 25 meters for the landside toe of the levee. A total of 202 MASW setups were conducted along different parts of the levee.

The experimental MASW data was processed using the frequency domain beamformer method in Matlab combined with the multiple source offset method (Zywicki *et al.*, 2005; Cox *et al.*, 2011). Multiple source offsets are used as a means to (1) identify potential near-field effects, (2) aid in selecting the fundamental mode of surface wave propagation, and (3) provide a robust means for estimating dispersion uncertainty (Cox *et al.*, 2011). For each dispersion dataset, the maximum spectral peak in the frequency-wavenumber domain was picked automatically for each frequency to reduce user bias. Dispersion data points can be fundamental, effective, and higher modes. Generally, the fundamental mode is dominant for most frequencies of interest (Foti *et al.*, 2014). In this investigation, the fundamental mode of propagation was used as the preferred mode for the inversion process.

In Figure 5.5a, the experimental dispersion data for Station 96+00 along the landside toe of the levee is shown as an example. The dispersion data contains both fundamental (7-50 Hz) and higher modes (50-80 Hz). The final experimental dispersion curve that was extracted from the raw data is shown in Figure 5.5b. The higher mode data and data affected by potential near field effects were removed in the final dispersion curve. For each testing location, the final dispersion data from all source offsets at the location was divided into 100 frequency bins from 1-125 Hz using a log distribution. The mean and standard deviation was estimated for each data bin resulting in a mean experimental dispersion curve with associated standard deviation.

The mean dispersion curve was then inverted using the software package Geopsy (Wathelet, 2008). Multiple parameterization options (i.e., variations in the number of layers and potential thickness of those layers) were attempted for the datasets. The best parameterization was found to consist of 11 layers with thicknesses increasing at a rate of 1.25 per layer (Cox *et al.*, 2016). The shear wave velocities of the layers were allowed to vary from 100 m/s to 400 m/s in the top three meters, 100 m/s to 800 m/s in the next six meters, 100 m/s to 1000 m/s from 8 to 15 meters, and then 100 m/s to 2000 m/s until bedrock or very hard material. These velocity ranges were chosen to match the material type as shown in Figure 5.2 provided by Geotz (2016). The depth to the water table was estimated at each location based on the free water surface visible across the site and P-wave refraction data, which was developed using the MASW data. For each dispersion curve, 110,000 Vs models were searched using the neighborhood algorithm in Geopsy. The goodness of fit between the experimental and theoretical dispersion curves was first judged based on the value of the calculated misfit parameter (collective squared error between experimental and theoretical dispersion curves) and then checked by visual comparison of the experimental and theoretical dispersion curves. This is necessary because the misfit parameter can only be used to compare the relative quality of fit of the theoretical dispersion curves for the same experimental dispersion data, as the values of the misfit parameter depends on both the quality and quantity of experimental dispersion data (i.e., misfit values lower than a particular value do not necessarily indicate a high-quality fit) (Griffiths *et al.*, 2016). The median of the 1000 best (lowest misfit) Vs profiles was taken as the 1D Vs profile for each setup location.

Shown in Figure 5.6 is the resulting 1000 lowest misfit Vs profiles, median Vs profile, lowest misfit Vs profile, and the associated standard deviation for Station 96+00 for the landside toe of the levee, as an example. As with many of the Vs profiles generated in this work, the uncertainty is quite small in the top 15-20 meters. However, at depths greater than 15-20 m, the uncertainty in the Vs increases significantly due to lower resolution in the dispersion data and changes in the subsurface materials. Bedrock at the site is estimated based on boring logs to be around 30 meters below the landside toe (Geotz 2016). However, this depth is very uncertain due to the existence of large boulders in the subsurface, making it difficult to interpret the true bedrock elevation. Once the final shear wave velocity profile for each station was determined, the individual 1D Vs profiles were combined together to develop pseudo 2D plots of the variation of shear wave velocity with distance along the line and depth using triangulation with linear interpolation in the Surfer software program (*Surfer® 14, Golden Software, LLC)*.

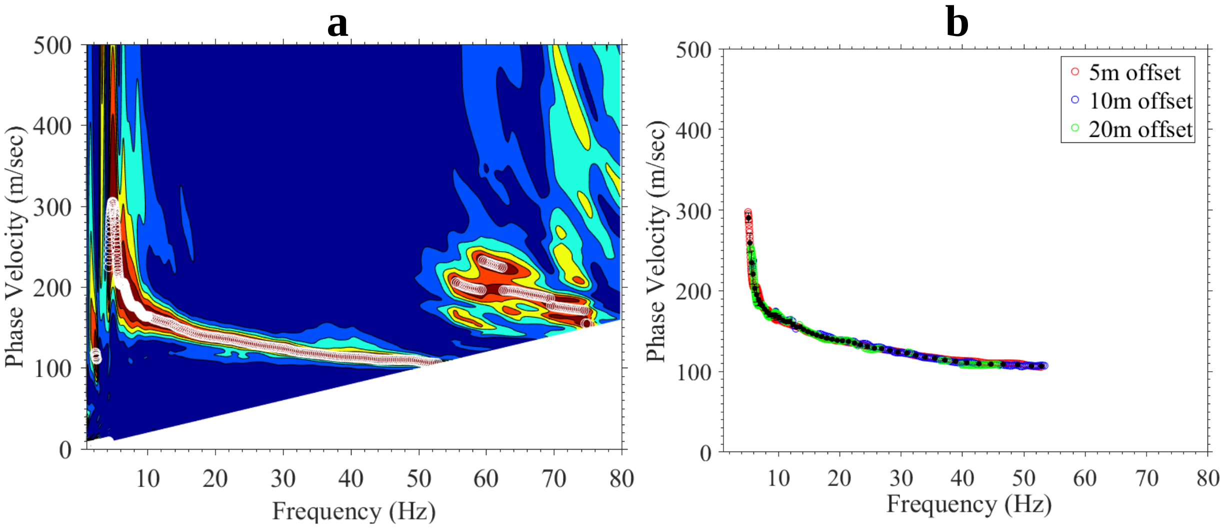

Figure 5.5. Typical experimental dispersion data points taken from Station 96+00 for the landside toe of the levee a) Raw and b) Refined.

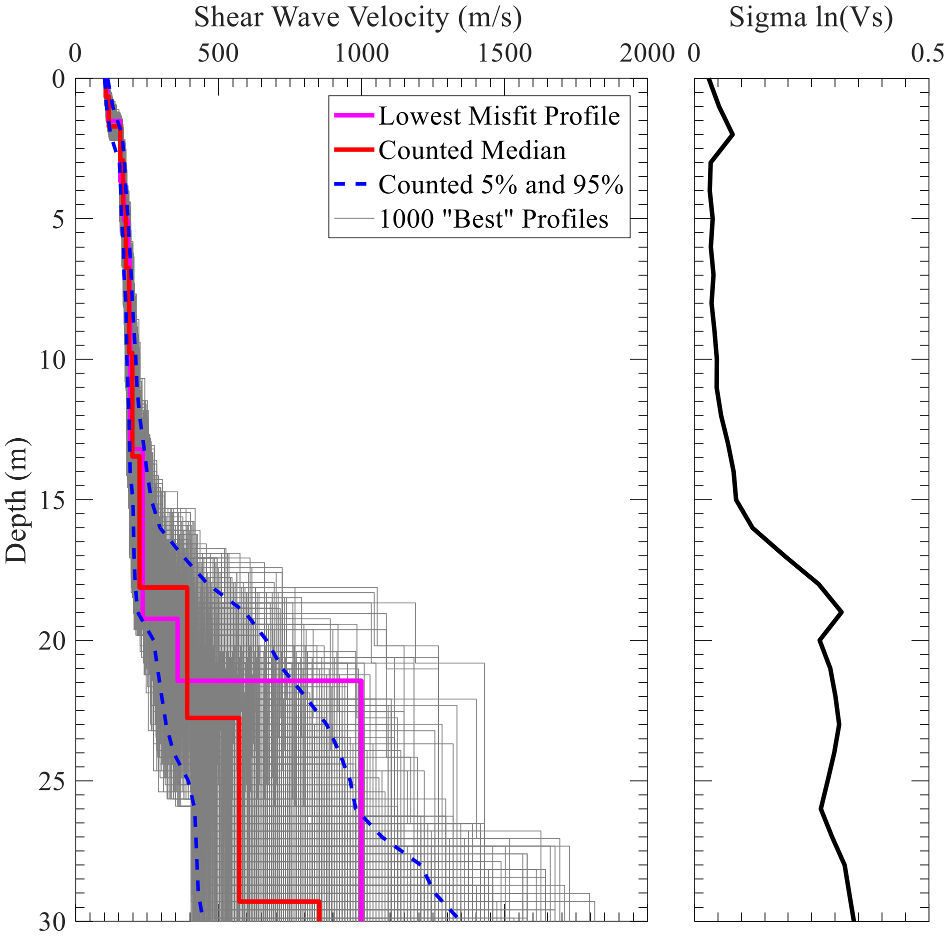

Figure 5.6. Result of inversion process for Station 96+00 located on the landside toe of the levee. Left, Vs profiles for the 1000 lowest misfit and median Vs profile, Right, Sigma ln (Vs) for the 1000 lowest misfit Vs profiles.

5.7 Results and findings

The processed data from the MASW and CCR surveys are used for soil characterization and are compared with existing information, including Standard Penetration Test (SPT) and general stratigraphy for the levee. In addition, an empirical correlation between the shear wave velocity (Vs) and uncorrected SPT blow count (N) is developed for the study area using co-located boreholes and shear wave velocity profiles. The results are discussed in the following sections, and their general application and direct applications to the Melvin-Price Levee are discussed in detail.

5.7.1 General observation

In Figure 5.7, the variation in Rayleigh wave phase velocity (V_R) (before completing the inversion process) with pseudo depth (wavelength divided by 2) and station number for the top of the levee is shown. Each point in this figure corresponds to a Rayleigh wave phase velocity point determined from the field data. The plot is used to identify any significant variations in the sub-surface prior to the inversion process. Based on Figure 5.7 and a-priori information regarding the levee structure, the levee body and foundation generally consists of a four-layer system: soft clay, soft sand, medium-dense sand, and very dense sand/gravel. The lateral variation in V_R in Figure 5.7 shows a few sharp increases in Rayleigh wave phase velocity that corresponds to the location of utilities that cross the levee (labeled in Figure 5.7). The most noticeable increase in V_R is near Station 50+00 (labeled as 1 in Figure 5.7), which matches the location of the old pump station and pipe. Moreover, near Station 80+00, the top 6 meters of soil around the flood gate built into the levee has a higher V_R than its surrounding areas indicating better compaction or a different material type around the flood gate than present at other sections of the levee.

While the development of a pseudo 2D plot of Vs from MASW data is common, this can potentially bias the data due to the non-unique nature of the inversion process required to obtain the Vs results. Using the Rayleigh wave phase velocity (dispersion data developed prior to inversion) can provide an unbiased view of the subsurface conditions, anomalies and avoid misinterpretation of the MASW data. Moreover, for some cases, it may be possible to understand the subsurface conditions using this type of plot, reducing the overall time required for data processing as the inversion process is often the most complex and time-consuming portion of the data analysis. Although this plot can be valuable, the averaging with depth effects of using phase velocity can make it more difficult to visualize some subsurface features like the subsurface clay layer discussed later in the text. However, all features visible in the Vs plots should be visible in raw dispersion data, but the contrast in velocity between different features will not be as great in the dispersion data. Overall, figures such as Figure 5.7 provide an unbiased view of the dispersion data, which are not influenced by the inherent non-uniqueness which accompanies the inversion process, and they can be useful for identifying areas of interest.

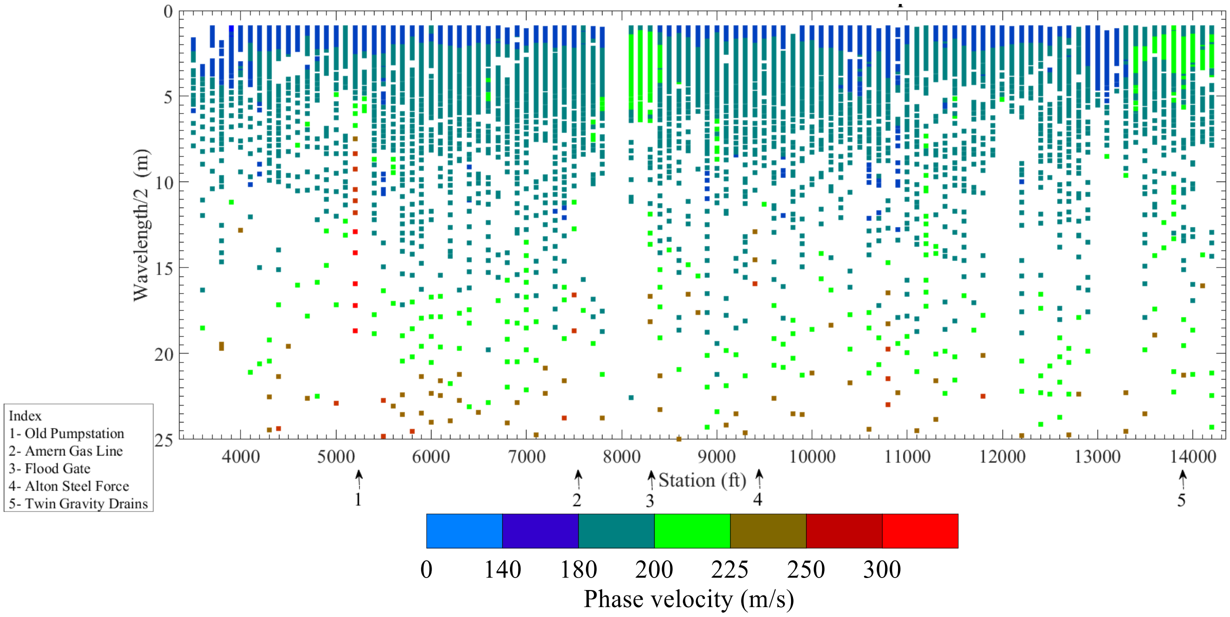

Figure 5.7-2D cross-section of the top of the Melvin-Price levee section with Rayleigh wave phase velocity versus pseudo depth (wavelength/2).

5.7.2 Landside toe of the Levee

Figure 5.8 represents the 2D Vs and resistivity profiles for the landside toe of the levee, along with an aerial image taken in 1941. The cyan points on the Google Earth image indicate the positions of the MASW testing locations along the landside toe portion of the levee. The ranges of resistivity and shear wave velocity that correspond to different soil types are indicated along with the color scales in Figure 5.8. The Vs ranges are based on reference Vs profiles (see Equation 53) for different material types presented by Lin et al. (2014), and the SPT blow count information from the boreholes along the survey line. Equation 28 solves for shear wave velocity as a function of mean confining stress.

$$V_S = V_{SR} \times (\sigma'_0/P_a)^{n_s} \tag{56}$$

Where V_S is the shear wave velocity, V_{SR} is the reference shear wave velocity at 1 atm effective mean stress, σ'_0 is the initial effective mean stress, P_a is the reference stress of 1 atm, and n_S is the exponent of normalized effective mean stress. V_{SR} and n_S values are provided for a number of different soil types and densities, ranging from soft clay to dense gravel (Lin *et al.*, 2014; Rahimi *et al.*, 2019d). These curves provide reasonable bounds for various soil types and densities as a function of overburden stress.

Soil type along the landside toe cross-section was also estimated based on resistivity. However, laboratory resistivity results indicate it is difficult to define soil type based solely on resistivity without a-prior knowledge of the soil saturation (Wood *et al.*, 2017a; Kouchaki *et al.*, 2018). Therefore, information from the available boreholes were used as a guide to define the specific resistivity correlation for this site. Comparison of the classification results from the borehole logs and laboratory defined ranges are similar when the soil is considered near saturation, which is very likely considering the static water level for the landside toe profile was very near the ground surface. The same procedures were followed for the determination of the shear wave velocity and resistivity ranges for the other sections of the levee (top and riverside berm). However, no invasive information was available for the top of the levee cross-section.

In Figure 5.8, the information from four boreholes is shown along with the Vs and resistivity 2D cross-sections. The numbers to the right of the boreholes for the 2D Vs cross-section in Figure 5.8a are the average uncorrected SPT-N values for each layer. Based on the Vs cross-section, the subsurface consists of five soil layers. A 2-3 m thick, soft clay layer at the surface, a soft sand layer from 3-14 m, a medium dense sand layer extends from the base of soft sand to depths ranging from 22-25 m, followed by a dense sand layer between 27-30 m depth, underlain by very dense material. The thickness of the various layers is fairly uniform across the cross-section, varying by up to 2-4 meters at discrete locations. Overall, the Vs cross-section is in good agreement with the borehole information indicating Vs can provide a good estimate of SPT N value and soil type/density, especially when some a-prior information is available.

The 2D resistivity cross-section along with USCS soil classification based on borehole logs is shown in Figure 5.8c**.** The resistivity results indicate the subsurface consists of a three-layer system that includes a top layer of lean clay from the surface to a depth of about 2-3m, underlain by a thin silty sand layer from 3-4m, and finally a poorly graded sand up to a depth of 10 m. Overall, the CCR soil classifications are in good agreement with the Vs and borehole results, but the resistivity only provides valuable information down to a depth of 10 m. This is one limitation of the CCR technique in it is only capable of mapping near-surface layering. However, the CCR method was able to resolve the silty sand layer, which was not resolvable using surface wave methods.

Examining the sand boil locations in Figure 5.8, the sand boils from Station 82+00 to 85+00 line up quite well with the location of the old river bar. The other two locations, where extensive sand boils were observed (Station 90+00 to 110+00), is a swamp located on the landside toe of the levee (see Figure 5.4). This area was used as a clay borrow pit for the construction of the levee's surface layer (Geotz 2016). Field investigations using a hand auger revealed that this area has a thinner surface clay layer than other areas around the levee, thus leading to a higher likelihood of sand boil formation. The thickness of a clay layer on the landside toe of a levee, which performs as a clay blanket, can have a significant impact on the seepage rate in the area. Because of the standing water in the swamp, geophysical testing could not be conducted in the area.

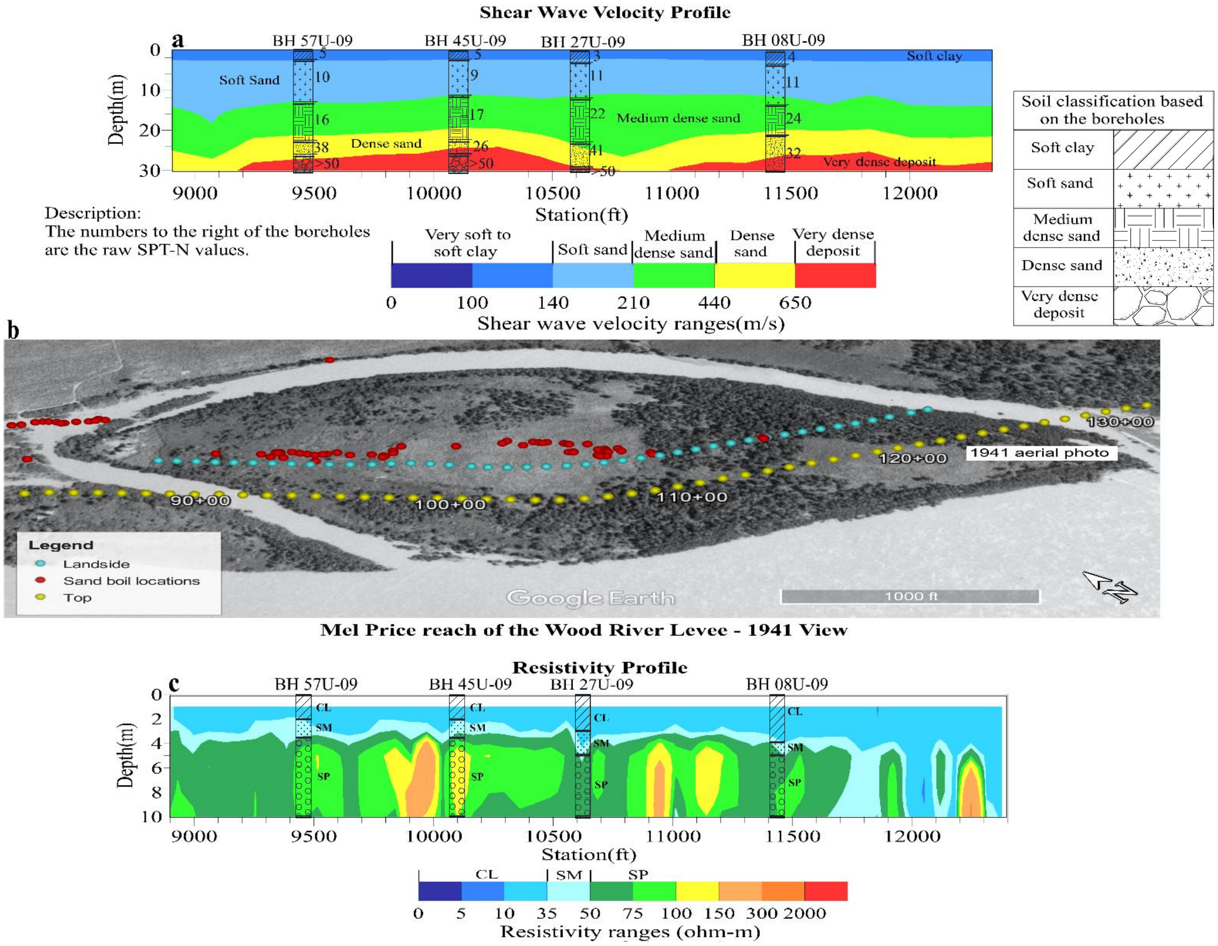

Figure 5.8-2D cross section for the landside toe of the Melvin Price reach of the Wood River levee, a) 2D Vs cross section b) 1941 aerial image of area c) 2D CCR cross section. Data from borings logs including uncorrected SPT N values and USCS soil classification are overlaid on the figures for comparison.

5.7.3 Top of the levee

The most extensive MASW and CCR testing was performed on the top of the levee. The 2D Vs and resistivity cross-sections for the top of the levee along with an aerial image taken in 1941 are shown in Figure 5.9. The ranges of resistivity and shear wave velocity that correspond to different soil types (colors) were chosen using a similar procedure to the landside toe.

However, a higher Vs range was chosen for the clay layer due to the increased overburden stress for a deeper clay layer present in the cross-section.

Based on the 2D Vs cross-section for the top of the levee (Figure 5.9a), the subsurface consists of a 5-layer system that includes a 2-3 m soft clay layer at the surface, a soft sand layer from 3-8m, a discontinuous soft clay layer from 8-12m, a soft sand layer from 17-22m, and finally a medium dense sand layer.

Examining the lateral variability of the cross-section in Figure 5.9a, the first area of interest is the near-surface clay layer, which appears to be discontinuous along the cross-section. However, these discontinuities are likely the result of better compaction in parts of the levee, which increases the shear wave velocity to a level similar to the underlying sand layer. This indicates one of the limitations of soil classification using shear wave velocity in that it is difficult to differentiate between different typical soil types used for levees (i.e. clay, silt, and sand) at shallow depth (i.e., low confining stress), as other parameters influence the behavior of the soil more than confining stress. The validity of this presumption is examined later using the resistivity results.

The second areas of interest are the discontinuities in the deeper clay layer between 8-12 meters. The existence or lack of existence of this clay layer along the cross-section is clearly visible in the experimental dispersion curves and 1D Vs profiles along the levee, as shown in Figure 5.10. Experimental dispersion curves from Station 40+00 (no clay layer present) and Station 108+00 (clay layer present) are compared in Figure 5.10a. For Station 40+00, the experimental dispersion curve is clearly normally dispersive (i.e., the phase velocity continually increases as frequency decreases), resulting in a constantly increasing shear wave velocity with depth, as shown in Figure 5.10b. However, Station 108+00 has a considerable drop in phase velocity for frequencies between 7-20 Hz resulting in a velocity inversion in the shear wave velocity profile (i.e., a soft layer between two stiffer layers), as shown in Figure 5.10b. The Vs of this softer layer corresponds well with the reference velocity for a soft clay and matches with the generalized layering for the area. Examining the locations along the cross-section where these discontinuities occur, they appear to correspond quite well with the location of the old river bars from the 1941 aerial image for the area, as shown in Figure 5.9. This indicates the deeper clay layer and, in some cases, the medium dense sand layer may have been eroded by the old river bars. These sections where the clay layer was not present are potential problem areas of the levee for piping and are areas of interest for improvements or further investigations. The reasons why these sections are considered as potential problem areas can be explained in two ways:

1) The absence of the deeper clay layer leads to a decrease in the length of the flow path (L), thus increasing the hydraulic gradient (i) of those sections based on the equation, $i=\Delta h/L$ (Δh is the hydraulic head difference between the riverside berm and landside toe of the levee). Therefore, sections, where the deeper clay layer disappears, would likely have the lowest factor of safety along the entire length of the levee and could be the potential problematic zones for piping.
2) Moreover, according to the Briaud (2008) erodibility classification, while sand and non-plastic silt have the highest erodibility potential among all soil types, clay is categorized as having a low erodibility. This means that sections where the deeper clay layer is replaced with soft sand likely have the highest erodibility potential along the levee.

Although the clay layer was able to be resolved using surface wave methods, the exact thickness of the clay may vary from that shown in Figure 5.9a due to the lower resolution ability for surface wave methods as depth below the surface increases.

Several sections not associated with old river bars from the 1941 aerial image (Stations 35+00 to 45+00, 82+00 to 85+00, and 120+00 to 125+00) appear to also have no clay layer present in the subsurface. Examining the locations of the recorded sand boils in Figure 5.3, it can be seen that the section from Station 82+00 to 85+00, where the deeper clay layer is missing, matches quite well with one of the extensive sand boil locations. The reason for not resolving/observing the deeper clay layer in the other two sections is currently unknown. However, based on the experimental dispersion data for these areas, which did not have an inversion (i.e., drop in phase velocity) at depth, the clay layer is unlikely to exist in these areas, or it has a significantly higher stiffness than the clay layer in other portions of the cross-section, which is less likely.

Also, in Figure 5.9a, two sharp increases in Vs are observed along the cross-section at Stations 52+00, and 76+00. These anomalies are clearly observed in the experimental dispersion curves, which are shown in Figure 5.11a. Also included in Figure 5.11a is a typical experimental dispersion curve from Station 108+00 for comparison. For frequencies greater than 20 Hz (shallow depths), all of the dispersion curves are very similar. However, for frequencies less than 20 Hz, the phase velocity of the dispersion curves corresponding to the anomalies (Station 52+00 and 75+00) increases rapidly at higher frequencies than the typical dispersion curve (Station 108+00), indicating a much stiffer layer is present closer to the surface than typically encountered in the cross-section. This sharp increase in Vs at shallow depths is mirrored in the Vs profiles for Stations 52+00 and 76+00, as shown in Figure 5.11b. The location of these anomalies corresponds very well with the location of major utilities crossing the levee, including a pump station pipe and the Ameren Gas Line. This emphasizes the abilities of surface wave methods to resolve these utilities at depth, which are thought to be less than 20 cm in diameter. However, since shear wave velocity is sensitive to changes in stiffness, it is likely that the utility trench or bore casing made the target large enough and with a large enough contrast in stiffness to resolve. The detection of major anomalies in the subsurface using MASW and other geophysical methods has also been shown by previous studies (Chlaib *et al.*, 2014; Samyn *et al.*, 2014; Gutiérrez *et al.*, 2018).

The results of the CCR survey for the top of the levee, along with the locations of the old river channel and utility crossings, are presented in Figure 5.9c. Based on the CCR survey, which only provides information for the top 9 m, the top of the levee consists of two layers: a clay layer from the surface to a depth of approximately 2-3 m, followed by a sand layer from 3-9m. Beyond the general layering, there a number of areas of interest. First, an area of very low resistivity extending from the surface down to the 9 m is observed at Station 133+00, which corresponds with the location of a twin gravity drain crossing the levee. This low resistivity section likely occurred due to the presence of metal in the twin gravity drain. Another possibility is that seepage paths around the twin gravity drain led to low resistivity values.

Two other lower resistivity areas are observed in the cross-section at Stations 50+00 and 93+00 which, match the location of the old river channel. These areas are observed as areas of lower resistivity from 3-9 m than the surrounding area. These sections with lower resistivity values correspond well with the locations of the old river bars indicating the soil deposits in these sections may have a higher degree of saturation than the surrounding area, thus resulting in lower resistivity values. In general, the areas of low resistivity match well with the results from the Vs cross-section but are not as clear in resolving the subsurface features in most cases, which could lead to errors in the interpretation if resistivity alone was used. Overall, the 2D resistivity cross-section is generally consistent with the results of the 2D Vs cross-section, with both methods providing independent verification of anomalies in the levee.

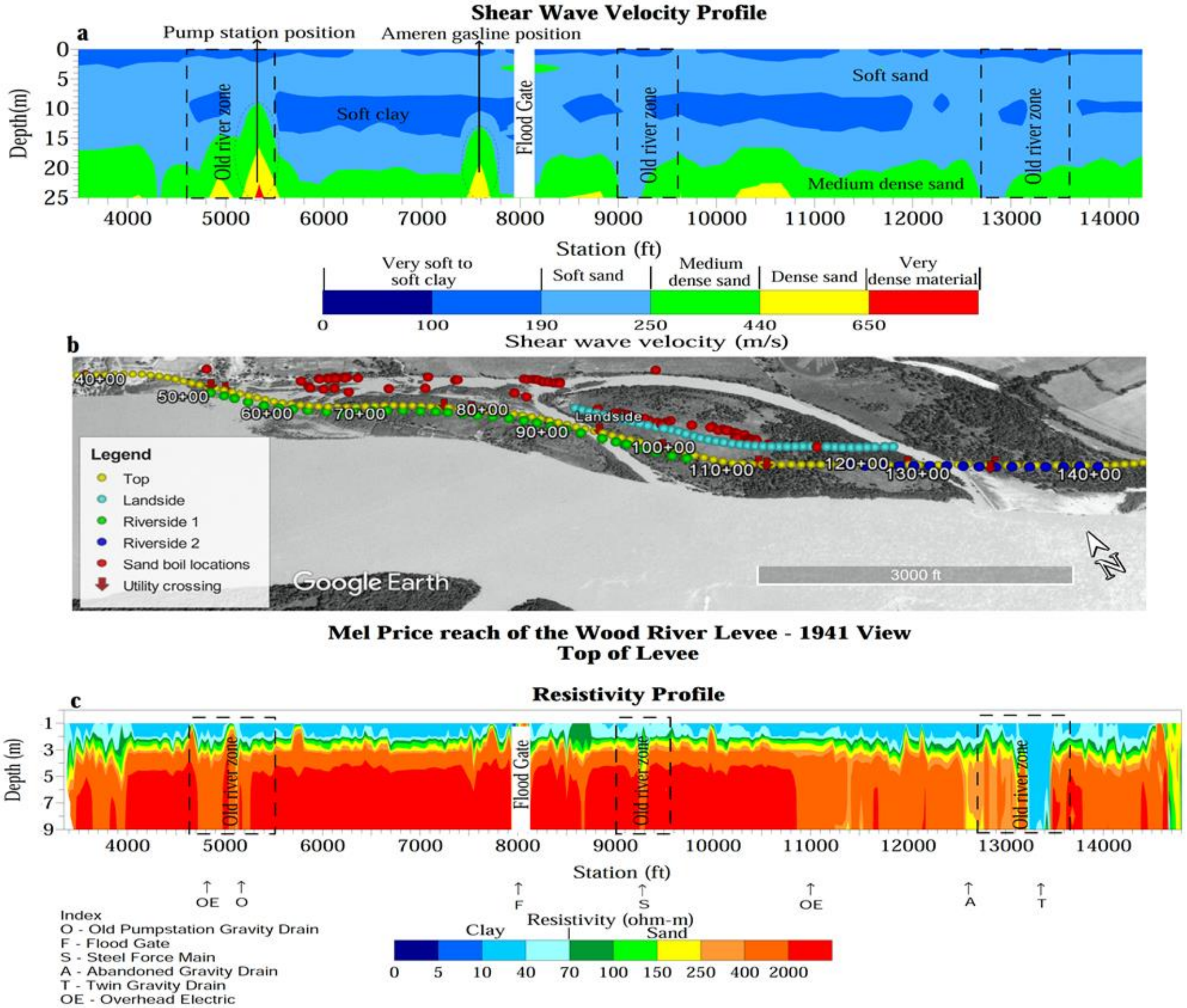

Figure 5.9- 2D cross section for the top of the Melvin Price reach of the Wood River levee, a) 2D Vs cross section b) 1941 aerial image of area c) 2D CCR cross section. Areas where the old river bars previously existed and the location of major utilities crossing the levee are identified on the figures.

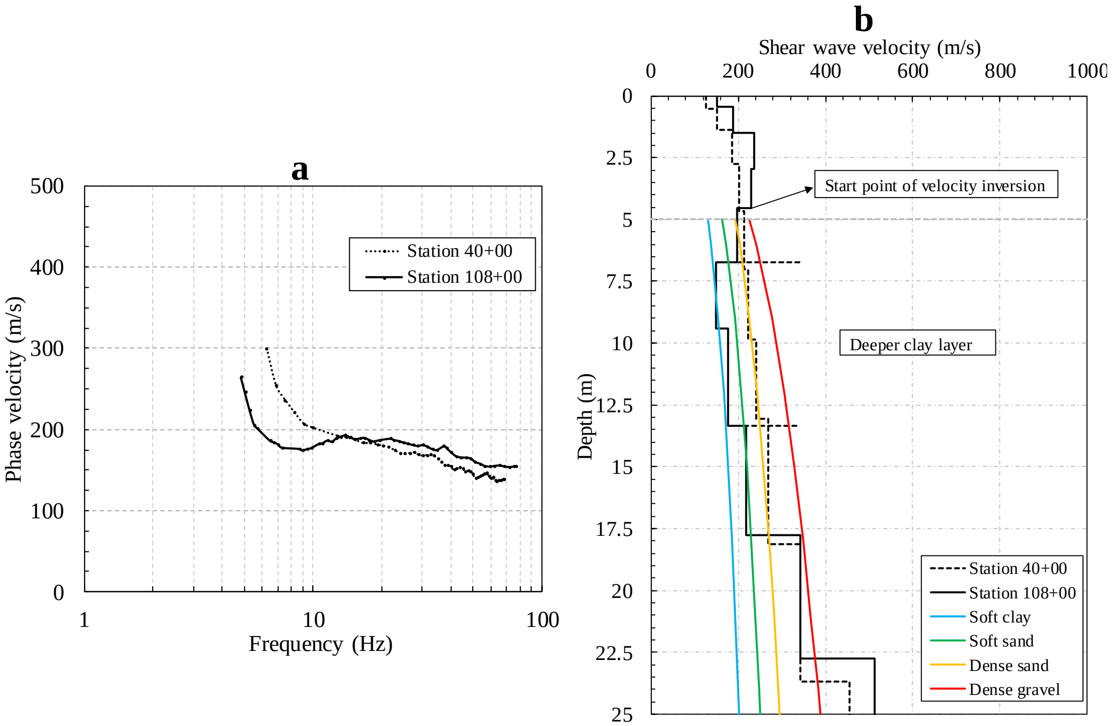

Figure 5.10- a) Experimental dispersion curves and b) shear wave velocity profiles for Stations 40+00 and 108+00 for the top of Melvin Price reach of the Wood River levee. Reference Vs profiles from Lin et al. (2014) are also shown for comparison.

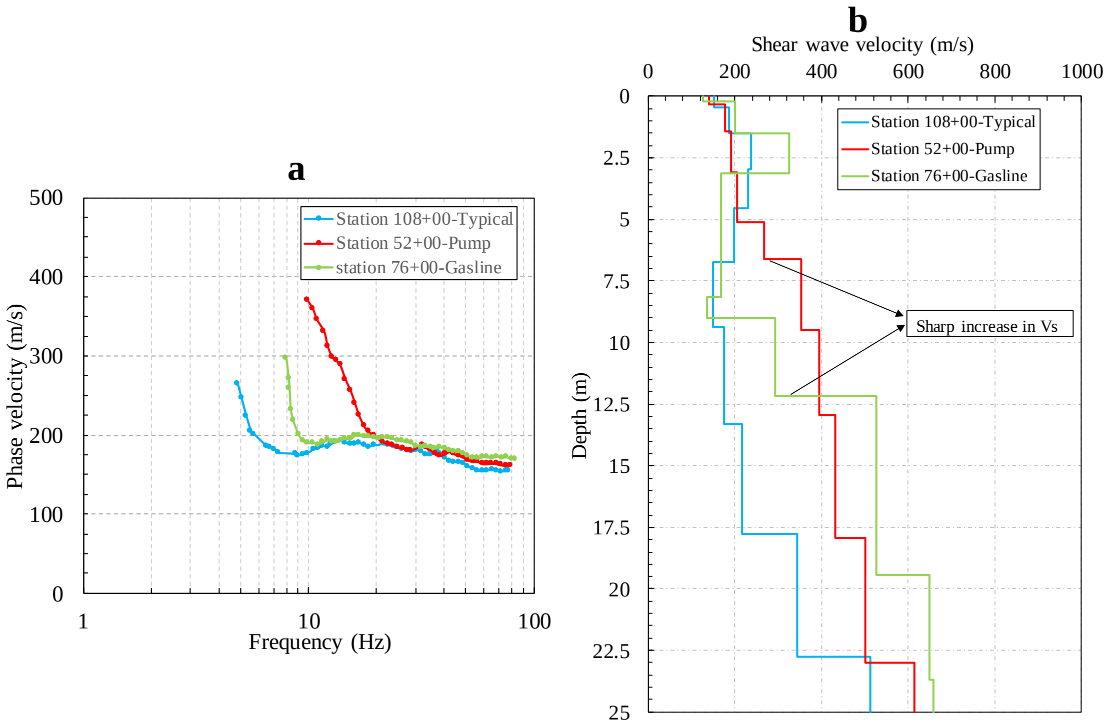

Figure 5.11- a) Dispersion curves b) shear wave velocity profiles for the Stations 108+00, 52+00, and 76+00 highlighting the sharp increase in Vs at Station 52+00 where a major utility crossing is located.

5.7.4 Riverside berm

In Figure 5.12, the results of the MASW and CCR surveys for the riverside berm of the levee, along with the current aerial photo of the area, are shown. The MASW survey was performed in two different paths, Riverside berm of the levee 1 and Riverside berm of the levee 2, as shown in the aerial photo. In Figure 5.12a, the 2D Vs cross-section for the riverside berm of the levee 1 and 2 are shown. The 2D Vs cross-section for the riverside berm of levee 1 indicates that the subsurface mainly consists of three layers: a thin, very soft soil layer, a soft soil layer from the surface to approximately 16 m depth, and a medium dense sand layer.

The results of the CCR in Figure 5.12c show a thin clay layer (approximately 2m thick) at the surface, which is slightly thicker than estimated using the Vs data. Generally, the results from the CCR are much noisy than other parts of the levee. This makes it difficult to characterize the material below the top clay layer, but two sections (Station 96+00 and 130+00) with lower resistivity values match up fairly well with the location of the old river bar zones. There is a possibility that the low resistive areas are indicators of high water content or internal seepage paths in the levee. However, due to the poor quality of the CCR data for these sections, there is a need for further investigations to determine the reason behind the low resistivity values. For sections where the resolution of CCR is inadequate or sections that are identified as high-risk zones, electrical resistivity tomography (ERT) could be a suitable alternative to CCR that has the capability of providing better resolution of subsurface conditions.

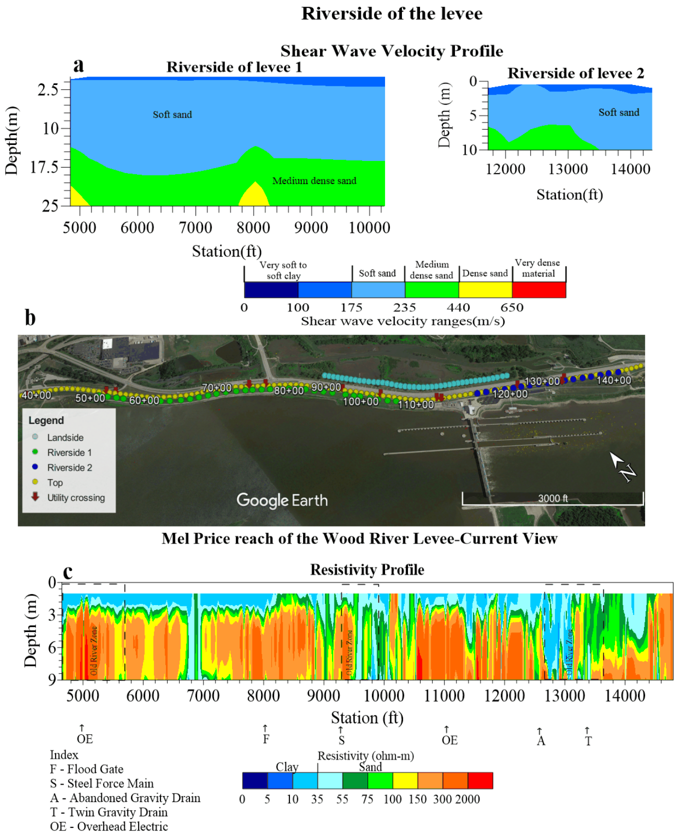

Figure 5.12- 2D cross section for the riverside berm of the Melvin Price reach of the Wood River levee, a) 2D Vs cross section b) current aerial image of area c) 2D CCR cross section. Areas where the old river bars previously existed and the location of major utilities crossing the levee are identified on the figures.

With the use of both CCR and MASW, one method can corroborate the results of the other. In cases where both methods resolve unexplained anomalies, more extensive geophysical investigations or invasive geotechnical investigations maybe needed. However, these can be more limited in scope rather than being conducted along the entire length of levee. More discussion regarding the combined use of CCR and MASW is provided in a later section.

5.7.5 Uncorrected N SPT-Vs correlation for the study area

Using the SPT borehole data and co-located Vs profiles along the landside toe portion of the levee, a power-type function, as shown in Equation 29, was developed.

$$V_S = A \times (N_{SPT})^B \tag{57}$$

Where A and B are regression coefficients. A total of 181 data pairs for the landside toe of the levee, which mostly consists of sand deposits, were used to develop the SPT-Vs correlation. Figure 5.13a represents the best-fit empirical correlation between the uncorrected N-SPT values and related shear wave velocities. The R^2 of 0.827 for 181 pairs of data is an indicator of a reliable correlation. In order to better evaluate the reliability of the proposed correlation, the normal consistency ratio (Cd, see Equation 58), which is defined as the ratio of the difference between the estimated and measured shear wave velocity to measured uncorrected N-SPT value, is calculated and the results are shown in Figure 5.13b.

$$Cd = (Vs_{measured} - Vs_{estimated})/(N\ SPT) \tag{58}$$

From Figure 5.13b, the average Cd value is close to zero, indicating that the estimated V_S values are very close to the measured values for N values greater than 5. For N values less than 5, the performance of the correlation is diminished due to variability of the N values in the very soft materials or difference in material type from most data points (i.e., clay versus sand).

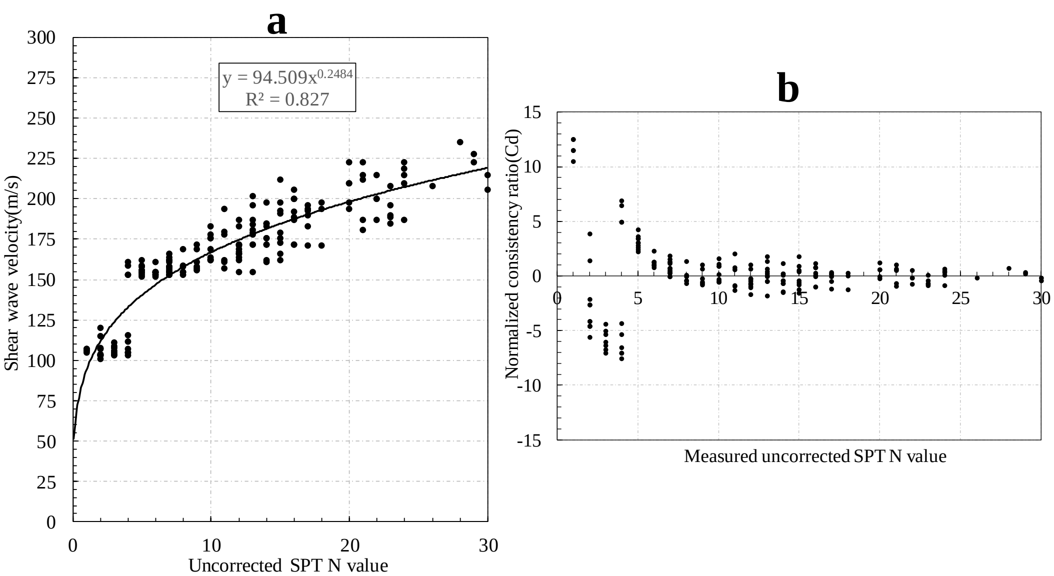

Figure 5.13- SPT-Vs correlation for the landside toe of the levee, a) Proposed SPT-Vs correlation for the study area, b) Normal consistency ratio (Cd) for the proposed SPT-Vs correlation.

Moreover, shown in Figure 5.14a is the scaled relative error in percent for the proposed correlation, which is calculated as:

$$E_r=100(Vs_{estimated}-Vs_{measured})/(Vs_{estimated}) \qquad (59)$$

From the figure, most of the estimated shear wave velocities from the proposed correlation are within 10% of the scaled relative error and only 5% of the estimated shear wave velocities have a scaled relative error higher than 15%, indicating the reliability of the proposed correlation for the study area. Also plotted in Figure 5.14b is the comparison of the estimated and measured shear wave velocities. As seen in this figure, the estimated shear wave velocity data points are between the lines 1:0.85 and 1:1.25, but the majority of the data points are scattered along line 1:1. Overall, the results of the statistical assessment illustrate the reliability of the proposed SPT-Vs correlation for the study area.

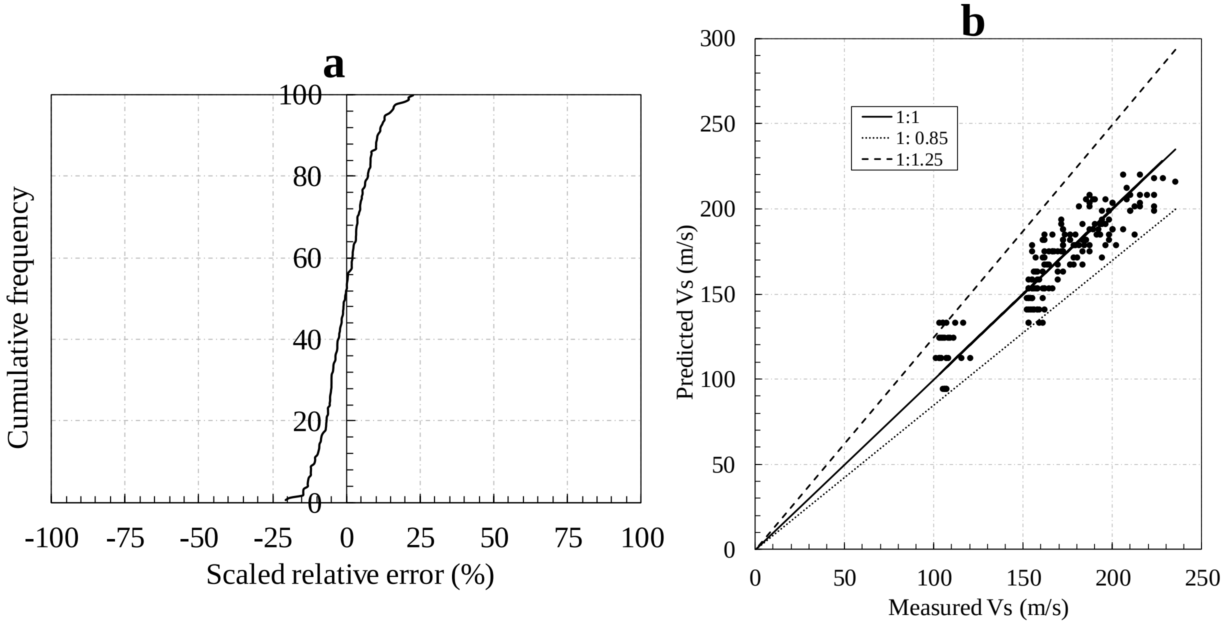

Figure 5.14- Statistical assessment of the proposed correlation, a) Scaled relative error of the proposed correlation, b) Comparison of the estimated and measured shear wave velocity.

To understand how the correlation developed in this study relates to previous SPT-Vs correlations, a comparison is shown in Figure 5.15 between the correlation developed in this study and correlations developed in previous studies for sand deposits. Summarized in Table 6, which is a modified version of the table provided by Fabbrocino et al. (2015), are the existing SPT-Vs correlations proposed in previous studies along with their soil type, number of data pairs, and the R^2 value. The lower and upper bounds for all proposed correlations are also plotted in Figure 5.15 along with their best-fit power function approximation. As observed in this figure, Seed and Idriss (1981), Athanasopoulos (1994), and Lee (1990) correlations are close to the upper bound and result in higher predicted shear wave velocities, whereas Raptakis et al. (1994) and Dikmen (2009) correlations are close to the lower bound and predict lower shear wave velocities as compared to the mean of the corrections. Other SPT-Vs correlations are closer to the middle bound.

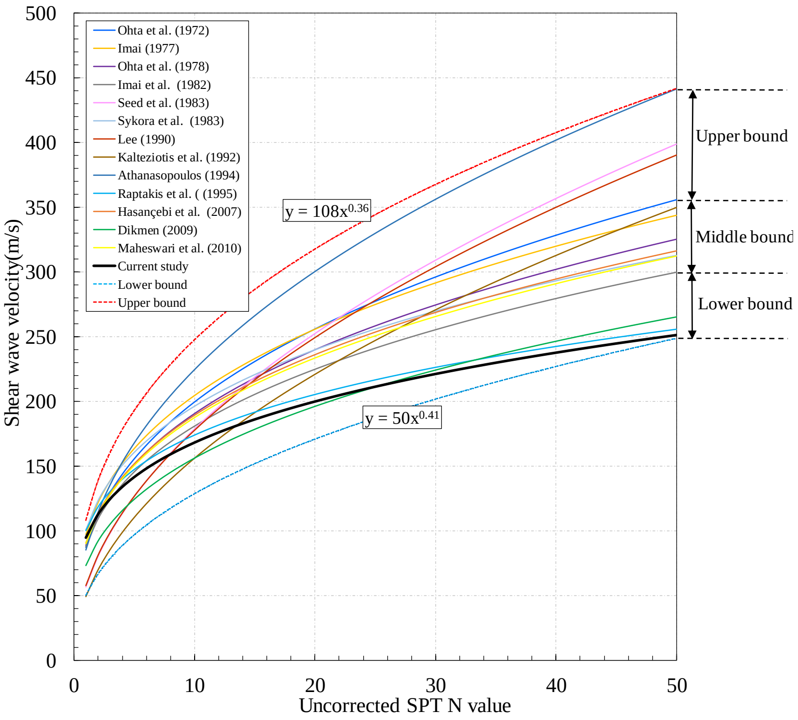

Figure 5.15- Comparison of the proposed SPT-Vs correlation with previous correlations. Upper, middle, and lower bound profiles are provided for comparison.

The proposed correlation from the current study falls into the lower bound zone, similar to those proposed by Raptakis et al. (1994) and Dikmen (2009) with the best agreement with the Raptakis et al. (1994) correlation. The agreement of this correlation with the lower bound correlations is believed to be driven by two characteristics of the site.

1. The majority of the N-SPT Vs pairs from the current study are from the soft to medium dense sand deposits with a maximum uncorrected blow count of 30. These soft to medium dense sand deposits are similar to the deposits used to develop the Raptakis et al. (1995) relationship. Most studies ignore the potential influence of the overall density of soil used in the correlation.
2. The effects of soil aging on the measured Vs values likely contributed to the lower bound behavior of the correlation. As discussed by Andrus et al. (2007), the geologic age of a deposit is one of the important factors controlling shear wave velocity in sands. Most of the soil deposits in the study area are categorized as young deposits (Holocene age) (Geotz 2016). As sand deposits age over time, the shear wave velocity of the deposits increase due to different process including changes in particles orientation and interlocking due to the load, change in cementation at particle contacts, and changes in the soil micro-structure (Schneider et al., 2004, Andrus et al. 2007). Because seismic stress wave methods, such as MASW, are small strain tests, they are influenced by the effect of aging on granular soil deposits resulting in higher Vs as deposit ages (Andrus et al. 2007, Wood et al. 2017). However, because the SPT test is a large strain test, the resulting N values are typically insensitive to aging effects in the sand. Given these facts, lower shear wave velocities for young Holocene deposits would be excepted compare to older deposits, and as a result, the SPT-Vs correlations

developed using young deposits should result in lower bound correlations similar to the one presented herein.

Table 6-Summary of existing SPT-Vs correlations developed for sand deposits

Author	**A**	**B**	**Soil type**	**All Data pairs**	**R^2**
Ohta et al. (1972)	87	0.36	Sand	100	-
Imai (1977)	97.2	0.323	Sand	100	-
Ohta and Goto (1978)	88.4	0.333	Sand	-	0.719
Imai and Tonouchi (1982)	87.8	0.314	Sand	-	0.69
Seed et al. (1983)	56.4	0.5	Sand	-	-
Sykora and Stokoe (1983)	100.5	0.29	Sand	97	0.84
Lee (1990)	57.4	0.49	Sand	22	0.62
Kalteziotis et al. (1992)	49.1	0.502	Sand/Silt	-	0.74
Athanasopoulos (1994)	85.3	0.42	Sand	-	0.68
Raptakis et al. (1995)	100	0.24	Medium sand	-	-
Hasançebi and Ulusay (2007)	90.82	0.319	sand	39	0.65
Dikmen (2009)	73	0.33	Sand	193	0.72
Maheswari et al. (2010)	100.5	0.262	Sand	200	0.84

Given these observations, it is important for users of SPT-Vs correlations to consider the overall stiffness and age of the soil deposits before choosing an appropriate correlation for a site. For typical levees, which are made of young soil deposits, a lower bound SPT-Vs correlation developed using similar soil deposits should be utilized.

5.8 Implication of the combined use of MASW and CCR surveys for levee evaluation

As discussed in the introduction, the section of a levee which fails during flood events is often related to differences in soil type (i.e. cohesive or non-cohesive) and soil stiffness within those sections, which are primary parameters affecting breaching and piping failures in such structures (Sills *et al.*, 2008). In this study, the strengths of MASW and CCR testing were combined to resolve the distribution and stiffness of cohesive and non-cohesive materials below the levee where no invasive testing was possible. Understanding the soil type throughout the levee is directly related to understanding the erodibility potential of the sections of the levee, which could lead to pipping failures (Briaud, 2008). The strength of the CCR technique was in the soil classification of near-surface soil layers, particularly those that had high degrees of saturation. Along the top of the levee, the surface clay layer was able to be resolved with a good degree of accuracy using CCR. However, CCR did not penetrate deep enough to characterize the deeper clay layer. With the addition of MASW, the deeper clay layer was also identified. This layer was classified using the Lin et al. (2014) reference Vs curves, which provided an accurate classification of soil type. However, for near-surface layers, the Lin et al. (2014) curves fell short of providing an accurate classification for the near-surface layers (<5 meters) as overburden stress has less influence on the Vs of shallow soil layers than for deeper soil layers. Therefore, combining the strengths of both methods, soils in the near-surface (0-9 meters) were classified using CCR and at deeper depths (>5 meters) using MASW to understand the entire distribution of soil type within the levee. For this particular levee, combining the methods proved valuable for identifying the paleo river bars which crossed under portions of the levee and eroded the deeper clay layer. These sections are considered to have contributed significantly to the formation of sand boils on the landside toe of the levee, leading to increase the hazard for the levee.

In addition to soil classification, co-located SPT and surface wave measurements on the landside toe of the levee were used to develop a site-specific SPT-Vs correlation, which can be used to understand the stiffness/strength of materials in the body and foundation of the levee where invasive testing was not possible. This correlation can be used to understand the design strength of the levee, which would not be possible using resistivity data alone. In addition, the SPT-Vs correlation for this levee was determined to be at the lower bound of SPT-Vs correlations from the literature. This lower bound behavior (lower Vs for a given SPT N value) is believed to be due to the medium dense sand used in the correlation, but also due to the lack of aging effects from the young soil deposits in the area. The aging effects of sand tend to increase the Vs of a deposit over time, with young deposits having a lower Vs than older deposits. As a result, when choosing a generic SPT-Vs correlation for relatively young deposits around a levee, the soil stiffness and age of the deposits used to create the correlation should be considered as these parameters can have a significant impact on correlated values.

Another interesting aspect of MASW and CCR surveys for levee evaluation is their capabilities for detecting potential problematic zones. As shown in the present study, while the MASW survey was able to resolve a variety of utilities, including drainage pipes, gas lines, and sewer lines crossing levees, CCR was more effective at detecting metal or highly conductive utilities that were not resolved using MASW. Given the fact that abandoned utilities could be the most susceptible locations for internal erosion through the body or foundation of levees, locating their positions is a crucial task for the evaluation of any earthen hydraulic structure. Moreover, MASW was determined to be particularly useful for detecting the location of the old river bars which crossed under the levee. The contrast in Vs between the sand and clay layers was effectively resolved at a depth of 10 meters, which was beyond the maximum depth of the CCR results. These river bars can contribute significantly to the hazard of a levee and are prime locations for the failure of the levee. The identification of the bars can allow selective repair of the levee, which would increase the resilience of the entire levee.

Overall, MASW and CCR surveys are used to complement the strengths and weaknesses of each other in order to characterize the soil type and stiffness of the entire levee body and foundation. With only one of the methods, critical blind spots would have been possible in the results. In locations where both methods provided useable data, the redundancy of the two methods prevented false positives in the near-surface due to noisy or poor data quality. In general, this study provides examples of how to build a site-specific correlation between geophysical results and invasive results and how to use the geophysical results with relationships such as the Lin et al. (2014) relationship to identify problematic sections of levees, which contribute significantly to the hazard of the levee.

5.9 Conclusion

MASW and CCR surveys were performed for over 6800 m along the top, the landside toe, and the riverside berm of the Melvin Price Reach of the Wood River Levee with the goal of mapping near-surface structure and providing information regarding potential problem areas along the levee. Based on the results of the present study, the joint use of MASW and CCR is a promising approach for evaluating earthen hydraulic structures. This method has the capability of resolving both soil type and soil stiffness, which are the main parameters causing levees' failure in past flood events. Both methods have strengths and weaknesses, but when the methods are used together, they can characterize the soil type and stiffness of the levee body and foundation.

Comparison of the laboratory and field testing with the joint use of MASW and CCR in the present study indicates that soil in the levees' internal body and foundation can be classified with confidence using MASW and CCR. CCR was found to be valuable when soil degree of saturation is high and the depth of interest is shallow. With the addition of knowledge of the water table location or even sparse in-situ data, the soil type can also be estimated with more confidence using CCR.

On the other hand, MASW was effective for the classification of soil located at deeper depths, where CCR was unable to measure. It was observed that without the combined use of CCR and MASW, some misinterpretations regarding soil type would have been made along the cross-section. Furthermore, MASW also provided valuable information about soil stiffness, which was in good agreement with SPT N values along the levee. Moreover, a site-specific SPT-Vs correlation was developed that can be used to estimate uncorrected SPT-N values from the continuous shear wave velocity information or vice versa in the study area. Comparison of the SPT-Vs correlation developed in the present study with those from previous investigations indicates that soil stiffness and geologic age are two important factors influencing such correlation. These factors have been ignored in most previous studies. When choosing some generic SPT-Vs correlations for future studies, the soil deposits and geologic age of the deposits should be considered, and likely, a lower bound correlation should be used for the typically young sandy deposits associated with vulnerable levees.

In addition, a variety of utilities, including drainage pipes, gas lines, and sewer lines crossing levees, were detected by primarily using surface wave methods but also, to a more limited extent, using resistivity. Resistivity was only effective at detecting metal or conductive utilities. This can have significant benefits if the location of abandoned utilities is not known as any elements which cross the levee can be primary locations for internal erosion to take place. Furthermore, MASW and CCR were able to detect several potential problem areas where old river bars crossed under the present-day location of the levee. These weak spots especially old river bars can be prime locations for piping through the foundation of the levee, which may have led to sand boils during large flooding events and can be a potential area of failure of the levee. Being able to rapidly identify soil type, soil stiffness, and potential problem zones along a levee in a non-destructive way provides a significant benefit to levee owners as the only repair of discrete areas is needed to significantly improve the resilience of the levee system.

Overall, the combined use of CCR and MASW surveys provides a rapid and near-continuous means to evaluate levees and earthen dams. The methods were shown to be capable of detecting many common defects in levees.

6 CHAPTER 6: APPLICATION OF GEOPHYSICAL METHODS FOR LANDSLIDE HEALTH MONITORING

6.1 Chapter overview

This chapter details the application of MASW and MHVSR methods for evaluating the conditions of two active landslides in Arkansas, U.S., that have recently experienced considerable slope movements. The geophysical measurements were processed and interpreted to identify the main reasons behind the continued slope movements for these sites and help for future rehabilitation efforts. The results are provided in the form of a journal paper published in Landslide Journal.

6.2 The MHVSR Technique as a Rapid, Cost-effective, and Noninvasive Method for Landslide Investigation: Case Studies of Sand Gap and Ozark, Arkansas, USA

Reference

Rahimi, S., Wood, C. M., & Bernhardt-Barry, M. (2021). The MHVSR technique as a rapid, cost-effective, and noninvasive method for landslide investigation: case studies of Sand Gap and Ozark, AR, USA. Landslides, 1-16.

6.1 Abstract

Landslides with a shallow and complex bedrock layer, where bedrock topography affects the stability of the slide, are a widespread phenomenon. The current methods for evaluating such landslides include conventional in-situ methods and array-based geophysical methods. However, these methods are not capable of characterizing the complete spatial extent of the bedrock layer cost-effectively and are difficult to conduct for steep slopes. Therefore, in this study, Microtremor Horizontal to Vertical Spectral Ratio (MHVSR) is proposed as an effective tool when used in conjunction with other methods to improve our understanding of the landslide. In this study, the method is used to make a tight grid of MHVSR measurements within the landslide. Using this method, a 3D image of bedrock topography can be created over a larger spatial extent to reveal the potential critical landslide zones. This method is employed for two active landslides that have recently experienced considerable movements. Using the MHVSR, several bowl-shaped features were detected in the bedrock layer, which were not detected using conventional invasive in-situ methods. These features play a key role in landslide behavior as they can trap water and create a fully saturated soft zone within the critical slide. Missing such key features in the geologic model of the landslide can lead to errors in the slope stability models and cost overruns in rehabilitation efforts. The grid pattern MHVSR method used in this study offers a simple, rapid, and cost-effective tool for landslide site characterization for sites with shallow and complex bedrock topography.

Keywords: Landslide, Geophysical testing, MHVSR, MASW, Shallow landside triggering, complex bedrock topography.

6.2 Introduction

Landslides are recognized as one of the major global natural hazards that have severe direct and indirect consequences. Landslides are particularly common for highway alignments passing through mountainous regions with a shallow and highly variable bedrock layer within the landslide, where the topsoil layers can easily become fully saturated during wet seasons. This is a growing concern in many countries due to the recent climate change that has led to more severe and unpredictable rainfall events. For highway alignments located within a potential landslide, considering the traffic loads being applied to the slip surface, the slope can easily translate into a moving mass. While this issue is unavoidable or even expected in certain areas, failing to fully understand the bedrock layer of such landslides with shallow and complex bedrock topography can lead to errors in slope stability models and increase the remediation costs.

Conventionally, subsurface conditions of landslides (i.e. bedrock layer) are assessed using spatially limited invasive in-situ testing (e.g. Standard Penetration Test or Cone Penetration Test). These methods provide an acceptable level of accuracy for sites where the bedrock layer is consistent in-depth and thickness. However, significant errors can occur in the bedrock topography model created using limited borings for landslides with highly variable and complex bedrock topography. This is because these methods only provide information regarding the bedrock at discrete locations (i.e. boring logs), and bedrock location is estimated based on engineering judgment between the available discrete testing locations. Therefore, the key missing information in the existing methods for landslide investigation is the spatial variation of the bedrock layer within the entire landslide area, an aspect that has not received enough attention in the literature. This is because it is very difficult and not often economically feasible to generate a 3D image of bedrock topography across the landslide using conventional methods, particularly for steep slopes. Therefore, there is a need for methods capable of providing an accurate 2D/3D image of bedrock topography for slope stability models or remediation efforts of landslides where bedrock is a key feature. Geophysical methods can be utilized for this purpose to provide additional resolution between borings (Jongmans *et al.*, 2007; Delgado *et al.*, 2021; Rahimi *et al.*, 2021a).

Among all the available geophysical methods, electrical resistivity and seismic methods are most commonly used for landslide investigations. Resistivity methods are valuable for rain-induced landslides as they can detect the highly saturated zones within the landslide (Naudet *et al.*, 2008; Perrone *et al.*, 2014; Lu *et al.*, 2021; Falae *et al.*, no date). Additionally, since the landslide body is typically associated with low resistive materials, the potential landslide body can be detected to some extent using the resistivity methods (Lapenna *et al.*, 2003; Bichler *et al.*, 2004). For example, Friedel et al. (2006) used Electrical Resistivity Tomography (ERT) to explore the cause of a series of landslides that happened in May 2002 in North Switzerland. Merritt et al. (2014) identified some flow regions along an active landslide in North Yorkshire, UK by generating a detailed 3D image of the subsurface using the ERT method.

Seismic methods that have been widely utilized for landslide investigations include seismic refraction and Multichannel Analysis of Surface Waves (MASW) (Park et al. 1999). These methods measure seismic waves, either body waves or surface waves, propagating through the subsurface layers. These methods have gained popularity in recent years for near-surface site characterization as they can provide a higher resolution image of subsurface layering compared to the other geophysical methods (e.g. resistivity methods) (Wotherspoon *et al.*, 2013; Foti *et al.*, 2014; Rahimi *et al.*, 2019c). Additionally, the resulting P-wave (V_p) or shear wave velocity (V_s) profile developed from the seismic methods provides fundamental properties of geo-materials that can be used to estimate other geotechnical properties using empirical correlations (Akin *et al.*, 2011; Fabbrocino *et al.*, 2015; Rahimi *et al.*, 2020d). For landslide investigations using seismic methods, the body of the landslide can be separated from the unaffected zone based on the velocity contrast observed at the subsurface. Moreover, the water table location or the saturated zone can be determined using P-wave refraction. Several studies have employed seismic methods for landslide investigations (Peng *et al.*, 2017; Berti *et al.*, 2019). For instance, Xu et al. (2016) detected the critical slip surface for a landslide in China based on the variation of V_s in the subsurface using both active and passive seismic methods.

The combined use of resistivity and seismic methods has also been used for landslide investigations (Hibert *et al.*, 2012; Perrone *et al.*, 2014; Okada *et al.*, 2019). For example, Okada and Konishi (2019) conducted both ERT and seismic methods on a rain-induced landslide in Japan to locate the critical zones of the landslide.

While both resistivity and seismic methods can be considered as reliable non-destructive techniques for landslide investigations, it is difficult and time-consuming to apply these array-based geophysical methods for rough terrain and steep slopes. Given that most landslides occur on steep slopes, sometimes densely covered with trees, there is a need for another method that can be utilized for such rough terrain. Additionally, for landslides with complex bedrock topography where a full understanding of the bedrock layer is required, creating a 3D image of the bedrock layer using resistivity or seismic method is costly and time prohibitive. In this respect, the single station microtremor horizontal to vertical spectral ratio (MHVSR) (Nakamura, 1989) method can be considered as a suitable complement or alternative to the resistivity and seismic methods for bedrock mapping.

The MHVSR method is a common passive geophysical method that has been widely utilized for seismic microzonation and estimation of fundamental site frequency (fr) (Eker *et al.*, 2015; Wood *et al.*, 2019b). This method is based on the analysis of the ratio between the amplitude of horizontal and vertical components (H/V) of microtremors or environmental noise. Generally, the noise wavefield and the peak H/V are dominated by surface waves (ellipticity of Rayleigh waves); however, the effects of body waves cannot be neglected in some conditions (Arai *et al.*, 1998). The amplitude of the surface waves and the H/V peak is a function of the source properties and subsurface velocity structure, but for a given source, the H/V peak is mainly controlled by the subsurface velocity structure. Studies have proven that the peak of the

MHVSR typically occurs at or close to the fundamental frequency (fr) of the site, which indicates the presence of a sharp V_s impedance contrast (ratio) in the subsurface (Malischewsky *et al.*, 2004; Yilar *et al.*, 2017). The impedance ratio (IR) is defined as the ratio of the product of mass density and V_s of two layers.

If a peak satisfies the requirements of a reliable peak (SESAME 2004; Rahimi et al. 2020), it can be used to estimate depth to the impedance contrast (i.e. bedrock) of the site. Using the MHVSR method, the locations of sharp impedance contrasts can be resolved, which may be related to the interface of the slide and unaffected zones. Moreover, it is possible to create a 3D map of bedrock topography rapidly and cost-effectively using a grid of MHVSR measurements. This is one of the main advantages of the MHVSR method over slower array-based geophysical methods for landslides with a complex bedrock topography where variation in the bedrock depth is a key factor for reliable landslide analysis. Creating such a 3D map with the same resolution using any array-based geophysical methods would significantly increase the cost and time of a project. Furthermore, the MHVSR method is a much simpler method in terms of data processing and data interpretation compared to the other commonly used geophysical methods for landslide investigation. Therefore, even though the MHVSR method has been rarely used for bedrock mapping for accurate slope stability models and remediation efforts in the literature (Burjánek *et al.*, 2010; Panzera *et al.*, 2012), it allows for rapid and cost-effective bedrock mapping, can be easily utilized for any site conditions, and only requires an independent single station measurement instead of an array of sensors. The MHVSR method can be used to complement the results from drilling and sampling or other array-based geophysical methods, or it can be used to locate some critical zones of the landslide to optimize the plan for further field measurements using more expensive methods.

This study presents the results of the geophysical field measurements for two active landslides (Sand Gap and Ozark) in Arkansas, USA, where bedrock topography is complex and is believed to have significant impacts on slope movements. In this regard, different geophysical methods were employed, including MHVSR, MASW, P-wave refraction, and ERT. The MHVSR was used as the primary technique of this study to generate a high-resolution 3D image of the bedrock topography across the entire landslide areas. Therefore, this study aims to investigate the reliability and efficiency of the MHVSR method as a potential candidate to complement conventional in-situ methods or array-based geophysical methods by providing information across a larger spatial extent for landslide investigations. It is worth mentioning that this study only focuses on landslides with shallow and complex bedrock topography, where bedrock is a key feature for landslide stability. The study area, site background, and recent movements of each landslide are presented first. This is followed by the field measurements that include a tight grid of MHVSR stations within the landslide areas along with the MASW, P-wave refraction, and ERT survey lines conducted parallel to the landslides and a brief explanation regarding data processing. Finally, the results are discussed with regard to the potentially unstable zone of each landslide.

6.3 Study areas

Two active landslides that have recently experienced slope movements (Ozark and Sand Gap) were selected in Arkansas, United States. Complex and highly variable geologic environments were expected for both sites. A brief explanation regarding the site stratigraphy and background is provided below.

6.3.1 Ozark site

The Ozark site is located just North-West of Ozark, Arkansas, along I-40 westbound, as shown in Figure 6.1. An orthomosaic image of the tested area (see Figure 6.1a) along with the areas where long cracks were observed during the field inspection in 2019 are shown in this figure. According to the geology background and pre-existing borings, the entire soil profile of this site consists of a shale rock formation, overlain by a stiff/very stiff clay layer with gravel. From the borings, the soil layering includes stiff to very stiff clay or sandy clay with rock fragments with SPT N values ranging from 5-15 to 30-40.The site slopes from South to North with a 30-40% grade.

After the construction of the highway alignment, slope movements and settlement were observed along this section of the highway. Due to the continuous movements of the slope, it has been redressed several times over the last 40 years, with a major slope repair performed in 2018. This repair consisted of the installation of 100 soil/rock anchors and horizontal drainage in three levels at the top section of the landslide. While this slope repair has likely prevented a global slope failure, the cracks and the slope movements have continued to occur even after the repair. The slope movements have caused several long and thick longitudinal cracks, including a crack along the westbound lane with a length of approximately 150 m that starts from the pavement and moves eastward (see section 1 in Figure 6.1a and b) and additional cracking to the West side of the landslide (see section 2 in Figure 6.1a and c).

6.3.2 Sand Gap Site

The second study area, Sand Gap, is located in the Ozark Mountain region in Northwest Arkansas, along Arkansas Highway 7, as shown in Figure 6.1d. The Ozark Mountains are a part of the Boston Mountains characterized by narrow V-shaped valleys and vertical bluffs of limestone and sandstone. The terrain is dominated by steep hillslopes underlain by sharply dipping bedrock sequences. Interbedded shale and sandstone layers mainly make up the bedrock system within this site (Koehn *et al.*, 2019).

According to the pre-existing borings, the subsurface consists of a stiff clay layer with gravel, followed by bedrock. The bedrock layer mostly consists of sandstone, but a thin, highly weathered shale layer was also observed in one of the borings. The tested area contains two slopes: one from North to South and one from East to West, but the latter is the steepest slope where several cracks in the pavement are observed and shown in Figure 6.1e and f.

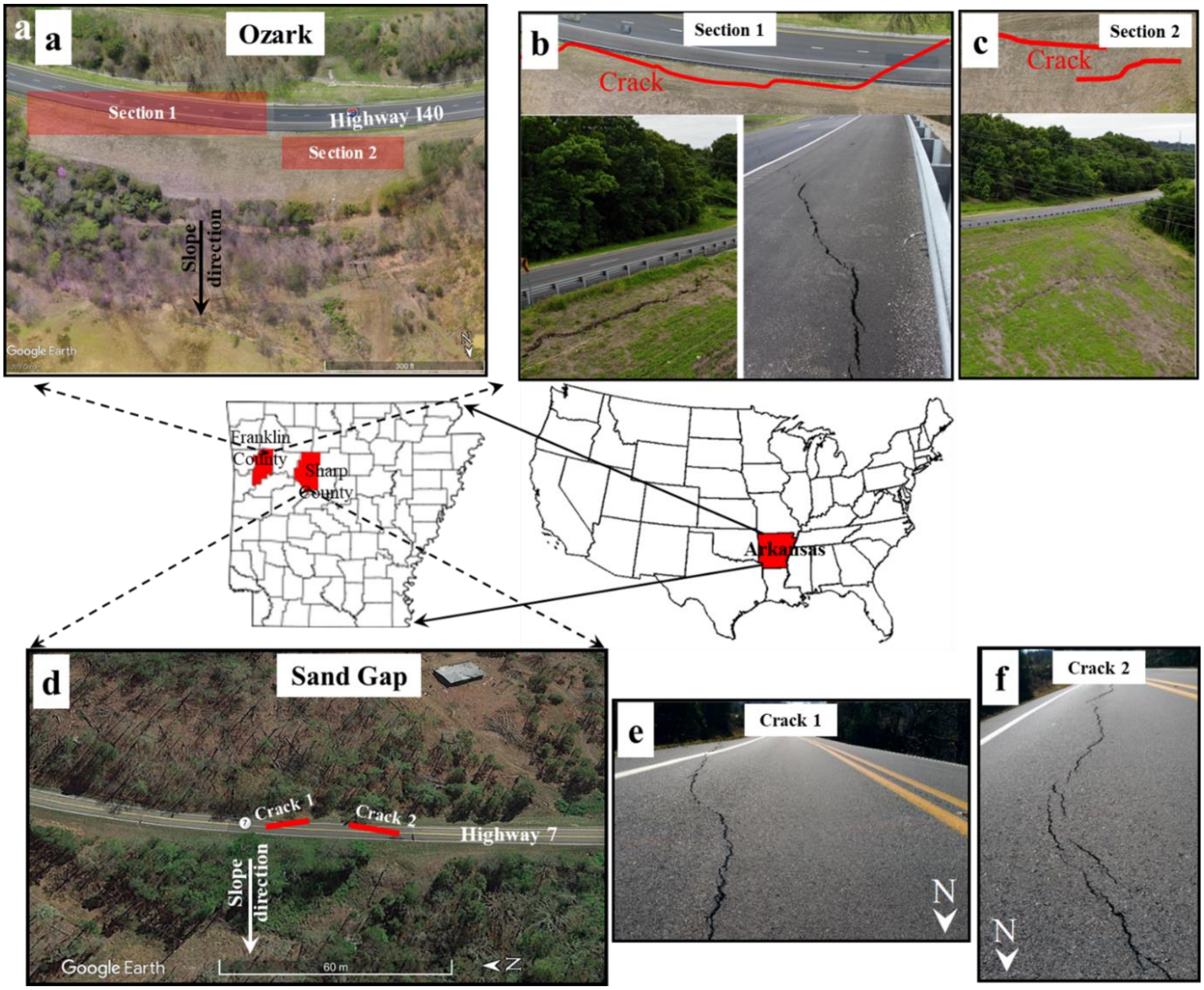

Figure 6.1- Study areas and landslide movements observed. a) Ozark site, b) cracking observed in section 1, c) cracking observed in section 2, d) Sand Gap site, e) crack 1, f) crack 2.

6.4 Methodology for the use of MHVSR for landslide studies

Shown in Figure 6.2 is the flowchart of the proposed method for the generation of a 3D map of bedrock topography using the MHVSR method. In this method, a tight grid of MHVSR measurements should be conducted across the landslide. The spacing between the measurements is recommended to be between 15-30 m, depending on the required resolution of the bedrock layer. MHVSR measurements are then processed individually to identify peaks that satisfy the requirements of a reliable peak with a stratigraphy origin, as described in detail in the next section. MHVSR measurements that fail to satisfy the criteria of a reliable peak with stratigraphy origin should be removed from the final results. The average V_s is then estimated either from direct field measurements (e.g. MASW testing) or empirical correlations between V_s and other geotechnical properties of soil. While direct field measurement of the average V_s is preferred, this is not always economically feasible. Therefore, the average V_s can also be back-calculated using the boring information and empirical correlations such as SPT N-V_s correlations (Fabbrocino et al., 2015; Rahimi, Wood, & Wotherspoon, 2020b). Moreover, for sites where information regarding soil type and soil stiffness are available, the reference V_s curves, which are available for various soil types (Lin *et al.*, 2014; Rahimi *et al.*, 2019d), can be used to generate a representative V_s profile for the site to estimate the average V_s. Using the reliable peak from the MHVSR measurements and the average V_s, depth to bedrock is estimated at each MHVSR station using the quarter-wavelength equation:

$$H= (V_{s,avg}/4f_r) \tag{60}$$

Where H is the thickness of sediments above the sharp impedance contrast, $V_{s,avg}$ is the average V_s of the materials above the sharp impedance contrast, and f_r is the frequency associated with the peak MHVSR. Finally, a 3D map of bedrock topography can be created by combining the information from the surface elevation and bedrock location estimated at each MHVSR station.

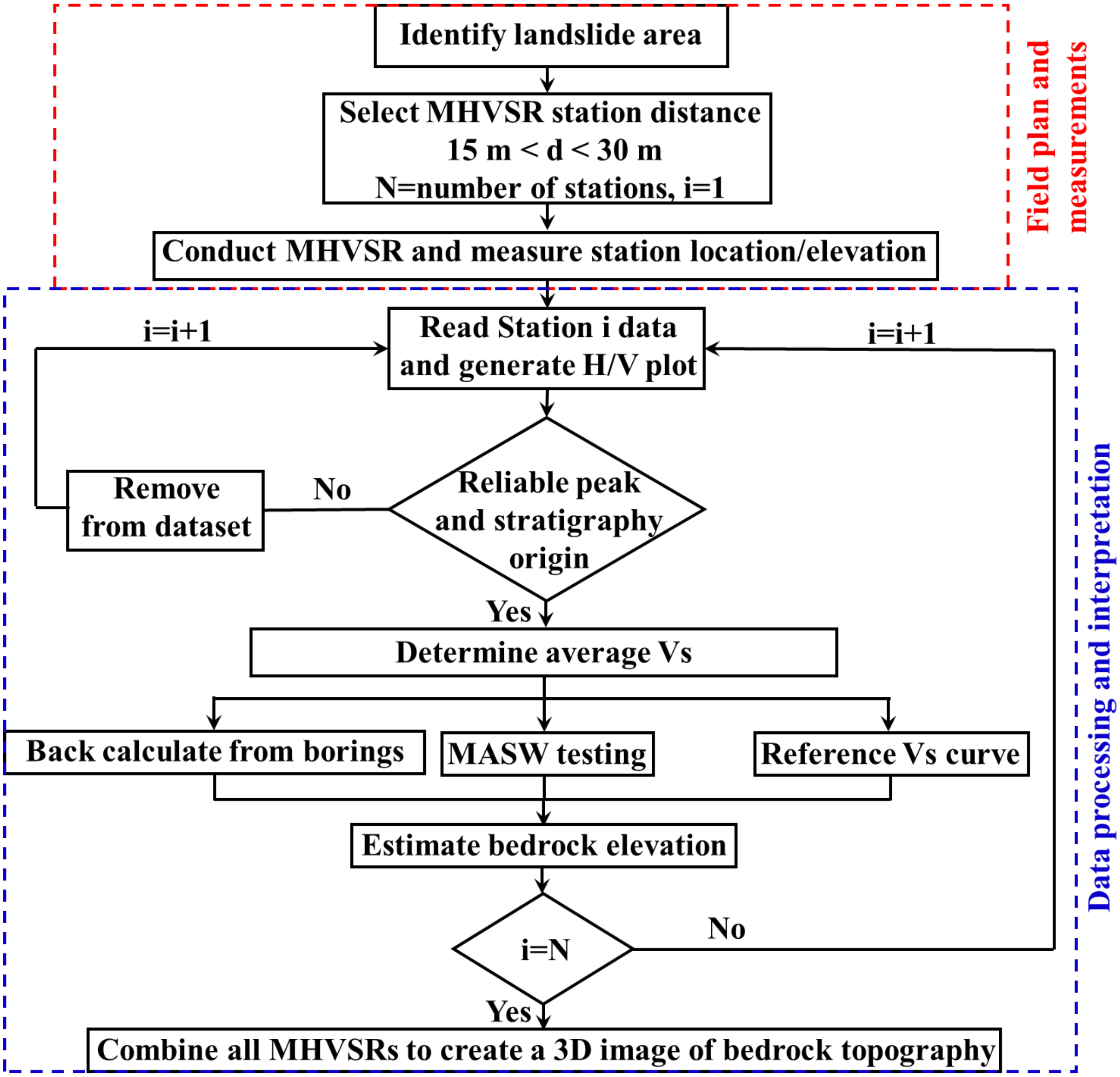

Figure 6.2- Flowchart of the proposed method for generation of 3D bedrock topography for landslide investigations.

6.5 Field measurements and data processing

Information regarding the field measurements and data processing of the MHVSR, MASW, and P-wave refraction methods is provided in this section. For the ERT method, since this information is provided in detail in Koehn et al. (2019), only the results of the ERT testing are included in this paper.

In this study, all the field measurements were taken simultaneously to save time during the field measurements. However, it is recommended to conduct a tight grid of the MHVSR measurements along with some limited measurements of other geophysical methods (e.g. MASW and ERT) in the initial phase to acquire a better understanding of the subsurface layering over a large spatial area and to identify any critical sections across the landslide. Then, the critical sections identified in the MHVSR results should be used as guides to plan for additional field measurements to further investigate the reason behind the slope movements and to evaluate the accuracy and the effectiveness of the MHVSR results.

6.5.1 Microtremor Horizontal to Vertical Spectral Ratio (MHVSR)

MHVSR testing was conducted within the landslide area in a tight grid pattern with an approximately 16 m spacing between measurements. Testing was conducted with a minimum recording time of 16 minutes for each station. The raw MHVSR data were processed in accordance with SESAME (2004). The raw data was divided into 2 minute non-overlapping time windows to allow for uncertainty in the MHVSR results to be estimated. The Fourier amplitude spectra (FAS) of each component was estimated for each time window and smoothed using a Konno and Ohmachi smoothing filter (Konno *et al.*, 1998). The geometric mean of the two horizontal components FAS was divided by the vertical FAS to calculate the amplitude of the MHVSR ratio.

The mean frequency peak of the MHVSR (f_M) and its standard deviation (σ) were computed from all individual time windows. A new frequency-domain window rejection tool was developed in Matlab and used in this study to reduce the uncertainty in the MHVSR peak frequency (f_I) estimates. This tool is very similar to the one developed by Cox et al. (2020), except it includes the amplitude in the window rejection algorithm, and it gives the users several more options for window rejection. In this tool, time windows that fail to satisfy the below conditions were first removed from the MHVSR data.

- Amplitude criterion: Amplitude > 2 at f_I
- Peak sharpness criterion: The difference between the amplitude at f_I and the mean amplitude for frequencies range between $[(2*\sigma - f_M), (2*\sigma + f_M)]$ is greater than 15%.

Then, the frequency-domain window rejection is conducted in an iterative process. The rejection process stops when the data satisfies the conditions defined by the user. The user needs to define the acceptable number of σ away from the f_M ($\pm 1*\sigma$ is recommended), as well as the acceptable σ as a percentage of the f_M value (5-10% is recommended). Moreover, users have the option to manually reject time windows at the final stage. This option is valuable when multiple peaks are present in the MHVSR.

Presented in Figure 6.3a and b are raw and adjusted MHVSR results, respectively, processed using the new frequency-domain window rejection tool, for an example MHVSR station with low-quality data. As shown in the adjusted MHVSR results in Figure 6.3b, this tool can improve the quality of the mean frequency peak and the final MHVSR results by removing all the unwanted time windows contaminated by noise. For this example, the iteration was stopped when the σ was less than 5% of the f_M ($\sigma = 0.39 < 0.05* f_M = 0.05*11.24 = 0.56$). From Figure 6.3b, the accepted time windows result in individual and mean peak frequencies that vary in a small frequency range, significantly enhancing the quality of the final MHVSR results. If the peak determined in this step relates to a stratigraphic origin, it was then used for further processing to estimate depth to the sharp impedance contrast of the site using Equation 39.

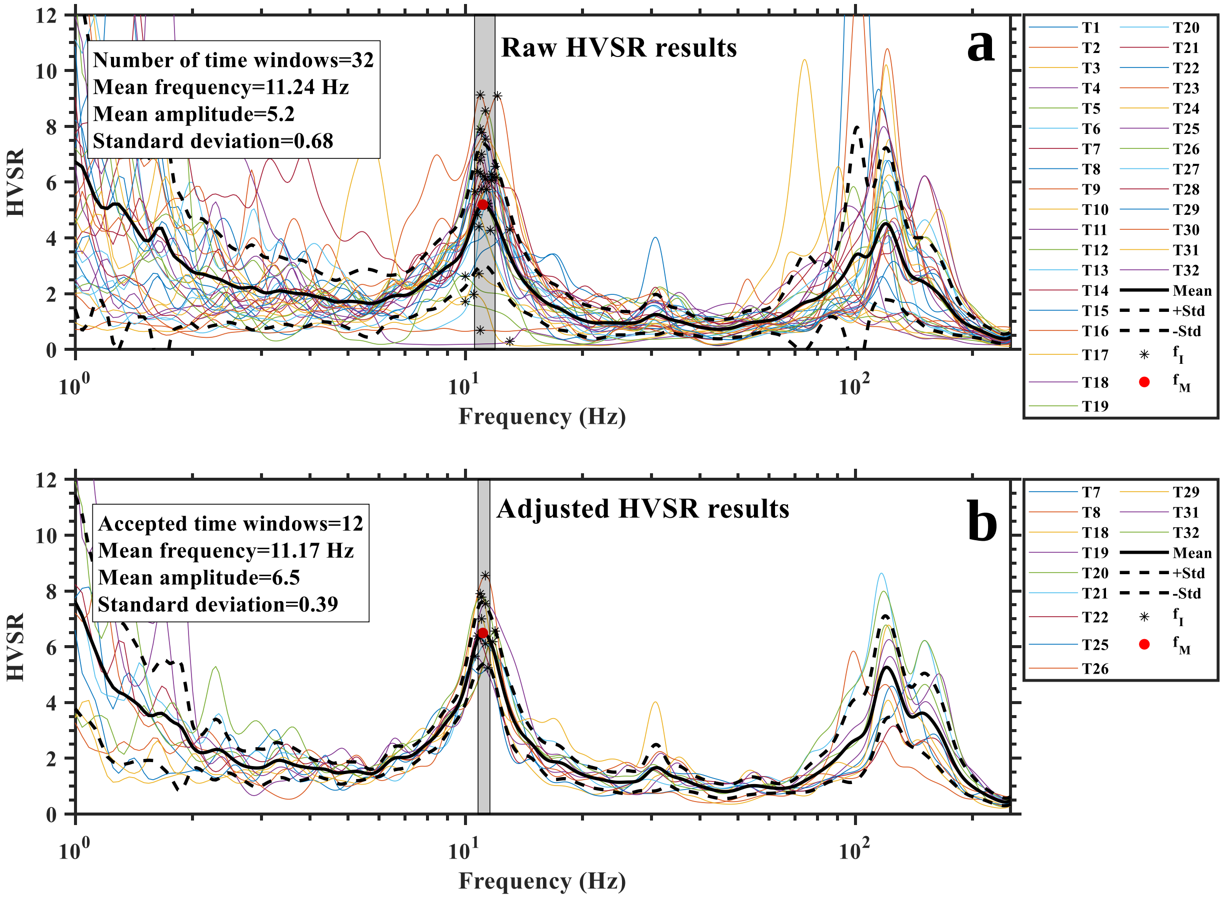

Figure 6.3- An example MHVSR data processing using new frequency-domain window rejection tool.

Four types of behavior were observed for the MHVSR measurements of the current study, including cases with a single clear peak (Figure 6.4a), cases with no clear peak (Figure 6.4b), cases with two clear peaks (Figure 6.4c), and cases with a broad peak (Figure 6.4d). The MHVSR measurements with a single clear peak (Figure 6.4a) indicate the presence of a sharp impedance contrast in the subsurface, whereas the MHVSR measurements with clear high and low-frequency peaks indicate the presence of two impedance contrasts in the subsurface.

MHVSR measurements with no clear peak were determined to be caused by an almost exposed rock unit with sediment thickness less than approximately 0.25 m. This indicates that the stiffness of the rock unit for these locations is almost constant within the depth of interest.

In this study, the procedures proposed in SESAME were followed to determine whether a peak has a stratigraphic or anthropic origin. For example, for cases with a broad peak, the peak is considered to have a stratigraphy origin if it remains stable by decreasing the smoothing bandwidth parameter (b). As an example, the variations of the MHVSR plot with a broad peak (Figure 6.4d) was evaluated using different smoothing bandwidths (b=40, 30, 20, and 10), and the results are presented in Figure 6.5. As shown in this figure, the MHVSR plot remains consistent for all smoothing bandwidths with negligible variations in the amplitude of the MHVSR. Additionally, the frequency associated with the peak MHVSR for this station corresponds very well with the peaks observed in the vicinity of this station. These indicate that the broad peak observed in the present study has a stratigraphy origin.

Based on the results of more than 150 MHVSR measurements for the Ozark and Sand Gap sites, it was observed that for Sand Gap, the majority of the measurements exhibit a single low-frequency peak ranging between 7-30 Hz. However, for the Ozark site, two clear peaks were observed for the majority of the MHVSR measurements, including a low-frequency peak ranging between 5-12 Hz and a high-frequency peak ranging between 40-100 Hz. The high-frequency peak (f_2 in Figure 6.4c) indicates the presence of an impedance contrast very near to the surface, which was determined to be the loose soil/very stiff soil interface according to the boring log, whereas the low-frequency peak (f_1 in Figure 6.4b) indicates the presence of a deeper impedance contrast at the site which was determined to be very stiff soil /weathered rock interface.

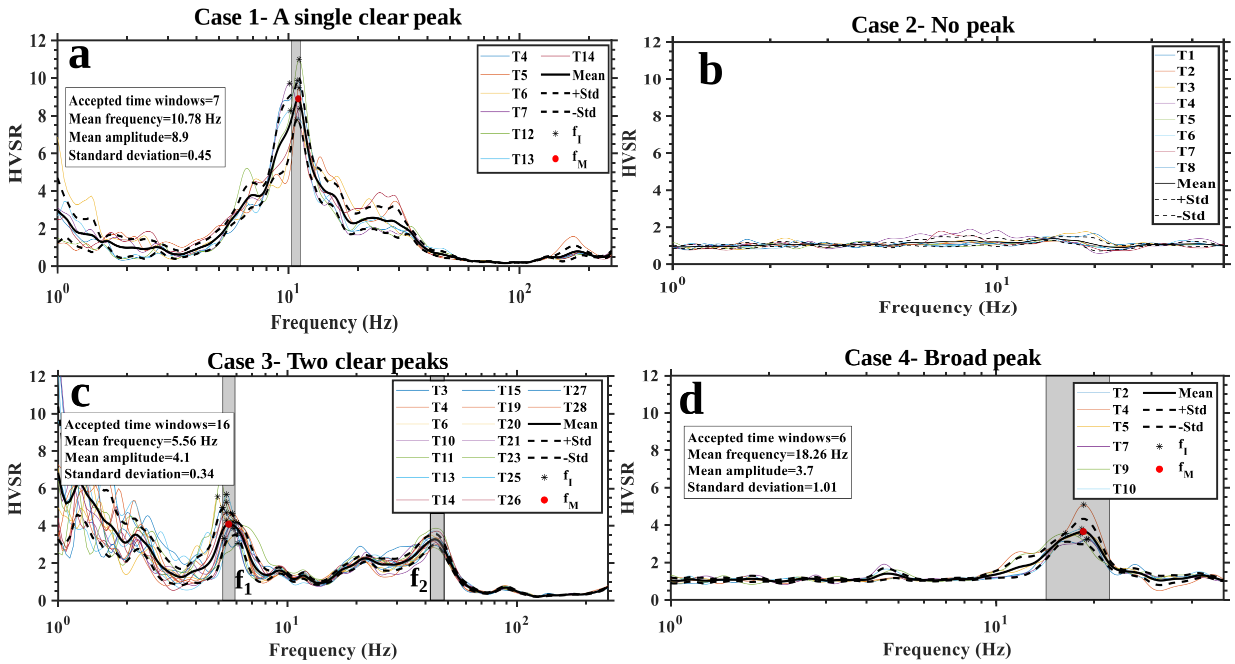

Figure 6.4- Different behaviors observed For the MHVSR measurements. a) MHVSR with a single clear peak, b) MHVSR with no peak, c) MHVSR with two clear peaks, d) MHVSR with a broad peak.

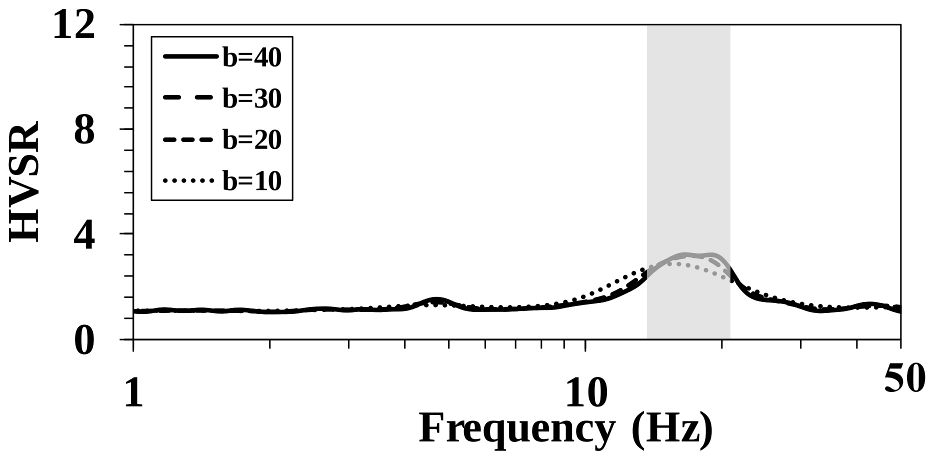

Figure 6.5- Variation of MHVSR by decreasing the smoothing bandwidth for the case of a broad peak.

6.5.2 MASW and P-wave refraction

MASW testing was conducted parallel to the slope to investigate the landslide conditions and evaluate the accuracy of the MHVSR measurements for landslide investigation. For each site, testing was performed using both Rayleigh and Love type surface waves to identify the method that resulted in higher resolution experimental dispersion data points. A linear array of 48, 4.5 Hz vertical/horizontal geophones with a uniform geophone spacing of 1 or 2 meters was used. A sledgehammer was used to generate Rayleigh or Love type surface waves. A minimum of three blows were stacked at each source offset to increase the signal-to-noise ratio of the data. For each array setup, waves were generated at multiple source offsets to decrease uncertainties regarding fundamental mode identification and also to generate multiple V_s profiles for each array setup using 24 geophone arrays within the larger 48 geophone array (Rahimi *et al.*, 2019a). Additionally, to be able to use the raw MASW shot data for the P-wave refraction analysis, a faster sampling rate of 0.125 milliseconds was used.

Provided in Table 7 is a summary table of MASW/P-wave refraction information for Sand Gap and Ozark sites. Given that the bedrock topography is expected to be complex and highly variable for the case histories, the P-wave refraction data were analyzed using the tomographic inversion method (SeisImager manual, 2019). This method models the subsurface layering using velocity cells and accounts for sharp changes in the P-wave velocity and layer thickness.

Table 7- MASW/P-wave refraction data acquisition configuration.

Site name	**Sampling rate (ms)**	**Number of setups**	**Number of geophones**	**Geophone spacing (m)**	**Number of shots**	**Array size (m)**	**Number of Vs profile generated**
Sand Gap	0.125	1	48	1	9	47	5
Ozark	0.125	3	48	2	25	94	11

For the MASW data processing, the Frequency Domain Beamformer (FDBF) method (Zywicki *et al.*, 2005) was used. For each frequency, the experimental dispersion data were determined by identifying the peak in the f-k spectra. Data points from different source offsets were combined to create the raw experimental dispersion curve. The fundamental mode of propagation was used as the final experimental dispersion curve. The final experimental dispersion curve from the MASW and the peak frequency from the MHVSR were inverted jointly within the Geopsy software package using weighting factors of 0.8 and 0.2, respectively (Teague *et al.*, 2018). The quality of the fit between the experimental and theoretical data was evaluated by visual inspection and the value of the calculated misfit parameter (Rahimi *et al.*, 2018). The median of the 1000 lowest misfit V_s profiles was taken as the final 1D Vs profile.

Two examples of the MASW and MHVSR joint inversion results that include the inverted V_s profile, the sigma ln(V_s), and the experimental MHVSR measurements along with the theoretical ellipticity curve are provided in Figure 6.6 and Figure 6.7. For the inverted V_s profiles in Figure 6.6a and Figure 6.7a, the best 1000 V_s profiles (solid gray lines), the lowest misfit V_s profile (dashed red line), and the median V_s profile (solid red line) are presented.

For Case 1 in Figure 6.6, the low-frequency peak (f_1=6.9 Hz) from the MHVSR measurement corresponds quite well with the peak from the theoretical ellipticity curve, as shown in Figure 6.6c. Additionally, one sharp impedance contrast is observed in the V_s profile in Figure 6.6c, confirming the MHVSR measurement results. This indicates that the peak from the MHVSR measurement is related to the stratigraphy of the site. For Case 2 in Figure 6.7c, two peaks are observed in the MHVSR measurement, including a low-frequency peak (f_1=8.2 Hz) and a high-frequency peak (f_1=20.9 Hz). While only the low-frequency peak was used in the joint inversion process to constrain the bedrock location, interestingly, two clear peaks are also observed in the theoretical ellipticity curve (red curve in Figure 6.7c), matching well with those from the experimental results. Moreover, these two peaks agree very well with the two sharp impedance contrasts from the V_s profile in Figure 6.7a. The presence of the two sharp impedance contrasts in the V_s profile indicates that the peaks from the MHVSR measurement have a stratigraphy origin rather than an anthropic origin.

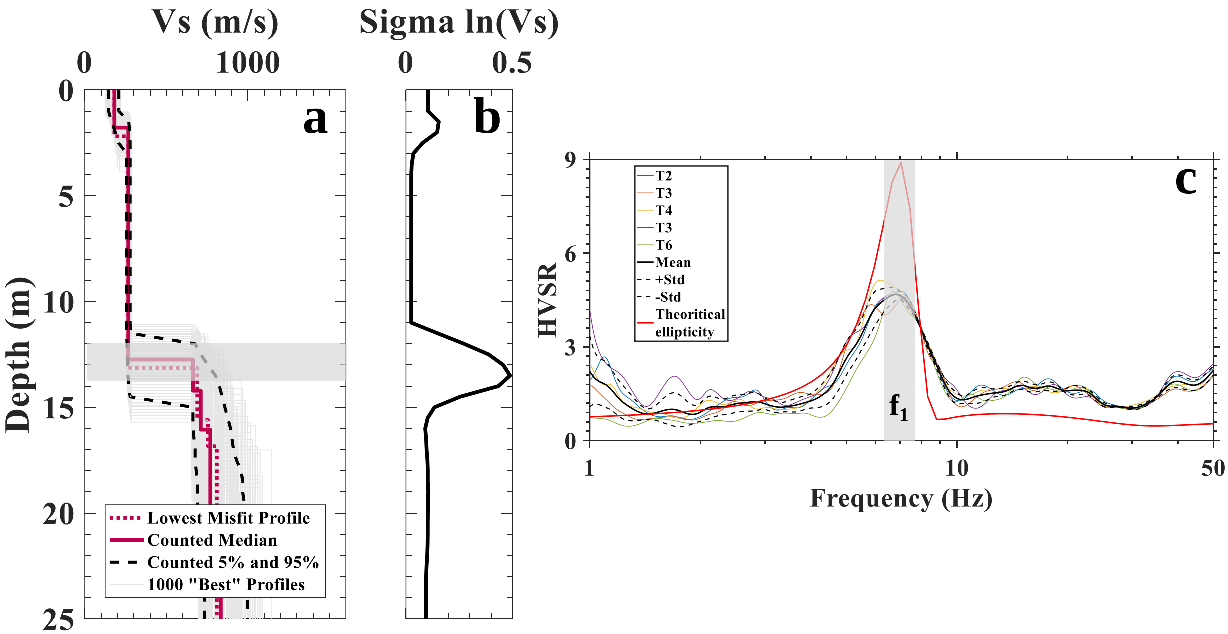

Figure 6.6- Case 1-Joint inversion results from the MASW and MHVSR measurements with one impedance contrast at subsurface. a) V_s profile, b) sigma ln (V_s), c) experimental MHVSR along with the theoretical ellipticity curve.

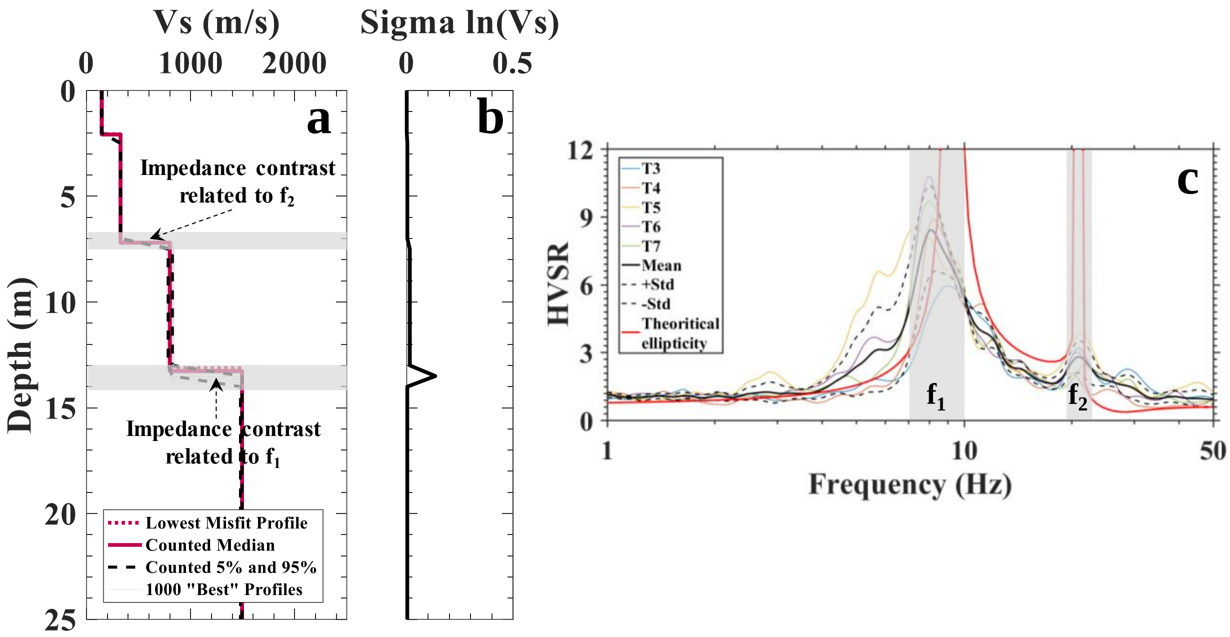

Figure 6.7- Case 2-Joint inversion results using the MASW and MHVSR measurements with two impedance contrasts at subsurface. a) V_s profile, b) sigma ln (V_s), c) experimental MHVSR along with the theoretical ellipticity curve.

6.5.3 Electrical Resistivity Tomography (ERT)

The ERT method was only used for the Sand Gap site to identify the high saturation areas along the critical section of the landslide. Testing was performed parallel to the landslide with a 56 electrode array with an electrode spacing of 0.91 m. A dipole-dipole/strong gradient array was used for testing and is an optimized array, which uses electrode configurations derived from the dipole-dipole and gradient arrays to collect data. This provides a measured dataset with a good vertical and horizontal resolution, allowing for the identification of vertical and horizontal discontinuities (Koehn *et al.*, 2019).

The raw data of the ERT surveys were inverted to produce a 2D plot of the true subsurface electrical resistivity using Earthimager 2D (2019). The Occam style inversion algorithm was used to find subsurface models within a pre-defined tolerance. Through an iterative process called inversion, the experimental apparent resistivity data measured in the field tests are compared with the theoretical response of the modeled subsurface to find the modeled subsurface which matches the experimental data best. The Gauss-Newton method is used to solve the inversion problem. The goodness of fit between the experimental data and theoretical model is evaluated based on the calculated misfit values (root mean squared, RMS) and L2-norm parameters. RMS values less than 10% and L2-norm values less than 1 are used as indicators of a relatively good and acceptable fit (Koehn *et al.*, 2019).

6.5.4 Comparison of the Geophysical Methods

For landslides with shallow and complex bedrock topography, where a full understanding of the bedrock layer is required, creating a 3D model of the bedrock topography using array-based geophysical methods (MASW, ERT, or P-wave refraction) is time- and cost-prohibitive. In this regard, the MHVSR can be used to fill in additional information regarding the bedrock topography between the other geophysical measurements in a rapid and cost-effective manner. To highlight the differences between the MHVSR and other array-based geophysical methods used in this study in terms of the rate of the field measurements and data processing, the Ozark site is discussed here as an example. The MASW, and P-wave refraction field measurements for the Ozark landslide that included 5 survey lines and only covered a portion of the landslide area took approximately twice as long as the MHVSR testing with more than 100 measurements that covered the entire landslide. Additionally, the MASW and P-wave refraction data processing took approximately five times longer than the data processing of the MHVSR. The rate of the field measurements for the ERT testing was almost similar to the MASW for the same number of survey lines, but the data processing of the ERT took approximately one-third the time as the MASW data processing. However, the data processing time of the MHVSR, which covered the entire landslide areas, was approximately half of the ERT. This highlights the advantage of the MHVSR method compared to the other array-based geophysical methods in terms of the rate of the field measurements and data processing, in which the entire landslide areas were able to be tested and processed in approximately half of the time required to collect 5 MASW, P-wave refraction, or ERT survey lines.

6.6 Results and discussions

6.6.1 Geophysical Investigation for the Sand Gap site

Shown in Figure 6.8a are the locations of the MHVSR measurements and the MASW and ERT survey lines for the Sand Gap site along with the two longitudinal cracks (see Figure 6.1e and f) that have been observed in the pavement. Thirty-six single station MHVSR measurements were carried out inside and outside the landslide on both the East and West sides of the highway. Besides the MHVSR measurements, MASW testing using Love type surface waves were conducted longitudinal to the slope (see Figure 6.8a) to further investigate the slope movements and validate the results and accuracy of the MHVSR measurements. The variations in the MHVSR peak frequencies within the landslide areas are shown in Figure 6.8a using graduated colors. As shown in this figure, for a line perpendicular to the cracks (i.e., parallel to the slope, East-West) such as the dashed white line in Figure 6.8a, the magnitude of the peak frequency first decreases and then increases as one moves down the slope. Using the peaks from the MHVSR and the $V_{s,avg}$ estimated from the MASW, depth to bedrock was calculated from Equation 1, and then the results were used to generate a contour map of bedrock depth for the landslide zone, as shown in Figure 6.8b. As observed in this figure, bedrock depth is very shallow within the landslide area, with depth varying from 2-12 m. The sharp variations in the bedrock depth are observed in the southwest landslide zone, where depth to bedrock changes from 9 m to 3 m in a short distance. This indicates the presence of a bowl-shaped feature (depression) in the bedrock, which can be considered as the potential slip surface zone. This is further investigated using the MASW and ERT methods since bedrock depressions within a slope zone can lead to instability issues during or after heavy rainfall events (Buttle *et al.*, 2004; Graham *et al.*, 2010; Lanni *et al.*, 2013).

Presented in Figure 6.8c and d are the pseudo 2D V_s profiles from the MASW and the resistivity profile from the ERT (Koehn *et al.*, 2019), respectively. As shown in these profiles, the same bowl-shaped feature is observed in the bedrock verifying the results of the MHVSR. Additionally, a very low resistive zone with resistivity close to the resistivity of water is observed very near the surface at the bowl-shaped feature location in Figure 6.8d. This indicates that the bowl-shaped feature in the bedrock layer is trapping water and creating a very soft zone at this location. This significantly impacts the landslide investigation, as it is explained later in the paper.

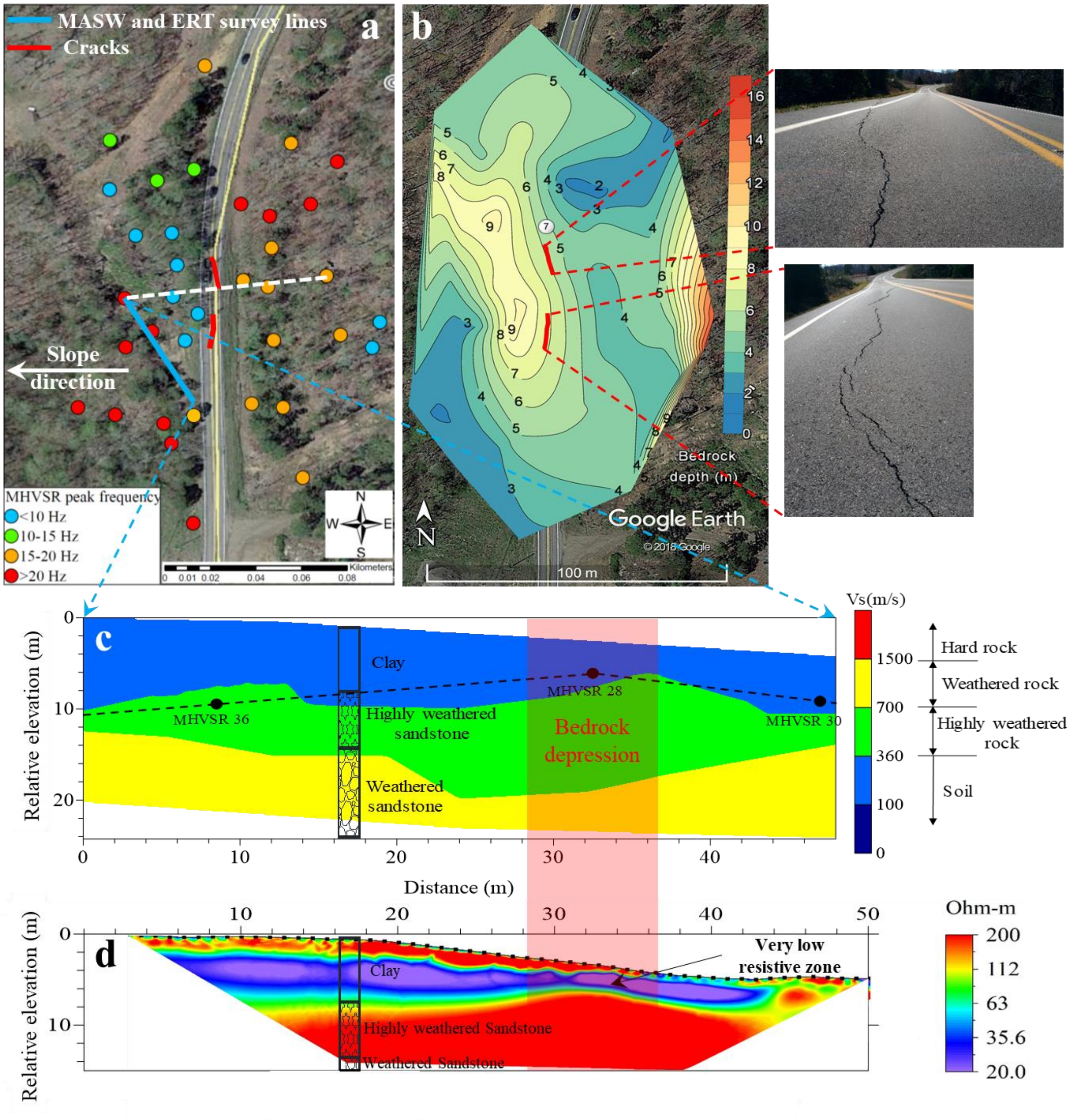

Figure 6.8- Sand Gap site. a) Locations of geophysical testing along with the MHVSR peak frequency variation shown in graduated color and the longitude cracks observed in the pavement, b) Contour map of bedrock depth from MHVSR, c) Pseudo 2D V_s profile from MASW, d) ERT profile.

To better illustrate the variations of the soil/bedrock interface across the landslide area at Sand Gap, the results of the MHVSR measurements were utilized to generate several cross-sections perpendicular to the highway. The location of these cross-sections (CS1-CS4) along with a 3D map of surface elevation and depth to bedrock estimated from the MHVSR measurements are shown in Figure 6.9. The 3D map of surface elevation was generated using the Kriging (Gaussian) interpolation method. As shown in CS2, the bedrock depth estimated from the MHVSR measurements and the boring log is slightly different, but overall, they are in good agreement.

Comparing the slope of the soil/bedrock interface beneath the highway alignment for the perpendicular cross-sections in Figure 6.9, relatively steeper rock-site slopes are observed for CS2 and CS3, indicating these sections are more susceptible to slope movements compared to CS1 and CS4 that have a gentle rock-site slope. Furthermore, a bowl-shaped feature in the bedrock layer is observed for CS2 and CS3 shown in Figure 6.9. Interestingly, these sections correspond quite well with the two longitudinal cracks observed in the pavement, as shown in Figure 6.8 and Figure 6.1.

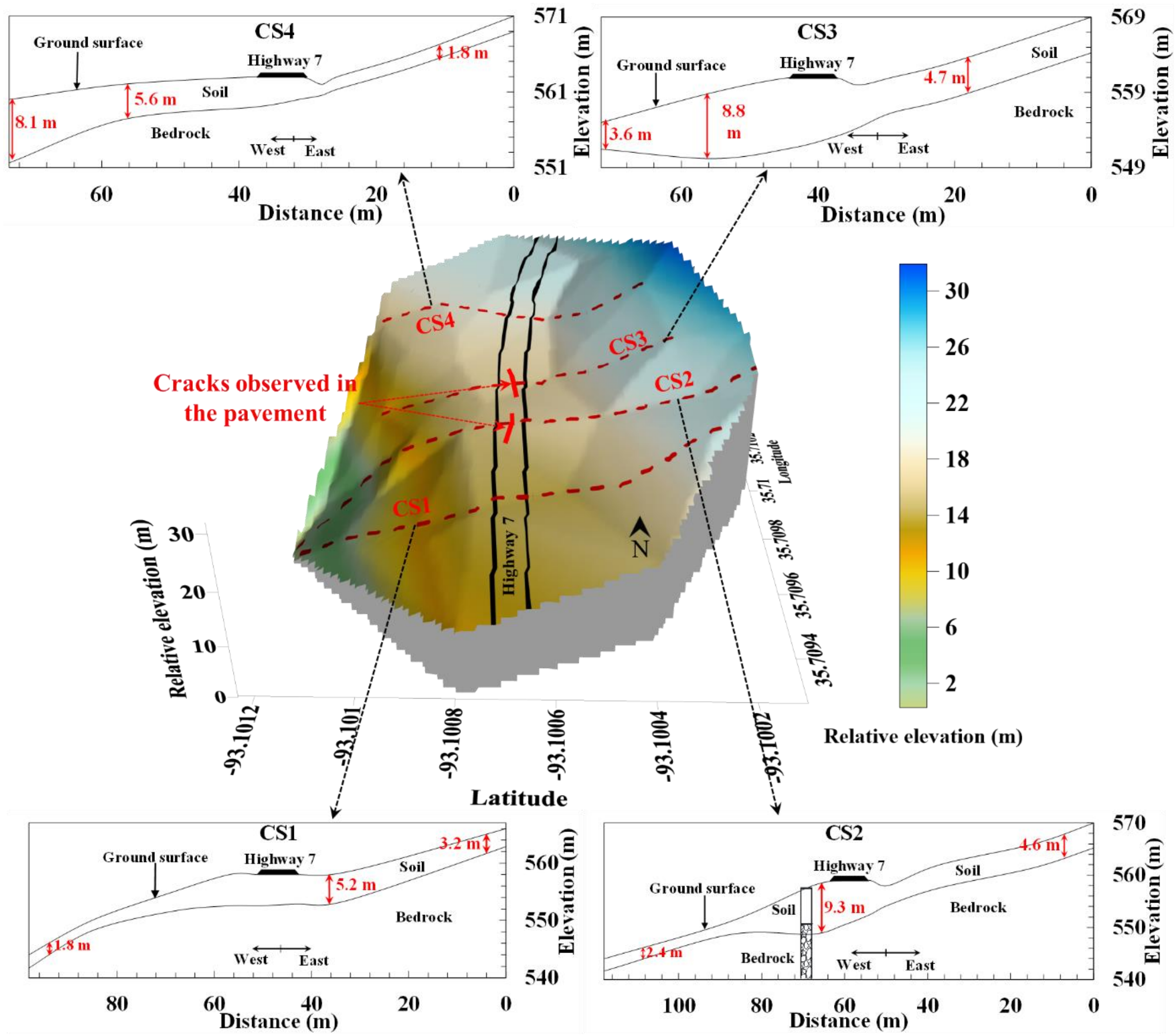

Figure 6.9- 3D plot of surface elevation along with the soil/bedrock cross sections for the Sand Gap site.

6.6.2 Geophysical Investigation for the Ozark site

A similar procedure was followed for the Ozark landslide to investigate the subsurface features contributing to the slope movements. The only difference between the investigations for the Ozark and Sand Gap landslides is that for the Ozark site, the P-wave refraction was used instead of ERT to determine the highly saturated areas. Shown in Figure 6.10 a, b, c, and d are the geophysical testing locations, a contour map of bedrock depth from the MHVSR, pseudo 2D

V_s profile from the MASW, and the 2D V_p profile from the P-wave refraction, respectively. Furthermore, the locations of several springs that were observed during the field measurements and a boring where the inclinometer readings were recorded are shown in Figure 6.10b with a blue star and black circle symbols, respectively. MHVSR testing of the Ozark site includes more than 100 stations, as shown in Figure 6.10a. A tight grid of the MHVSR measurements, spaced 15 m apart, were used at the toe of the landslide as the section of the interest. The variations of the magnitude of the peak frequencies from the MHVSR measurements are shown in Figure 6.10a using graduated colors. From Figure 6.10a, the magnitude of the peak frequencies is consistent for all the stations located on the top section of the landslide, while meaningful variations are observed in the magnitude of the peak frequencies for stations located at the toe. Using the peaks from the MHVSR measurements and the $V_{s,avg}$ from the MASW, a contour map of bedrock depth was created for the slope area, as shown in Figure 6.10b.

Bedrock depth is estimated to be very shallow for this site ranging between 6-14 m across the landslide area, as shown in Figure 6.10b. Examining depth to bedrock in Figure 6.10b, several depressions in the bedrock layer are observed at the toe, where the bedrock layer shallows drastically. These depressions in the bedrock layer correspond well with the four spring locations at the toe, as shown in Figure 6.10b. This indicates that the bowl-shaped features in the bedrock layer are trapping water at these locations, leading to a highly saturated and soft zone for these areas. During heavy rainfall events, depth to the groundwater table can decrease drastically at these locations, and so the trapped water appears at the ground surface as springs. To confirm the presence of bedrock depression observed in the MHVSR and identify the fully saturated areas along the critical landslide zone, co-located MASW and P-wave refraction measurements are shown for a line parallel with the slope, where the bedrock depression was observed in the MHVSR results.

Examining the variation of the bedrock depth from the MASW testing in Figure 6.10c, a similar feature (depression) is observed in the bedrock layer at the toe. From the 2D V_p plot in Figure 6.10d, it is observed that depth to the fully saturated area of the landslide, where the measured V_p matches the V_p of water, shallows drastically at the bedrock depression at the toe. This confirms the fact that the water is trapped at this location due to the depression in the bedrock layer. It should be mentioned that the V_p of 1600 m/s, which is used in this study to identify the fully saturated areas of the landslide, can be associated with either rock materials or fully saturated soils. In this study, this value is related to the fully saturated soils because the line associated with the V_p of 1600 m/s is much shallower than the true bedrock depth identified from the MASW measurements. This is illustrated in Figure 6.10c where the line associated with the V_p of 1600 m/s (the white dashed line) is overlaid on the pseudo 2D V_s profile.

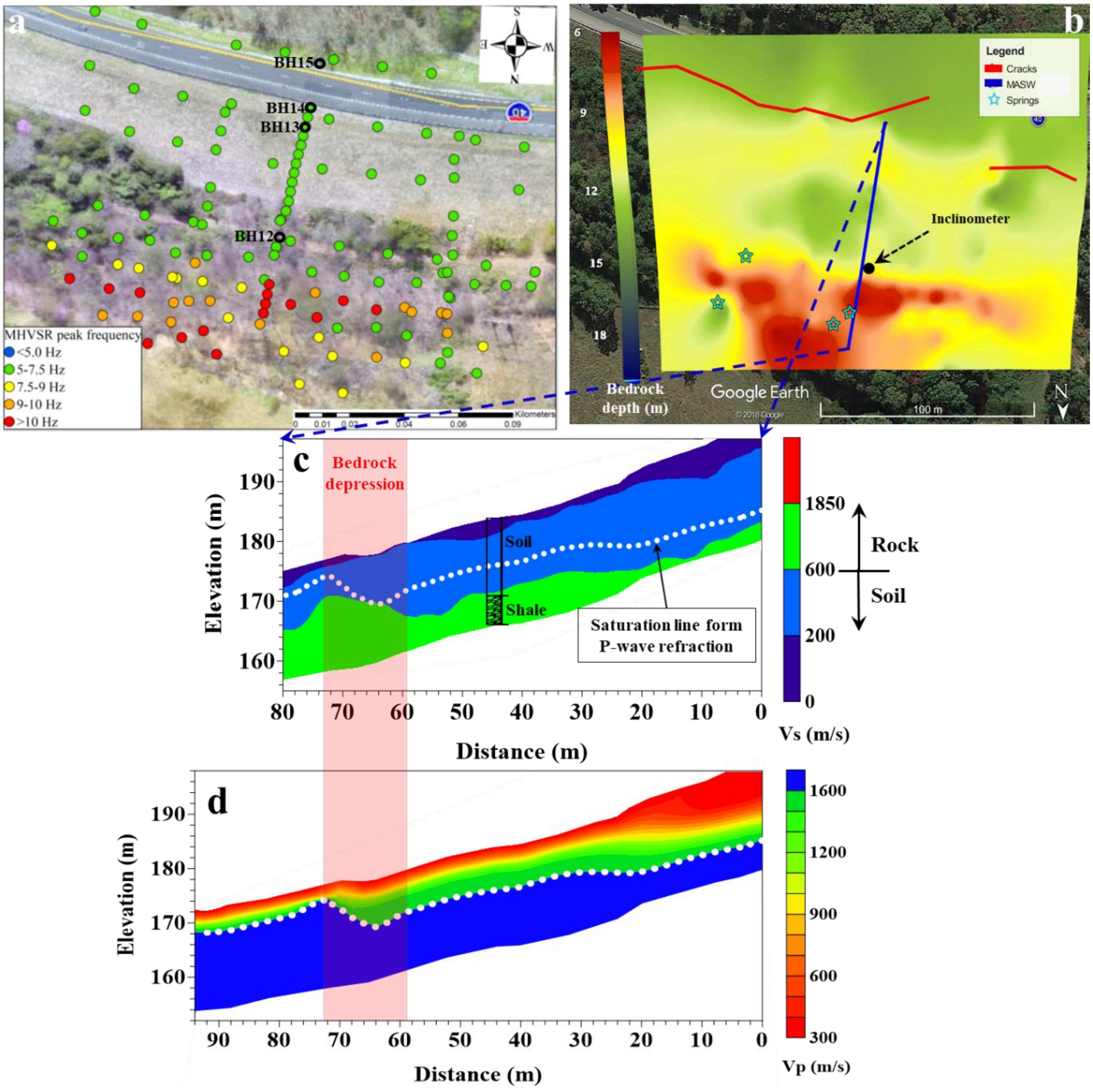

Figure 6.10- Ozark site. a) Locations of geophysical testing along with the MHVSR peak frequency variations shown in graduated colors and borings, b) Contour map of bedrock depth from MHVSR along with the cracks, springs, and inclinometer, c) Pseudo 2D V_s profile from MASW along with the fully saturated line from the P-wave refraction, d) 2D V_p profile from P-wave refraction.

Bedrock depths identified from the MHVSR testing are combined with the surface elevation determined from total station, GPS, and LiDAR data to create a 3D map of bedrock elevation across the landslide and the results are presented in Figure 6.11. Shown in Figure

6.11a, b, and c are the North-South, West-East, and East-West views of the 3D map of the bedrock elevation. From Figure 6.11, bedrock elevation decreases sharply at the toe, resulting in several depressions in the bedrock layer. The depressions in the bedrock layer are clearly visible in the West-East, and East-West views of the 3D map. It is worth mentioning that the depression in the bedrock layer observed in the 3D map in Figure 6.11 is also verified using the MASW testing. An example 2D Vs profile from the MASW measurements that confirmed the depression in the bedrock is shown in Figure 6.10c.

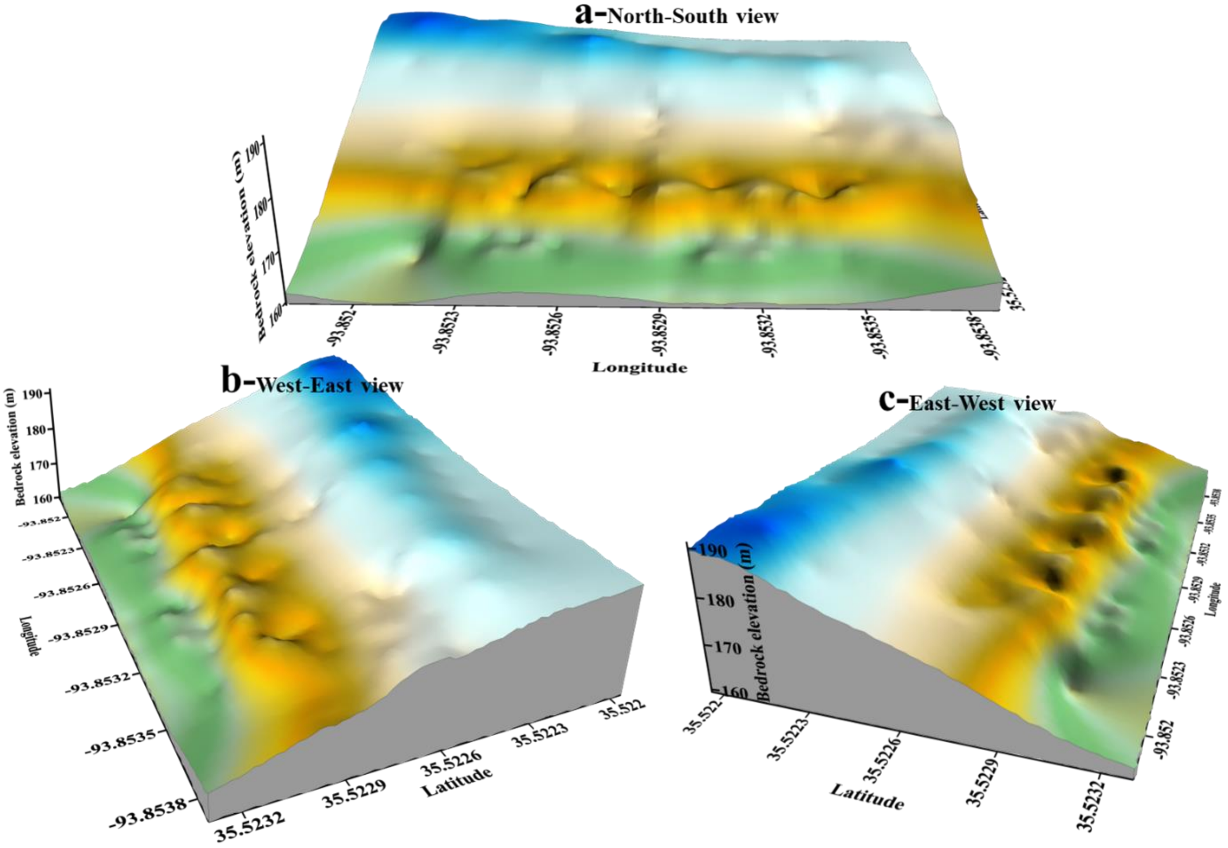

Figure 6.11- 3D map of bedrock elevation across the Ozark slope site.

Considering the very shallow bedrock layer at this site along with the depressions in the bedrock layer at the toe, the potential slip surfaces at this site were expected to be located at the soil/bedrock interface. The accuracy of this assumption was confirmed by inclinometer readings collected in February 2017 at the toe, as shown in Figure 6.10a. Presented in Figure 6.12a and b are the co-located V_s profile from the MASW and the cumulative displacements recorded from the inclinometer in the north-south direction, respectively. As observed in Figure 6.12b, while no displacement is observed for the top 10 m of the profile, a large displacement is recorded for depths ranging between 10-12 m. Also, no displacement is observed for depths greater than 12 m. Comparing the zone of displacement from the inclinometer with the V_s profile in Figure 6.12a, this zone exactly matches with the depth where a large jump in the V_s profile is observed. This increase in the V_s profile is related to the bedrock layer. This indicates that the zone of displacement corresponds to the soil/bedrock interface as expected. More discussions regarding the reasons behind the slope movements for the Sand Gap and Ozark sites are provided in the next section.

In general, at these sites, MHVSR results shed light on key subsurface features of the landslides, which were not observed in previous borings and complement the information from the limited borings or other array-based geophysical methods. Furthermore, the MHVSR was able to identify the critical zones of the landslide (i.e. the bowl features) at the toe. These zones were used as guides to plan for further field measurements for the landslide investigations using more expensive technologies and methods. Overall, the MHVSR is valuable for landslides that involve a shallow and complex bedrock topography, where a true understanding of the bedrock layer in a 3D manner is required for reliable slope stability models and remediation efforts.

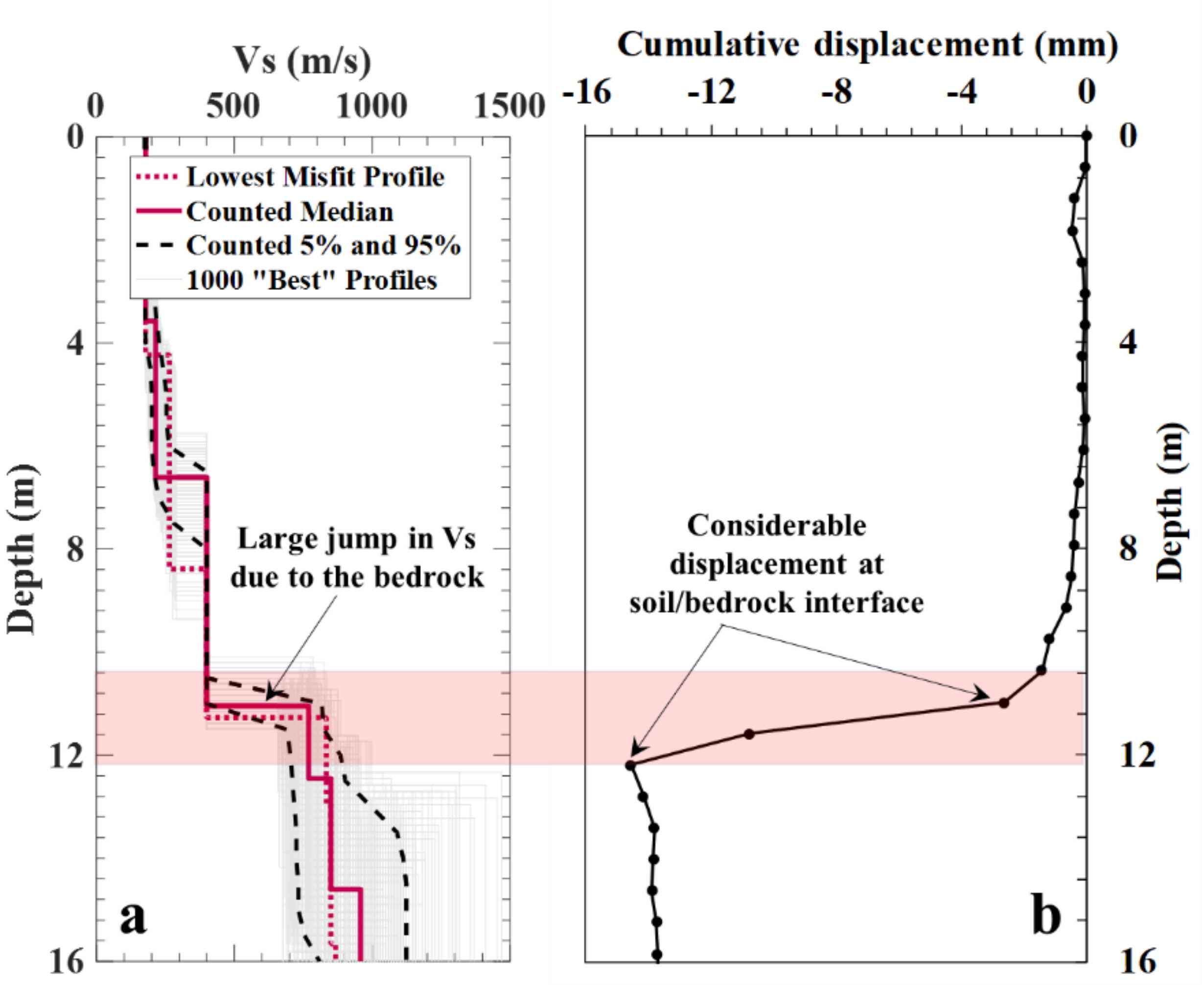

Figure 6.12- Comparison of the V_s profile from MASW and displacements recorded using an inclinometer. a) V_s profile, b) Cumulative displacement.

6.6.3 Discussions regarding slope movements at the Sand Gap and Ozark sites

From the geophysical results for the Sand Gap and Ozark sites, depth to the bedrock was determined to be very shallow (<14 m) and highly variable within the landslide zones. The most critical features of the bedrock layer for these two landslides are several bowl-shaped features in the bedrock layer at the toe. Several researchers have shown the impacts of microtopographic depressions in the bedrock layer on hillslope hydrology, which includes filling and spilling of water perched at soil/bedrock interface, and its effects on positive pore water pressure generation and landslide triggering (Buttle *et al.*, 2004; Graham *et al.*, 2010; Lanni *et al.*, 2013). Depressions in the bedrock within the landslide play a key role in slope instability as they can trap water during or shortly after a high rainfall event. This is particularly important for landslides with very shallow bedrock as rainfall infiltration can quickly accumulate and create a fully saturated soft zone at bedrock depression. To better illustrate this, a cross-section profile of the Ozark site (parallel to the slope) is shown in Figure 6.13 along with the highway alignment and depression in the bedrock. The bedrock estimated from the borings and the MHVSR are provided in Figure 6.13a and b, respectively.

Examining the difference in the estimated bedrock layer from the borings in Figure 6.13a and the MHVSR in Figure 6.13b, it is observed that the bedrock location is misinterpreted in some locations using the borings alone. While the bedrock estimated from the MHVSR are almost consistent for the top portion of the slope, the key feature of the bedrock, which is the depression in the bedrock at the toe, is not observed in the borings. Missing such key features in the slope stability model can lead to significant cost overruns for the slope rehabilitation efforts, and in the worst-case scenario, it can lead to slope failure. For instance, at the Ozark site, a slope repair project was conducted in 2018 based on a slope stability model created using the borings alone. The approximate cost of this slope repair job was more than $2.3 million dollars. While this slope repair has reduced the slope movement rate and likely prevented a global slope failure, two long cracks were observed (see Figure 6.1b and c) a few months after the repair. These cracks are clear indicators of continued slope stability issues even after the slope repair. With the addition of the information from the MHVSR testing, a more accurate bedrock layer has been used for the slope stability model, which is being used to design another repair for the project. This example illustrates the need for a high-resolution 3D image of the bedrock topography as one of the main inputs to the slope stability model to avoid cost overruns and potential slope failure. The reason why such bowl-shaped features in the bedrock can lead to slope failure is explained in the following.

During a heavy rainfall event, the rainfall infiltration is trapped in the bowl area on top of the bedrock due to the low permeability of the bedrock layer. This results in a highly saturated and soft zone at the toe (as shown in blue in Figure 6.13b). The area affected by the bedrock depression and rainfall infiltration (soft zone) can increase in size in both the North and South directions, depending on the severity and duration of the rainfall event. The trapped water at this location can trigger the landslide through different mechanisms, including:

- Rainfall infiltration reduces the soil shear strength, which is a resistant force against landslide movements by decreasing the soil interparticle contacts and removing the positive effect of negative pore water pressure.
- Total weight of the slip surface increases due to the addition of water.
- Soil apparent cohesion can be reduced or completely removed due to the dissolution of mineral cement, which hold the soil grains together when rainfall infiltrates into the soil.
- The friction at the soil/bedrock interface decreases due to the addition of water that fills in the micro gaps at the soil/bedrock interface.
- Positive pore water pressure is generated at the bowl location due to the presence of water and the dynamic loads from the vehicles passing the highway.

All the above-mentioned factors can lead to a considerable reduction in the factor of safety of the critical slip surface, as the resisting force decreases and the driving force increases.

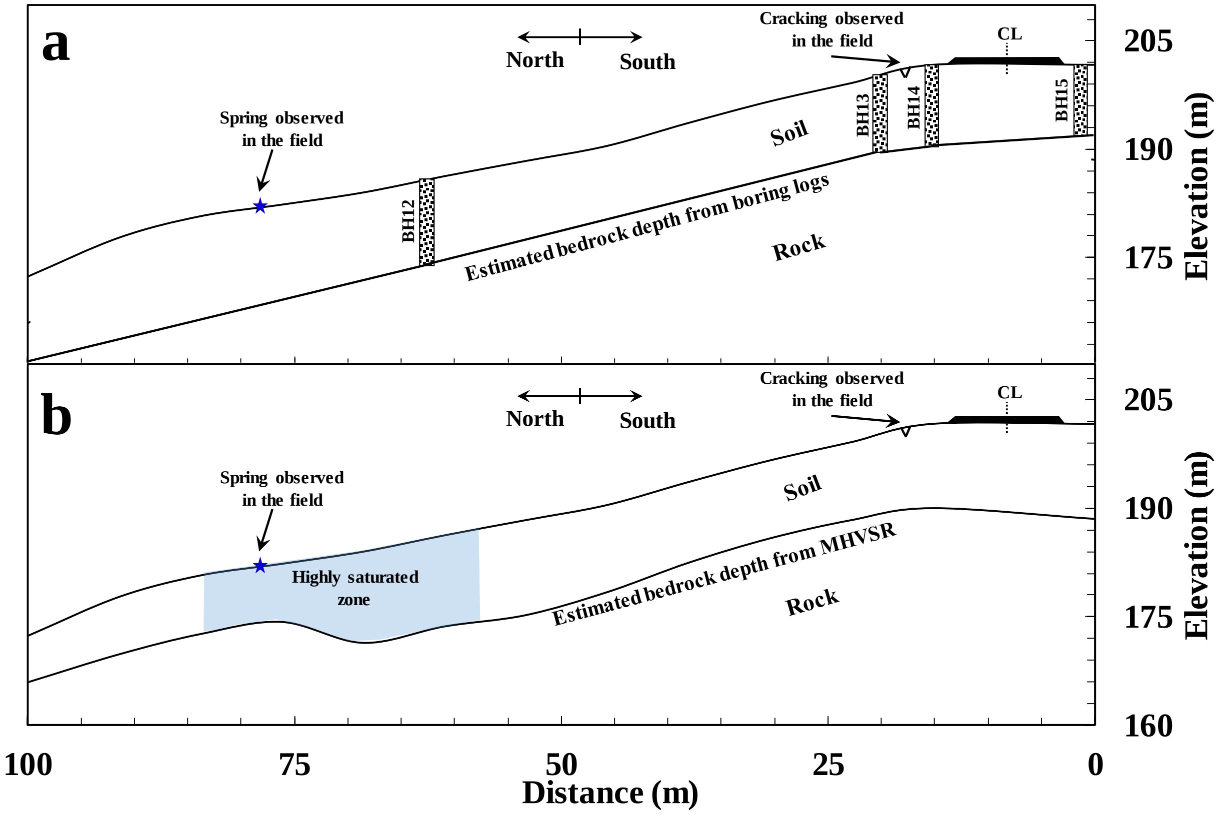

Figure 6.13- Estimated bedrock layer for the Ozark site using borings and MHVSR. a) bedrock layer estimated from the borings along with the boring locations, b) bedrock layer estimated from the MHVSR along with the example potential slip surface.

6.7 Conclusion

Four non-destructive geophysical methods, including MHVSR, MASW, P-wave refraction, and ERT were applied for two active landslides with shallow and complex bedrock topography that have recently experienced cracking as a result of the slope movements. The MHVSR was used as the primary method for the landslide investigation to understand the 3D bedrock topography under the landslide. The MHVSR was used as the primary method for locating the bedrock because developing the same 3D information over the entire landslide using drilling and sampling or other array-based geophysical methods would have taken significantly more time, field effort, and data processing effort compared to MHVSR.

For field measurements, a tight grid of MHVSR tests is first recommended with a distance of approximately 15-30 m between stations. Depth to bedrock can be estimated at each station, and then the results are combined to create a 3D map of bedrock and its variation across the landslide. Then, further borings or array-based geophysical measurements can be performed along the critical sections of the landslide that were identified from the MHVSR results to further investigate the slope movements and assess the accuracy of the MHVSR method. It should be mentioned that this method is only recommended for landslides with a very shallow and complex bedrock topography, where the bedrock layer contributes to the landslide instability.

From the MHVSR results at the Sand Gap and Ozark sites, several bowl-shaped features were observed in the bedrock layer at each site. The same features were also observed in the MASW and ERT profiles, confirming the accuracy of the MHVSR method. However, these features were missed in the bedrock profile interpreted from the borings alone. The bowl-shaped features in the bedrock layer are believed to be the primary factor causing the landslide movements at the Sand Gap and Ozark sites. This is driven by the shallow bedrock depth at the bowl locations, and the low permeability of the bedrock layer as the rainfall infiltrations are trapped and quickly accumulated in the bowl locations and creates a fully saturated soft zone within the critical slip surfaces. This hypothesis was verified by the ERT and P-wave refraction profiles, in which fully saturated zones were observed above the bowl locations. Moreover, the bowl locations correspond well with several springs that were observed during the field measurements. The trapped water in the bowl locations reduces the factor of safety of the critical slip surfaces through different mechanisms, as discussed in Section 5.3.

Overall, using the MHVSR method, a spatially high-resolution image of the bedrock topography was created in a rapid, cost-effective, and non-destructive manner. This image revealed several key features in the bedrock that contribute to the slope instability issues. These critical features were not detected using the traditional geotechnical methods such as drilling and sampling because of the limited spatial extent where the testing was conducted. Missing such key features in the slope stability model can lead to errors in the slope stability models and significant cost overruns for the slope rehabilitation efforts.

Therefore, the MHVSR method is recommended as a simple and valuable tool for rapid and cost-effective bedrock mapping for landslides with shallow and complex bedrock topography, where bedrock is a key feature for an accurate slope stability model. The MHVSR can complement other geophysical methods or drilling and sampling results by providing subsurface information over a much larger spatial extent. Additionally, this would help to optimize further field investigations required for landslide investigations using more expensive technologies and methods. The complementary method that is recommended to be used along with the MHVSR should be determined based on the landslide characteristic. Accordingly, for rainfall-induced landslides, the ERT method is recommended to be used as a complementary method in conjunction with the MHVSR. For landslides, where the stiffness of the subsurface materials (soils or rocks) is a key to landslide behavior, the MASW method is suggested to be employed along with the MHVSR.

Acknowledgments

This material is based upon work supported by the Arkansas Department of Transportation (ARDOT) under Project TRC1803. The authors would like to thank the many people at ARDOT that made the project successful, including Paul Tinsley, Matt Green, Paul Campbell, Patrick Phillips, and Tymli Frierson.

Data Availability Statement

Data used in this study are available from the corresponding author by request.

7 SUMMARY AND CONCLUSIONS

The conclusions that were drawn from this dissertation are outlined in this chapter. Additionally, recommendations regarding future works are also provided.

7.1 Conclusions

The main conclusions that were drawn from this dissertation can be divided into three main sections as below.

7.1.1 Improving derived dispersion data from MASW using the four transformation techniques

While the users of the MASW method in geotechnical and geophysical communities are often blindly selecting the transformation technique for MASW data processing, this is a critical decision influencing the reliability of the outcome of the MASW method. Therefore, the below recommendations should be taken into account by the users of the MASW method when selecting the transformation technique for data processing.

- The performance of the four transformation methods is identical for both Rayleigh and Love waves for sites with a deep bedrock layer, a low-frequency point of curvature (<10 Hz), relatively uniform soil conditions, and a low noise level. Therefore, any of the four transformation methods can be used for these sites.
- For sites with a very shallow and complex (highly variable) bedrock topography and a high-frequency point of curvature (>20 Hz), regardless of the site noise level and geophone coupling conditions, the PS transformation method results in a very poor-resolution dispersion image for both Rayleigh and Love waves. For

these sites, the quality of the experimental data from the PS transformation method is often very poor in such a way that no clear dispersion curve can be extracted from the experimental results. However, the other transformation methods (FDBF-cylindrical, FK, and τp) generated a clear, high-resolution dispersion image for both Rayleigh and Love waves for the same sites. Therefore, it is recommended not to use the PS method for sites with very shallow and complex bedrock topography with a high-frequency point of curvature (>20 Hz). If the PS method is used for such a site, the experimental dispersion curve from the PS method should be compared to at least one of the other transformation methods to ensure the accuracy of the experimental dispersion data.

- For sites with a velocity reversal (i.e. stiff over soft soil layer), the τp transformation method fails to generate Rayleigh wave dispersion data points for the layers located below the velocity reversal layer. However, the other transformation methods developed an experimental Rayleigh dispersion curve that contains information from the velocity reversal layer and the layers below it. Therefore, it is suggested not to use the τp method for sites with a velocity reversal layer located within the MASW target depth.
- The FDBF-cylindrical is often more sensitive to effective and higher modes than the other transformation methods. This means that more dispersion data points from effective and higher modes can be generated using the FDBF-cylindrical transformation technique. However, caution should be taken to use the FDBF-cylindrical transformation technique for sites with effective and higher modes, as sometimes it can lead to mode misidentification. Therefore, a combined

dispersion image using different transformation methods (at least two different methods) is suggested for such sites to avoid potential mode misidentification and to be able to identify different modes of propagation.

- Overall, the FDBF-cylindrical generally outperforms the other transformation methods (FK, PS, and τp) in terms of experimental dispersion resolution. The FDBF-cylindrical transformation technique provides a stable, high-resolution dispersion image for various subsurface layering and noise conditions, mitigates the near-field effects by modeling a cylindrical wavefield, and provides a high-resolution dispersion image over a broad range of frequencies, including the low frequency portion of the dispersion curve. The FDBF-cylindrical transformation technique is, therefore, recommended to use as the primary method if users of the MASW method are willing to only use one transformation technique for MASW data processing.
- The best practice is to combine all the transformation methods or at least use two different transformation methods for MASW data processing, particularly for complex stratigraphy environments (e.g. sites where higher modes are present). The combined method can be used as a means to (1) enhance the quality and reliability of the experimental dispersion curve, (2) reduce the uncertainty regarding the experimental dispersion curves and the final inverted V_s profile, (3) accurately determine different modes of propagation, and (4) define and remove data corrupted by near-field effects if any are present.

7.1.2 Mitigating near-field effects on MASW method

While the near-field effect is one of the main issues of the MASW method reducing the reliability of the experimental data and limiting the maximum resolvable depth of the MASW results, there are no acceptable criteria in the literature to mitigate such effects on the MASW technique for all field conditions. Therefore, considering different parameters influencing near-field effects, the below recommendations and criteria are suggested for mitigating near-field effects.

- The near-field effect is independent of surface wave type (i.e. Rayleigh or Love type surface waves). Accordingly, the normalized array center distance criteria for near-field mitigation of Rayleigh and Love waves are the same. Therefore, all the recommendations provided below apply to both Rayleigh and Love type surface waves.
- The near-field effect is also independent of depth to the impedance contrast [i.e. very shallow (~< 30 m) versus very deep sharp (~> 100 m) impedance contrasts]. In this regard, the normalized array center distance criteria for near-field mitigation of sites with very shallow and very deep sharp impedance contrasts are similar. Therefore, all the recommendations provided below apply to both sites with very shallow and very deep impedance contrasts (i.e. bedrock depth).
- For sites with a very shallow impedance contrast within the target depth of surface wave testing (~< 30 m), the FDBF-cylindrical transformation technique provides a significantly longer wavelength dispersion image than the other transformation methods (FK, PS, and τp) with fewer ill-effects from near-field effects. The FDBF-cylindrical transformation technique reduces the near-field

effect, particularly near-field effects due to mode incompatibility, by using a cylindrical wavefield model rather than a plane wavefield model. Therefore, for sites with a very shallow impedance contrast, the FDBF-cylindrical transformation technique is recommended for data processing to minimize near-field effects and achieve longer wavelengths (i.e. depth of investigation). When FDBF-cylindrical is used for data processing of sites with a very shallow impedance contrast, the typical normalized array center distance criteria for near-field mitigation can be violated. Overall, the best practice for near-field mitigation of sites with a very shallow impedance contrast is to use the multiple source offset approach along with the FDBF-cylindrical transformation technique for data processing.

- For sites with a very deep impedance contrast, generally, the four different transformation techniques provide the same resolution dispersion image in terms of near-field effects. Therefore, any of the four transformation methods can be used for data processing of these sites.
- The source type is an important factor influencing near-field effects. When a more controllable source type such as a vibroseis source is used for active surface wave testing, less restrictive near-field criteria can be used. Accordingly, using a 10-15% error boundary to define the near-field criteria, a normalized array center distance of 0.5 should be used as the practical criterion when using a vibroseis source. However, for a low-output sledgehammer source, a normalized array center distance of 1.0 should be used as the practical criterion for near-field effects mitigation.

- The criteria defined for near-field mitigation should not be violated when a limited number of source offsets (1 or 2) are used. But, if the multiple source offset approach (≥3 different source offsets) is used for active surface wave testing, the near-field criteria can be violated for some of the source offsets.
- The multiple source offset approach is an effective method for near-field mitigation. At least three different source offsets located 2-20 m away from the array (given a typically ~25-100 m array length) should be used when using the multiple source offsets approach. The most suitable source offset location is a complex function of normalized ACD criteria, subsurface conditions, source type, and array length. Generally, for sites with a very shallow impedance contrast using a sledgehammer source, shorter source offsets are recommended compared to sites with a very deep impedance contrast.
- Researchers and practitioners are widely using short source offsets such as 2 and 5 m for active surface wave testing without considering subsurface conditions and confirming the reliability of such short source offsets. These short source offsets are generally effective for generating high frequencies dispersion data (characterizing very near-surface layers). But for low frequencies dispersion data (i.e. long wavelengths), these source offsets are often contaminated with severe near-field effects. Therefore, relying solely on short source offsets could significantly underestimate the measured phase velocity and the subsurface layers' properties. Therefore, it is recommended to at least include one longer source offset (e.g. a source offset ranging between 10-20 m) along with the short

source offsets to prevent underestimation of the measured phase velocity and verify the reliability of the short source offsets at longer wavelengths.

- Overall, a normalized array center distance criterion of 1.0 is suitable for near-field mitigation on active surface wave testing when using a sledgehammer source, and a normalized array center distance criterion of 0.5 is suitable when using a vibroseis source.

7.1.3 Infrastructure health monitoring using geophysical methods

A variety of geophysical methods can be used for infrastructure health monitoring. However, this dissertation focused on the application of the MASW and MHVSR techniques. Accordingly, the conclusions below were made when using MASW and MHVSR for infrastructure health monitoring:

- For earthen hydraulic structures such as levees and embankment dams, the MASW method can provide valuable information regarding soil type, soil stiffness, and potential problematic zones of these structures. MASW was able to detect several potential weak areas of the Melvin Price Reach of the Wood River Levee, where a deeper clay layer was eroded due to the old river bars activities. These weak spots are the prime locations for piping through the foundation of the levee, which may have led to sand boils during large flooding events and can be a potential area of failure of the levee.
- When using the MASW method to evaluate the current conditions of infrastructure, it is important to use the reference shear wave profiles, which are available for different soil types, to accurately determine the soil types and subsurface conditions. This is very important because failing to use these profiles could lead

to misinterpretations of the subsurface conditions and, therefore, misleading future rehabilitation efforts.

- The MHVSR is very beneficial for landslide assessment with a very shallow and complex bedrock topography, where the bedrock layer contributes to the landslide instability. A tight grid of MHVSR measurements is recommended for such sites with a distance of approximately 15-30 m between stations. Using this method, a spatially high-resolution image of the bedrock topography can be created in a rapid, cost-effective, and non-destructive manner.
- Using a tight grid of the MHVSR for two active landslides, several key features in the bedrock that contribute to the slope instability issues were determined. These critical features were not detected using the traditional geotechnical methods such as drilling and sampling because of the limited spatial extent where the testing was conducted. Missing such key features in the slope stability model can lead to errors in the slope stability models and significant cost overruns for the slope rehabilitation efforts.
- The grid pattern MHVSR method is recommended as a simple and valuable tool for rapid and cost-effective bedrock mapping for landslides with shallow and complex bedrock topography, where bedrock is a key feature for an accurate slope stability model. The complementary method that is recommended to be used along with the MHVSR should be determined based on the landslide characteristic. Accordingly, for rainfall-induced landslides, the ERT method is recommended to be used as a complementary method in conjunction with the MHVSR. For landslides, where the stiffness of the subsurface materials (soils or rocks) is a key

to landslide behavior, the MASW method is suggested to be employed along with the MHVSR.

7.2 Recommendations for future works

According to the results of this dissertation, the following recommendations for future works are suggested.

- The performance of the four common transformation techniques could be evaluated for several sites with different velocity reversal layers to determine the impact of the thickness and impedance ratio of the velocity reversal layer on the derived dispersion data from the four transformation techniques. This is important because the velocity reversal layer is considered the most critical layer for many geotechnical analyses (e.g. liquefaction assessment). Therefore, it is valuable to understand the sensitivity of the four transformation techniques to a velocity reversal layer with different characteristics.
- Further investigations are required to identify the performance of the four common transformation techniques for sites where more than two modes of propagation are present. This would help to advance our knowledge regarding multimodal detection using different transformation techniques.
- More studies could be conducted to examine the performance of other available source types for MASW testing (different than sledgehammer and vibroseis investigated in this dissertation) on near-field effects to improve our understanding in this regard.
- Some guidelines need to be developed for the most effective source offsets considering different factors, including subsurface conditions, source type, and

array configuration. This would help to optimize the field measurement plan and improve the accuracy of the MASW method.

- Another important study that could help identify the efficiency of the multiple source offset approach for near-field mitigation is to determine the performance of the multiple source offset approach for sites where multiple modes of propagation are present. This is important because longer source offsets are generally dominated by higher modes, but more investigations are required to advance our understanding in this regard.

REFERENCES

Acerra, C. *et al.* (2004) 'Guidelines for the implementation of the H/V spectral ratio technique on ambient vibrations measurements, processing and interpretation', *European Commission–EVG1-CT-2000-00026 SESAME*.

Akin, M. K., Kramer, S. L. and Topal, T. (2011) 'Empirical correlations of shear wave velocity (Vs) and penetration resistance (SPT-N) for different soils in an earthquake-prone area (Erbaa-Turkey)', *Engineering Geology*, 119(1–2), pp. 1–17.

Anbazhagan, P. and Sitharam, T. G. (2008) 'Site characterization and site response studies using shear wave velocity', *Journal of Seismology and Earthquake Engineering*, 10(2), pp. 53–67.

Arai, H. and Tokimatsu, K. (1998) 'Evaluation of local site effects based on microtremor H/V spectra', in *Proceeding of the second international symposium on the effects of surface geology on seismic motion*. Yokohama Japan, pp. 673–680.

ASCE (2017) '2017 infrastructure report card'.

Bayoumi, A. and Meguid, M. A. (2011) 'Wildlife and Safety of Earthen Structures: A Review', *Journal of Failure Analysis and Prevention*, 11(4), pp. 295–319. doi: 10.1007/s11668-011-9439-y.

Beaty, K. S., Schmitt, D. R. and Sacchi, M. (2002) 'Simulated annealing inversion of multimode Rayleigh wave dispersion curves for geological structure', *Geophysical Journal International*, 151(2), pp. 622–631.

Berti, M., Bertello, L. and Squarzoni, G. (2019) 'Surface-wave velocity measurements of shear stiffness of moving earthflows', *Landslides*, 16(3), pp. 469–484.

Bichler, A. *et al.* (2004) 'Three-dimensional mapping of a landslide using a multi-geophysical approach: the Quesnel Forks landslide', *Landslides*, 1(1), pp. 29–40.

Bodet, L., Abraham, O. and Clorennec, D. (2009) 'Near-offset effects on Rayleigh-wave dispersion measurements: Physical modeling', *Journal of Applied Geophysics*, 68(1), pp. 95–103.

Bolt, B. A. (1993) 'Earthquakes, WH Freeman and Company', *San Francisco*.

Briaud, J.-L. (2008) 'Case Histories in Soil and Rock Erosion: Woodrow Wilson Bridge, Brazos River Meander, Normandy Cliffs, and New Orleans Levees', *Journal of Geotechnical and Geoenvironmental Engineering*, 134(10), pp. 1425–1447. doi: 10.1061/(ASCE)1090-0241(2008)134:10(1425).

Burjánek, J. *et al.* (2010) 'Ambient vibration analysis of an unstable mountain slope', *Geophysical Journal International*, 180(2), pp. 820–828.

Busato, L. *et al.* (2016) ‘Combined geophysical surveys for the characterization of a reconstructed river embankment’, *Engineering Geology*, 211, pp. 74–84. doi: 10.1016/j.enggeo.2016.06.023.

Buttle, J. M., Dillon, P. J. and Eerkes, G. R. (2004) ‘Hydrologic coupling of slopes, riparian zones and streams: an example from the Canadian Shield’, *Journal of Hydrology*, 287(1–4), pp. 161–177.

Capon, J. (1969) ‘High-resolution frequency-wavenumber spectrum analysis’, *Proceedings of the IEEE*, 57(8), pp. 1408–1418.

Cardarelli, E., Cercato, M. and De Donno, G. (2014) ‘Characterization of an earth-filled dam through the combined use of electrical resistivity tomography, P- and SH-wave seismic tomography and surface wave data’, *Journal of Applied Geophysics*, 106, pp. 87–95. doi: 10.1016/j.jappgeo.2014.04.007.

Chen, R., Tran, K. T. and Wang, Y. (no date) ‘2D time-domain full-waveform inversion of SH- and Love-waves for geotechnical site characterization’, *Near Surface Geophysics*.

Cheng, F. *et al.* (2019) ‘Automated data selection in the Tau–p domain: application to passive surface wave imaging’, *Surveys in Geophysics*, 40(5), pp. 1211–1228.

Chlaib, H. K. *et al.* (2014) ‘Using ground penetrating radar in levee assessment to detect small scale animal burrows’, *Journal of Applied Geophysics*, 103, pp. 121–131. doi: 10.1016/j.jappgeo.2014.01.011.

Choudhury, P. B., Chakraborty, A. K. and Sitharam, T. G. (2009) ‘Near Surface Vs Profiling Using MASW For Rippability Assessment of Milliolithic Limestone’, in *ISRM International Symposium on Rock Mechanics-SINOROCK 2009*. International Society for Rock Mechanics and Rock Engineering.

Comina, C. *et al.* (2011) ‘Reliability of VS,30 Evaluation from Surface-Wave Tests’, *Journal of Geotechnical and Geoenvironmental Engineering*, 137(6), pp. 579–586. doi: 10.1061/(ASCE)GT.1943-5606.0000452.

Cox, B. R. *et al.* (2020) ‘A statistical representation and frequency-domain window-rejection algorithm for single-station HVSR measurements’, *Geophysical Journal International*, 221(3), pp. 2170–2183.

Cox, B. R. and Teague, D. P. (2016) ‘Layering ratios: a systematic approach to the inversion of surface wave data in the absence of a priori information’, *Geophysical Journal International*, 207(1), pp. 422–438. doi: 10.1093/gji/ggw282.

Cox, B. R. and Wood, C. M. (2011) ‘Surface wave benchmarking exercise: methodologies, results, and uncertainties’, in. (Geo-Risk 2011: Risk Assessment and Management), pp. 845–852.

Cox, B. R., Wood, C. M. and Teague, D. P. (2014) ‘Synthesis of the UTexas1 surface wave dataset blind-analysis study: Inter-analyst dispersion and shear wave velocity uncertainty’, in *Geo-Congress 2014: Geo-Characterization and Modeling for Sustainability*, pp. 850–859.

Dal Moro, G. *et al.* (2003) ‘Determination of Rayleigh wave dispersion curves for near surface applications in unconsolidated sediments’, in *SEG Technical Program Expanded Abstracts 2003*. Society of Exploration Geophysicists, pp. 1247–1250.

Delgado, J. *et al.* (2021) ‘Ambient Noise Measurements to Constrain the Geological Structure of the Güevéjar Landslide (S Spain)’, *Applied Sciences*, 11(4), p. 1454.

Deschenes, M. R. *et al.* (2018) ‘Development of deep shear wave velocity profiles in the Canterbury Plains, New Zealand’, *Earthquake Spectra*, 34(3), pp. 1065–1089.

Dikmen, Ü. (2009) ‘Statistical correlations of shear wave velocity and penetration resistance for soils’, *Journal of Geophysics and Engineering*, 6(1), pp. 61–72.

Eker, A. M., Koçkar, M. K. and Akgün, H. (2015) ‘Evaluation of site effect within the tectonic basin in the northern side of Ankara’, *Engineering Geology*, 192, pp. 76–91.

Ellis, H. L., Groves, C. B. and Fischer, G. R. (2012) ‘Rapid Levee Assessment for Reliability and Risk Analysis’, pp. 170–177. doi: 10.1061/40971(310)21.

Fabbrocino, S. *et al.* (2015) ‘SPT blow count vs. shear wave velocity relationship in the structurally complex formations of the Molise Region (Italy)’, *Engineering Geology*, 187, pp. 84–97.

Fäh, D., Kind, F. and Giardini, D. (2001) ‘A theoretical investigation of average H/V ratios’, *Geophysical Journal International*, 145(2), pp. 535–549.

Falae, P. O. *et al.* (no date) ‘Interpretation on water seepage and degree of weathering in a landslide based on pre-and post–monsoon electrical resistivity tomography’, *Near Surface Geophysics*.

Feng, S., Sugiyama, T. and Yamanaka, H. (2005) ‘Effectiveness of multi-mode surface wave inversion in shallow engineering site investigations’, *Exploration Geophysics*, 36(1), pp. 26–33.

Foster, M., Fell, R. and Spannagle, M. (2011) ‘The statistics of embankment dam failures and accidents’, *Canadian Geotechnical Journal*. doi: 10.1139/t00-030.

Foti, S. *et al.* (2000) ‘Notes on fk analysis of surface waves’, *Annals of Geophysics*, 43(6).

Foti, S. *et al.* (2014) *Surface wave methods for near-surface site characterization*. CRC press.

Friedel, S., Thielen, A. and Springman, S. M. (2006) ‘Investigation of a slope endangered by rainfall-induced landslides using 3D resistivity tomography and geotechnical testing’, *Journal of Applied Geophysics*, 60(2), pp. 100–114.

Gabriels, P., Snieder, R. and Nolet, G. (1987) ‘In situ measurements of shear-wave velocity in sediments with higher-mode Rayleigh waves’, *Geophysical Prospecting*, 35(2), pp. 187–196.

Gao, L. *et al.* (2016) ‘Reason and condition for mode kissing in MASW method’, *Pure and Applied Geophysics*, 173(5), pp. 1627–1638.

Gao, L., Xia, J. and Pan, Y. (2014) ‘Misidentification caused by leaky surface wave in high-frequency surface wave method’, *Geophysical Journal International*, 199(3), pp. 1452–1462.

Garofalo, F. *et al.* (2016) ‘InterPACIFIC project: Comparison of invasive and non-invasive methods for seismic site characterization. Part I: Intra-comparison of surface wave methods’, *Soil Dynamics and Earthquake Engineering*, 82, pp. 222–240.

Graham, C. B., Woods, R. A. and McDonnell, J. J. (2010) ‘Hillslope threshold response to rainfall:(1) A field based forensic approach’, *Journal of Hydrology*, 393(1–2), pp. 65–76.

Griffiths, S. C. *et al.* (2016) ‘Surface-Wave Dispersion Approach for Evaluating Statistical Models That Account for Shear-Wave Velocity Uncertainty’, *Journal of Geotechnical and Geoenvironmental Engineering*, 142(11), p. 04016061. doi: 10.1061/(ASCE)GT.1943-5606.0001552.

Gutiérrez, F. *et al.* (2018) ‘Identifying the boundaries of sinkholes and subsidence areas via trenching and establishing setback distances’, *Engineering Geology*, 233, pp. 255–268. doi: 10.1016/j.enggeo.2017.12.015.

Haghshenas, E., Bard, P.-Y. and Theodulidis, N. (2008) ‘Empirical evaluation of microtremor H/V spectral ratio’, *Bulletin of Earthquake Engineering*, 6(1), pp. 75–108.

Hamimu, L., Safani, J. and Nawawi, M. (2011) ‘Improving the accurate assessment of a shear-wave velocity reversal profile using joint inversion of the effective Rayleigh wave and multimode Love wave dispersion curves’, *Near Surface Geophysics*, 9(1), pp. 1–14.

Harba, P., Pilecki, Z. and Krawiec, K. (2019) ‘Comparison of MASW and seismic interferometry with use of ambient noise for estimation of S-wave velocity field in landslide subsurface’, *Acta Geophysica*, 67(6), pp. 1875–1883. doi: 10.1007/s11600-019-00344-9.

Harder, L. F. *et al.* (2016) ‘Preliminary observations of levee performance and damage following the 2015-16 midwest floods in Missouri and Illinois’, in *Association of State Dam Safety Officials Annual Conference 2016, Dam Safety 2016. Association of State Dam Safety Officials Annual Conference 2016, Dam Safety 2016*, [Association of State Dam Safety Officials], pp. 86–170. Available at: https://experts.illinois.edu/en/publications/preliminary-observations-of-levee-performance-and-damage-followin (Accessed: 31 December 2020).

Hasancebi, N. and Ulusay, R. (2007) ‘Empirical correlations between shear wave velocity and penetration resistance for ground shaking assessments’, *Bulletin of Engineering Geology and the Environment*, 66(2), pp. 203–213. doi: 10.1007/s10064-006-0063-0.

Hayashi, K. *et al.* (2014) ‘Statistical Soil Type Estimation Using Cross-Plots of S-Wave Velocity and Resistivity in Japanese Levees’, pp. 2460–2468. doi: 10.1061/9780784413272.238.

Hebeler, G. L. and Rix, G. J. (2007) ‘Site characterization in Shelby County, Tennessee using advanced surface wave methods’, *MAE Center CD Release 06-02*.

Heerden, I. L. V. (2007) ‘The failure of the New Orleans levee system following Hurricane Katrina and the pathway forward’, *Public administration review*, 67, pp. 24–35.

Hibert, C. *et al.* (2012) ‘Characterizing landslides through geophysical data fusion: Example of the La Valette landslide (France)’, *Engineering Geology*, 128, pp. 23–29.

Himel, A. K. and Wood, C. M. (2021) ‘Developing an updated set of VS profiles for the central United States seismic observatory with estimates of uncertainty between different methods’, *Soil Dynamics and Earthquake Engineering*, 143, p. 106594.

Hussain, Y. *et al.* (2020) ‘Characterization of Sobradinho landslide in fluvial valley using MASW and ERT methods’, *REM-International Engineering Journal*, 73(4), pp. 487–497.

Imai, T. (1982) ‘Correlation of N-value with S-wave velocity and shear modulus’, in *Proceedings of the 2nd European Symposium of Penetration Testing, Amsterdam, 1982*.

Irikura, K. (1999) *The effects of surface geology on seismic motion: Recent progress and new horizon on ESG study*. Taylor & Francis.

Ismail, A., Brett Denny, F. and Metwaly, M. (2014) ‘Comparing continuous profiles from MASW and shear-wave reflection seismic methods’, *Journal of Applied Geophysics*, 105, pp. 67–77. doi: 10.1016/j.jappgeo.2014.03.007.

Johnson, D. H. and Dudgeon, D. E. (1993) *Array signal processing: concepts and techniques*. PTR Prentice Hall Englewood Cliffs.

Jongmans, D. and Garambois, S. (2007) ‘Geophysical investigation of landslides: a review’, *Bulletin de la Société géologique de France*, 178(2), pp. 101–112.

Koehn, W. J. *et al.* (2019) ‘Enhanced Analysis of Landslide Failure Mechanisms in the Ozark Plateau Region with Electrical Resistivity Tomography’, in *Geo-Congress 2019: Engineering Geology, Site Characterization, and Geophysics*. American Society of Civil Engineers Reston, VA, pp. 197–203.

Konno, K. and Ohmachi, T. (1998) ‘Ground-motion characteristics estimated from spectral ratio between horizontal and vertical components of microtremor’, *Bulletin of the Seismological Society of America*, 88(1), pp. 228–241.

Kouchaki, B. M. *et al.* (2018) ‘A Laboratory Investigation of Factors Influencing the Electrical Resistivity of Different Soil Types’, *Geotechnical Testing Journal*, 42(4), pp. 829–853. doi: 10.1520/GTJ20170364.

Kumar, J. and Naskar, T. (2018) ‘Multimodal phase velocity-frequency dispersion images using different MASW transformation techniques’, *arXiv preprint arXiv:1901.08660*.

Lacoss, R. T., Kelly, E. J. and Toksöz, M. N. (1969) ‘Estimation of seismic noise structure using arrays’, *Geophysics*, 34(1), pp. 21–38.

Lai, C. G. *et al.* (2002) ‘Simultaneous measurement and inversion of surface wave dispersion and attenuation curves’, *Soil Dynamics and Earthquake Engineering*, 22(9–12), pp. 923–930.

Lai, C. G. and Rix, G. J. (1998) ‘Simultaneous inversion of Rayleigh phase velocity and attenuation for near-surface site characterization’.

Lanni, C. *et al.* (2013) ‘Simulated effect of soil depth and bedrock topography on near-surface hydrologic response and slope stability’, *Earth surface processes and landforms*, 38(2), pp. 146–159.

Lapenna, V. *et al.* (2003) ‘High-resolution geoelectrical tomographies in the study of Giarrossa landslide (southern Italy)’, *Bulletin of Engineering Geology and the Environment*, 62(3), pp. 259–268.

Lee, S. H.-H. (1990) ‘Regression models of shear wave velocities in Taipei basin’, *Journal of the Chinese Institute of Engineers*, 13(5), pp. 519–532. doi: 10.1080/02533839.1990.9677284.

Li, C.-H. (2011) *Influence of site conditions on near-field effects in multi-channel surface wave measurements*. PhD Thesis. University of Missouri–Columbia.

Li, J. and Rosenblad, B. (2011) ‘Experimental study of near-field effects in multichannel array-based surface wave velocity measurements’, *Near Surface Geophysics*, 9(4), pp. 357–366.

Lin, Y.-C., Joh, S.-H. and Stokoe, K. H. (2014) ‘Analyst J: Analysis of the UTexas 1 surface wave dataset using the SASW methodology’, in *Geo-Congress 2014: Geo-characterization and Modeling for Sustainability*, pp. 830–839.

Lontsi, A. M., Ohrnberger, M. and Krüger, F. (2016) ‘Shear wave velocity profile estimation by integrated analysis of active and passive seismic data from small aperture arrays’, *Journal of Applied Geophysics*, 130, pp. 37–52.

Louie, J. N. (2001) ‘Faster, better: shear-wave velocity to 100 meters depth from refraction microtremor arrays’, *Bulletin of the Seismological Society of America*, 91(2), pp. 347–364.

Lu, K. *et al.* (2021) ‘Using electrical resistivity tomography and surface nuclear magnetic resonance to investigate cultural relic preservation in Leitai, China’, *Engineering Geology*, 285, p. 106042.

Mahvelati, D. S. *et al.* (2020a) *Recovery of Small-Strain Stiffness Following Blast-Induced Liquefaction Based on Shear Wave Velocity Measurements, https://doi.org/10.1139/cgj-2019-0658*. doi: 10.1139/cgj-2019-0658.

Mahvelati, S. *et al.* (2020b) ‘Recovery of Small-Strain Stiffness Following Blast-Induced Liquefaction Based on Shear Wave Velocity Measurements’, *Canadian Geotechnical Journal*, (ja).

Malischewsky, P. G. and Scherbaum, F. (2004) ‘Love’s formula and H/V-ratio (ellipticity) of Rayleigh waves’, *Wave Motion*, 40(1), pp. 57–67.

Martinez-Pagan, P. *et al.* (2012) ‘Comparative Study of SPAC and MASW Methods to Obtain the Vs30 for Seismic Site Effect Evaluation in Lorca town, SE Spain’, in. *Near Surface Geoscience 2012 – 18th European Meeting of Environmental and Engineering Geophysics*, European Association of Geoscientists & Engineers, p. cp. doi: 10.3997/2214-4609.20143468.

McMechan, G. A. and Yedlin, M. J. (1981) ‘Analysis of dispersive waves by wave field transformation’, *Geophysics*, 46(6), pp. 869–874.

Menq, F. (2003) *Dynamic properties of sandy and gravelly soils*. PhD Thesis.

Merritt, A. J. *et al.* (2014) ‘3D ground model development for an active landslide in Lias mudrocks using geophysical, remote sensing and geotechnical methods’, *Landslides*, 11(4), pp. 537–550.

Mi, B. *et al.* (2020) ‘Estimating near-surface shear-wave-velocity structures via multichannel analysis of Rayleigh and Love waves: an experiment at the Boise Hydrogeophysical research site’, *Surveys in Geophysics*, 41(2), pp. 323–341.

Michel, C. *et al.* (2014) ‘Assessment of site effects in alpine regions through systematic site characterization of seismic stations’, *Bulletin of the Seismological Society of America*, 104(6), pp. 2809–2826.

Nakamura, Y. (1989) ‘A method for dynamic characteristics estimation of subsurface using microtremor on the ground surface’, *Railway Technical Research Institute, Quarterly Reports*, 30(1).

Nakamura, Y. (2000) ‘Clear identification of fundamental idea of Nakamura’s technique and its applications’, in *Proceedings of the 12th world conference on earthquake engineering*. Auckland New Zealand, pp. 25–30.

Nakamura, Y. (2019) ‘What is the Nakamura method?’, *Seismological Research Letters*, 90(4), pp. 1437–1443.

Naudet, V. *et al.* (2008) ‘Integrated geophysical and geomorphological approach to investigate the snowmelt-triggered landslide of Bosco Piccolo village (Basilicata, southern Italy)’, *Engineering Geology*, 98(3–4), pp. 156–167.

Nobes, D. C. *et al.* (2015) ‘Geophysical imaging of the post-earthquake structural integrity of flood-control stopbanks, Christchurch, New Zealand’, *Journal of Geophysics and Engineering*, 12(5), pp. 857–865. doi: 10.1088/1742-2132/12/5/857.

Nogoshi, M. and Igarashi, T. (1971) ‘On the amplitude characteristics of ambient noise (Part 2)’, *J Seismol Soc Jpn*, 24, pp. 26–40.

Nolet, G. and Panza, G. F. (1976) ‘Array analysis of seismic surface waves: limits and possibilities’, *Pure and Applied Geophysics*, 114(5), pp. 775–790.

Ohta, Y. and Goto, N. (1978) ‘Empirical shear wave velocity equations in terms of characteristic soil indexes’, *Earthquake Engineering & Structural Dynamics*, 6(2), pp. 167–187. doi: https://doi.org/10.1002/eqe.4290060205.

Okada, Y. and Konishi, C. (2019) ‘Geophysical features of shallow landslides induced by the 2015 Kanto-Tohoku heavy rain in Kanuma city, Tochigi Prefecture, Japan’, *Landslides*, 16(12), pp. 2469–2483.

Olafsdottir, E. A., Erlingsson, S. and Bessason, B. (2018) ‘Tool for analysis of multichannel analysis of surface waves (MASW) field data and evaluation of shear wave velocity profiles of soils’, *Canadian Geotechnical Journal*, 55(2), pp. 217–233.

O’Neill, A., Dentith, M. and List, R. (2003) ‘Full-waveform P-SV reflectivity inversion of surface waves for shallow engineering applications’, *Exploration Geophysics*, 34(3), pp. 158–173.

O’Neill, A. and Matsuoka, T. (2005) ‘Dominant higher surface-wave modes and possible inversion pitfalls’, *Journal of Environmental & Engineering Geophysics*, 10(2), pp. 185–201.

Panzera, F. *et al.* (2012) ‘Seismic site response of unstable steep slope using noise measurements: the case study of Xemxija Bay area, Malta’, *Natural Hazards and Earth System Sciences*, 12(11), p. 3421.

Park, C. B., Miller, R. D. and Xia, J. (1998) ‘Imaging dispersion curves of surface waves on multi-channel record’, in. Society of Exploration Geophysicists (SEG Technical Program Expanded Abstracts 1998), pp. 1377–1380.

Pastén, C. *et al.* (2016) ‘Deep characterization of the Santiago Basin using HVSR and cross-correlation of ambient seismic noise’, *Engineering Geology*, 201, pp. 57–66.

Peng, J. *et al.* (2017) ‘Shear wave velocity imaging of landslide debris deposited on an erodible bed and possible movement mechanism for a loess landslide in Jingyang, Xi’an, China’, *Landslides*, 14(4), pp. 1503–1512.

Penumadu, D. and Park, C. B. (2005) ‘Multichannel analysis of surface wave (MASW) method for geotechnical site characterization’, in *Earthquake engineering and soil Dynamics*, pp. 1–10.

Perri, M. T. *et al.* (2014) ‘River embankment characterization: The joint use of geophysical and geotechnical techniques’, *Journal of Applied Geophysics*, 110, pp. 5–22. doi: 10.1016/j.jappgeo.2014.08.012.

Perrone, A., Lapenna, V. and Piscitelli, S. (2014) ‘Electrical resistivity tomography technique for landslide investigation: a review’, *Earth-Science Reviews*, 135, pp. 65–82.

Pilecki, Z. *et al.* (2017) ‘Capabilities of seismic and georadar 2D/3D imaging of shallow subsurface of transport route using the Seismobile system’, *Journal of Applied Geophysics*, 143, pp. 31–41. doi: 10.1016/j.jappgeo.2017.05.016.

Rahimi, S. *et al.* (2018) ‘The combined use of MASW and resistivity surveys for levee assessment: A case study of the Melvin Price Reach of the Wood River Levee’, Engineering Geology, 241, pp. 11–24. https://doi.org/10.1016/j.enggeo.2018.05.009

Rahimi, S. *et al.* (2019a) ‘Mapping Subsurface Conditions and Detecting Seepage Channels for an Embankment Dam Using Geophysical Methods: A Case Study of the Kinion Lake Dam’, Journal of Environmental and Engineering Geophysics, 24(3), pp. 373–386. https://doi.org/10.2113/JEEG24.3.373

Rahimi, S., Wood, C. M., Bernhardt-Barry, M., & Himel, A. K. (2019b, March). Updated reference shear wave velocity curves for near-surface site characterization. In Geo-Congress 2019: Engineering Geology, Site Characterization, and Geophysics (pp. 324-333). Reston, VA: American Society of Civil Engineers. https://doi.org/10.1061/9780784482131.033

Rahimi, S. *et al.* (2020a) ‘Efficacy of Aging Correction for Liquefaction Assessment of Case Histories Recorded during the 2010 Darfield and 2011 Christchurch Earthquakes in New Zealand’, *Journal of Geotechnical and Geoenvironmental Engineering*, 146(8), p. 04020059. doi: 10.1061/(ASCE)GT.1943-5606.0002294.

Rahimi, S. *et al.* (2021a) ‘Advantages of Geophysics to Improve Site Characterization and Reliability for Transportation Projects’, Transportation Research Record, p. 0361198121996362. https://doi.org/10.1177/0361198121996362

Rahimi, S., Wood, C. M. and Bernhardt-Barry, M. (2021b) ‘The MHVSR technique as a rapid, cost-effective, and noninvasive method for landslide investigation: case studies of Sand Gap and Ozark, AR, USA’, *Land*slides, pp. 1–16. DOI 10.1007/s10346-021-01677-7

Rahimi, S., Wood, C. M., & Teague, D. P. (2021c). ‘Performance of Different Transformation Techniques for MASW Data Processing Considering Various Site Conditions, Near-Field Effects, and Modal Separation‘. Surveys in Geophysics.

Rahimi, S., Wood, C. M. and Himel, A. K. (2021d) ‘Practical Guidelines for Near-field Mitigation on Array-based Active Surface Wave Testing‘. Geophysical Journal International.

Rahimi, S., Wood, C. M., Rieth, R., & Himel, A. K. (2021e). Application of Shear Wave Velocity to Rock Rippability Estimates Based on Poisson’s Ratios Determined from Laboratory and Field Measurements. In IFCEE 2021 (pp. 339-349). https://doi.org/10.1061/9780784483428.035

Rahimi, S., Wood, C. M. and Himel, A. K. (2020b) ‘Application of Microtremor Horizontal to Vertical Spectra Ratio (MHVSR) and Multichannel Analysis of Surface Wave (MASW) for

Shallow Bedrock Mapping for Transportation Projects', in *Geo-Congress 2020: Modeling, Geomate*rials, and Site Characterization. American Society of Civil Engineers Reston, VA, pp. 622–632. https://doi.org/10.1061/9780784482803.066

Rahimi, S., Wood, C. M. and Wotherspoon, L. M. (2020c) 'Influence of soil aging on SPT-Vs correlation and seismic site classification', Engineering Geology, p. 105653. https://doi.org/10.1016/j.enggeo.2020.105653

Rix, G. J., Hebeler, G. L. and Orozco, M. C. (2002) 'Near-surface Vs Profiling in the New Madrid Seismic Zone Using Surface-wave Methods', *Seismological Research Letters*, 73(3), pp. 380–392. doi: 10.1785/gssrl.73.3.380.

Rong, M. *et al.* (2017) 'On the Amplitude Discrepancy of HVSR and Site Amplification from Strong-Motion ObservationsOn the Amplitude Discrepancy of HVSR and Site Amplification from Strong-Motion Observations', *Bulletin of the Seismological Society of America*, 107(6), pp. 2873–2884.

Rosenblad, B. L. and Li, J. (2009) 'Comparative study of refraction microtremor (ReMi) and active source methods for developing low-frequency surface wave dispersion curves', *Journal of Environmental & Engineering Geophysics*, 14(3), pp. 101–113.

Roy, N. and Jakka, R. S. (2017) 'Near-field effects on site characterization using MASW technique', *Soil Dynamics and Earthquake Engineering*, 97, pp. 289–303.

Ryden, N. and Mooney, M. A. (2009) 'Analysis of surface waves from the light weight deflectometer', *Soil Dynamics and Earthquake Engineering*, 29(7), pp. 1134–1142.

Sacchi, M. D. and Ulrych, T. J. (1995) 'High-resolution velocity gathers and offset space reconstruction', *Geophysics*, 60(4), pp. 1169–1177.

Samyn, K. *et al.* (2014) 'Integrated geophysical approach in assessing karst presence and sinkhole susceptibility along flood-protection dykes of the Loire River, Orléans, France', *Engineering Geology*, 183, pp. 170–184.

Schneider, J., Mcgillivray, A. V. and Mayne, P. W. (2004) 'Evaluation of SCPTU intra-correlations at sand sites in the lower Mississippi River Valley, USA', in *Proceedings of the 2nd International Conference on Site Characterisation. Evaluation of SCPTU intra-correlations at sand sites in the lower Mississippi River Valley, USA*, Millpress Science Ltd, pp. 1003–1010. Available at: https://research-repository.uwa.edu.au/en/publications/evaluation-of-scptu-intra-correlations-at-sand-sites-in-the-lower (Accessed: 31 December 2020).

Seed, H. B., Idriss, I. M. and Arango, I. (1983) 'Evaluation of Liquefaction Potential Using Field Performance Data', *Journal of Geotechnical Engineering*, 109(3), pp. 458–482. doi: 10.1061/(ASCE)0733-9410(1983)109:3(458).

Sills, G. L. *et al.* (2008) 'Overview of New Orleans levee failures: lessons learned and their impact on national levee design and assessment', *Journal of Geotechnical and Geoenvironmental Engineering*, 134(5), pp. 556–565.

Sjödahl, P., Dahlin, T. and Johansson, S. (2010) ‘Using the resistivity method for leakage detection in a blind test at the Røssvatn embankment dam test facility in Norway’, *Bulletin of Engineering Geology and the Environment*, 69(4), pp. 643–658.

Socco, L. V. and Strobbia, C. (2004) ‘Surface-wave method for near-surface characterization: a tutorial’, *Near surface geophysics*, 2(4), pp. 165–185.

Stefano, P. D. *et al.* (2014) ‘Integration of HVSR measures and stratigraphic constraints for seismic microzonation studies: the case of Oliveri (ME)’, *Natural Hazards and Earth System Sciences Discussions*, 2(4), pp. 2597–2637.

Stokoe, K. H. *et al.* (1994) ‘Characterization of geotechnical sites by SASW method’, in *Geophysical characterization of sites*, pp. 15–25.

Stokoe, K. H. and Santamarina, J. C. (2000) ‘Seismic-wave-based testing in geotechnical engineering’, in *ISRM International Symposium*. International Society for Rock Mechanics and Rock Engineering.

Teague, D. *et al.* (2018) ‘Development of deep shear wave velocity profiles with estimates of uncertainty in the complex interbedded geology of Christchurch, New Zealand’, *Earthquake Spectra*, 34(2), pp. 639–672.

Teague, D., Cox, B. and El-Afifi, T. (2017) ‘Site response implications of using VS profiles derived from “Blind” and geologically-guided surface wave inversions’, in *Proceedings of the 16th World Conference on Earthquake Engineering*.

Tingey, B. E. *et al.* (2007) ‘Study of a prehistoric landslide using seismic reflection methods integrated with geological data in the Wasatch Mountains, Utah, USA’, *Engineering Geology*, 95(1–2), pp. 1–29.

Tobin, G. A. (1995) ‘The Levee Love Affair: A Stormy Relationship?1’, *JAWRA Journal of the American Water Resources Association*, 31(3), pp. 359–367. doi: https://doi.org/10.1111/j.1752-1688.1995.tb04025.x.

Tokimatsu, K. (1997) *Geotechnical site characterization using surface waves*.

Tran, K. T. and Hiltunen, D. R. (2008) ‘A comparison of shear wave velocity profiles from SASW, MASW, and ReMi techniques’, in *Geotechnical earthquake engineering and soil dynamics IV*, pp. 1–9.

Tremblay, S.-P. and Karray, M. (2019) ‘Practical considerations for array-based surface-wave testing methods with respect to near-field effects and shear-wave velocity profiles’, *Journal of Applied Geophysics*, 171, p. 103871.

Uma Maheswari, R., Boominathan, A. and Dodagoudar, G. R. (2010) ‘Use of Surface Waves in Statistical Correlations of Shear Wave Velocity and Penetration Resistance of Chennai Soils’, *Geotechnical and Geological Engineering*, 28(2), pp. 119–137. doi: 10.1007/s10706-009-9285-9.

Vantassel, J. *et al.* (2018) ‘Mapping Depth to Bedrock, Shear Stiffness, and Fundamental Site Period at CentrePort, Wellington, Using Surface-Wave Methods: Implications for Local Seismic Site Amplification’, *Bulletin of the Seismological Society of America,* 108(3B), pp. 1709–1721.

Wathelet, M. (2008) ‘An improved neighborhood algorithm: Parameter conditions and dynamic scaling’, *Geophysical Research Letters*, 35(9). doi: https://doi.org/10.1029/2008GL033256.

Wood, C. M. (2009) *The impact of source type, source offset, and receiver spacing on experimental MASW data at soft-over-stiff sites*. University of Arkansas.

Wood, C. M. *et al.* (2017a) ‘Rapid and Non-Destructive Assessment of Levees for Strength and Liquefaction Resistance’. Available at: https://rosap.ntl.bts.gov/view/dot/32818.

Wood, C. M. *et al.* (2017b) ‘Vs-based evaluation of select liquefaction case histories from the 2010–2011 Canterbury earthquake sequence’, *Journal of Geotechnical and Geoenvironmental Engineering*, 143(9), p. 04017066.

Wood, C. M. *et al.* (2019a) *Deep shear wave velocity profiling in Northeastern Arkansas*.

Wood, C. M. *et al.* (2019b) ‘Dynamic site characterization of areas affected by the 2017 Puebla-Mexico city earthquake’, *Soil Dynamics and Earthquake Engineering*, 125, p. 105704.

Wood, C. M. and Cox, B. R. (2012) ‘A comparison of MASW dispersion uncertainty and bias for impact and harmonic sources’, in *GeoCongress 2012: State of the Art and Practice in Geotechnical Engineering*, pp. 2756–2765.

Wotherspoon, L. M. *et al.* (2013) ‘Geotechnical characterization of Christchurch strong motion stations’.

Wotherspoon, L. M. *et al.* (2015) ‘Soil profile characterisation of Christchurch central business district strong motion stations’.

Xia, J. *et al.* (2003) ‘Inversion of high frequency surface waves with fundamental and higher modes’, *Journal of Applied Geophysics,* 52(1), pp. 45–57.

Xu, X., Su, L. and Zhu, H. (2017) ‘Analysis on shear wave velocity structure of a gravel landslide based on dual-source surface wave method’, *Landslides,* 14(3), pp. 1127–1137.

Xu, Y., Xia, J. and Miller, R. D. (2006) ‘Quantitative estimation of minimum offset for multichannel surface-wave survey with actively exciting source’, *Journal of Applied Geophysics,* 59(2), pp. 117–125.

Yilar, E., Baise, L. G. and Ebel, J. E. (2017) ‘Using H/V measurements to determine depth to bedrock and Vs30 in Boston, Massachusetts’, *Engineering Geology*, 217, pp. 12–22.

Yilmaz, O. (1987) ‘Seismic Data Processing’. Society of Exploration Geophysicists, Tulsa’.

Yoon, S. (2005) ‘Array-Based Measurements of Surface Wave Dispersion and Attenuation Using Frequency-Wavenumber Analysis’, *Array-Based Measurements of Surface Wave Dispersion and Attenuation Using Frequency-Wavenumber Analysis*.

Yoon, S. and Rix, G. J. (2009) ‘Near-field effects on array-based surface wave methods with active sources’, *Journal of Geotechnical and Geoenvironmental Engineering*, 135(3), pp. 399–406.

Zhang, S. X. and Chan, L. S. (2003) ‘Possible effects of misidentified mode number on Rayleigh wave inversion’, *Journal of Applied Geophysics*, 53(1), pp. 17–29.

Zywicki, D. J. (1999) *Advanced signal processing methods applied to engineering analysis of seismic surface waves*.

Zywicki, D. J. and Rix, G. J. (2005) ‘Mitigation of near-field effects for seismic surface wave velocity estimation with cylindrical beamformers’, *Journal of Geotechnical and Geoenvironmental Engineering*, 131(8), pp. 970–977.

APPENDIX- MORE EXAMPLES OF THE PERFORMANCE OF THE FOUR DIFFERENT TRANSFORMATION TECHNIQUES

This appendix provides some more experimental dispersion curves generated using the four different transformation techniques to highlight the differences observed between the four different transformation techniques in terms of dispersion resolution.

Similar performance for sites with a deep bedrock layer

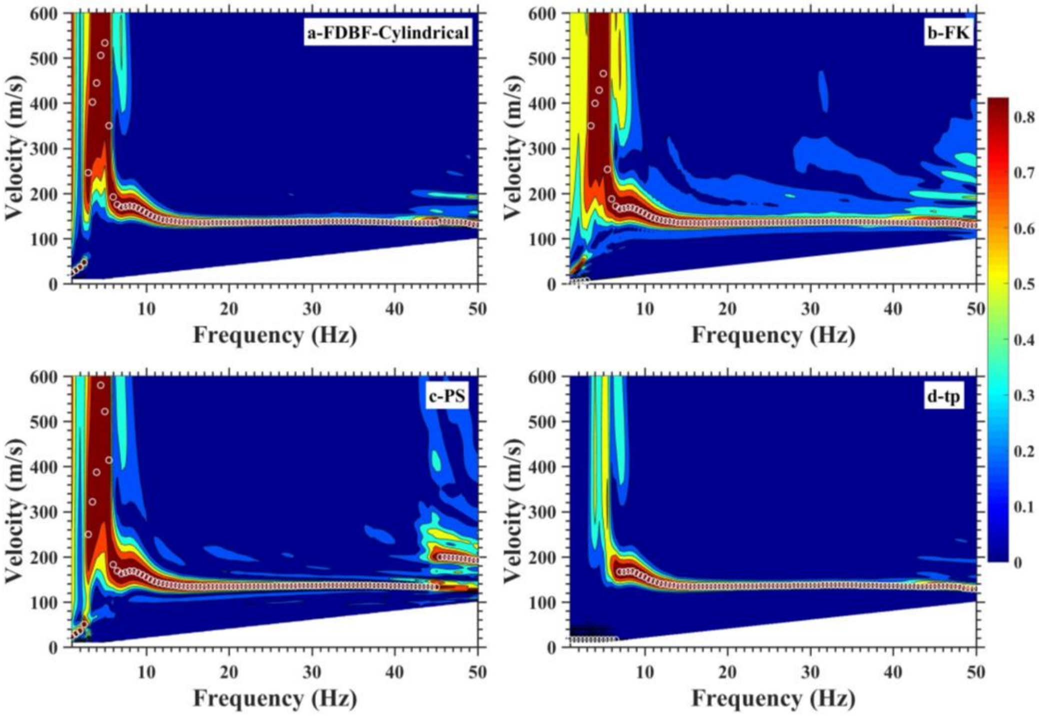

Figure A.1- Rayleigh wave dispersion curves generated using the four transformation methods for the PVMO site with a deep bedrock layer, a low-frequency point of curvature, and low noise levels. a) FDBF-cylindrical, b) FK, c) PS, and d) τp.

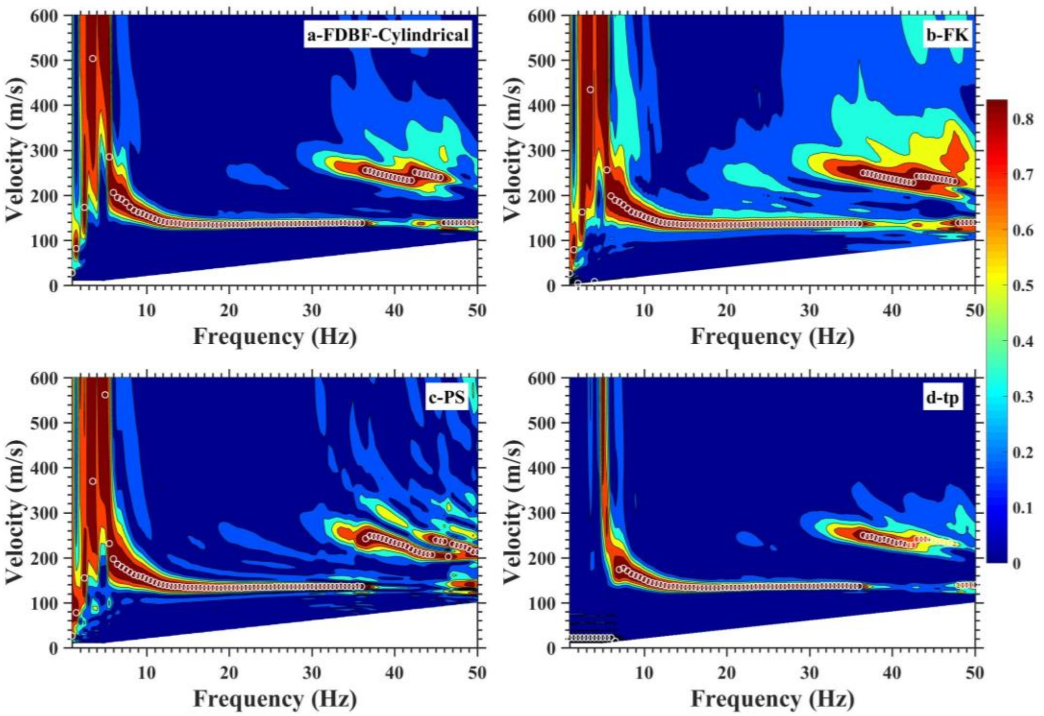

Figure A.2 - Rayleigh wave dispersion curves generated using the four transformation methods for the PVMO site with a deep bedrock layer, a low-frequency point of curvature, and low noise levels. a) FDBF-cylindrical, b) FK, c) PS, and d) τp.

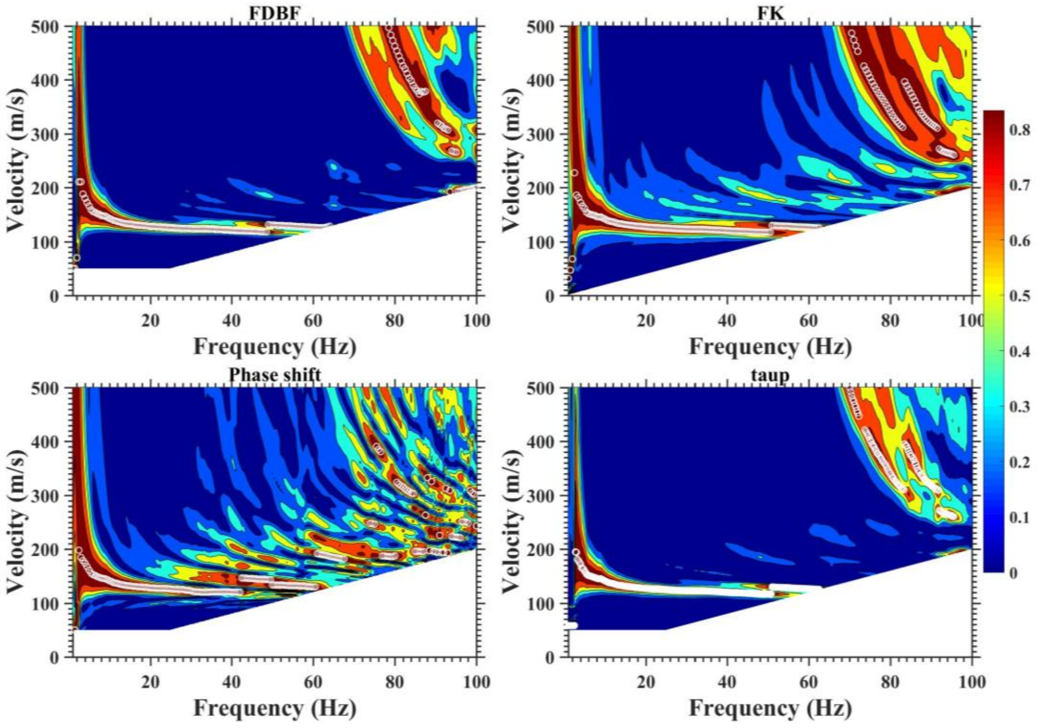

Figure A.3- Love wave dispersion curves generated using the four transformation methods for the PEBM site with a deep bedrock layer, a low-frequency point of curvature, and low noise levels. a) FDBF-cylindrical, b) FK, c) PS, and d) τp.

PS issue for sites with a very shallow and complex bedrock topography

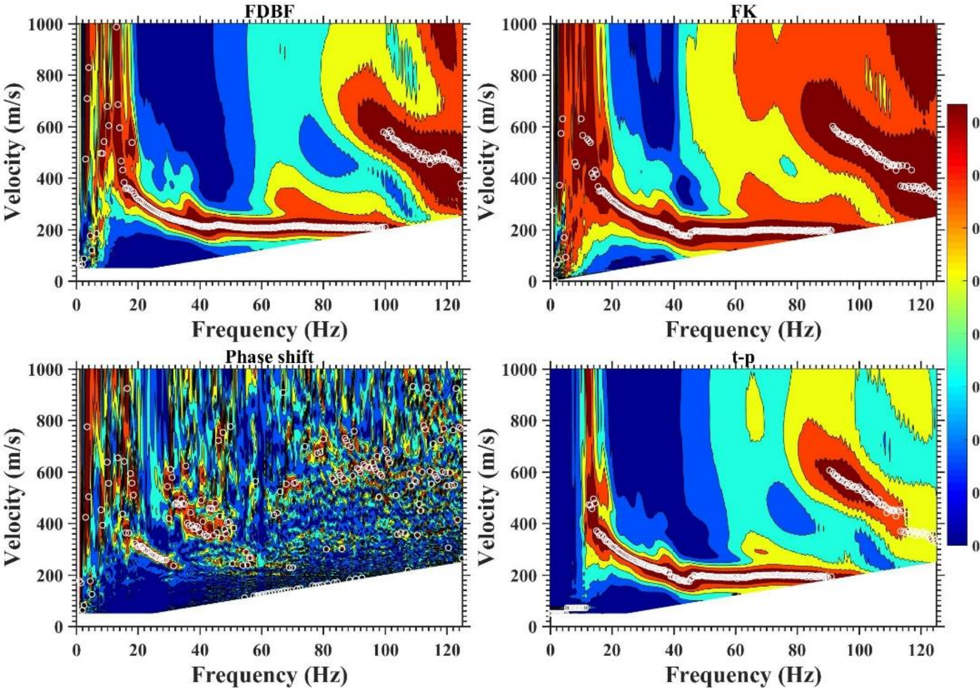

Figure A.4- Rayleigh wave dispersion curves generated using the four transformation methods for the Ozark site with a very shallow and complex bedrock topography, a high-frequency point of curvature, and high noise levels. a) FDBF-cylindrical, b) FK, c) PS, and d) τp.

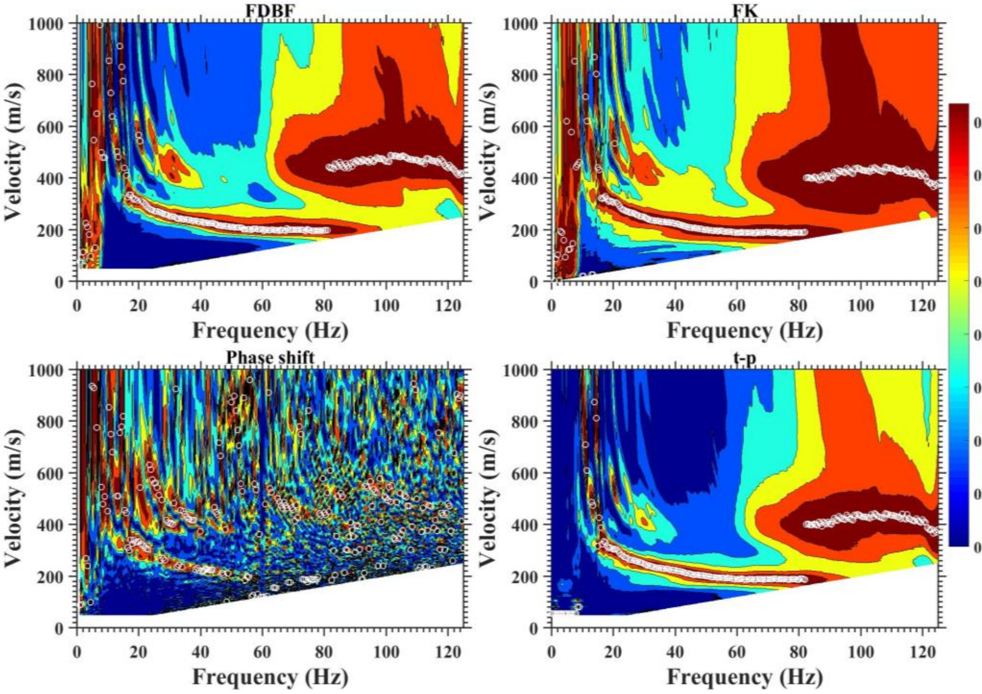

Figure A.5- Rayleigh wave dispersion curves generated using the four transformation methods for the Ozark site with a very shallow and complex bedrock topography, a high-frequency point of curvature, and high noise levels. a) FDBF-cylindrical, b) FK, c) PS, and d) τp.

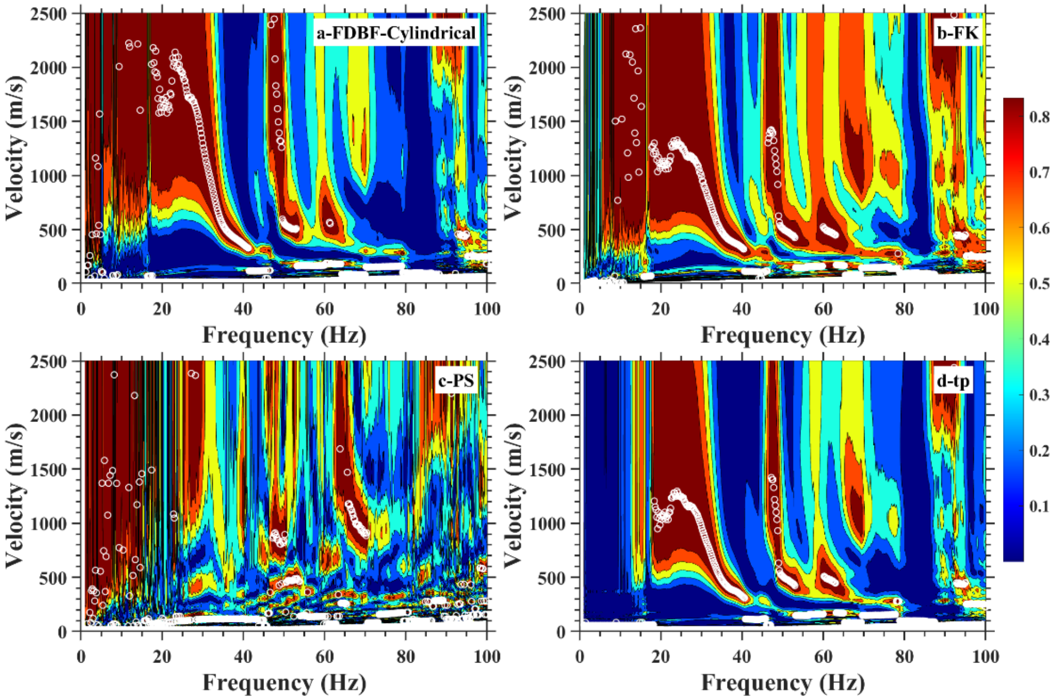

Figure A.6- Rayleigh wave dispersion curves generated using the four transformation methods for the Hot Springs site with a very shallow and complex bedrock topography, a high-frequency point of curvature, and low noise levels. a) FDBF-cylindrical, b) FK, c) PS, and d) τp.

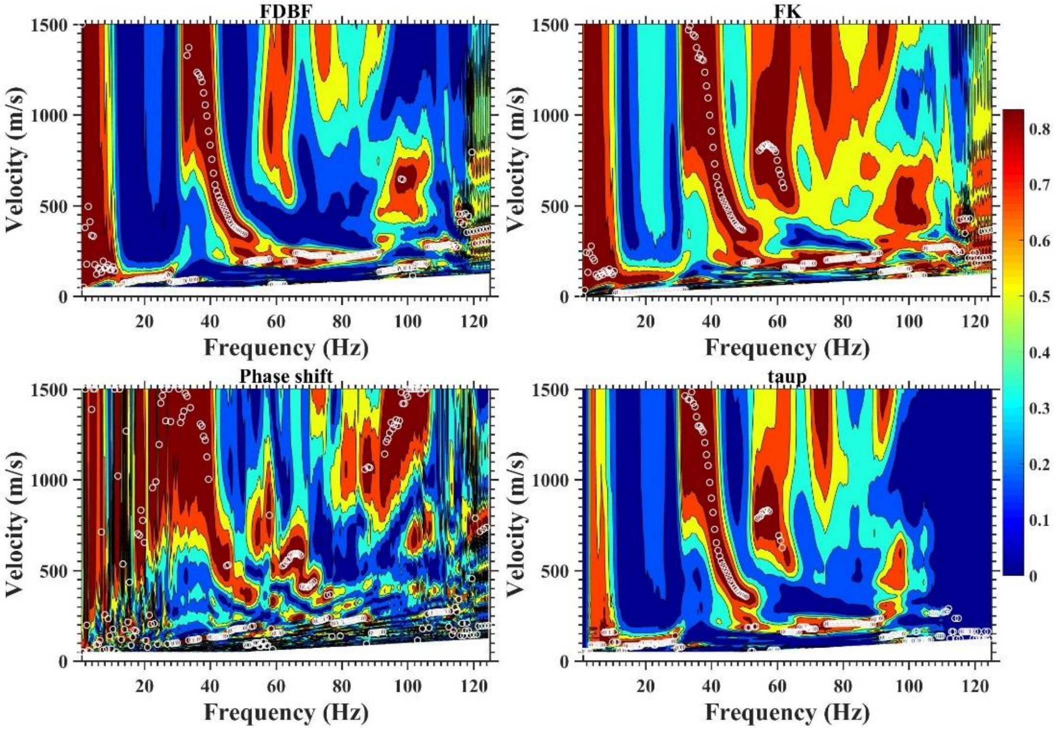

Figure A.7- Love wave dispersion curves generated using the four transformation methods for the Hot Springs site with a very shallow and complex bedrock topography, high-frequency point of curvature, and low noise levels. a) FDBF-cylindrical, b) FK, c) PS, and d) τp.

FDBF-cylindrical outperformance for sites with clear near-field effects

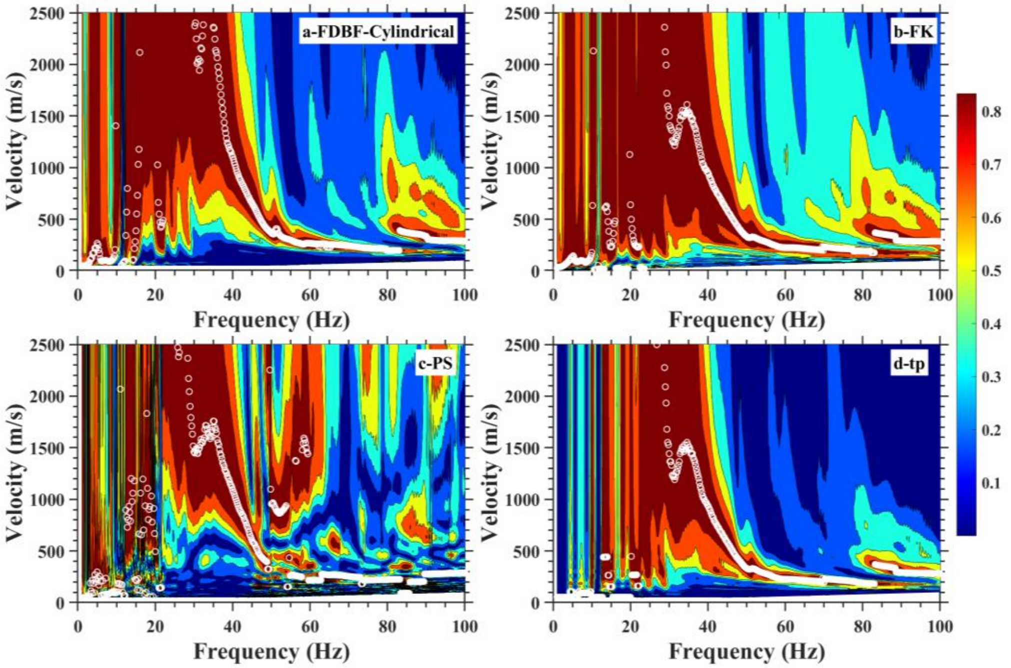

Figure A.8- Rayleigh wave dispersion curves generated using the four transformation methods for the Hardy site with a very shallow and complex bedrock topography, high-frequency point of curvature, and low noise levels. a) FDBF-cylindrical, b) FK, c) PS, and d) τp.

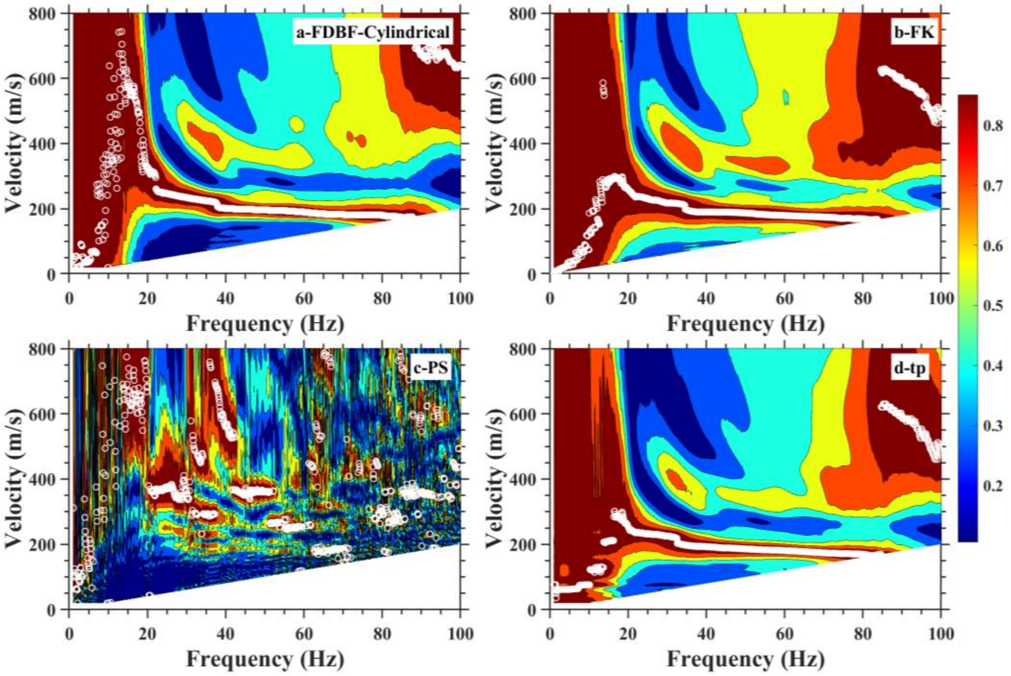

Figure A.9- Rayleigh wave dispersion curves generated using the four transformation methods for the Ozark site with a very shallow and complex bedrock topography, high-frequency point of curvature, and high noise levels. a) FDBF-cylindrical, b) FK, c) PS, and d) τp.

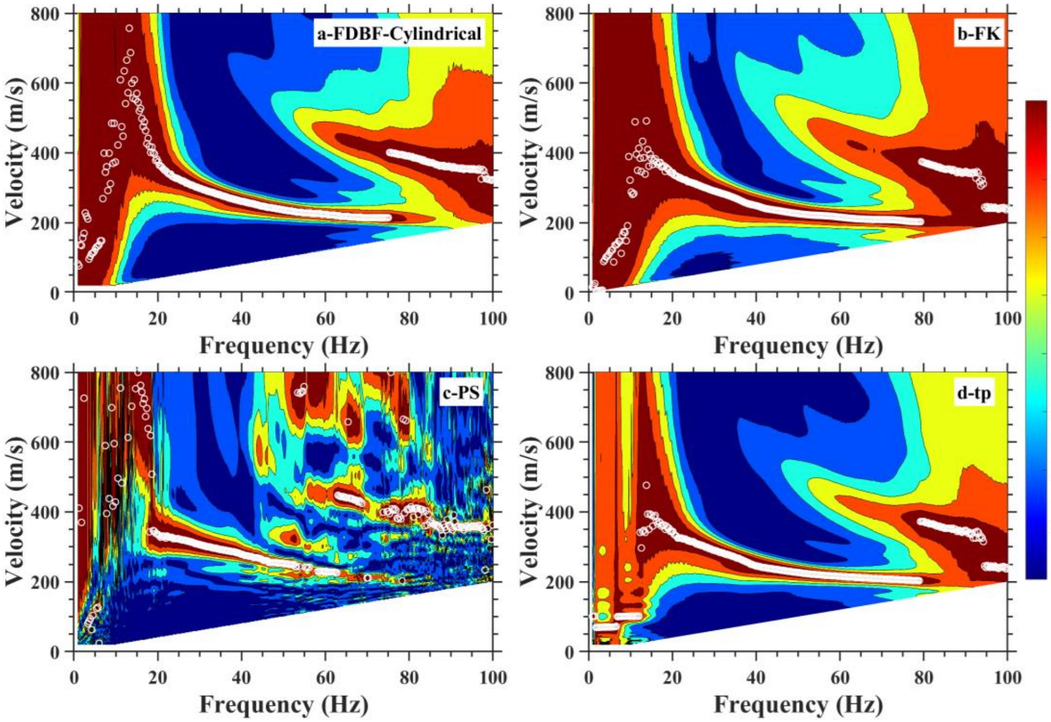

Figure A.10- Rayleigh wave dispersion curves generated using the four transformation methods for the Hardy site with a very shallow and complex bedrock topography, high-frequency point of curvature, and low noise levels. a) FDBF-cylindrical, b) FK, c) PS, and d) τp.

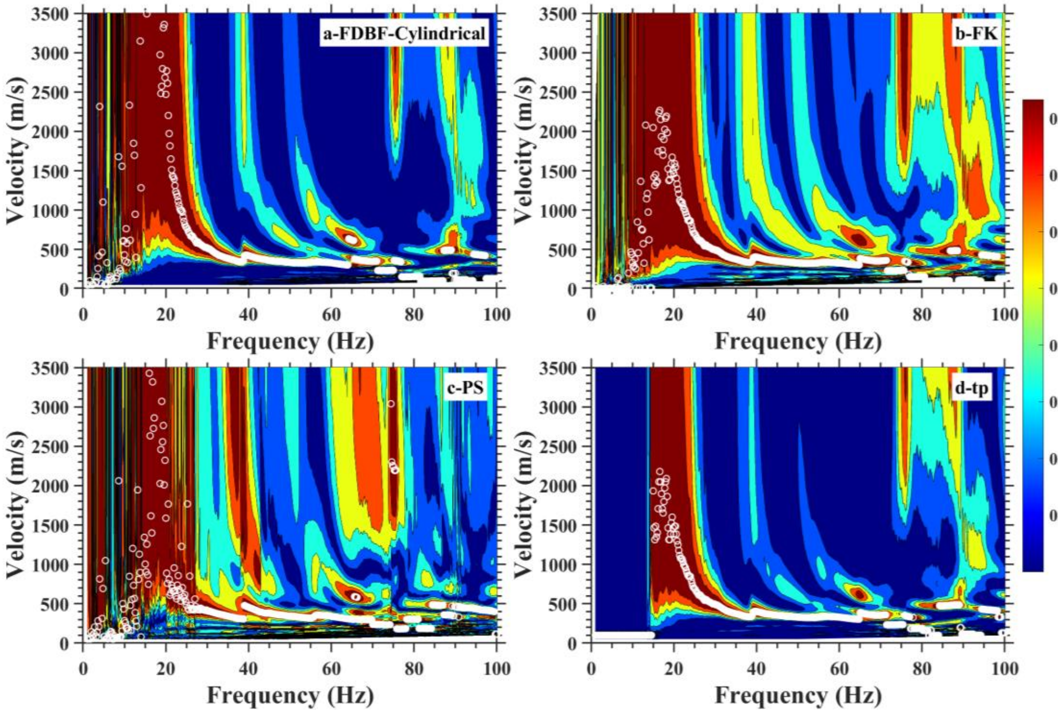

Figure A.11- Love wave dispersion curves generated using the four transformation methods for the Hardy site with a very shallow and complex bedrock topography, high-frequency point of curvature, and low noise levels. a) FDBF-cylindrical, b) FK, c) PS, and d) τp.

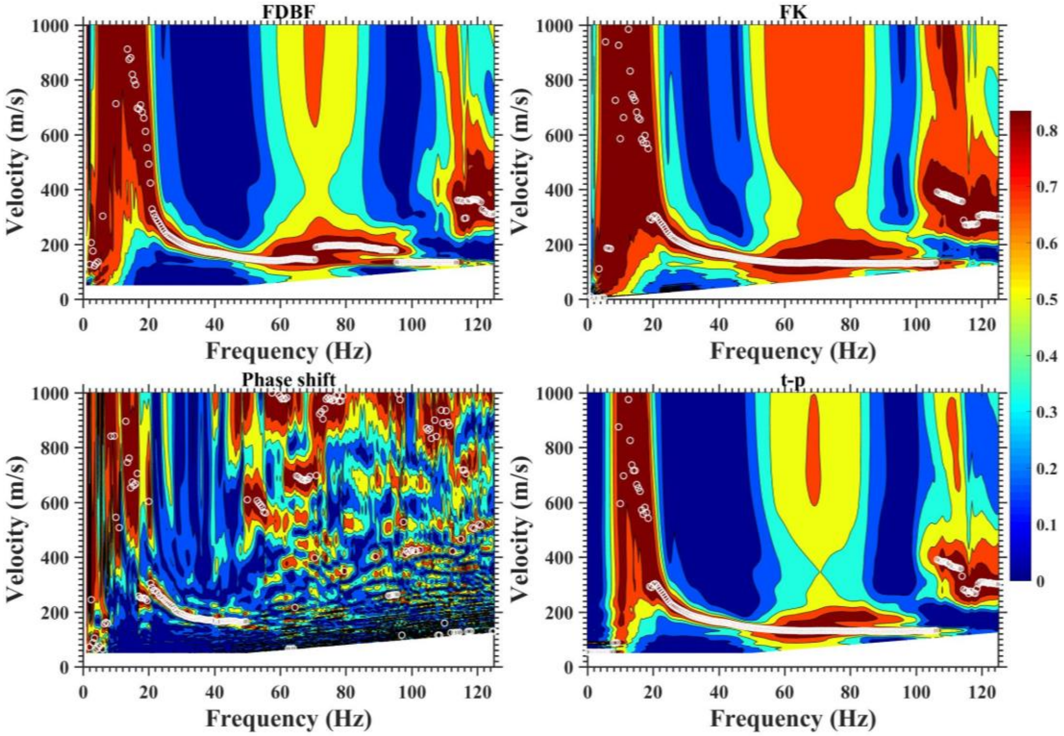

Figure A.12- Love wave dispersion curves generated using the four transformation methods for the Sand Gap site with a very shallow and complex bedrock topography, high-frequency point of curvature, and medium noise levels. a) FDBF-cylindrical, b) FK, c) PS, and d) τp.

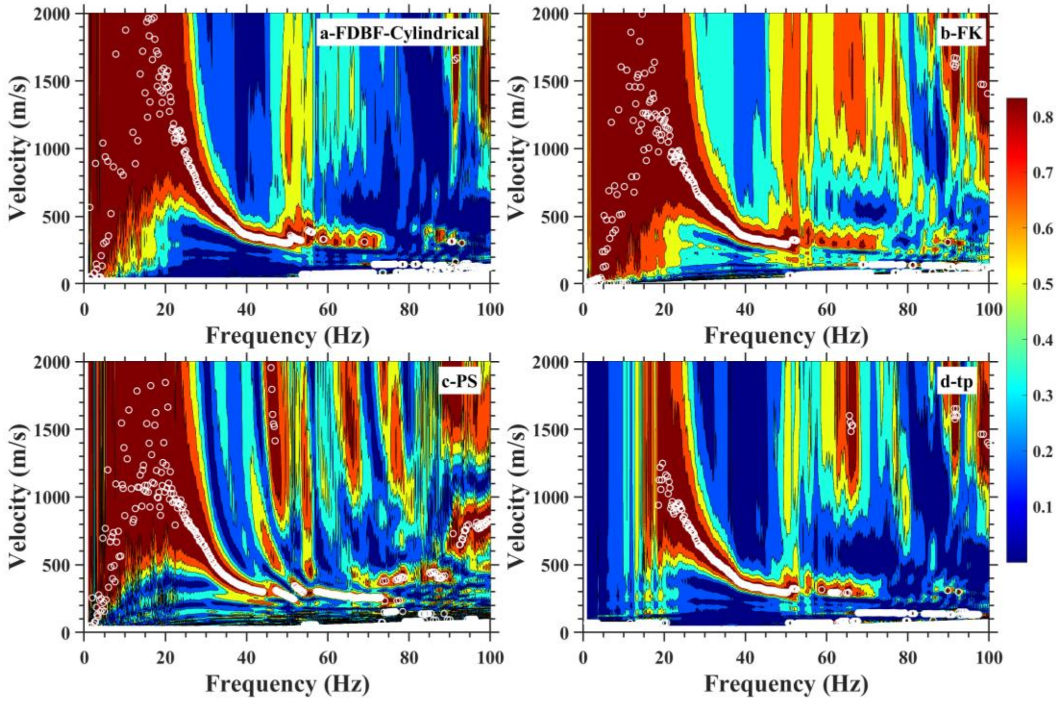

Figure A.13- Love wave dispersion curves generated using the four transformation methods for the Hot Springs site with a very shallow and complex bedrock topography, high-frequency point of curvature, and low noise levels. a) FDBF-cylindrical, b) FK, c) PS, and d) τp.

Sites with clear higher modes dispersion data

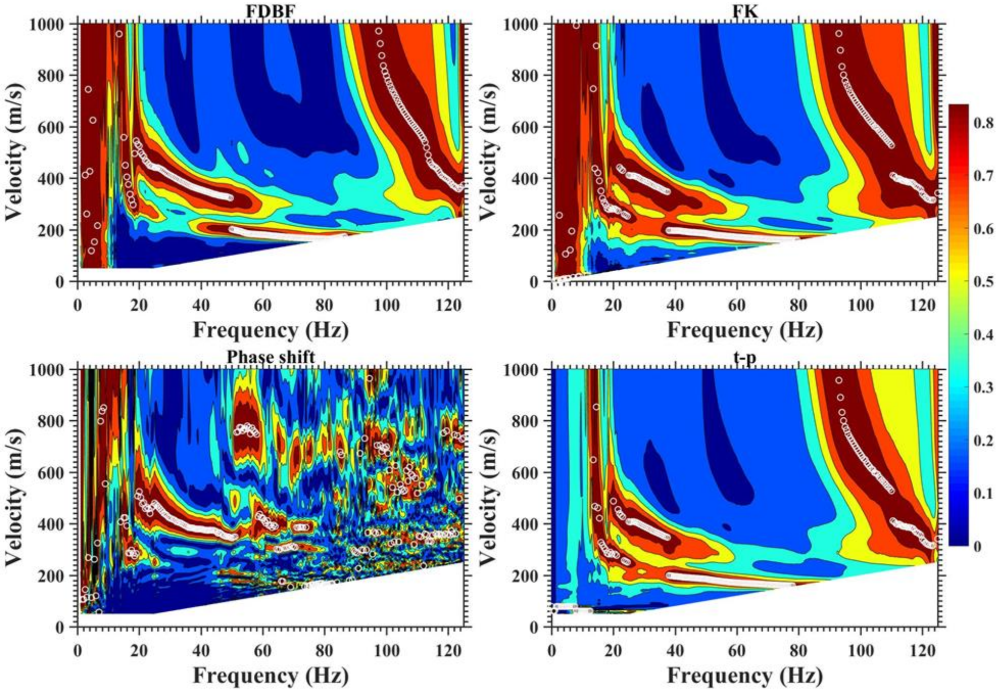

Figure A.14- Rayleigh wave dispersion curves generated using the four transformation methods for the Ozark site with a very shallow and complex bedrock topography, high-frequency point of curvature, and high noise levels. a) FDBF-cylindrical, b) FK, c) PS, and d) τp.

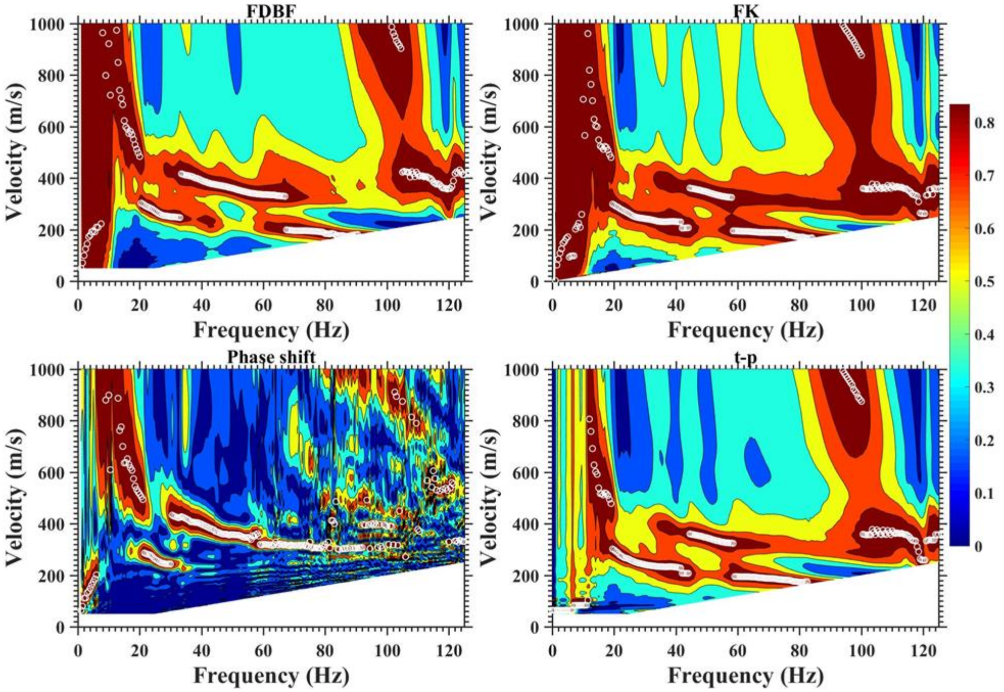

Figure A.15- Rayleigh wave dispersion curves generated using the four transformation methods for the Ozark site with a very shallow and complex bedrock topography, high-frequency point of curvature, and high noise levels. a) FDBF-cylindrical, b) FK, c) PS, and d) τp.

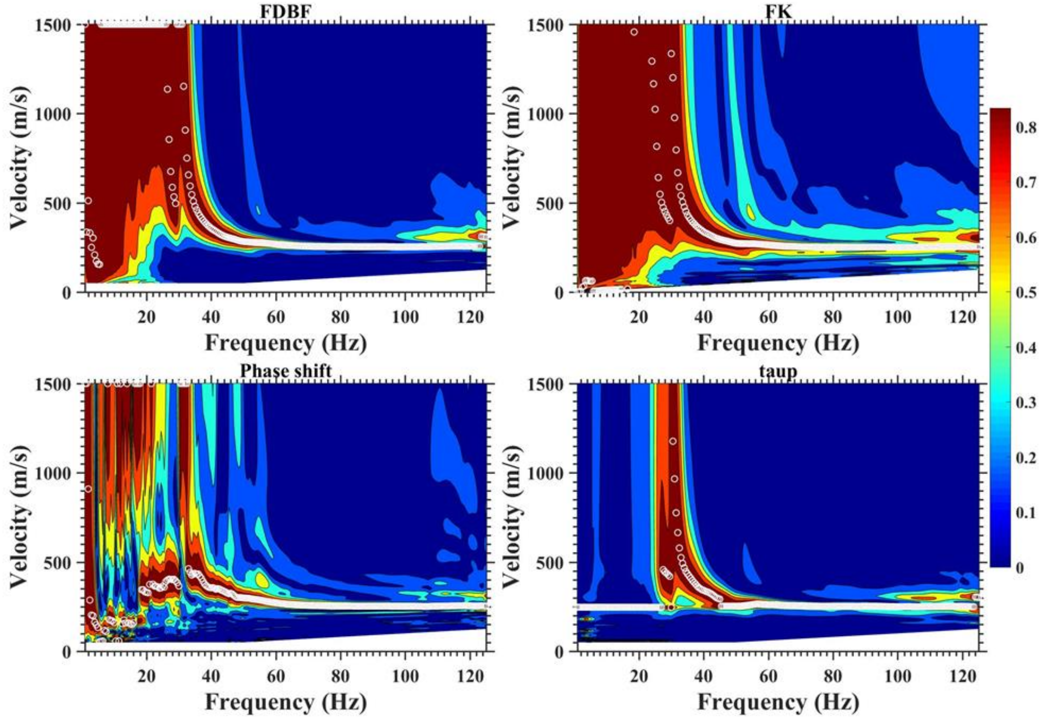

Figure A.16- Rayleigh wave dispersion curves generated using the four transformation methods for the Hardy site with a very shallow and complex bedrock topography, high-frequency point of curvature, and low noise levels. a) FDBF-cylindrical, b) FK, c) PS, and d) τp.

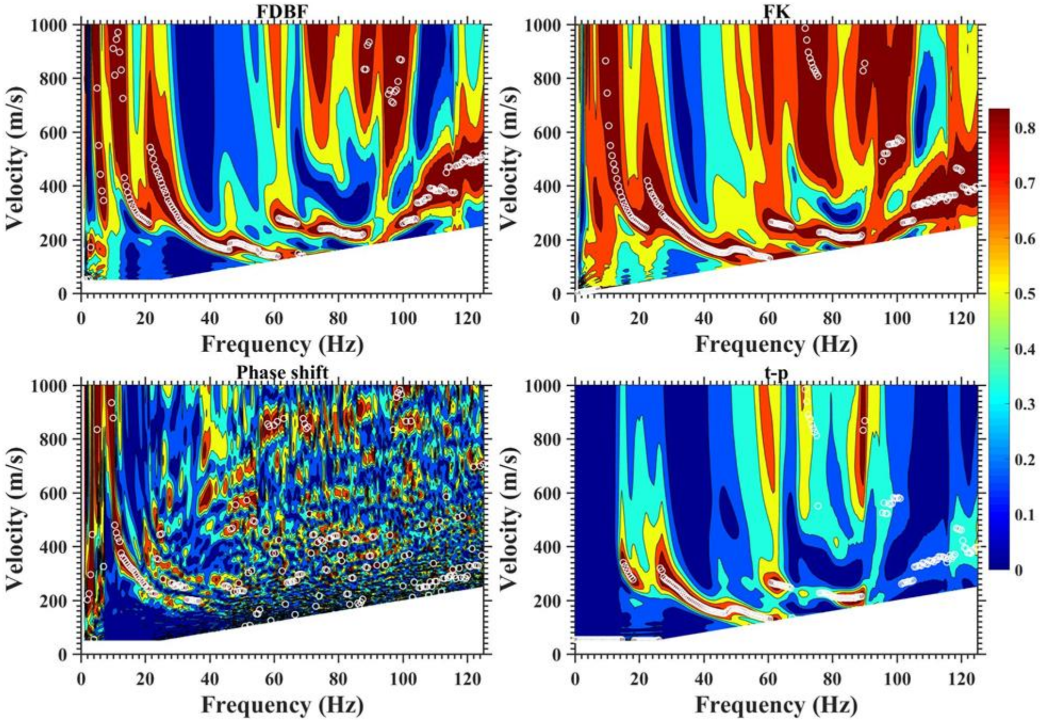

Figure A.17- Love wave dispersion curves generated using the four transformation methods for the Sand Gap site with a very shallow and complex bedrock topography, high-frequency point of curvature, and medium noise levels. a) FDBF-cylindrical, b) FK, c) PS, and d) τp.

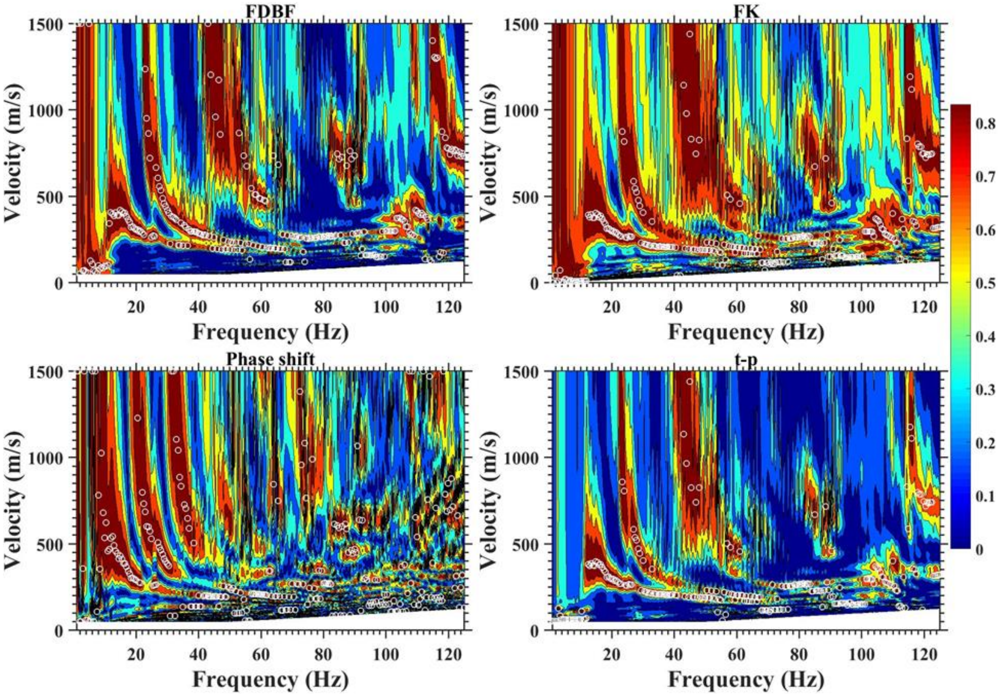

Figure A.18- Love wave dispersion curves generated using the four transformation methods for the Hot Springs site with a very shallow and complex bedrock topography, high-frequency point of curvature, and low noise levels. a) FDBF-cylindrical, b) FK, c) PS, and d) τp.

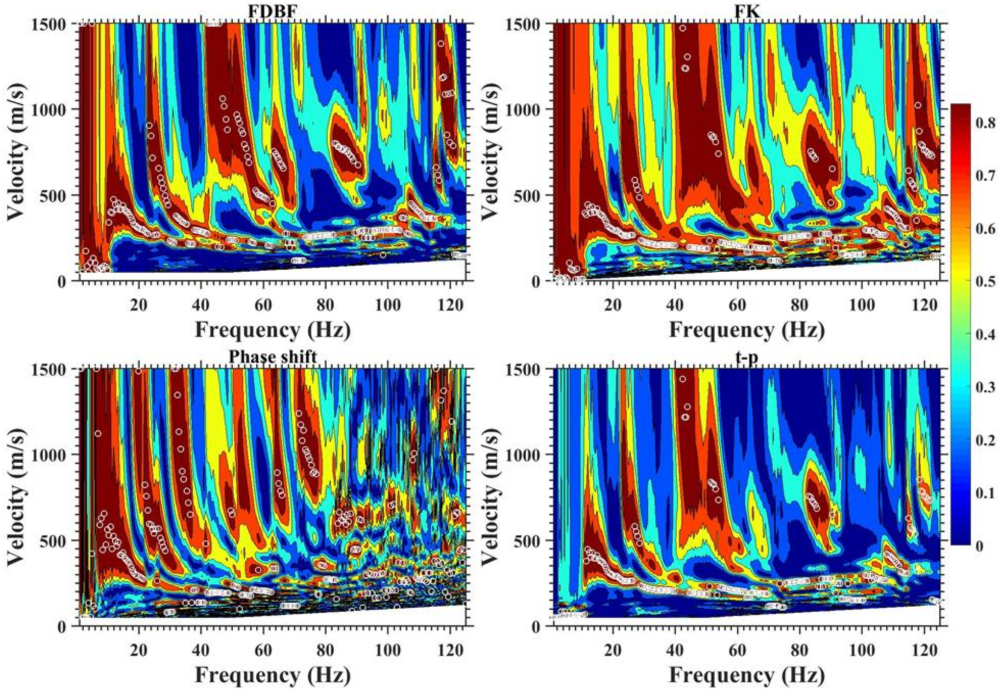

Figure A.19- Love wave dispersion curves generated using the four transformation methods for the Hot Springs site with a very shallow and complex bedrock topography, high-frequency point of curvature, and low noise levels. a) FDBF-cylindrical, b) FK, c) PS, and d) τp.